Dissertation

submitted to the
Combined Faculties for the Natural Sciences and for Mathematics
of the Ruperto-Carola University of Heidelberg, Germany
for the degree of
Doctor of Natural Sciences

Put forward by
Nikolas David Schnellbächer
born in Frankfurt am Main
Oral examination: 18.10.2017

Particle-based computer simulations of biological reaction-diffusion systems

Referees: Prof. Dr. Ulrich Schwarz
Prof. Dr. Heinz Horner

Summary

Particle-based computer simulations of biological reaction-diffusion systems

As the life sciences become more quantitative, particle-based simulation tools can be used to model the complex spatiotemporal dynamics of biological systems with single particle resolution. In particular, they naturally account for the stochastic nature of molecular reactions. Here I apply this approach to three different biological systems that are intrinsically stochastic. As an example for cellular information processing, we investigate the receptor dynamics of the interferon type I system and show that asymmetric dimerization reactions between signaling receptors in the plasma membrane enable cells to discriminate between different ligands. Using an information theoretic framework, we show why the binding asymmetry enables this system to become robust against ligand concentration fluctuations. As an example for structure formation, we analyze the role of stochasticity and geometrical confinement for the Min oscillations that bacteria use to determine their middle. We predict mode selection as a function of geometry in excellent agreement with recent experiments and quantify the stochastic switching of oscillation modes leading to multistable oscillation patterns. As an example for self-assembly, we use a multiparticle collision dynamics (MPCD) approach to address how shear flow modulates the assembly of rings and capsids. We find that an intermediate level of shear flow can help to suppress the emergence of malformed structures. Together, these projects demonstrate the power and wide applicability of particle-based computer simulations of biological reaction-diffusion systems.

Zusammenfassung

Teilchenbasierte Computersimulationen von biologischen Reaktions-Diffusions Systemen

Im Rahmen der zunehmenden Quantifizierung der Lebenswissenschaften ist es naheliegend, die komplexe räumliche und zeitliche Dynamik von biologischen Systemen mit teilchenbasierten Simulationsmethoden zu modellieren. Insbesondere wird dadurch der stochastischen Natur von molekularen Reaktionen auf natürliche Weise Rechnung getragen. Als ein Beispiel für zelluläre Informationsverarbeitung untersuchen wir die Rezeptordynamik des Interferon Typ I Systems und zeigen, dass Zellen durch asymmetrische Dimerisierungsreaktionen zwischen Signalrezeptoren in der Plasmamembran eine große Spannbreite von Liganden unterscheiden können. Mit einem informationstheoretischen Ansatz können wir zudem erklären, dass asymmetrische Bindungseigenschaften diesen Mechanismus robust gegen Fluktuationen in der Ligandenkonzentration machen. In einem Beispiel zur Strukturbildung analysieren wir die Rolle von stochastischen Effekten und räumlicher Begrenzung für Min-Oszillationen, die von Bakterien benutzt werden, um ihre Zellmitte zu finden. Wir untersuchen Modenselektion als Funktion der Systemgeometrie in exzellenter Übereinstimmung mit jüngsten Experimenten und quantifizieren den stochastischen Wechsel zwischen multistabilen Oszillationsmoden. Als ein Beispiel für Selbstassemblierung verwenden wir einen Multiparticle Collision Dynamics (MPCD) Ansatz, um der Frage nachzugehen wie Scherfluss die Assemblierung von Ringen und Kapsiden moduliert. Wir zeigen, dass für mittlere Werte der Scherrate Fehlbildungen unterdrückt werden können. In ihrer Gesamtheit zeigen diese Projekte klar die Stärke und vielfältigen Anwendungsmöglichkeiten von teilchenbasierten Computersimulationen von biologischen Reaktions-Diffusions Systemen.

Contents

1 Introduction

In this thesis I use modern tools of theoretical and computational physics to investigate three reaction-diffusion systems of large biological relevance to gain a deeper understanding of their stochastic dynamics. As an overarching theme I focus on the use of particle-based approaches and their advantage when trying to elucidate the molecular mechanisms which are at work in living cells. This allows me to address explicitly the role of fluctuations and spatial correlations for biological dynamics, reflecting on the discrete nature of molecular events. I pursue this aim in the light of recent advances towards quantitative biology, appreciating the interdisciplinary nature of modern life science where physics and biology meet in a very fruitful and promising way.

1.1 Signal transduction

Cells constantly process information about their environment, responding both to external and internal stimuli. The machinery that processes these information in living cells is made up of proteins and genes, which form highly intertwined interaction networks. Successful information processing is necessary to ensure that cells can make important decision given their current state and the environment they find themselves in. As a whole these networks can be understood as complex signal-processing units, that can communicate with each other by sending out various forms of signals. Here I will consider only biochemical signals, although cells can use their mechanical properties, their shape and their motility as well to send a signal to other cells.

On the single cell level this information processing task has a primary signal direction (going from top to bottom in figure 1.1A), and the process and the underlying mechanisms of how input signals are transmitted downstream to trigger cellular responses is what is best known as cellular signal transduction. Many signaling cascades are initiated by binding events of ligand molecules from the extracellular domain to cell-surface receptors. In this context cell surface receptors act as molecular sensors that probe the environment. These receptors are membrane proteins and can show rich behavioral dynamics and

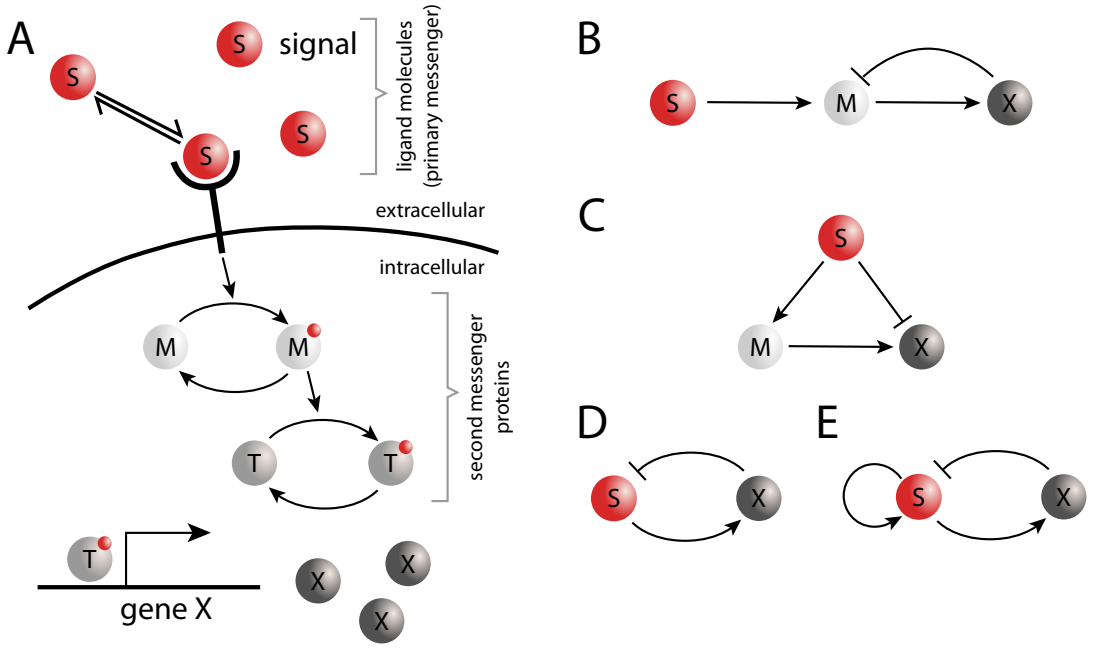

Figure 1.1 | Paradigmatic signaling motifs. **A** Generic depiction of a prototypical signal transduction cascade. Ligand molecules act as an initial signal (S), that start a cascade of further downstream reactions in the interior of a cell, which often leads to the synthesis of new proteins X. **B** – **E** Typical biochemical network motifs. **B** shows a classical negative feedback motif, **C** an *incoherent feed-forward loop*, while D depicts a delayed negative feedback for a two component system and **E** negative feedback coupled with a positive feedback loop. Figure conception adapted from de Ronde [1].

aggregation properties, as well as structural changes together with chemical modifications. They are for many signaling processes the bottleneck from the extracellular to the intracellular domain and thus responsible for how cells create an internal representation of the information that they receive in form of external signals.

Figure 1.1A shows a paradigmatic signal transduction pathway. Typically, soluble ligand molecules act as primary messengers and start the signal cascade by binding to their complementary cell surface receptor [2]. Activated receptors then relay the signal downstream by activating so-called effector proteins. These type of proteins are often called secondary messengers. In real signaling cascades these intracellular components typically form a complex and intricate protein interaction network, which in turn can trigger different cell responses, such as cell differentiation, proliferation, apoptosis or altered motility and migration patterns. Binding of transcription factors to specific promoter regions on the DNA then leads to altered gene expression profiles which eventually leads to the new synthesis of desired target proteins. Many of the involved intracellular reactions include chemical modifications, such as for example the addition of a phosphate or methyl group to messenger proteins (as indicated by the small red dot on the messenger (M) and transcription factor protein (T) in figure 1.1A). Typically,

only the modified state is the active one which relays the signal further downstream.

The increasing progress of fluorescence microscopy and super resolution techniques [3–10] allows us to quantify cellular signaling processes with unprecedented precision. On the theoretical side, a major breakthrough in the field of cellular signaling came with the realization that many aspects of biochemical signaling networks share common motifs, that give rise to similar behavior, independent of their explicit molecular implementation on the protein level [11, 12]. Dissecting these networks into smaller modular subunits often allows the identification and analysis of such network motifs, of which a few are exemplary shown in figure 1.1 B–E. By identifying generic network motifs and reaction topologies one hopes to distill general principles of how biochemical networks work [11, 13]. Having understood these principles on a modular level, the goal is to predict cellular responses by rewiring these modules according to their physiological layout. Many of the complex biochemical networks have a large resemblance to electronic wire diagrams of modern electric devices. This realization initiated a strong interdisciplinary effort from physics, mathematics and engineering sciences towards a new quantitative foundation of biology [14–16]. In the last two decades this approach has proven to be very successful and broadened our understanding of how cellular processes work from protein-protein interactions all the way up to tissue level responses.

A central question in cellular signaling is how cells can reliably perform various signal processing tasks in noisy environments [13]. Especially signaling molecules have been shown to occur at extremely low copy numbers, literally reaching the single molecule level. This naturally calls for an understanding of the role of stochasticity and noise propagation in signal pathways. Borrowing concepts from the engineering world and from signal and information theory, it has proven to be an interesting task to ask how cells process signals as robustly and with the degree of precision that is necessary to ensure successful cellular communication. Further hallmarks of cellular signal processing include the ability to adapt or align responses according to environmental cues and to process multiple stimuli of information simultaneously. In particular the ability to process signals robustly is a widely acknowledged feature [17–21], which deserves further attention.

1.2 The interferon system

In this thesis we study receptor signaling of the type I interferon system. Interferons are a class of soluble signaling molecules, that play a pivotal role in the innate immune response against viral disease. They owe their name to the fact that they are known to

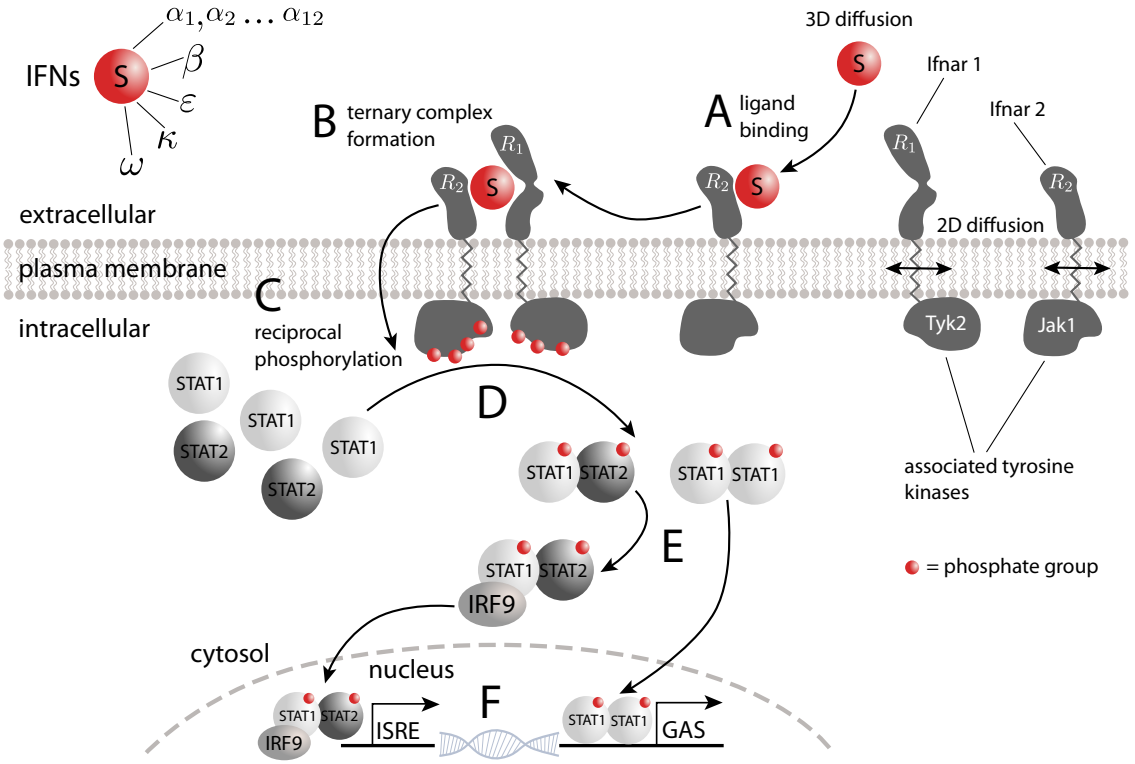

Figure 1.2 | Receptor dynamics and downstream signaling in the type I interferon system. The interferon (IFN) ligands can bind either of the two receptor subunits (R_1 or R_2) to form ligand bound receptor monomers (**A**). Upon recruitment of a complementary free receptor in the plasma membrane a ternary signaling complex can be established (**B**). This triggers further downstream processes on the intracellular side of the type I interferon signaling pathway (**C** – **F**). Although the ligand binding, receptor dimerization and downstream reactions are here depicted with unidirectional arrows to emphasize the primary signal flow in this pathway, they are all fully reversible chemical reactions.

interfere with viral replication [22] and can initiate a so-called antiviral state in cells, which is used to signal the presence of viral infections to neighbor cells. Interferons are a subfamily of the larger group of cytokine ligands. These signaling molecules can be secreted by almost all nucleated cells and act as molecular messengers to orchestrate parts of the immune response by recruiting immune cells to targeted locations within an organism.

For this purpose it is important to recapitulate that the immune response of living organisms is a very complex entity that works on different hierarchical and organizational levels. While almost any living organism has at least a rudimentary immune system, the degree of sophistication of the immune system increases with higher developed organisms. This explains why only jawed vertebrates have developed what is today summarized as an adaptive immune system which is not present in simpler life forms. In a nutshell, the immune system is composed of many cellular and non-cellular components broadly

ordered by assigning them into two orthogonal categories. The first is whether they are part of the *cellular* or the *humoral* part of the immune system, and the second axis groups them into *innate* or *adaptive* immunity. This overwhelming complexity makes it evident, that the coordination of the immune response strongly relies on inter-cellular communication. And this is where the interferons come into play. They act as immunomodulatory messenger molecules and orchestrate important parts of the immune response. In this role they are most well known for their antiviral protection. As a part of the innate immune response one often refers to them as the first line of defense against viral infections [22]. For a comprehensive overview over the type I interferon system and all its molecular details we refer to recent reviews on the subject [22, 23].

We will be interested in the early stage of interferon signaling at the receptor level. The binding of ligands initiates a signal which is relayed further downstream. The striking observation, that different ligands can elicit different cellular responses is our motivation to ask how information processing at the interferon type I receptor works. In this way we look at this classical signal transduction pathway as a cellular information processing task.

1.3 Pattern formation in biological systems

Patterns are ubiquitous in biological systems. They emerge in so many different places and on so many different scales, that it is challenging to find a unifying framework to describe them. Many patterns emerge through the principle of self-organization and include processes that range from autocatalytic reactions, intracellular protein gradients, cytoskeletal networks and developmental processes up to tissue morphogenesis [24]. Self-organization describes the emergence of structure in a system consisting out of many individual units, that individually are not ordered. The emergence of patterns is then caused by collective and typically highly dynamic interactions between the individual units, which cannot be explained by the individual properties alone. While the first observations and attempts in this direction were based on theoretical considerations by the work from Lotka [25, 26], Bray [27] and for example by the famous Belousov-Zhabotinsky reaction [28–30] it has nowadays become clear, that self-organization principles are of fundamental relevance in cell biology and are highly responsible for many of the rich cellular dynamics.

Self-organization manifests itself here in rich dynamical processes that the molecular machinery undergoes under the consumption of energy in the form of ATP or GTP. For this reason the interesting dynamics emerging from such systems have often been

referred to as dissipative systems and been dealt with in a more broader conceptual context by Priogine [31–33] and Haken [34]. Prominent examples which were used to explicitly showcase these characteristics in the intracellular domain are the self-organized structures and patterns generated by the interplay of Microtubuli (MT) and molecular motors which pull on them [35–37]. Similar patterning phenomena have also been observed for the acto-myosin network [38], where myosin II motors crosslink the system and are able to create rich actin network patterns. Since the role of active elements, such as the mentioned molecular motors of the last two examples, have been identified as crucial ingredients for the self-organization processes described here, systems of this kind are often referred to as *active gels* [39]. The maybe best studied example of a temporal pattern can be found in the eukaryotic cell cycle. Here the temporal oscillations of the cyclin-dependent kinase (CDK) act as a master regulator for cell cycle control [40, 41], giving a very prominent and important example for a self-organizing system that gives rise to a temporal oscillation.

For spatial pattern generation in biological systems the work by Alan Turing [42] is an important milestone. He proposed a mechanism that can lead to spatially inhomogeneous patterns by a diffusion-driven instability (*Turing instability*). This work has inspired much follow-up research until today [43–45] and is clearly a seminal contribution to the field. In his theory he introduced so-called morphogens as diffusible molecules that interact *via* a nonlinear reaction mechanism. However, it was criticized that there are almost none real-life systems which actually implement the Turing patterning mechanism on a molecular level. Still, his theoretical considerations were important, as they suggested a mechanism for a dynamic instability and inspired many others to work in the field of pattern formation. Although it turns out to be hard to find actual Turing systems, biological cells show many other interesting dynamic patterning systems. Many of those create very fascinating waves and show rich oscillatory behaviors [46] and are not seldom responsible for important biological functions. Today we have just started to understand the molecular basis and the physical mechanisms behind protein pattern formation [47]. The Min system in *E. coli* bacteria is an example of such a protein pattern forming system for which the molecular mechanism is well studied and which will be the topic of the next section.

1.4 The bacterial Min system

The bacterial Min proteins are a well studied example of a pattern-forming protein system that gives rise to rich spatiotemporal oscillations. It was discovered as a spatial

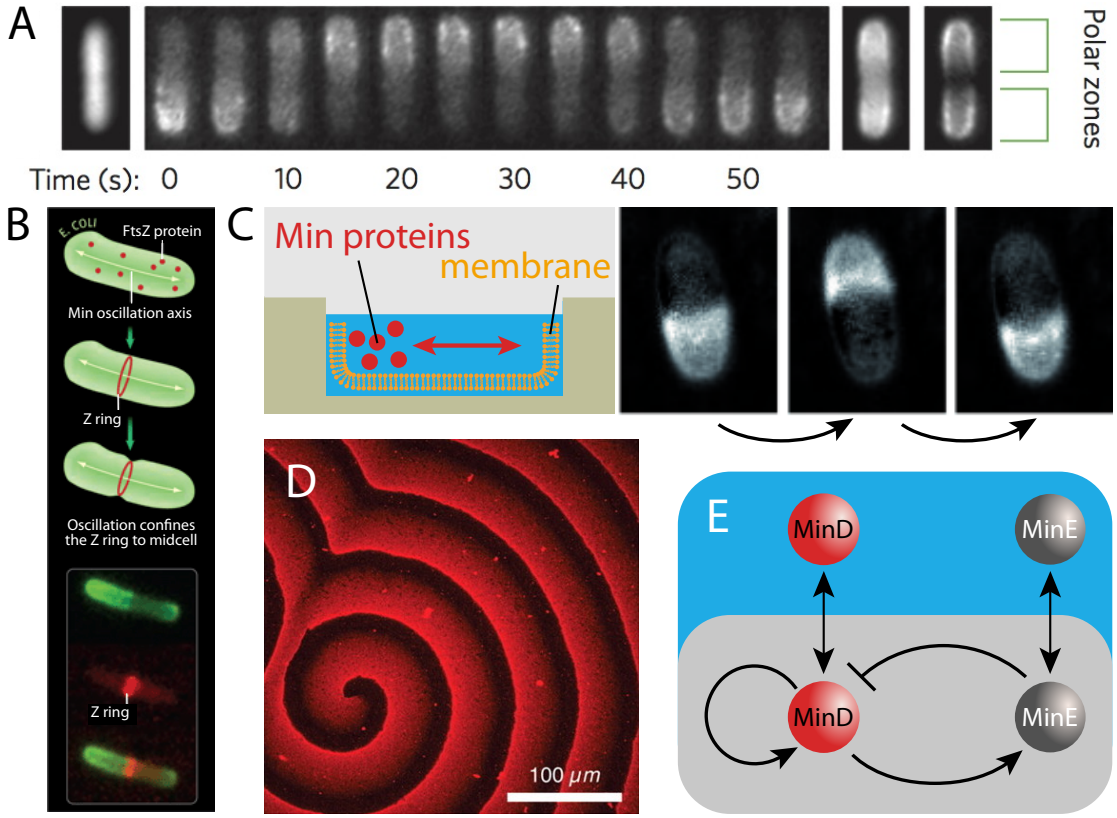

Figure 1.3 | The bacterial Min system. **A** shows characteristic pole-to-pole oscillations of fluorescently labeled Min proteins in an *E. coli* bacterium (image taken from [53]). **B** The oscillation patterns are used to determine midcell for symmetric cell division (image taken from [54]). **C** In confinement, Min oscillations can also be observed in *in vitro* experiments while they form traveling surface wave patterns on flat supported bilayers (**D**). Figures taken from [55] and [56], respectively. **D** Simplified reaction scheme of the Min proteins as a modified activator-inhibitor model with additional bulk-membrane cycling.

regulator in bacterial cell division, where it ensures symmetric division by precise localization of the divisome to midcell [48]. The dynamic nature of this protein system was demonstrated by live cell imaging in *E. coli* bacteria, where these proteins oscillate along the longitudinal axis between the cell poles of the rod-shaped bacterium, forming so-called *polar zones* [49–52] (compare figure 1.3).

Most bacteria use a cytoskeletal structure, a so-called Z-ring, for the completion of bacterial cytokinesis [57]. This Z-ring self-assembles from filaments of polymerized FtsZ-proteins, the prokaryotic homolog of the eukaryotic protein tubulin [58], which serve as a scaffold structure for midcell constriction and the eventual septum formation in the midplane. If successful, this process creates two equally sized daughter cells with an identical set of genetic information [59]. A necessary prerequisite for successful symmetric cell division is hence the targeted assembly of FtsZ towards midcell. In *E. coli* cells this is mediated by two independent mechanisms, nucleoid occlusion and the

dynamic oscillations of the MinCDE proteins [52, 60, 61]. While nucleoid occlusion prevents division near the chromosome, the Min system actively keeps the divisome away from the cell poles through the MinC-protein acting as FtsZ-polymerization inhibitor [52]. The characteristic pole-to-pole oscillations create a time-averaged concentration gradient with a minimal inhibitor concentration of MinC at midcell, suppressing Z-ring assembly at the cell poles [50–52]. Although MinC is indispensable for correct division site placement, it acts only as a passenger molecule, passively following the oscillatory dynamics of MinD and MinE [49, 50, 62].

On the molecular level, the oscillations emerge from the cycling of the ATPase MinD between a freely diffusing state in the cytosolic bulk and a membrane-bound state, induced by its activator MinE under continuous consumption of chemical energy by ATP-hydrolysis. In its ATP-bound form MinD homodimerizes and can subsequently attach to the inner bacterial membrane as ATP-bound dimers using a membrane targeting sequence in form of a C-terminal amphipathic helix [63–65]. Despite the fact that the physicochemical details of MinD membrane binding are not yet fully understood, it has been demonstrated that MinD membrane binding is a cooperative process [63, 66]. When being bound, MinD diffuses along the membrane. It also recruits MinE which in turn triggers the ATPase activity of MinD, breaking the complex apart and releasing all constituents back into the cytosol. MinD then freely diffuses in the bulk and can, after renewed loading of ATP and dimerization, rebind to the membrane at a new position. This cycling of MinD between two states is the core mechanism for wave propagation of the Min proteins. For a comprehensive overview on the underlying molecular processes, we refer to recent reviews on this topic [67–72].

1.5 Self-assembly

Self-assembly describes the spontaneous process by which a (seemingly) unordered system of constituents forms higher order complexes with a regular architecture. Protein self-assembly in biological system is a hallmark of living cells, with examples ranging from small signaling complexes through clathrin coats or viral capsids to large-scale cytoskeletal structures. Vital cellular functions rely on supramolecular protein complexes which self-assemble in the cellular context. Many biological self-assembly systems have inspired soft-matter approaches and were used as templates for synthetic material design. Inspired by the rich and diverse range of biomolecules which self-assemble into such supramolecular complexes, we try to understand the nature of the interactions that give rise to such complex architectures. A cornerstone for self-assembly is the

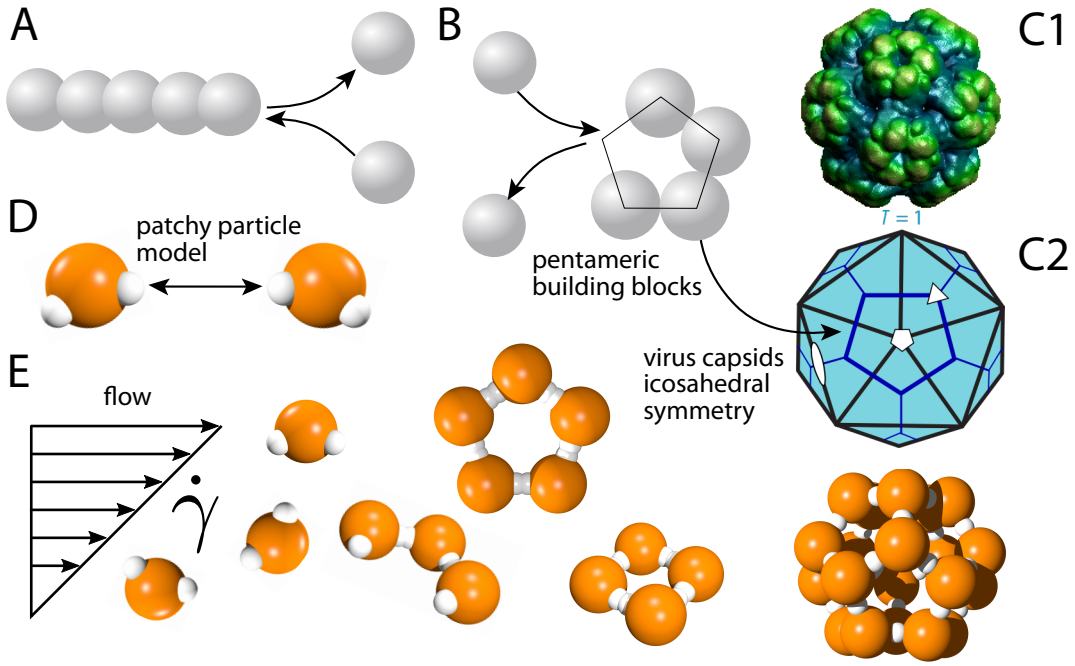

Figure 1.4 | **A** Polymerization reactions are a common self-assembly strategy to form filaments. **B** Ring assembly, here shown for pentameric rings, as an intermediate assembly structure. **C1** X-ray reconstruction of a Brome Mosaic virus capsid (Image taken from [73]). **C2** Schematic representation of an icosahedral $T = 1$ capsid with pentameric building blocks (Image taken from [74]). **D** Two monomeric patchy particles that interact *via* patches (small white spheres) on their surface. **E** Assembly of rings and capsids under the influence of shear flow.

selectivity of interactions. These selective interactions can be modeled or synthesized by using anisotropic interactions between monomeric assembly building blocks. A common approach to do so, is to use sticky patches on the surfaces of molecules, which convey selective interactions. From a theoretical point of view this approach is straight forward, since it is an easy way of approximating the true nature of actual anisotropic reactive properties of biomolecules. Also experimentally, modern patterning techniques allows to imprint sticky patches or surfaces on the molecular building blocks. The rich shape spectra that can be implemented arise from an intricate interplay of forces, particle shape and the topology of the molecular building blocks. Combined, they dictate the assembly outcome in a intertwined and highly dynamic way [75]. For this reason patchy particles are sometimes also referred to as *shape amphiphiles*, which is meant to emphasize their new role in potentially providing highly functional and designed assembly structures, and is used in contrast to the more classical notion of amphiphiles, by which one more typically would think of surfactants or block copolymers. In this work we use computer simulations to study assembly properties of patchy particle models theoretically. We are interested in rings and capsids as target structures. Capsids are the protein shells that virus particles build as a part of their replication life-cycle (compare figure 1.4). In

this way our approach here is one side inspired by the self-assembly of protein systems, but on the other side has clear implications for colloid science, where spherical shell particles could act as cargo containers with potential applications in drug delivery.

1.6 Outline of the thesis

Chapter 2 gives a brief overview over the methods and algorithms, that we used and developed for the work presented in this thesis. This mostly covers particle-based methods such as reactive Brownian dynamics in three and two dimensions and will also give an overview over related approaches with a similar scope.

Then we move to signal transduction in chapter Chapter 3. There we study the signal initiation of the type I interferon system. We focus on the receptor dynamics of this system, meaning the binding modes and their implications for the functionality of this signaling system. This involves a detailed treatment of the receptor ligand dynamics, which allow this system to act as a robust molecular sensor in noisy environments. For this purpose we analyzed the binding properties of the interferon system and compared them to standard pharmacological results. To address the question of how such systems in a more general way are able to discriminate signals, we developed an information theoretic framework to answer the question of *ligand discrimination* in a more rigorous and fully quantifiable way in Chapter 4. We conclude this part on signal transduction with a brief excursion into spatial stochastic receptor dynamics in Chapter 5.

Chapter 6 starts the second major part of this thesis and shows our results from stochastic particle-based simulations of the Min system. We used many of the presented methods from chapter 2 and focused on the role of stochasticity for oscillation mode stability. This lead to the observation of transient switching events between different oscillation modes and hence addresses the role of *multistability* in such nonlinear oscillatory systems.

Chapter 7 concludes this thesis and shows our results from a patchy particle self-assembly model. We use a mesoscopic simulation technique called multiparticle collision dynamics (MPCD) to analyze how forced flow can modulate the self-assembly process, using ring and capsid structures as exemplary self-assembly models. This is inspired by the very fascinating an efficient self-assembly that viruses demonstrate in physiological conditions. As an integral part of their replication cycle they very robustly and efficiently construct their protein shell, a protein container typically showing a high degree of symmetry. This allows us to study the intricate interplay between complex

assembly, kinetic trapping and malformed assembly intermediates, while having a sound hydrodynamic resolution and the possibility to apply non-equilibrium conditions to the system. Although this route we take here is inspired by viral capsid self-assembly, it has clear general implications for colloidal and soft-matter systems, with an application for synthetic self-assembly processes in mind. For the latter it will be crucial to find optimal self-assembly conditions and show how for example flow can be used to enhance assembly yields.

I

Methods

2 Particle-based simulation methods

2.1 Overview

Biological function arises directly through the diffusion and reaction of its constituents in and around living cells. This shall motivate us to try to understand how diffusive motion of biomolecules and reactions among them lead to emergent phenomena on the ground of their physical properties. In the following I will use the term particles to simply describe the biomolecules (proteins, lipids, ions, etc.) of interest. For most of this work I will consider proteins and reactions will mean protein-protein interactions, although many aspects of the theoretical treatment are equally applicable in a more general setting.

The degree of molecular detail that one needs to account for depends very much on the kind of question one addresses. Conceptually it is clear that reaction-diffusion processes can always be decomposed into two coupled parts, a transport process, which determines the particle motion and a reaction process which describes chemical reactivity. At the very least it is conceptually evident that two particles must come in close proximity of each other in order to undergo a chemical reaction. From this point of view one might assume that by default their spatial localization must play a key role in this process.

Although it is clear that fundamentally the reaction process itself is a process of quantum chemical nature, for our purpose it is prohibitive to study the systems of interest at quantum chemical level of detail, since this would prevent us from resolving sufficiently long time scales and sufficiently large systems.

Concerning the transport process I will focus on diffusive motion, meaning the Brownian motion of biomolecules in a solvent. Different transport modes like advection and active transport processes are of course also important in many cellular contexts, but beyond the scope of this work.

If diffusive time scales are fast compared to reactive time scales, a *well-mixed* assumption might be valid and one can convert the single particle resolution to effective

concentrations $c(t)$. In this limit the spatial resolution is not important and reactions between chemical species are typically set up following *mass action kinetics* leading to systems of ordinary differential equations (ODEs) which can readily be solved numerically. If space does matter, one can describe the system at hand in a deterministic manner by setting up the corresponding set of partial differential reaction-diffusion equations (PDEs). In terms of concentration fields $c(\boldsymbol{r}, t)$, the PDE for a generic species i reads

$$\frac{\partial c_i(\boldsymbol{r}, t)}{\partial t} = \Delta c_i(\boldsymbol{r}, t) + R\Big(\{c_j(\boldsymbol{r}, t)\}, t\Big). \tag{2.1}$$

The reaction term R on the right hand side accounts for all reactions and thus can in principle be a function of all concentrations in the system.

The use of concentrations assumes that the actual copy numbers of molecules are large, for this macroscopic mean field description to hold. If this is no longer the case, the system is best described by stochastic methods. If the diffusive time scale is again fast compared to all other time scales, we can again make the *well-mixed* assumption but still consider single particles, leading to the *chemical master equation* (CME). Simple systems with constant or linear rates can often be solved analytically on this level. More complex systems can then be addressed by direct stochastic simulations [76–78] or faster approximate stochastic simulation algorithms (SSAs) [79–82]. Since this field was pioneered by Gillespie, these techniques are often loosely grouped under the common reference to Gillespie-type algorithms. These methods account for stochasticity that results from fluctuations in copy numbers of the involved particles, but assume a spatially homogeneous reaction volume.

The logical consequence, when both spatial and single particle resolution are required, is the use of so-called stochastic spatial simulation algorithms. Since many biochemical processes that carry out important biological functions, *e.g.* controlling cellular communication, signal transduction and gene regulation, happen in a low copy number regime, they are the perfect application field of such methods. Although the goal is clear, there are still many different methods using different strategies to solve reaction diffusion problems on this level of molecular detail. A straight forward extension of the above mentioned Gillespie type SSAs is the reaction-diffusion master equation (RDME). In this approach the system volume Ω is split up into smaller sub-volumes, with each of them assumed to be *well-mixed*. Hence in each sub-volume one can solve the *well-stirred* chemical master equation and includes particle exchange between such sub-volume voxels to account for molecular transport mechanisms.

Another criterion for methodological distinction is the use of so-called on- versus

off-lattice methods. If particle positions are restricted to a lattice, one obviously gains computational efficiency but must adjust lattice constants and jump processes between lattice sites to match macroscopic transport characteristics of the molecular process, that one wishes to map. In the sake of brevity I will only focus on off-lattice methods, where particle positions are continuous space variables $\boldsymbol{r} \in \mathbb{R}^d$, for a d-dimensional system.

A second conceptual difference between stochastic spatial simulation algorithms is the distinction between iterative fixed time step schemes (often loosely referred to as normal Brownian dynamics (BD)) and event-driven schemes. In standard iterative schemes one fixes a global propagation time step Δt, which sets the accuracy of the method and must be chosen to resolve all spatial and temporal features of relevance. For dilute systems it has long been realized that fixed time steps can become inefficient, since most of the computational time could be "wasted" by diffusing particles in rather empty space.

Using more sophisticated event-driven algorithms can help to overcome this shortcoming. A very accurate event-driven spatial stochastic algorithm is the application of Green's function reaction dynamics (GFRD) [83, 84]. It uses analytical calculations and solves the reaction-diffusion dynamics on the level of two-particle interactions exactly. By calculating so-called protective domains around all particles, the algorithm finds the largest diffusive jumps that the system can do, before it must resolve the next reaction event, and iterates diffusive motion and reactions based on a next-event list. In the most recent version this algorithm is implemented in eGFRD and has also successfully combined in hybrid schemes with conventional BD and molecular dynamics (MD) [85]. This algorithm is particularly suited to assess the fundamental precision with which biochemical networks can function, as demonstrated in [86], where the authors revisit the classical Berg-Purcell limit [87] with spatial stochastic simulations. The above mentioned Gillespie algorithm is also an example for an event-driven method. It calculates next reaction event times and moves forward in time by iterating through reaction events.

An alternative route has been taken by Schöneberg *et al.* [88]. The authors use a normal Brownian dynamics setup but use potentials and interaction forces to describe both reaction events and geometrical properties such as confinement and volume exclusion. The usage of potentials in BD settings by itself is rather conventional, and has been widely applied in the past, also for protein-protein diffusional encounters [89, 90], but not with the notion of explicit chemical reactions. While allowing more molecular detail in the type of physical interactions, it equally becomes computationally more demanding. A successful application of this approach for G-protein coupled receptor systems can be found in [91].

Overall speaking, stochastic spatial simulation tools have proven to be an invaluable tool to understand the role of spatial organization for many cellular functions. For a protein kinase signaling cascade Takanase *et al.* [92] could show that the spatiotemporal correlations can qualitatively change the response properties. In a similar manner Mugler *et al.* [93] showed that membrane clustering of receptors and rebinding processes are important for biochemical signaling in general and addressed the role of spatial partitioning for common reoccurring signaling motifs [94]. The role of serial rebinding of ligands to receptor clusters has also been explored by Andrews [95]. By explicitly resolving the diffusion of transcription factors Van Zon *et al.* [96] showed that the noise characteristics can change significantly and found lower bounds for the precision of transcriptional regulation [97]. And even in simple enzymatic schemes Van Albada and coworkers demonstrated that the spatial localization of enzymes leads to drastically changed outcomes, when compared to standard mean-field results [98].

For the work in this thesis we used standard Brownian dynamics methods with fixed propagation time steps Δt and different reactivity models for different biological systems, as I will explain in the following. I will refer to these kind of techniques collectively as reactive Brownian dynamics. For a review on continuous space (off-lattice) particle-based simulation tools see [99], and for a detailed comparison of reactive Brownian dynamics and the state of the art of event-driven methods (in particular GFRD) we refer to a recent review by Sokolowski and ten Wolde [100]. A more general review article in this broader field can be found here [101].

2.2 Free diffusion

The motion of molecules in absence of any confinement or additional forces will be described by free diffusion. This constitutes the standard method for particle motion for many simulations we used in this work, unless otherwise noted. In the picture of a single particle, free diffusion is governed by the Fokker-Planck equation (FPE)

$$\frac{\partial}{\partial t}\, p(\boldsymbol{r}', t + \Delta t \,|\, \boldsymbol{r}, t) = D\, \nabla^2 p(\boldsymbol{r}', t + \Delta t \,|\, \boldsymbol{r}, t). \tag{2.2}$$

This FPE is identical to what is commonly referred to as the standard diffusion equation [102] with diffusion coefficient D, where $p(\boldsymbol{r}', t + \Delta t \,|\, \boldsymbol{r}, t)$ is the probability to find the particle at time $t + \Delta t$ at position $\boldsymbol{r}'$ given that it was at $\boldsymbol{r}$ at time t. We use the initial

condition

$$p(\boldsymbol{r}', t\,|\boldsymbol{r}, t) = \delta\Big(\boldsymbol{r}' - \boldsymbol{r}\Big) \tag{2.3}$$

and demand that large diffusive jumps happen with vanishing probability

$$p(r' \to \infty, t + \Delta t\,|\,\boldsymbol{r}, t) = 0\,, \quad \text{for} \quad r' = |\boldsymbol{r}'|. \tag{2.4}$$

Then equation (2.2) is solved by the free diffusion *Green's function*

$$p(\boldsymbol{r}', t + \Delta t\,|\,\boldsymbol{r}, t) = \frac{1}{(4\pi D\Delta t)^{d/2}} \exp\Big(-(\boldsymbol{r}' - \boldsymbol{r})^2/(4D\Delta t)\Big) = p_{\text{free}}(\Delta\boldsymbol{r}, \Delta t)\,, \tag{2.5}$$

which is also better known as the free diffusion propagator p_{free}, which only depends on $\Delta\boldsymbol{r} = \boldsymbol{r}' - \boldsymbol{r}$ and Δt. Here d is the dimensionality of the system or the diffusion process we describe. Since this diffusion propagator is nothing more but a d-dimensional normal distribution, one can propagate particle positions in space by drawing normally distributed random variates, with the appropriate variance as specified in equation (2.5). This is equivalent to the commonly derived overdamped *Langevin* equations, where the stochastic dynamics for the Brownian motion come from a *Wiener process*, which in practice leads to an identical implementation for the particles position update per time step Δt. Since diffusive motion and the statistics of diffusion is one of the best studied processes in physics, there exist many solutions for diffusion equations with different types of boundary conditions in the rich literature on the subject [102, 103].

2.3 Reactivity models

By reactions we refer to chemical reactions and will borrow the typical terminology from chemical kinetics to describe them. We will focus on first order (unimolecular) and second order (bimolecular) reactions only, since they are sufficient to cover most of the biological processes that we are interested in and additionally allow for a clear interpretation in terms of molecular events on the level of spatial resolution that we are working at.

First order reactions

A generic unimolecular reaction has the form

$$A \underset{k_{\text{off}}^{(1)}}{\overset{k_{\text{on}}^{(1)}}{\rightleftharpoons}} B\,, \tag{2.6}$$

where $k_{\text{on}}^{(1)}$ and $k_{\text{off}}^{(1)}$ are the macroscopic forward and reverse reaction rates. This means that $k_{\text{on}}^{(1)}$ quantifies the macroscopic rate of change of the product concentration c_B in the sense that

$$\frac{dc_B(t)}{dt} = +k_{\text{on}}^{(1)} c_A(t) = -\frac{dc_A(t)}{dt} \tag{2.7}$$

is satisfied. Without further ado we could allow several product species in reaction scheme (2.6), but since this would not alter the reaction mechanism for the unimolecular case we will not consider this case for now. The standard exponential solution to equation (2.7) reveals immediately that the macroscopic first order reaction rate $k_{\text{on}}^{(1)}$ is the inverse of the mean life time $\tau^{(1)}$ that an educt particle of type A needs to "decay" into a particle of type B *via* this reaction channel ($k_{\text{on}}^{(1)} = 1/\tau^{(1)}$). Using the system volume Ω to convert the concentration of A particles $c_A(t)$ back to particle copy numbers $n_A(t)$ *via* $n_A(t) = \Omega\, c_A(t)$, we immediately note that after a finite time period of Δt, on average $n_{A,r}$ A-particles will have decayed due to this reaction. $n_{A,r}$ is given by

$$n_{A,r}(\Delta t) = n_A(0) - n_A(\Delta t) = n_A(0)\Big(1 - \exp(-k_{\text{on}}^{(1)}\Delta t)\Big)\,, \tag{2.8}$$

such that, on a single particle level, the probability for a particle of type A to react during a time window Δt is given by

$$p_{\text{react}}(\Delta t) = \frac{n_{A,r}(\Delta t)}{n_A(0)} = 1 - \exp\Big(-k_{\text{on}}^{(1)}\Delta t\Big) = k_{\text{on}}^{(1)}\Delta t + \mathcal{O}\Big(\Delta t^2\Big). \tag{2.9}$$

The last approximation is valid for $k_{\text{on}}^{(1)}\Delta t \ll 1$, which constrains the choice of Δt. The most important realization from this consideration is that first-order reactions are independent of the spatial configuration. Secondly, the microscopic reaction picture as given in equation (2.9) tells us that for first order processes the macroscopic reaction rate is equivalent to the microscopical reaction rate $k_{\text{on}}^{1} = k_a^1$, where we introduce k_a to denote intrinsic microscopic reaction rates. The difference between the two will become apparent in the treatment of bimolecular reaction events. Typically, the reaction rates that can be measured in common experimental settings correspond to macroscopic rates, although the explicit experimental settings must be taken into account very carefully in

all cases. For all practical purposes this tells us that first order processes are *Poisson* processes and their reaction probability is calculated as given in equation (2.9).

If a given particle can react *via* multiple first order reactions (reaction channels), a sequential application of equation (2.9) would lead to a bias towards the first reaction that is attempted. Instead the correct probability for reaction channel j to "fire" among N available reactions must be calculated as

$$p_{\text{react},j}(\Delta t) = \underbrace{\frac{k^{(1)}_{\text{on},j}}{\sum_{i=1}^{N} k^{(1)}_{\text{on},i}}}_{\text{statistical weight of } j\text{-th channel}} \times \underbrace{\left[1 - \exp\left(-\Delta t \sum_{i=1}^{N} k^{(1)}_{\text{on},i}\right)\right]}_{\text{prob. for any first order reaction to occur}} , \tag{2.10}$$

avoiding any bias in the reaction attempt.

Bimolecular encounter

Next we consider bimolecular reactions of the following type

$$A + B \underset{k_{\text{off}}}{\overset{k_{\text{on}}}{\rightleftharpoons}} C \,, \tag{2.11}$$

where again k_{on} and k_{off} describe the macroscopic reaction rates in the sense that they quantify the rate of change for a spatially homogeneous concentration such that

$$\frac{dc_C(t)}{dt} = k_{\text{on}} c_A(t) c_B(t) - k_{\text{off}} c_C(t) \tag{2.12}$$

holds. Equation (2.12) also reveals why explicit spatial treatment of bimolecular reactions is starting to become more challenging, merely by the fact of being the lowest order reaction process that is nonlinear in the educt concentration. While the uniform counterpart in equation (2.7) is still linear in concentrations, this is no longer the case here. In the generic scheme (2.11) the macroscopic equilibrium constant K_{eq} for reactions of this type is then simply

$$K_{\text{eq}} = \frac{k_{\text{on}}}{k_{\text{off}}} = \frac{c_C}{c_A\, c_B} = \frac{1}{K_{\text{D}}} \,, \tag{2.13}$$

where c_x denotes the concentration of species x, and the equilibrium dissociation constants $K_{\text{D}} = 1/K_{\text{eq}}$ is simply the inverse equilibrium constant.

Now the fundamental difference compared to the first order case lies in the fact, that a pair of A and B particles must first be in close spatial proximity in order for a reaction event to happen. At this point it is very helpful to conceptualize bimolecular

reactions as a clear two step process. 1) The diffusive motion can create an encounter between the two educt particles (a state that we will from now on refer to as *encounter complex/state* $\mathcal{E}$), which has not yet reacted to the final product state. 2) A particle pair that happens to be in such an encounter state by their diffusive transport properties can subsequently react to form the product according to the available reaction channels, such as for example given in (2.11). The *encounter complex* picture can be cast into the following schematic two-step description

$$A + B \underset{k_{\mathrm{D,b}}}{\overset{k_{\mathrm{D}}}{\rightleftharpoons}} \underbrace{A \cdot B}_{\mathcal{E}} \underset{k_{\mathrm{d}}}{\overset{k_{\mathrm{a}}}{\rightleftharpoons}} C\,, \tag{2.14}$$

where the macroscopic reaction (2.11) is extended by an intermediate $A \cdot B$ state, denoting an A–B pair in encounter $\mathcal{E}$. Here k_{D} and $k_{\mathrm{D,b}}$ denote the diffusive forward and reverse rates, by which the encounter situation is created due to particle diffusion, and k_a and k_d are the intrinsic (microscopic) association and dissociation rates, respectively. This concept of an *encounter complex* as an intermediate step is at the very least conceptually very valuable since it allows to decouple the diffusive motion and the pure reactive process from each other in a clear way. Assuming the concentration of the encounter complex $(A \cdot B)$ to be in steady state, *i.e.* $\partial_t c_{A\cdot B} = 0$, one can derive the following useful relations

$$k_{\mathrm{on}} = \frac{k_D\, k_a}{k_a + k_{D,b}} \quad \text{and} \quad k_{\mathrm{off}} = \frac{k_{D,b}\, k_d}{k_a + k_{D,b}}\,, \tag{2.15}$$

connecting the macroscopic reaction rates from equation (2.11) with the microscopic ones from equation (2.14) and makes it possible to express the equilibrium constant K_{eq} as

$$K_{\mathrm{eq}} = \frac{c_C}{c_A c_B} = \frac{k_{\mathrm{on}}}{k_{\mathrm{off}}} = \frac{k_D k_a}{k_{D,b} k_d} = \left(\frac{k_D}{k_{D,b}}\right)\left(\frac{k_a}{k_d}\right). \tag{2.16}$$

The result from equation (2.15) has interesting limiting cases. For reactions which are **diffusion limited** we assume $k_a \gg k_{D,b}$, leading to

$$k_{\mathrm{on}} \simeq k_{\mathrm{D}} \quad \text{and} \quad k_{\mathrm{off}} = k_{\mathrm{D,b}} \frac{k_d}{k_a}. \tag{2.17}$$

If, on the other end of the spectrum, we have a **reaction limited** scenario, assuming $k_{D,b} \gg k_a$, we find that

$$k_{\mathrm{on}} \simeq k_a \frac{k_D}{k_{D,b}} \quad \text{and} \quad k_{\mathrm{off}} \simeq k_d \tag{2.18}$$

holds. These central results can be nicely recast as

$$\frac{1}{k_{\text{on}}} = \frac{1}{k_a} + \frac{1}{k_D} \quad \text{and} \quad \frac{1}{k_{\text{off}}} = \frac{1}{k_d} + \frac{K_{\text{eq.}}}{k_D}. \tag{2.19}$$

Agmon *et al.* [104] also showed that the equilibrium constant is now in this context given by

$$K_{\text{eq}} = \frac{k_{\text{on}}}{k_{\text{off}}} = \frac{k_a}{k_d}. \tag{2.20}$$

The rate k_{D} at which the diffusive encounter state is formed has been derived exactly 100 years ago by Smoluchowski [105], who found that this diffusion-limited rate constant is given by

$$k_D = 4\pi DR\,, \tag{2.21}$$

where $R = R_A + R_B$ is the cross section (or sometimes referred to as reaction distance)[1] and $D = D_A + D_B$ the mutual diffusion coefficient. R_X and D_X are the radius and diffusion coefficient of particles of type X, respectively. For typical proteins the Smoluchowski rate is of the order of $k_{\text{D}} \simeq 6 \times 10^9\,(\text{Ms})^{-1}$. Comparing this value to typical experimentally measured protein-protein association reaction rate constants, as for example reviewed by Schreiber *et al.* [106], one realizes that this value is almost never achieved and seems orders of magnitude too large. For this reason this value has been termed the diffusive speed limit for protein-protein association. The Smoluchowski rate clearly overestimates measured association rates, since it assumes isotropic reactivity, whereas many proteins have binding pockets, such that they do not only need to be in close proximity but also in a matching mutual orientation, explaining why the isotropic reactivity picture cast by the Smoluchowski diffusion-limited k_{D} rate is a universal upper limit. Strikingly, Milles *et al.* [107] observed that this limit can in fact be reached for intrinsically disordered proteins (IDPs), showing really impressively that the orientation constraint is only relevant for folded proteins.

For this reason it is important to explicitly define what we mean by an *encounter complex*. Figure 2.1 shows several popular choices of how the encounter state can be defined. Figure 2.1A shows a reactivity model where particles themselves are considered as point particles, but for a given reaction they participate in, one assigns a reaction radius r_{reactive} creating a spherical reactive volume V^* around the center of the particle

[1] The reaction distance can coincide with the physical size of the particles, but does not have to. An accurate treatment requires these choices to be consistent to the degree that detailed balance is obeyed and no equilibrium properties are violated.

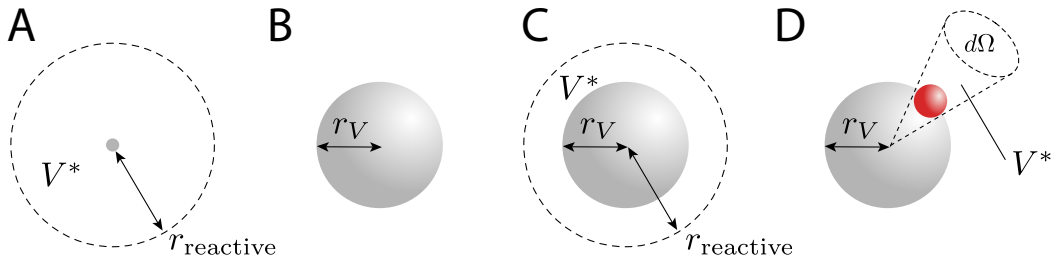

Figure 2.1 | Different reactivity models. While **A**–**C** lead to isotropic reactivity, the patchy particle approach as depicted in **D** is a convenient choice to implement anisotropic reactivity.

[108, 109]. An A–B pair is then considered in diffusional encounter when the two reactive spheres overlap. If one wishes to consider volume exclusion one needs to set a particle radius r_V and modify the diffusive propagation scheme such that particle overlaps $r_{AB} < r_{V,A} + r_{V,B}$ are rejected during the positional sampling (figure 2.1B). Combining volume exclusion with the isotropic reactivity from A one can create a spherical shell around the actual particle (figure 2.1C), such that the overlap over two such spherical shells defines an encounter state. While all three of these approaches implement an isotropic reactivity model, introducing reactive patches on the surface of the particles is a popular choice to implement anisotropic reactivity (figure 2.1D). This was successfully applied in several Brownian dynamics simulation studies in the past [110–113]. Often the reaction patch is only a graphical depiction of an angularly constrained reactive volume V^*. This way of defining anisotropic reactivity does not yet fix the precise mechanism of how reactivity is implemented. This can be done using stochastic reaction rates as demonstrated by Klein & Schwarz [113], where the patch geometry is used to convey orientational specificity, but can also be used in conjecture with interaction potentials [88] allowing flexible interactions. Either way, this extension allows to include oligomerization and assembly processes [91, 114], which are known to be important for many cellular processes.

2.4 Detailed balance condition

While the left part of the encounter picture scheme in equation (2.14) is implemented by the particle propagation scheme as explained in section 2.2, the actual reaction formalism is still pending. For three dimensional ($d = 3$) Brownian dynamics simulations I implemented an algorithm proposed by Morelli *et al.* [115]. To ensure that a simulation model recaptures important physical properties accurately one must ensure that the underlying reaction model for equilibrium reactions satisfies detailed balance. For a

reacting particle pair the detailed balance condition, that we want to satisfy reads

$$p_u(\boldsymbol{r}_d)\,|d\boldsymbol{r}_d|\,\pi_{u\to b}(\boldsymbol{r}_d) = p_b\,\pi_{b\to u}(\boldsymbol{r}_d). \tag{2.22}$$

This condition must hold for any inter-particle vector $\boldsymbol{r}_d$, making sure that the flux from unbound states (u) is matched by the flux from bound states (b). p_u and p_b denote the probability of finding the particle pair in an unbound or bound state, respectively, where of course only $p_u(\boldsymbol{r}_d)$ depends on their mutual spatial configuration, such that $p_u(\boldsymbol{r}_d)|d\boldsymbol{r}_d|$ is the probability of being unbound and separated by a vector between $\boldsymbol{r}_d$ and $\boldsymbol{r}_d + d\boldsymbol{r}_d$. And finally, $\pi_{u\to b}$ and $\pi_{u\to b}$ are the transition probabilities for going from an unbound state to a bound state and vice versa. Morelli suggested a reaction scheme in which every particle overlap is considered as an *encounter state* $\mathcal{E}$ which allows to derive exact expressions for the transition probabilities by appropriate reweighting, such that the detailed balance condition in equation (2.22) is fulfilled. Our clear conception of bimolecular binding as a two step process is well reflected in the following ansatz for the transition probabilities

$$\pi_{u\to b}(\boldsymbol{r}_d) = P_{\text{gen}}^{u\to\mathcal{E}}(\boldsymbol{r}_d, \Delta t)\, P_{\text{acc}}^{\mathcal{E}\to b}(\Delta t) \tag{2.23a}$$

$$\pi_{b\to u}(\boldsymbol{r}_d) = P_{\text{acc}}^{b\to\mathcal{E}}(\Delta t)\, P_{\text{gen}}^{\mathcal{E}\to u}(\boldsymbol{r}_d, \Delta t), \tag{2.23b}$$

where a successful binding event means going from an unbound to a bound state $u \to b \mathrel{\widehat{=}} u \to \mathcal{E} \to b$ *via* an encounter state $\mathcal{E}$, and conversely a complete unbinding reaction means just the opposite, namely $b \to u \mathrel{\widehat{=}} b \to \mathcal{E} \to u$, as the superscripts of (2.23a) and (2.23b) indicate. Using the fact that the equilibrium constants K_{eq} sets the ratio $K_{\text{eq}} = p_{\text{b}}/p_u(\boldsymbol{r}_d)$ and referring back to equation (2.9) from section 2.3 we already know that the acceptance rate $P_{\text{acc}}^{b\to\mathcal{E}}$ describes a first-order decay and hence can be set to $P_{\text{acc}}^{b\to\mathcal{E}} \simeq k_d\Delta t$. One can establish the following expression for the acceptance probability

$$\begin{aligned} P_{\text{acc}}^{\mathcal{E}\to b}(\Delta t) &= \frac{p_b}{p_u(\boldsymbol{r}_d)|d\boldsymbol{r}_d|}\,\frac{P_{\text{gen}}^{\mathcal{E}\to u}(\boldsymbol{r}_d, \Delta t)}{P_{\text{gen}}^{u\to\mathcal{E}}(\boldsymbol{r}_d, \Delta t)}\; P_{\text{acc}}^{b\to\mathcal{E}}(\Delta t) \\ &= \frac{k_a}{k_d\,|d\boldsymbol{r}_d|}\,\frac{P_{\text{gen}}^{\mathcal{E}\to u}(\boldsymbol{r}_d, \Delta t)}{P_{\text{gen}}^{u\to\mathcal{E}}(\boldsymbol{r}_d, \Delta t)}\; k_d\Delta t. \end{aligned} \tag{2.24}$$

The last remaining ingredient to establish an expression for $P_{\text{acc}}^{\mathcal{E}\to b}(\Delta t)$ is the ratio of the overlap generation move and the generation step for the reverse process when moving out of the encounter state $\mathcal{E}$. Since we assume the particle pair to be separated by $\boldsymbol{r}_d$ and know the free diffusion propagator p_{free} from equation (2.5), one can analytically

find

$$P_{\text{gen}}^{u\to\mathcal{E}}(\boldsymbol{r}_d,\Delta t) = \int\limits_{|\boldsymbol{r}'_d|=r'_d<R} p_{\text{free}}(\boldsymbol{r}'_d, t+\Delta t, \boldsymbol{r}_d, t)\; d\boldsymbol{r}'_d =: g(\boldsymbol{r}_d,\Delta t) = g(r_d,\Delta t)\,, \tag{2.25}$$

where $R = R_A + R_B$ is the previously defined cross section. This distribution function $g(r_d,\Delta t)$ is now only a function of the initial radial separation $r_d = |\boldsymbol{r}_d|$ and the propagation time step Δt. For the closed form solution of g see appendix A1.1. The key step in [115] is now to set $P_{\text{gen}}^{u\to\mathcal{E}}(\boldsymbol{r}_d,\Delta t) \propto P_{\text{gen}}^{\mathcal{E}\to u}(\boldsymbol{r}_d,\Delta t)$, *i.e.* to set these distributions in principle equal, with the slight adjustment that $P_{\text{gen}}^{\mathcal{E}\to u}(\boldsymbol{r}_d,\Delta t)$ still needs to be properly normalized. Since we now address the unbinding step, the normalization constant $4\pi\mathcal{N}_{\text{D}}$ is a volume integral over $|\boldsymbol{r}_d| \geq R$ outside the mutual encounter volume. This can be understood as the statistical weight from generating a trial position move over all valid target positions outside the encounter $\mathcal{E}$. The normalization constant is calculated as

$$\int\limits_{|\boldsymbol{r}_d|=r_d\geq R} g(\boldsymbol{r}_d,\Delta t)\, d\boldsymbol{r}_d = 4\pi \int\limits_{R}^{\infty} g(r_d,\Delta t)\, r_d^2 dr_d =: 4\pi\mathcal{N}_{\text{D}}(\Delta t)\,, \tag{2.26}$$

such that the trial move for the backward step ($\mathcal{E}\to u$) is sampled from the distribution

$$P_{\text{gen}}^{\mathcal{E}\to u}(\boldsymbol{r}_d,\Delta t) = \begin{cases} \dfrac{1}{4\pi\mathcal{N}_{\text{D}}(\Delta t)} P_{\text{gen}}^{u\to\mathcal{E}}(\boldsymbol{r}_d,\Delta t) \\ 0 \end{cases} = \begin{cases} \dfrac{g(\boldsymbol{r}_d,\Delta t)}{4\pi\mathcal{N}_{\text{D}}(\Delta t)} & \text{for} \quad r_d \geq R \\ 0 & \text{elsewhere.} \end{cases} \tag{2.27}$$

Having established expressions for $P_{\text{acc}}^{b\to\mathcal{E}}$, $P_{\text{gen}}^{u\to\mathcal{E}}$ and $P_{\text{gen}}^{\mathcal{E}\to u}$ we are all set to go back to equation (2.24) and insert them to find a detailed balance expression for the forward acceptance rate $P_{\text{acc}}^{\mathcal{E}\to b}$

$$P_{\text{acc}}^{\mathcal{E}\to b}(k_a,\Delta t) = \frac{k_a\,\Delta t}{4\pi\,\mathcal{N}_{\text{D}}(\Delta t)}\,, \tag{2.28}$$

which is now a function of the propagation time step Δt and the intrinsic association rate k_a. By isolating the above expression for the intrinsic association rate k_a one can see that this leads to a very intuitive interpretation of

$$k_a = \underbrace{\frac{4\pi\,\mathcal{N}_{\text{D}}(\Delta t)}{\Delta t}}_{\text{collision frequency}} \times \underbrace{P_{\text{acc}}^{\mathcal{E}\to b}}_{\text{association probability}} \tag{2.29}$$

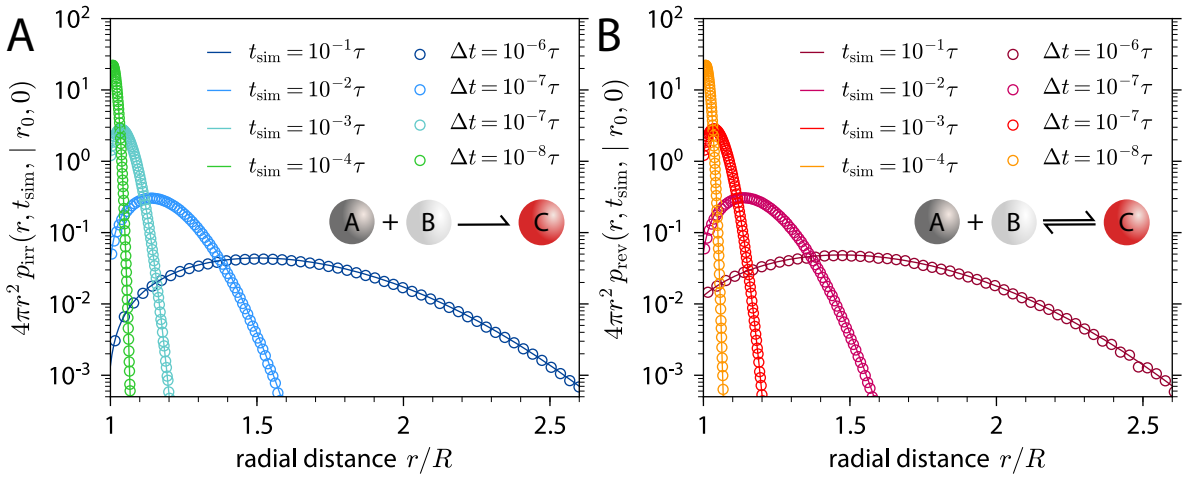

Figure 2.2 | Radial probability distribution for an irreversible (**A**) and a fully reversible (**B**) bimolecular reaction of an isolated particle pair. Different colors stand for different evaluation time points t_{sim} at which the radial distribution functions were evaluated.

as a product of a collision frequency and the probability that a collision leads to a successful association event. This coincides with the definition of an intrinsic association rate constant k_a within the GFRD framework.

2.5 Reactive Brownian dynamics benchmarks

We performed several tests to verify that the algorithm as presented in the previous section 2.4 is physically correct. The first set of tests were performed for an isolated A–B particle pair in unbounded space. This is a suitable choice to test several properties of our approach rigorously, in particular since the isolated pair problem, as considered here, has been solved exactly [116]. This allows us to compare our reactive BD scheme with analytical distribution functions. We start with an irreversible reaction

$$A + B \xrightarrow{k_{on}} C\,, \tag{2.30}$$

and record the radial pair distribution p_{irr} for several time points as shown in figure 2.2A. These radial histograms can be compared with the analytical expressions by [116], who calculated the probability $p(\boldsymbol{r}, t \mid \boldsymbol{r}_0, t_0)$ to find an isolated pair at time t with a inter particle vector $\boldsymbol{r}$ given that their initial displacement at time t_0 was $\boldsymbol{r}_0$, and we find them to be in excellent agreement with the closed form solution, for all time points considered.

For these simulations we defined the intrinsic time scale $\tau = R^2/D$ and used an intrinsic association rate constant $k_a = 1000R^3/\tau$. The time steps Δt used are indicated

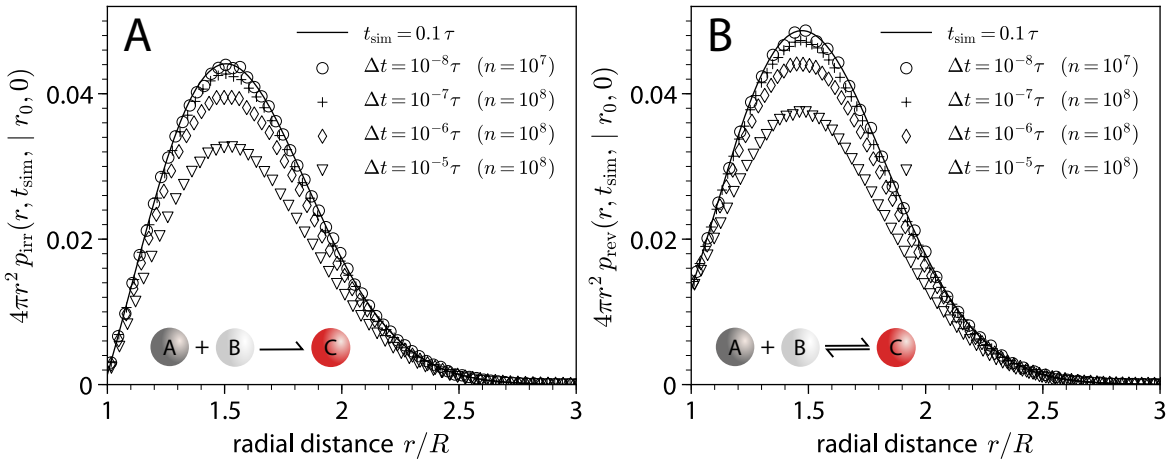

Figure 2.3 | Time step dependency of the radial probability distribution for an irreversible (**A**) and a fully reversible (**B**) reaction of an isolated particle pair. The solid line shows the theoretical prediction while the different marker symbols show the sampled results from Brownian dynamics simulations for various time step sizes Δt.

in the corresponding figure legends of figure 2.2 and 2.3. At the start of each independent run we place the particles in contact, $r_0 = R = R_A + R_B$, and used $R_A = R_B = R/2$, fixing R as intrinsic length scale. Figure 2.3A shows the same quantity in a linear scaling for a single end time point (t_{sim}) but now for various time steps Δt, clearly illustrating how the choice of a too large fixed propagation time leads to a systematic underestimation of the exact radial distribution function $p_{irr}(r)$.

Figures 2.2B and 2.3B show the same analysis for a reversible reaction as given by equation (2.11), which we equally find in good agreement to the analytical results by Kim *et al.* [116]. We observe the same underestimation effect if the propagation time step Δt is set too large.

A second rigorous test for this setup is to calculate the area under the recorded radial density histograms and compare it to the the analytically available survival probability $S(t \,|\, \boldsymbol{r}_0) = S(t \,|\, r_0)$

$$S(t\,|r_0) = 4\pi \int_R^\infty p(r, t \,|\, r_0, t_0)\, r^2 dr. \tag{2.31}$$

A systematic evaluation of how accurately this quantity is achieved is given in figure 2.4. Here we show again the results for both the irreversible (equation (2.30)) and the reversible (equation (2.11)) case. Apart from an erroneous phase at the spectrum of very large time steps we observe a monotonic improvement of the sampled survival probability in comparison with the theoretical prediction as it is shown in both sub-figures by the corresponding dashed horizontal lines. The figure legends also show the exact percentage

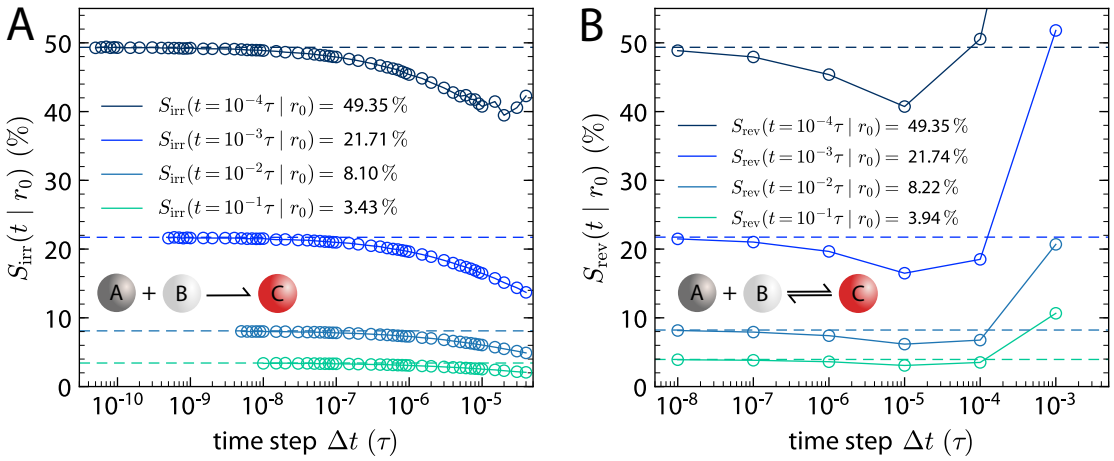

Figure 2.4 | Survival probability $S(t\,|\,r_0)$ for an irreversible (**A**) and reversible (**B**) bimolecular reaction. In both cases the dashed horizontal lines show the theoretical expectation value for the corresponding survival probability $S(t\,|\,r_0)$, here shown for different time points as calculated by [116]. The circles show the ensemble averaged results from several BD simulations, where each circle is the ensemble averaged result from 100 simulations for this time step Δt. In both cases we also calculated the corresponding error bars, but did not include them here, since they were in all cases smaller than the used symbol size.

value that the survival probability $S(t\,|\,r_0)$ takes for the different times.

The following test considers a similar setup as before but now we confine the particles to a cubic bounding box with side length $20R$. We analyze the equilibrium bound state probability p_b as a function of the number of B particles n_B in the system, while only a single A particle ($n_A(0) = 1$) is placed at the center of the system volume Ω. Solving the macroscopic rate equation (2.12) at steady state one finds

$$p_b = \frac{n_B}{n_B + K_{\mathrm{D}}\Omega^*} \tag{2.32}$$

with the equilibrium dissociation constant $K_{\mathrm{D}} = k_d/k_a$ and $\Omega^* = \Omega - 4\pi(R_A + R_B)^3/3$. Furthermore, we made the choice $K_D = 1/\Omega^*$, which sets $p_b(n_B = 1) = 1/2$. Varying n_B from 1 to 100 we observe very good agreement between the results from our BD simulations with the mean-field prediction as shown in figure 2.5. This test is very important, as it verifies that the detailed balance rule as suggested by Morelli [115] indeed leads to correct equilibrium properties. To demonstrate that these properties are indeed violated if one deviates from the proposed detailed balance scheme, we performed the same assay as for figure 2.5 but put all particles in the unbinding step in direct contact at $r = R$, instead of sampling from the derived radial distribution as specified in equation (2.27). This corresponds to using $g(r) = \delta(r - R)$ as the new radial distribution function. This move-rule violates the detailed balance condition (2.22) and leads to a clear overestimation of the theoretical values for the bound state probabilities. It is

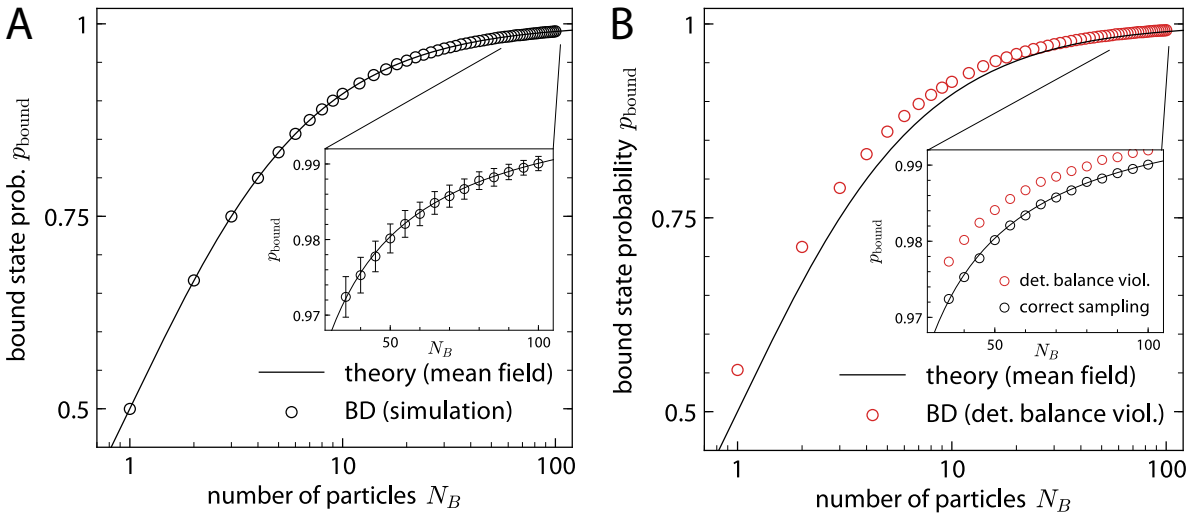

Figure 2.5 | A Probability p_{b} for a single A particle of being in a bound state, shown as a function of the number of B particles n_B present in the system. The solid line shows the expected equilibrium prediction for a mean field model, while the circular symbols show the ensemble averaged results from spatial reactive Brownian dynamics simulations in three dimensions. For this assay we used a fixed propagation time $\Delta t = 10^{-4}\tau$. **B** Bound state probability p_p as before but now using a wrong positional resampling algorithm. This resampling leads to a violation of the detailed balance condition and consequently to a systematic overestimation of the bound state probability p_{b}, as shown by the colored symbols. In the inlet results from using both the correct sampling algorithm (black symbols) and the wrong resampling algorithm (colored symbols) are shown in a direct comparison. This systematic deviation is particularly notable when directly comparing them to **A**. While this deviation becomes less pronounced for larger n_B it is very strongly notable in particular for the first shown data point at $n_B = 1$, where the equilibrium condition dictates $p_{\mathrm{b}} = 1/2$, for our given choice for K_{eq}.

most clearly visible for $n_B = 1$ in figure 2.5B, while appearing less pronounced for larger copy numbers of B particles.

The last example we show here is a very intriguing example, since it shows how the added spatial resolution can indeed fundamentally change the underlying statistics of the reaction processes. Here we consider the reversible reaction from equation (2.11) but now for an isolated pair ($n_A = n_B = 1$) and compare distributions of association times t_{assoc} for a well-mixed stochastic simulation and the space-resolved BD scheme. We implemented the well-mixed approach using a self-written direct Gillespie algorithm [76, 77] which solves the corresponding chemical master equation exactly. For a chosen intrinsic association rate k_a for the spatial BD scheme we can convert it into a macroscopic rate using equation (2.19) to find

$$\frac{1}{k_{\mathrm{on}}} = \frac{1}{k_{\mathrm{D}}} + \frac{1}{k_a} = \frac{1}{4\pi DR} + \frac{1}{k_a}. \tag{2.33}$$

Using the macroscopic rates ($k_{\mathrm{on}}, k_{\mathrm{off}}$) for the well mixed scenario we show the distribution

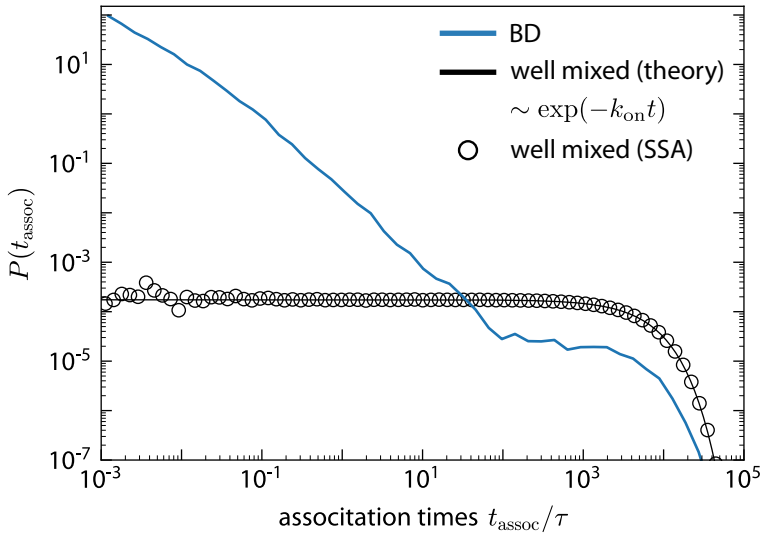

Figure 2.6 | Distribution of association times t_{assoc} for a fully reversible bimolecular encounter. While the black solid line shows the theoretical prediction for a well mixed system, the black circles show the results from a direct stochastic simulation, in excellent agreement with the exponentially decaying distribution. As soon as one takes the spatial resolution into account the distribution $P(t_{\text{assoc}})$ changes its qualitative behavior drastically (blue solid line).

of association times $P(t_{\text{assoc}})$ in figure 2.6, which follows an exponential distribution

$$P_{\text{well-mixed}}(t_{\text{assoc}}) = \begin{cases} k_{\text{on}}\, e^{-k_{\text{on}} t_{\text{assoc}}} & \text{for} \quad t_{\text{assoc}} \geq 0 \\ 0 & \text{elsewhere}\,, \end{cases} \tag{2.34}$$

with mean $\langle t_{\text{assoc}} \rangle = 1/k_{\text{on}}$. This corresponds to the solid black line in figure 2.6. Comparing the two distributions for the well-mixed case and for the spatially resolved one, we clearly see a significant increase for short association times in the spatial model, while in the asymptotic long time limit both decay exponentially with mean $1/k_{\text{on}}$. This is remarkable, since it is a clear footprint of a purely spatial effect and was also investigated by [83, 96]. The implications from these results are very clear. If there are competing processes at time scales for which the spatial distribution in figure 2.6 is different from the well-mixed result, the spatial picture will lead to qualitatively different behavior. In the long time limit both distributions agree again, corresponding to a regime where the diffusive motion was sufficiently long to render the spatial configuration of the system *well stirred*.

The reactive Brownian dynamics scheme, as outlined in section 2.4, is very elegant since it offers a clear microscopic picture for bimolecular reactions. The most elaborate part from an algorithmic point of view is the correct sampling of new particle positions after a successful dissociation step. Since we assume the particles to be spherical, their angular distribution is uniform on the unit sphere, but their radial distribution

function is given by equation (2.27). Correct radial sampling is important to obtain accurate equilibrium properties. I implemented this sampling procedure by analytically calculating this radial distribution function and storing it in a large tabulated form, such that it can be accessed in the simulation by a look-up table approach. This already illustrates that the analytical overhead for implementing a reactive BD scheme, that obeys detailed balance, involves quite some subtleties and analytical considerations. This becomes even more so in the case of the earlier mentioned GFRD approach which fully exploits the availability of analytical solutions for pair reaction-diffusion problems, and samples stochastic trajectories according to these analytic distribution functions. Despite being very elegant, it is hard to generalize the approach by Morelli [115] to arbitrary dimensions (other than $d = 3$) and for non-spherical particles. A generalization of a reactive Brownian dynamics method for patchy particles has been derived by Klein & Schwarz, who showed how the detailed balance condition (2.22) has to be generalized for anisotropic reactivity, which is very important for a more realistic depiction of many protein-protein interactions [113].

2.6 Reactive volume method

To overcome the afore mentioned caveats we also implemented a reactive Brownian Dynamics scheme for two dimensions, which we used to understand receptor dynamics in the cellular plasma membrane. The main reason why the 3D scheme from section 2.4 fails in two dimensions arises from the problem that the analytical evaluation of $g(\boldsymbol{r}_d, \Delta t)$ as shown in equation (2.25) does not work as seamlessly in 2D. The core ideas of this alternative *reactive volume method* are however very similar to the previous approach in the sense, that we equally demand detailed balance to be satisfied (2.22) and equally make a two-step composition ansatz for the transition probabilities $\pi_{b\to u}(\boldsymbol{r}_d)$ and $\pi_{u\to b}(\boldsymbol{r}_d)$ as before in (2.23a) – (2.23b). Around each particle we now consider a reactive shell which defines a reactive volume V^* (as depicted in figure 2.1C), and accordingly consider two particles in encounter $\mathcal{E}$ if their reactive shells overlap. Recalling that intrinsic dissociation follows a Poisson statistic $P_{\text{acc}}^{b\to\mathcal{E}} \simeq k_d \Delta t$ (see 2.3), we find an expression for the acceptance rate of the forward association step, that is scaled precisely by the reactive volume V^*, such that

$$P_{\text{acc}}^{\mathcal{E}\to b} = \frac{k_a \Delta t}{V^*}. \tag{2.35}$$

In this way $P_{\text{acc}}^{\mathcal{E}\to b}$ becomes a function of the intrinsic parameters k_a, Δt and V^*. We notice that the above expression is very similar to the one for the three dimensional

scheme in equation (2.28). A correct application of the *reactive volume method* requires that V^* is sufficiently and uniformly sampled by the diffusive particle motion. In the reverse unbinding step a dissociated particle has to be put uniformly in V^*, followed by a single diffusive move step to ensure microscopic reversibility. This is just a mirrored version of the order of events of the binding process, where a normal diffusive move step into V^* leads to an reaction attempt, which might be successful according to $P_{\text{acc}}^{\mathcal{E}\to b}$.

We use this algorithm to simulate 2D reactive Brownian dynamics to investigate receptor assembly and dynamics in cellular plasma membranes.

2.7 Approximate reactive BD methods

For larger systems with particle numbers that easily exceed $n \sim 10^4$ particles, we will turn to more approximate reactive BD schemes as they have been for example suggested by Andrews *et al.* [108, 109, 117]. We will use these more approximate algorithms to stochastically simulate the bacterial Min System as shown in chapter 6. This involves two not yet covered types of particle reactions, namely first and second order membrane attachment. Many proteins, like for example the Min proteins in bacteria, can cycle between freely diffusing in a three-dimensional cytosolic bulk and a two-dimensional membrane bound state. To create a consistent particle-based simulation algorithm including these membrane attachment reactions, I compare the implemented reactive Brownian dynamics algorithm that I use for the Min system with corresponding mean-field partial differential equations, as they are for example studied in [118]. For this purpose I consider the two missing reaction types individually using only a simplified minimal setting for each of them separately in the following two sections.

First order membrane attachment

For the first type of a membrane attachment reaction I consider a setting with a two dimensional membrane as the bottom surface at $z = 0$ of a rectangular simulation volume Ω in three dimensions, to which a molecular species A can attach. In this scenario the lateral displacements in both the x- and y-direction can be integrated out in a straightforward way allowing us to reduce the system to an effective one-dimensional system where z is the only spatial dependency that remains. In the resulting one-dimensional domain we have a membrane at $z = 0$ and impose a reflecting no-flux boundary condition at $z = L_z$, considering a $[0, L_z]$ domain. The corresponding

differential equation for the particle density $c(z,t)$ now reads

$$\frac{\partial c(z,t)}{\partial t} = D\frac{\partial c(z,t)}{\partial z^2} - \sigma\delta(z)c(z,t) \quad \text{with} \quad 0 \leq z \leq L_z \tag{2.36}$$

subject to the boundary condition $\partial_z c(z,t)|_{z=L_z} = 0$. Since we consider in this first reaction type only a unimolecular process, we want to again implement this first-order process using a Poisson rate $k_{1,m}$, which can then be converted into a reaction probability $p_{\text{react},1m}(\Delta t)$ as explained earlier in section 2.3 and equation (2.9), giving the probability that an A particle has attached to a reactive surface within a fixed propagation time step Δt. Since we only want those particles that are in close proximity to the membrane to be able to attach to it, we introduce a finite distance d_m to encode this spatial confinement. In this way only particles within a distance $z < d_m$ to the bottom surface at $z = 0$ can attempt this first order attachment reaction. In this picture the actual system boundary at $z = 0$ is also treated as a reflective no-flux boundary like the opposite boundary at $z = L_z$, since the adsorption step can now happen anywhere in the layer of thickness d_m above the bottom surface.

To relate the Poisson rate $k_{1,m}$ to the first order membrane attachment rate constant σ of the mean-field equation (2.36) we approximate the δ-functional in equation (2.36) by a Θ function of width d_m

$$\delta(z) \longrightarrow \frac{1}{d}\Theta(d_m - z) \quad \text{with} \quad z > 0, \tag{2.37}$$

mimicking the setup of the spatial particle-based approach. Using the approximation from above one obtains

$$\frac{\partial c}{\partial t} = D\frac{\partial c}{\partial z^2} - \frac{\sigma}{d_m}\Theta(d_m - z)c\,, \tag{2.38}$$

which, after integration over the full z domain gives

$$\partial_t n(t) = \int_0^{L_z} \partial_t c\, dz = \int_0^{L_z} \left[D\partial_{zz}c - \frac{\sigma}{d_m}\Theta(d_m - z)c\right] dz. \tag{2.39}$$

Here $n(t) = n_A(t)$ denotes the total copy number of A particles in the system, while the term

$$\int_0^{L_z} \Theta(d_m - z)c(z,t)\, dz =: n_{d_m}(t) \tag{2.40}$$

denotes all particles n_{d_m} that are in the layer of thickness d_m above the bottom surface at $z = 0$. The term $\int_0^{L_z} D\partial_{zz}c\, dz$ vanishes because of the reflecting boundary conditions

($\partial_z c(0) = \partial_z c(L_z) = 0$). With this we obtain

$$\partial_t n(t) = -\frac{\sigma}{d_m} n_{d_m}(t). \tag{2.41}$$

Since in this setting n can only change by membrane attachment of the particles n_{d_m}, one can identify σ/d_m as the desired Poisson rate

$$k_{1,m} = \frac{\sigma}{d_m} \tag{2.42}$$

for the first-order reaction step that we wish to implement. This means that a single particle that is within distance d_m of a reactive surface of the system has a probability of

$$p_{\text{react},1m}(\Delta t) = 1 - \exp(-k_{1,m}\Delta t) = 1 - \exp\left(-\frac{\sigma}{d_m}\Delta t\right) \tag{2.43}$$

to react during each time step of length Δt. The actual choice for d_m is of course as usual subject to the natural tradeoff between keeping it as small as possible to ensure that the approximation in equation (2.37) is still valid, while wanting it to be large enough at the same time, such that the diffusive tracks of the particles can sample it with sufficient accuracy. For the Min system, where we did not use compartment heights below $L_z = 0.5\,\mu$m, we picked $d_m = 2 \times 10^{-2}\mu$m keeping the ratio $d_m/L_z < 5\,\%$.

Bimolecular membrane attachment

Secondly, we cover second order membrane attachment reactions. They involve a bimolecular encounter between a freely diffusing particle in a three-dimensional bulk and a freely diffusing surface-bound particle in a two-dimensional domain. The corresponding mean-field differential equation for this type of reactions reads

$$\frac{\partial c(\boldsymbol{r}, t)}{\partial t} = D\nabla^2 c(\boldsymbol{r}, t) - \sigma\delta(z) c_m(\boldsymbol{r}, t) c(\boldsymbol{r}, t), \tag{2.44}$$

where c denotes the density of free particles of species A and c_m is the density of surface-bound particles. For the particle-based framework we adopt an algorithm used in the software package Smoldyn [108]. The treatment for irreversible bimolecular association reactions follows the spirit of the classical Smoluchowski picture for irreversible diffusion-limited reactions [105], where two particles instantaneously react upon collision, leading

to the diffusion-limited on-rate for bimolecular association of

$$k_D = 4\pi D R_S \,, \tag{2.45}$$

as discussed earlier (2.21). Here D denotes the mutual diffusion coefficient of the reacting pair and R_S is the effective collision distance as before, here shown with a subscript S to indicate the Smoluchowski picture. To also address reaction-limited or only partially diffusion-limited reactions, Collins and Kimball [119] proposed to impose a radiation-boundary condition which nicely conveys the picture of a finite reaction-limited reaction probability once a pair of reactants has met *via* diffusional encounter. For the sake of simplicity and algorithmic speed, Andrews and Bray [108] came up with an algorithm which keeps the spirit of the original idea by Smoluchowski by introducing a binding radius σ_b and letting particles react instantaneously once they are separated by $r < \sigma_b$ with $r = |\boldsymbol{r}_A - \boldsymbol{r}_B|$. To account for reaction-limited effects the sum of the molecular radii is replaced by this effective binding radius $\sigma_b \leq R_S$ in this picture. They propose an algorithm which calculates σ_b for a given diffusion coefficient D, time step Δt and a forward rate constant k_{on}. In fact the algorithm solves the forward problem of determining the effective simulated forward rate constant k_{on} for a given time step Δt, diffusion coefficient D and binding radius σ_b and stores these results in a look-up table, which is then inverted to interpolate a binding radius for a given reaction rate k_{on}.

The forward problem itself is solved numerically by propagating an initial radial distribution function (RDF) $g(r)$ forward in time, by carrying out alternating diffusion and irreversible reaction steps. The diffusive steps are implemented by convolving the full radial distribution function with a three-dimensional Gaussian and in each reaction step the RDF is set to zero in the range $0 \leq r \leq \sigma_b$ to account for the irreversible reactions that have taken place. In each iteration the effective reaction rate is then given by integrating the area under the RDF from 0 to σ_b after the diffusive step. This procedure is repeated iteratively until convergence is achieved. By inverting the tabulated relation between the k_{on}'s and the σ_b's one solves the inverse problem and can thus obtain $\sigma_b = \sigma_b(D, \Delta t, k_{\text{on}})$ as a function of the diffusion coefficient D, the time step Δt and the forward rate constant k_{on}. The radial distribution functions $g(r)$ one obtains using this algorithm reduce to the radial distribution function of the Smoluchowski model $g_S(r)$ in the limit of small time steps $\Delta t \to 0$, as to be expected for infinitely detailed Brownian motion. For irreversible bimolecular reactions the RDF in the Smoluchowski model reads

$$g_S(r) = \begin{cases} 1 - \frac{\sigma_b}{r} & \text{for} \quad r \geq \sigma_b \\ 0 & \text{for} \quad r < \sigma_b. \end{cases} \tag{2.46}$$

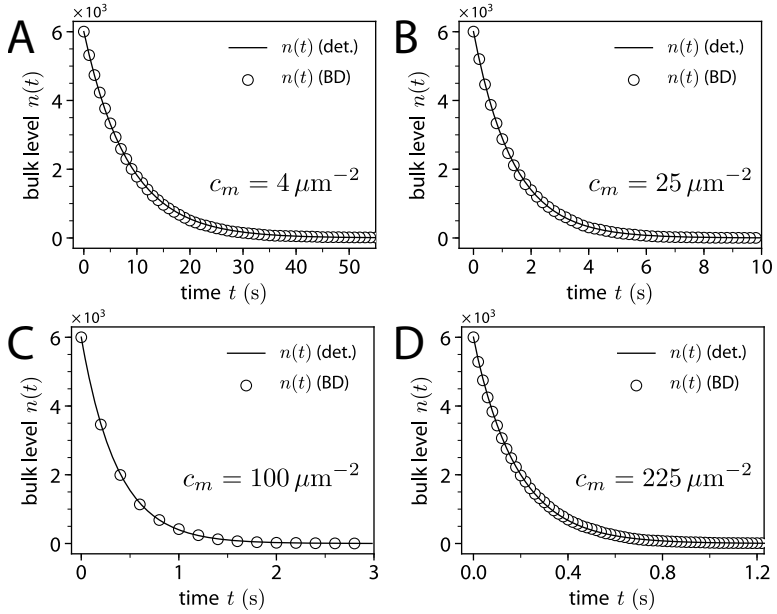

Figure 2.7 | Bimolecular membrane attachment. In all cases shown here we placed $n_A = 6000$ free particles in a simulation volume Ω. Upon reaction with evenly distributed bound particles on the bottom surface of the rectangular simulation volume they were removed from the system. N denotes the copy number of remaining free particles in the bulk volume of the system. The solid black line depicts the numerical solution of equation (2.44) and the black circles represent the results from the particle-based simulation algorithm. The parameters used were $D = 2.5\,\mu\text{m}^2/\text{s}$, $L_z = 0.5\,\mu\text{m}$ and $\sigma = 0.0149\,\mu\text{m}^3/\text{s}$. In the four sub-figures different values for the density of the bound particles c_m were used: top left $c_m = 4\,\mu\text{m}^{-2}$, top right $c_m = 25\,\mu\text{m}^{-2}$, bottom left $c_m = 100\,\mu\text{m}^{-2}$ and bottom right $c_m = 225\,\mu\text{m}^{-2}$.

In general however, the RDFs qualitatively resemble the functional form of the radial distribution function according to the Collins and Kimball [119] model. The major drawback of this approximate reaction scheme is that strongly activation-limited reactions lead to vanishing reaction cross-sections R_S. Since these must be sufficiently sampled to ensure correct dynamics of the system, they put a constraint on the propagation time step Δt.

For a quantitative test of this algorithm on the basis of the corresponding mean-field results we solved equation (2.44) numerically using a finite difference scheme. In order to do so, we made further simplifying assumptions. For arbitrary distributions of the bound particles c_m the differential equation (2.44) cannot be reduced to one dimension as before; however, it is possible to do so for evenly distributed bound particles. Then one can solve this PDE numerically, assuming evenly distributed bound particles c_m on the bottom surface of a rectangular simulation box of volume Ω. To match this scenario of the mean-field model in the particle-based framework, we consider a molecular species A of freely diffusing particles in a simulation volume Ω which can react with membrane-bound particles of another species B. For the sake of simplicity, particles of

species A are removed after a successful reaction step with a membrane-bound particle, while the bound-particles are not removed after the reaction step to keep $c_m = \text{const}$. The results of this comparison using the Min system's parameter set (see table 6.1 in chapter 6) and several different values for the bound particle surface densities c_m are shown in figure 2.7.

II

Signal transduction

3 Ligand discrimination through receptor dimerization in interferon signaling

Interferon type I signaling starts by ligand-receptor interactions in the cellular plasma membrane. Many biochemical *in vitro* and *in vivo* studies [120–122] have shown that interferons cross-link the two interferon α receptor chains (Ifnar1 and Ifnar2), to form an active ternary signaling complex; a process that is known as *ligand-induced receptor cross-linking* or equally *ligand-induced receptor dimerization*, since receptor interactions are mediated by the ligand molecule.

It is a long standing puzzle how this system can discriminate a large range of different ligands (see figure 1.2 and 3.1) in a cell-type specific manner with a single heterodimeric receptor pair. The key observation is, that different ligands can trigger different cellular responses [22, 23]. The downstream signaling cascades might seem like a natural explanation to account for different cellular responses, but it does not alleviate the problem, that any external signal must be processed through the same receptor complex. This view renders the receptor stage of interferon type I signaling a natural information bottleneck, through which any signal must be relayed (see figure 3.1).

For this reason I am interested in the receptor engagement of the interferon signaling system, which constitutes the early stage of signal initiation. In this work I suggest a mechanism that explains ligand discrimination based on ligand binding affinity for heterodimeric receptor systems. This mechanism exploits the fact, that dimeric signaling receptors show non-monotonic binding curves, which translate binding affinity into different receptor activation levels. Since many of these results apply for dimeric receptor systems in general, they might have equal implications for other receptor systems, that possess similar receptor binding characteristics. In short, I show that the dimerization motif allows cell-surface receptors to sense ligand affinity, a way for cells to tell ligands apart by their binding strength. And secondly, I will demonstrate that the more this binding process is asymmetric, the more it becomes robust against ligand

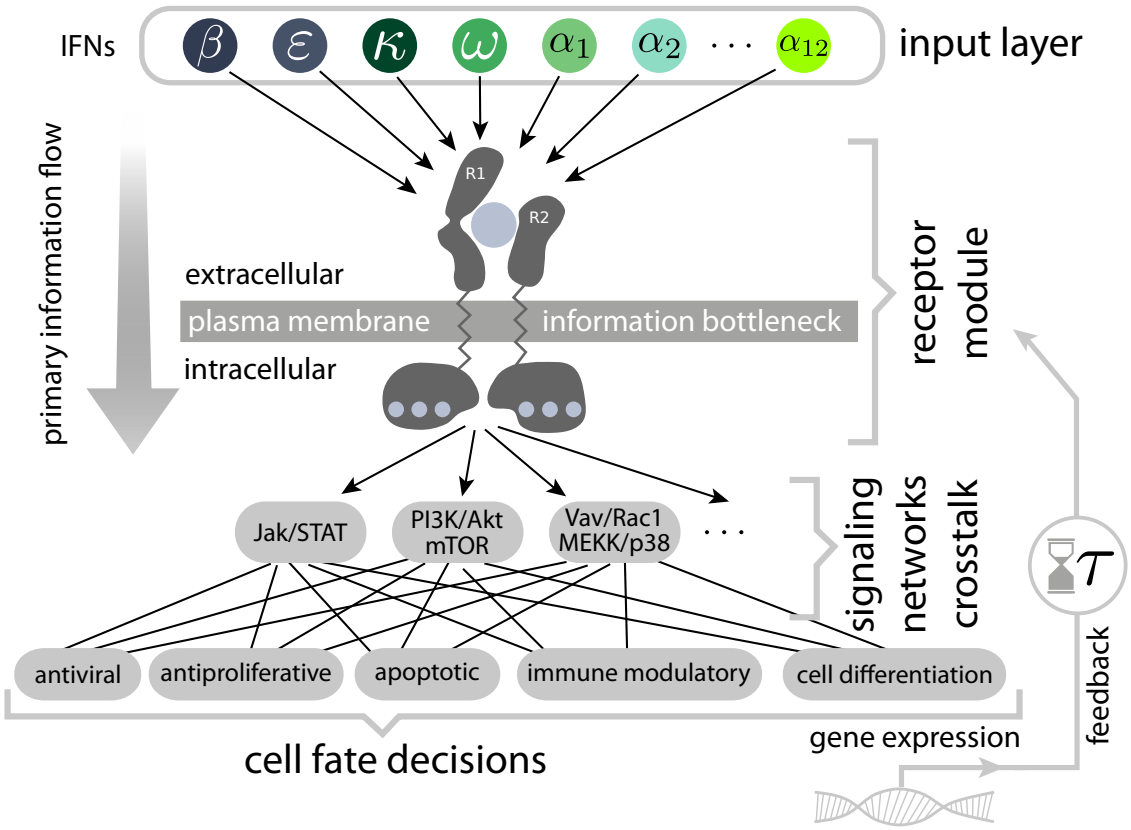

Figure 3.1 | Information processing at the interferon type I receptor. The family of homologous interferon type I (IFN) ligands spans 16 distinct ligands (input layer) which share the same hetero-dimeric cell surface receptor (R1 and R2). These two transmembrane proteins transduce the signal downstream triggering multiple cell fate decisions. A hallmark of interferon type I signaling is the potency of different ligands to trigger different cell responses although they must be squeezed through the same information bottleneck, a shared hetero-dimeric receptor pair. In this way the plasma membrane does not only function as a passive diffusion barrier but can also be understood as an information bottleneck.

concentration fluctuations.

3.1 Ligand-receptor binding

The discrimination mechanism I suggest exploits the characteristic binding properties of *ligand-induced* hetero-dimerization. To understand this argument it is insightful to compare hetero-dimerization against standard monomeric receptor-ligand binding as a default binding model. Hence I will use the first part of this chapter to revisit the equilibrium binding properties of these receptor models and then use them to demonstrate the discrimination mechanism. Since the non-monotonic receptor response does already occur for homo-dimeric receptors as well, I will also introduce them as an

intermediate step to the hetero-dimeric case, which is relevant for the interferon system.

Throughout the rest of this chapter I will use uppercase normal letters such as R_i to denote both the concentration of receptor species i, but also use it as a simple name for this species itself. In the context of the interferon system I will refer to the interferon alpha receptor subunits Ifnar 1 and Ifnar 2 by R_1 and R_2, respectively.

I make the assumption that ligand binding to cell surface receptors does not deplete the ligand reservoir. This is typically referred to as *ligand excess assumption* and for a system volume Ω and a membrane patch of area A, means that $\Omega L \gg AR_i$, where R_i is the surface concentration of receptor type i. Recalling the notoriously low copy numbers of receptors per cell in the interferon system [22], this assumptions seems well justified.

Molecular readout

A central quantity for my analysis is the amount of activated receptors. Regardless of any downstream machinery, active receptor complexes are a check-point for signal-transduction. To compare the results from the different receptor models, I will use the fractional receptor activation f. This is the relative amount of activated receptors in the cell membrane and will serve as the primary readout for the remainder of this section. Although the definition of an active receptor complex C changes in dependence of the underlying receptor-ligand model, the central quantity will always be

$$f(L, \boldsymbol{\beta}) = \frac{C}{R_0}\,, \tag{3.1}$$

where R_0 has to be chosen, to ensure proper normalization. This fractional response f viewed as a function of the ligand concentration is typically called *binding curve*, or equivalently *dose response curve*. The vectorial quantity $\boldsymbol{\beta}$ will carry all other model parameters which determine f apart from the ligand concentration L itself.

3.1.1 Monomeric ligand-receptor binding

As the simplest receptor-ligand model I consider the reversible binding of a ligand L to a monomeric receptor R, which when bound forms an active ligand-receptor complex $C \equiv RL$ according to

$$R + L \underset{k_\mathrm{u}}{\overset{k_\mathrm{b}}{\rightleftharpoons}} C. \tag{3.2}$$

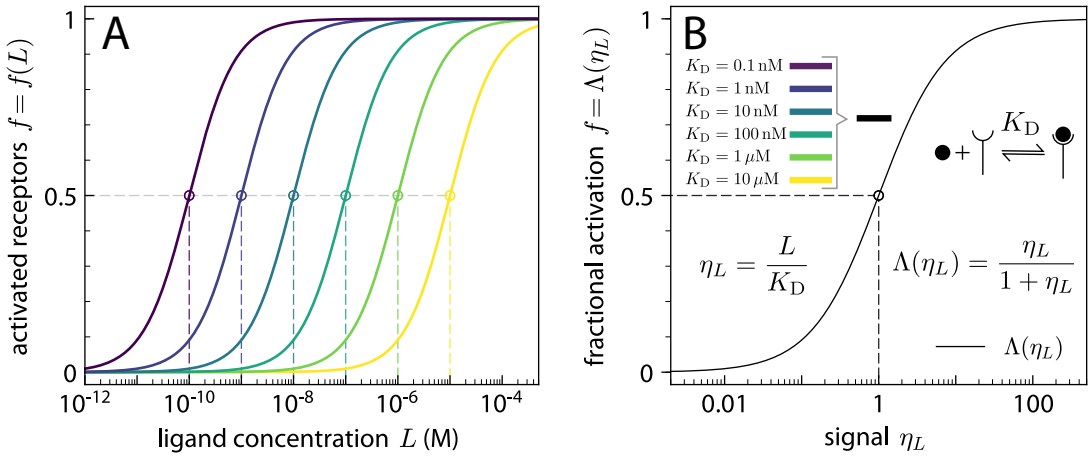

Figure 3.2 | Hyperbolic saturation kinetics of monomeric ligand-receptor binding for different ligand affinities. **A** shows several dose response curves for different ligand affinities ranging from 0.1 nM to 10 μM. This clearly illustrates, that on the level of monomeric response functions, ligand affinity only translates into lateral shifts in concentration space. Dashed lines indicate half saturation (occupancy) at $L = K_D$. **B** All response functions f collapse onto a universal response curve Λ when normalized by their own affinity K_D. All curves show a monotonic dose response relationship, where more ligand translates into more activated receptor.

Equilibrium binding is set by the equilibrium dissociation constant $K_D = k_u/k_b$ (b for binding, u for unbinding), and is given by

$$K_D = \frac{L\,R}{C} = \frac{k_u}{k_b}\,, \tag{3.3}$$

where I use L, R and C to denote the concentrations of the respective species. In conjecture with receptor (mass)-conservation, $R_0 = \text{const} = R(t) + C(t)$, one can immediately determine the binding curve as

$$C = R_0\,\frac{L}{K_D + L}. \tag{3.4}$$

The fractional response f is then simply obtained by normalizing with the total receptor concentration R_0 to get

$$f^{\mathrm{M}}(L, K_D) = \frac{C}{R_0} = \frac{L}{K_D + L} \tag{3.5}$$

with half saturation (receptor occupancy) at $L = K_D$. I use the superscript M to denote that this is the response function for a monomeric receptor. In the language of enzyme kinetics the binding characteristics according to (3.5) give rise to *hyperbolic saturation kinetics*. Its main characteristics are an initially linear binding response which saturates in the asymptotic limit. This functional relationship occurs frequently in

various biophysical scenarios and is equally known as *Langmuir adsorption isotherm* or alternatively as *Hill equation* with Hill coefficient $n = 1$. Since I will mostly use a logarithmic scaling in ligand concentration space, this hyperbolic relation will appear sigmoidal in shape. Equation (3.5) has equally a nice interpretation on the single receptor level from a statistical mechanics point of view. The receptor occupation probability in a *canonical ensemble* is given by the identical result

$$p_{\text{bound}} = \frac{C}{R + C} = \frac{L/K_{\text{D}}}{1 + L/K_{\text{D}}}\,, \tag{3.6}$$

which of course is also identical to equation (2.32) in section 2.5. By rescaling the ligand concentration L by its own binding affinity K_{D}, $\eta_L = L/K_{\text{D}}$, we obtain the universal binding curve

$$\Lambda(\eta_L) = \frac{\eta_L}{1 + \eta_L} \quad \text{with} \quad \Lambda(x) := \frac{x}{1 + x}\,, \tag{3.7}$$

onto which all binding curves for different ligand affinities K_{D} collapse through this non-dimensionalization (see figure 3.2B). The monomeric case serves as the default binding model against which I will compare the dimerization schemes of the following sections.

3.1.2 Homo-dimerization

Next, I consider the binding curve for a homo-dimerizing receptor system. By this I mean ligand-induced receptor dimerization according to the the following reaction scheme

$$R + L \underset{k_{\text{u}}}{\overset{2k_{\text{b}}}{\rightleftharpoons}} RL \tag{3.8a}$$

$$RL + R \underset{2k_{\text{d}}}{\overset{k_{\text{a}}}{\rightleftharpoons}} C\,, \tag{3.8b}$$

where a bivalent ligand L can cross-link two monovalent receptors R to form a ternary receptor complex $C \equiv RLR$. Both occurrences of factors of two in the above scheme are owed to the fact, that the ligand is bivalent and thus either binding site can bind to a monovalent receptor ($2k_b$), and either bound site from a complex C can dissociate ($2k_d$). I use $K_{\text{D}}^B = k_u/k_b$ to denote the 3D equilibrium dissociation constant for the ligand binding reaction and $K_{\text{D}}^X = k_d/k_a$ for the 2D equilibrium dissociation constant for the receptor cross-linking reaction (X for cross-linking). Invoking receptor (mass)-conservation we have the constraint that $R_0 = \text{const} = R(t) + RL(t) + 2C(t)$, with

R_0 being the total receptor concentration. The goal is again to derive a binding curve $C = C(L)$ for the active receptor complexes. The fastest way to get there is to invoke the *law of mass action*, which applied to (3.8a) – (3.8b) yields

$$K_{\mathrm{D}}^{B} = \frac{2R \cdot L}{(RL)} \qquad K_{\mathrm{D}}^{X} = \frac{R \cdot (RL)}{2C}. \tag{3.9}$$

Combined with the receptor mass conservation relation this can be written as

$$R^2 + \frac{\Lambda}{K_{\mathrm{D}}^{X}} R - \frac{K_{\mathrm{D}}^{B}}{2L} K_{\mathrm{D}}^{X} R_0 = 0 \quad \text{with} \quad \Lambda(L, K_{\mathrm{D}}^{B}) = \frac{2L/K_{\mathrm{D}}^{B}}{1 + 2L/K_{\mathrm{D}}^{B}}, \tag{3.10}$$

with a standard solution

$$R = \frac{R_0(1-\Lambda)}{2\Delta}\left[-1 \pm \sqrt{1+4\Delta}\right] \quad \text{where} \quad \Delta = \underbrace{\Lambda(1-\Lambda)}_{\text{parabolic scaling}} \times \left(\frac{R_0}{K_{\mathrm{D}}^{X}}\right). \tag{3.11}$$

In the context of the homo-dimerization scheme it is convenient to identify $\tilde{K}^X := R_0/K_{\mathrm{D}}^{X}$ is a dimensionless 2D equilibrium cross-linking constant and $\eta_L = 2L/K_{\mathrm{D}}^{B}$ as a dimensionless ligand concentration. Having established the solution for R in equation (3.11), where we only considered the positive root to obtain a valid expression for the receptor concentration, we immediately find the binding curve $C(L)$ by reinserting both the root for R and $RL = (2L/K_{\mathrm{D}}^{B})\, R$ from (3.9) into the above conservation relation to get the binding curve

$$C = \underbrace{\left(\frac{R_0}{2}\right)}_{C_{\max}} \left[\frac{1 + 2\Delta - \sqrt{1+4\Delta}}{2\Delta}\right]. \tag{3.12}$$

This is identical to the solution by Perelson [123], who studied a similar question in a ligand-centered picture to understand receptor aggregation by immunoglobulin. To get the fractional receptor occupancy f, we note, that for the homo-dimerization scheme, as given in (3.8a)–(3.8b), the maximal number of activated receptors (cross-links) is given by $C_{\max} = R_0/2$, such that we always do have $2\,C/(R_0) \leq 1$ and can write the fractional binding curve in the following form

$$f^{\mathrm{Ho}}(L, \boldsymbol{\beta}) = \frac{1 + 2\Delta - \sqrt{1+4\Delta}}{2\Delta} \quad \text{with} \quad \boldsymbol{\beta} = (K_{\mathrm{D}}^{B}, K_{\mathrm{D}}^{X}, R_0)^T. \tag{3.13}$$

The graph of f has previously been termed *cross-linking* curve [123]. Since for binding curves the canonical independent variable in this context is the ligand concentration L, I grouped the remaining parameters of the fractional response f into a parameter

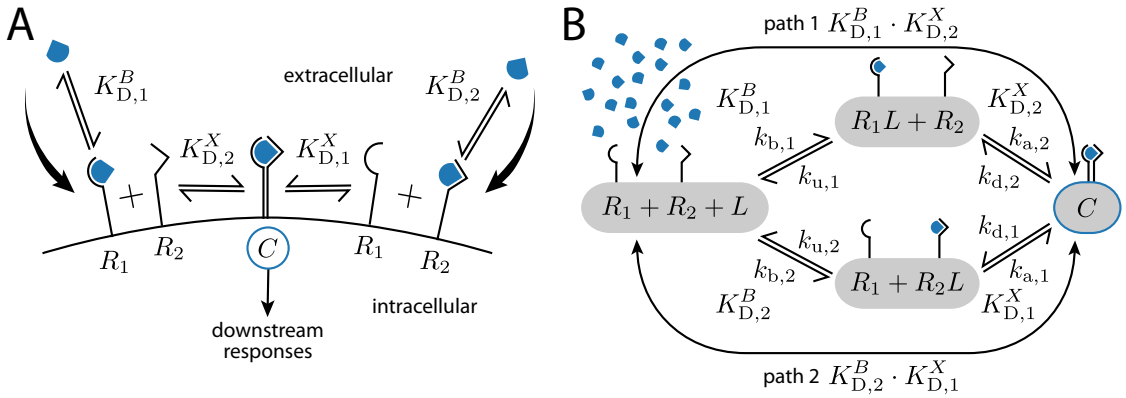

Figure 3.3 | A Schematic diagram of the receptor activation pathways for hetero-dimerization by ligand induced cross-linking. This illustrates the two-step binding process, which starts by ligand binding from a 3D bulk and is concluded by free complementary receptor recruitment by lateral association in the 2D plasma membrane. **B** Reaction scheme of the two-step cross-linking mechanism. The two pathways leading to the ternary complex formation C give rise to a *diamond* like kinetic topology, which defines the unique binding characteristics. The capital K's denote equilibrium dissociation constants while the normal sized k's show the respective forward and backward rate constants for each of the eight involved elementary reactions.

vector $\boldsymbol{\beta} \in \mathbb{R}^3$ and use the abbreviation Ho to indicate the homo-dimeric case.

3.1.3 Hetero-dimerization

Now I will present the equilibrium solution for the hetero-dimerizing receptor scheme, which the interferon system implements. Figure 3.3 shows the reaction scheme, which consists of two competing dimerization pathways, which both lead to the formation of a active receptor complex. The equilibrium solution for this bivalent receptor engagement with two different receptor subunits (chains) has previously been studied by Perelson in the context of histamine release by mast cells and basophils [124], which I will now apply to the interferon system. The two independent assembly pathways from figure 3.3B give rise to the following set of reversible reactions

$$R_i + L \underset{k_{u,i}}{\overset{k_{b,i}}{\rightleftharpoons}} R_iL \qquad \text{for} \quad i \in \{1,2\} \tag{3.14a}$$

$$R_i + R_jL \underset{k_{d,i}}{\overset{k_{a,i}}{\rightleftharpoons}} C \qquad \text{for} \quad (i,j) \in \{(1,2),(2,1)\}\,, \tag{3.14b}$$

where I use C to denote the hetero-dimer (ternary ligand receptor complex) $C \equiv R_1LR_2 \equiv R_2LR_1$ and the subscripts i and j are used to label the two distinct receptors. The full dynamic system of differential equations for these reactions are shown in the appendix A2. At equilibrium the four reactions defined from above are solely governed

by the following for equilibrium dissociation constants

$$K^B_{\mathrm{D},i} = \frac{k_{u,i}}{k_{b,i}} \quad \text{and} \quad K^X_{\mathrm{D},i} = \frac{k_{d,i}}{k_{a,i}} \qquad i \in \{1,2\}. \tag{3.15}$$

To find the equilibrium binding curve we once more apply the *law of mass action* in combination with now two receptor conservation laws which read

$$R_{1,0} = \text{const} = R_1(t) + R_1L(t) + C(t) \tag{3.16a}$$
$$R_{2,0} = \text{const} = R_2(t) + R_2L(t) + C(t). \tag{3.16b}$$

I further introduce $R_T = R_{1,0} + R_{2,0}$ to denote the total surface concentration of receptors. Assuming *detailed balance* [125], all reactions individually must be in equilibrium and hence satisfy

$$(R_1L) = \frac{R_1 \cdot L}{K^B_{D,1}} \qquad (R_2L) = \frac{R_2 \cdot L}{K^B_{D,2}} \tag{3.17}$$
$$\frac{R_2\,(R_1L)}{K^X_{D,2}} = C = \frac{R_1\,(R_2L)}{K^X_{D,1}}\,, \tag{3.18}$$

which in combination yields the interesting result, that

$$K^B_{D,1}K^X_{D,2} = K^B_{D,2}K^X_{D,1} \tag{3.19}$$

must hold. This result is a direct consequence of the reaction topology (see figure 3.3B). Since at equilibrium there can be no free energy gain by any cycle in the reaction network (and we also do not consider any actively driven processes), the equilibrium constants are not independent, but connected according to (3.19) as a direct consequence of the principle of detailed balance. This means, that only a set of three of the four given K_{D}'s are independent.

Combining the conservation laws from (3.16b) with the results from (3.18) we find the binding curve $C(L)$ for the hetero-dimerization scheme as

$$C = \frac{R_T}{4\tilde{\Delta}}\left[1 + 2\tilde{\Delta} - \sqrt{1 + 4\tilde{\Delta} + 4\tilde{\Delta}^2\left(1 - \frac{4R_{1,0}R_{2,0}}{R_T^2}\right)}\right], \tag{3.20}$$

where I defined the dimensionless shortcut

$$\tilde{\Delta} := \Lambda_1(1-\Lambda_2)\frac{R_T}{2K^X_{D,2}} \quad \text{with} \quad \Lambda_i := \Lambda\left(\frac{L}{K^B_{\mathrm{D},i}}\right), \tag{3.21}$$

Receptor topology	Response function $f = f(L, \boldsymbol{\beta})$	Parameters $\boldsymbol{\beta}$
monomer	$f^{\mathrm{M}} = \dfrac{L}{K_{\mathrm{D}} + L} = \Lambda$	K_{D}
homo-dimer	$f^{\mathrm{Ho}} = (1 + 2\Delta - \sqrt{1 + 4\Delta})/2\Delta$ $\Delta = \Lambda(1 - \Lambda)\, R_0/K_{\mathrm{D}}^X$	$K_{\mathrm{D}}^B, K_{\mathrm{D}}^X, R_0$
hetero-dimer	$f^{\mathrm{He}} = (1 + 2\tilde{\Delta} - \sqrt{1 + 4\tilde{\Delta}})/2\tilde{\Delta}$ $\tilde{\Delta} = \Lambda_1(1 - \Lambda_2)\, R_0/K_{D,2}^X$	$K_{D,1}^B, K_{D,2}^B, K_{D,2}^X, R_0$

Table 3.1 | Dose response functions f for the three introduced receptor-ligand binding motifs. While the monomeric response function follows hyperbolic saturation kinetics (monotonic increase), the two dimerization motifs have a biphasic response characteristic, which in log-space has a characteristic bell-shape. The result for the hetero-dimeric case assumes $R_{1,0} = R_{2,0} = R_0$ as before, and Λ_1 and Λ_2 are defined in equation (3.21).

recalling the Λ definition from equation (3.7). We notice the similarity of this expression to Δ in the homo-dimeric case and also reiterate, that $R_T/K_{D,2}^X$ takes again the role of a dimensionless cross-linking equilibrium constant. For further details see appendix A2. In most cases discussed below, I will assume both receptor types to be equally abundant $R_{1,0} = R_{2,0} =: R_0$, which renders $R_T = 2R_0$. With this assumption, the fraction of activated hetero-dimers is found to be

$$f^{\mathrm{He}}(L, \boldsymbol{\beta}) = \frac{C}{R_0} = \frac{1 + 2\tilde{\Delta} - \sqrt{1 + 4\tilde{\Delta}}}{2\tilde{\Delta}} \quad \text{with} \quad \boldsymbol{\beta} = (K_{D,1}^B, K_{D,2}^B, K_{D,2}^X, R_0)^T\,, \tag{3.22}$$

which appears on this level identical to the result for the homo-dimer in equation (3.13), but with $\tilde{\Delta}$ in place of Δ. Setting both receptor surface concentrations equal changes $\tilde{\Delta}$ to

$$\tilde{\Delta} = \Lambda_1(1 - \Lambda_2)\,\frac{R_0}{K_{D,2}^X} = \Lambda_2(1 - \Lambda_1)\,\frac{R_0}{K_{D,1}^X}\,, \tag{3.23}$$

where the second identity results from the overall symmetry of the two available assembly pathways.

Now we have the dose response curves for all three introduced receptor-ligand binding models at our finger tip, as summarized in table 3.1, and I will proceed by explaining the discrimination mechanism.

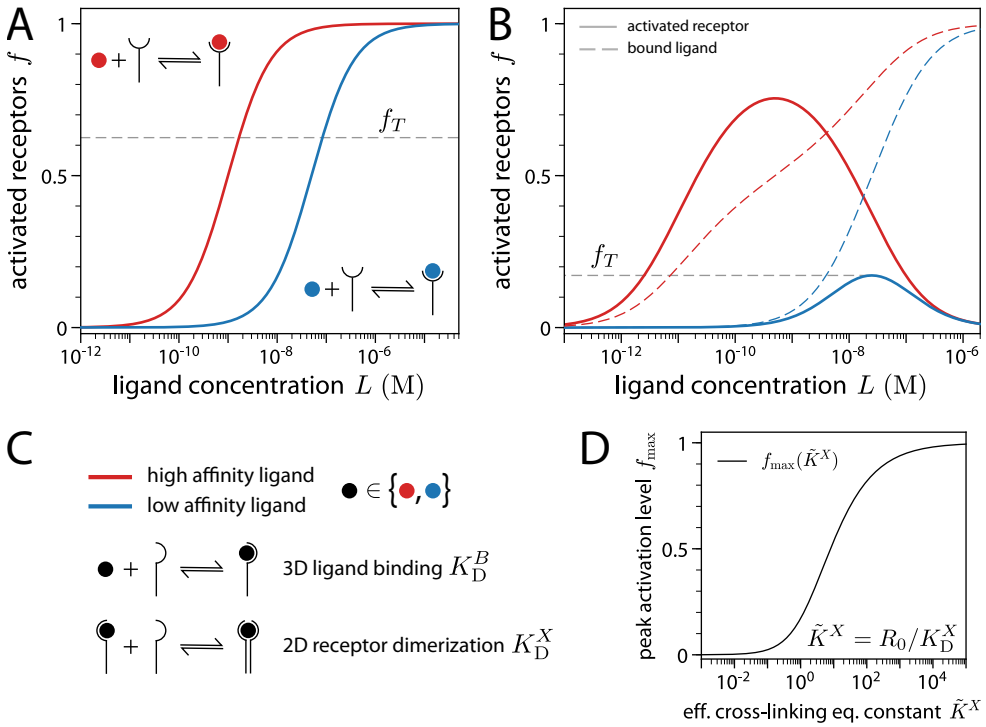

Figure 3.4 | Qualitatively different dose response characteristics from monomeric and dimeric surface receptors. **A** shows the hyperbolic dose response curves for a high and low affinity ligand, respectively. **B** shows the same, but now for a system where a bivalent ligand engages two receptor chains to form a dimeric receptor complex. The characteristic *log-bell shapes* show very different peak activation levels, allowing ligand discrimination based on their affinity. **C** Figure legend and (homo-) dimerization reaction scheme. **D** Peak activation levels $f_{\max}$ as a function of the effective cross-linking equilibrium constant $\tilde{K}^X$. The colored dashed lines in **B** show the fraction of surface bound ligand f_L for both the high and low affinity case. Care must be taken, since this fraction is normalized by R_0 instead of $R_0/2$. The 3D binding constant K_D^B was chosen identical in both **A** and **B**, where the high affinity ligand was set to be more affine by a factor of 50.

3.2 Ligand discrimination mechanism

The central observation in this section are the qualitatively different dose response curves of monomeric and dimeric receptors as shown in figure 3.4. While monomeric receptors show monotonic response curves (hyperbolic kinetics, see figure 3.4A), dimeric receptors have biphasic binding curves with a maximal activation level around which they are symmetric [123, 126] (see figure B). For this reason the binding curves are called *log-bell shaped*.

The nature of this non-monotonic response characteristic is easily explained. At low ligand concentrations empty receptors are filled up with free ligand, creating ligand-bound receptor units in the membrane (R_iL). An increasing fraction of ligand bound

receptors increases the reactive flux into the dimeric state (C) by recruitment of empty receptors (R_j). This explains the increasing slope of the bell-shaped response curves up to their maximal activation level. Beyond this point, the presence of more ligand leads to a competition for free monomeric receptor sites, and accordingly in the limit of large ligand excess shifts the equilibrium to all receptors being ligand bound, which blocks dimer formation.

To understand how this forms the basis for ligand discrimination, I compare the response of a high affinity ligand (red lines) with a low affinity ligand (blue lines) for both the monomeric case and the (homo-) dimeric case. Since the core mechanism works for homo-dimers, I use the homo-dimeric case here instead of the full hetero-dimeric picture. In the monomeric case (3.4A) any given activation level of active receptors f_T can either be established by a high affinity ligand at a low ligand concentration, or equally by a low affinity ligand at high ligand concentration. This is indicated by the dashed line in figure 3.4A, which illustrates how a given activation threshold f_T can be triggered in both ways. Thus, low affinity can always be compensated by high ligand concentration, which is a direct consequence of the monotonic response profile, where in the limit of large ligand excess all ligands will saturate at full activation ($f = 1$). Dimeric receptor engagement however shows different maximal activation levels as a function of binding strength (according to equations (3.13) and (3.22)). Thus binding affinity is translated into different maximal activation amplitudes. If one now sets a given activation level f_T to the maximal activation level of the weak ligand (as shown in figure 3.4B), any measured activation level $f > f_T$ above this threshold must be caused by the high affinity ligand. This allows cells in principle to discriminate ligands based on equilibrium affinity sensing. Figure 3.4D shows how the amplitude grows monotonically as a function of the 2D receptor binding strength as expressed by $\tilde{K}^X$ (here shown for the homo-dimeric case).

3.3 Application to the interferon system

I will now demonstrate why this mechanism is well suited to the interferon system. The 16 different interferon (IFN) ligands share a conserved binding asymmetry towards the two receptor subunits, with all of them showing a high affinity towards Ifnar 2 (R_2) and a low affinity towards Ifnar 1 (R_1). This asymmetry is a common property of many cytokine receptor systems [127]. Furthermore they span a wide range of global affinities, easily differing by orders of magnitude when comparing very strong binding ligands (such as IFNβ) against rather weakly binding ones (*e.g.* IFNα2). The natural

Reaction rate	Unit	Weak (IFNα2)	Strong (IFNβ)
$k_{b,1}$	$(\mathrm{Ms})^{-1}$	$2 \cdot 10^5$	$5 \cdot 10^5$
$k_{u,1}$	s^{-1}	1	0.01
$k_{b,2}$	$(\mathrm{Ms})^{-1}$	$3 \cdot 10^6$	10^7
$k_{u,2}$	s^{-1}	0.02	0.001
$k_{a,1}$	$(\mu\mathrm{m})^2\mathrm{s}^{-1}$	$5.48 \cdot 10^{-2}$	$1.67 \cdot 10^{-2}$
$k_{d,1}$	s^{-1}	0.4	$3.3 \cdot 10^{-3}$
$k_{a,2}$	$(\mu\mathrm{m})^2\mathrm{s}^{-1}$	$1.67 \cdot 10^{-2}$	$1.67 \cdot 10^{-2}$
$k_{d,2}$	s^{-1}	$4.4 \cdot 10^{-3}$	$3.3 \cdot 10^{-4}$

Table 3.2 | Parameter set for a weakly binding (IFNα2) and a tightly binding (IFNβ) ligand. The values were extracted and converted from [120, 121, 128].

receptor expression levels are notoriously low for the interferon system with only a few hundred copies per cell, leading to typical receptor surface densities in the range of $R_0 = (0.1 - 1)\,(\mu\mathrm{m})^{-2}$ [22]. Since interferon β is a prominent candidate for a tightly binding interferon ligand and interferon α2 on the other hand a good representative for a rather weak binding ligand, I collected the following set of rate constants (see table 3.2) from the literature, which were measured in experimental *in vitro* studies [120, 121, 128]. I will use these to model these two representative ligands as a benchmark case to study ligand discrimination for the interferon system.

3.4 Asymmetric dimerization enhances robust affinity sensing

Inspired by the fact that interferons show strong asymmetric binding properties, I analyzed the effect of asymmetry on the dose response curves and its implications for ligand discrimination. Figure 3.5A shows how the shape of the bell-shaped binding curves increasingly broadens, with increasing binding asymmetry. To quantify the degree of binding asymmetry a natural choice is the ratio of the two 3D equilibrium dissociation constants. I will use the symbol $\mathcal{A}$ to denote this binding asymmetry parameter

$$\mathcal{A} = \frac{K_{D,1}^B}{K_{D,2}^B}\,, \tag{3.24}$$

where I assume $K_{D,1}^B \geq K_{D,2}^B$ without loss of generalization. The transition from a hetero-dimer with identical subunit affinities (red curve in 3.5A for $\mathcal{A} = 1$) to asymmetric hetero-dimers with $\mathcal{A} > 1$ clearly shows how the left shoulder of the bell shape is set by

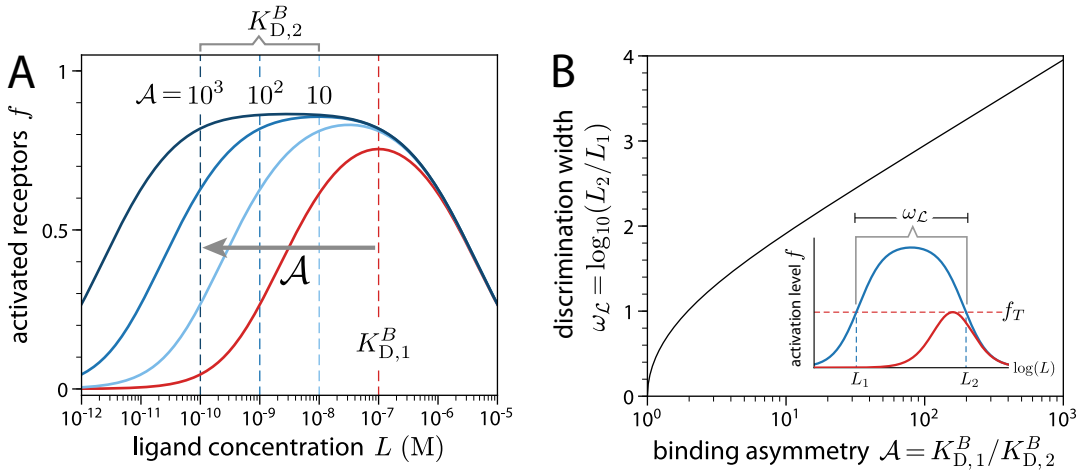

Figure 3.5 | Binding asymmetry enhances robust affinity sensing. **A** illustrates how the bell-shaped dose response curves develop broad plateau regions with increasing binding asymmetry $\mathcal{A}$. The asymmetric response curves (in blue) are compared against a homo-dimeric case (red curve) where $K_{\mathrm{D}}^{B} = 10^{-7}\,\mathrm{M}$, $K_{\mathrm{D}}^{X} = 0.2\,(\mu\mathrm{m})^{-2}$ and $R_0 = 10\,(\mu\mathrm{m})^{-2}$ was used. Broader activation plateaus lead to roughly constant activation levels over an increasingly larger ligand concentration range. **B** Discrimination width $\omega_{\mathcal{L}}$ as a function of the binding asymmetry $\mathcal{A}$. The discrimination width quantifies the concentration range in which ligand discrimination through this mechanism is possible. The inset shows a sketch of how this width is defined for a given reference activation level f_T, which sets a threshold, above which any measured activation level must be created by the higher affinity ligand. For the reference activation level (red bell shape) I used $K_{\mathrm{D}}^{B} = 10^{-7}\,\mathrm{M}$ and $K_{\mathrm{D}}^{X} = R_0 = 10\,(\mu\mathrm{m})^{-2}$.

the high affinity dissociation constants and thus effectively creates a plateau region. The more asymmetric the binding, the more this plateau broadens. This effect is indicated by the dashed vertical lines in figure 3.5A. The two 3D equilibrium binding constants define the onset and decay point of these plateaus. Here the left shoulder (in low concentration regimes) is naturally set by the high-affinity- and the decay point by the low-affinity binding constant. Thus a rough measure for the width of the plateau ω_P would be based on the binding asymmetry parameter $\mathcal{A}$ such that

$$\omega_P = \log_{10}\left(\mathcal{A}\right) = \log_{10}\left(\frac{K_{D,1}^{B}}{K_{D,2}^{B}}\right). \tag{3.25}$$

This is a very striking observation in the context of the explained discrimination mechanism from section 3.2. When trying to discriminate a strong from a weak ligand, broadened response curves increase the range of ligand concentrations over which ligand discrimination is possible. For a given reference ligand (here for example a weak ligand), the width of the concentration regime in which the discrimination can work is defined by the region where $f_{\mathrm{strong}} > f_T$. For the biphasic bell-shapes this region is thus defined by the two roots L_1 and L_2, where $f_{\mathrm{strong}}(L_1) = f_{\mathrm{strong}}(L_2) = f_T = f_{\mathrm{max,weak}}$ is satisfied (see

inset of figure 3.5B for a schematic depiction). Putting these considerations together we can equally quantify this concentration region in which ligand discrimination (w.r.t. a reference ligand) is possible. I denote this discrimination width parameter by $\omega_{\mathcal{L}}$ and calculate it as

$$\omega_{\mathcal{L}} = \log_{10}\left(\frac{L_1}{L_2}\right), \tag{3.26}$$

analogously to the definition of the plateau widths ω_P. For $\mathcal{A} = 1$, (*i.e.* $K^B_{D,1} = K^B_{D,2}$) the discrimination width in figure 3.5B $\omega_{\mathcal{L}} = 0$, since we are effectively considering two ligands with identical binding properties. But for increasing $\mathcal{A} > 1$ the region for ligand discrimination grows monotonically as a function of the binding asymmetry $\mathcal{A}$.

I interpret this effect as a *buffering mechanism*. Stronger asymmetry broadens the concentration regime where the discrimination mechanism can work, making it robust against external variations in the ligand concentration itself.

3.5 Response modulation through receptor density

A comparison of the solution for the binding curves in equations (3.5), (3.13) and (3.22) immediately reveals, that the binding curves for dimerizing receptor systems are a function of the receptor surface density R_0. Although this might not seem like a very profound statement by itself, it is an important observation that this density dependence cancels out for the monomeric case, while it remains for the dimeric case. While less exciting from a mathematical point of view, I do think that the implications for cellular signaling systems are very relevant.

For the homo-dimer the maximal peak activation levels occurs at $L_{\max} = K^B_{\mathrm{D}}/2$ and attains a maximal amplitude of

$$f^{\mathrm{Ho}}_{\max}(K^X_{\mathrm{D}}, R_0) = 1 + \frac{2K^X_{\mathrm{D}}}{R_0}\left(1 - \sqrt{1 + \frac{R_0}{K^X_{\mathrm{D}}}}\right). \tag{3.27}$$

I already showed the scaling of the maximal amplitude $f_{\max}$ as a function of $\tilde{K}^X$ in figure 3.4D. But for a given ligand K^X_{D} is fixed and I will now address the role of the receptor density R_0. A similar expression like equation (3.27) is also available in closed-form for the hetero-dimeric case, but I omit the closed-form expression here for the sake of brevity.

The central role of R_0 is that it allows to continuously tune the overall binding curve

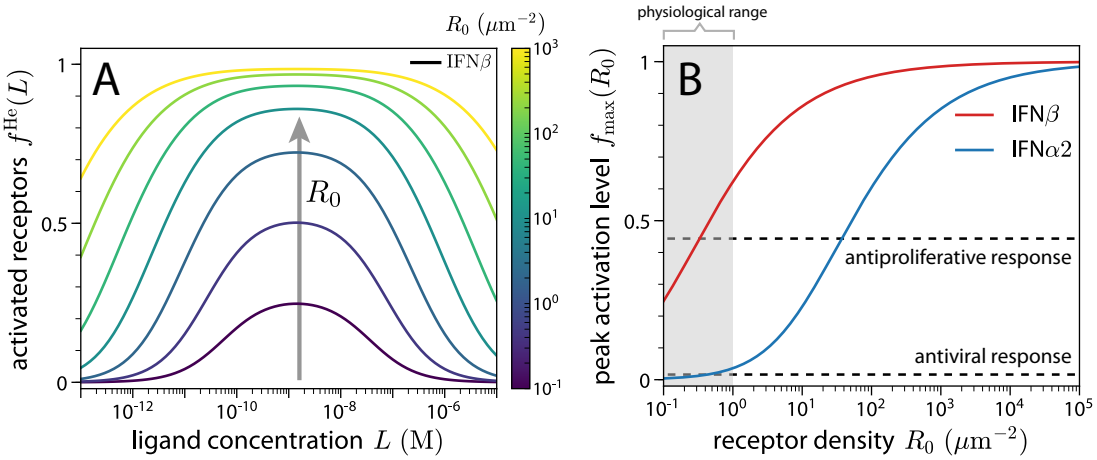

Figure 3.6 | Binding curve modulation through surface receptor density R_0. **A** shows binding curves for the interferon β ligand for various receptor surface densities R_0 as indicated by the color bar. Both the peak level and the width of the dose response curves increase monotonically as a function of R_0. **B** Maximal activation level $f_{\max}$ as a function of the receptor surface density R_0 for a weak (IFNα2) and a strong (IFNβ) ligand. The gray shaded region at the left border indicates physiologically reported receptor expression levels [22]. Within this range both ligands show well separated peak levels.

and accordingly modulates the ability for ligand discrimination. I show this tuning for several density values in figure 3.6A, where the binding parameters for IFNβ were used. The R_0 range is varied over several orders of magnitude including the physiological range and exceeding it to regions which address overexpression artifacts, as they might occur in *in vitro* studies.

Model predictions

The implications of this tuning mechanism are shown in figure 3.6B. There I show the peak activation level $f_{\max}$ for both IFNβ and IFNα2 as a function of R_0. The clear separation of the peak amplitudes when comparing the two ligands within the physiological range, is a restatement that for them ligand discrimination works well. But secondly it also illustrates nicely, that if any downstream response of the signal pathway is associated to a certain threshold value f_T of activated receptors, cells can use their receptor expression levels to tune the response functions, such that a given threshold is crossed or not. This is to say, that R_0 could act as a cellular tuning valve to determine which response can be triggered by which ligand. And even more so, it would allow a clear mechanism to account for cell-type specific responses. If two different cell-types were to use strongly differing receptor surface densities, receptor dimerization allows them to control threshold based activations by using their R_0 expression levels. Since two of the well known biological functions of interferons are to trigger antiviral

and antiproliferative responses, I schematically drew two horizontal thresholds for those two exemplary activities in figure 3.6B. These thresholds are of course not precisely known, but they offer an idea of how one could explain the robust initiation of antiviral states, whereas only tight binding ligands in conjecture with sustained signaling typically trigger antiproliferative responses [22, 23].

This model can therefore be used to make the prediction, that in an overexpression scenario weak ligands can trigger antiproliferative responses, while in the converse situation even strong ligands might fail to elicit antiviral responses, for a strong underexpression (knockout) scenario. In summary I suggest that the dimerization motif, additionally to a ligand discrimination mechanism, endows the signaling system with a certain degree of *functional plasticity* by using its receptor expression levels (R_0) as a tuning valve.

3.6 Sensitivity enhancement

While analyzing the binding properties of dimeric signaling receptors I also noticed that the effective sensitivity of the receptor system can be significantly enhanced when compared to the monomeric receptor as a default. By ligand sensitivity in this context, I mean the characteristic onset point of the output response. For pedagogical reasons I will use again the homo-dimer to explain this effect, although the qualitative picture stays the same for the hetero-dimer.

Monomeric receptor-ligand binding has its characteristic half-saturation point at $L^M_{0.5\mathrm{max}} = K_\mathrm{D}$ (see figure 3.2). If I equally define the onset point for the dimeric case as the ligand concentration $L^{\mathrm{Ho}}_{0.5\mathrm{max}}$, where the half maximal activation $f_{0.5\mathrm{max}}$ is attained, one observes that this onset point is shifted towards low concentration regimes, making the response very sensitive. To compare the monomeric case with the homo-dimer, I analyze a homo-dimer with $K^B_\mathrm{D} = K_\mathrm{D}$ and define the ratio

$$\frac{L^{\mathrm{Ho}}_{0.5\mathrm{max}}}{L^M_{0.5\mathrm{max}}} := s(\tilde{K}^X) = \frac{3}{4}(1+\sqrt{1+\tilde{K}^X}) + \frac{\tilde{K}^X}{8} - \frac{1}{8}\sqrt{\left(\tilde{K}^X + 6\left(1+\sqrt{\tilde{K}^X}\right)\right)^2 - 16} \tag{3.28}$$

as a sensitivity enhancement factor $s(\tilde{K}^X)$. Figure 3.7 shows this effect using a monomeric receptor with $K_\mathrm{D} = 1\mathrm{nM}$ as a benchmark. While the position of the maximum of the homo-dimer with equal 3D binding properties is set to $L_\mathrm{max} = K^B_\mathrm{D}/2$ the maximal value itself is a monotonic function of $\tilde{K}^X$, since $\tilde{K}^X$ is strictly positive (it

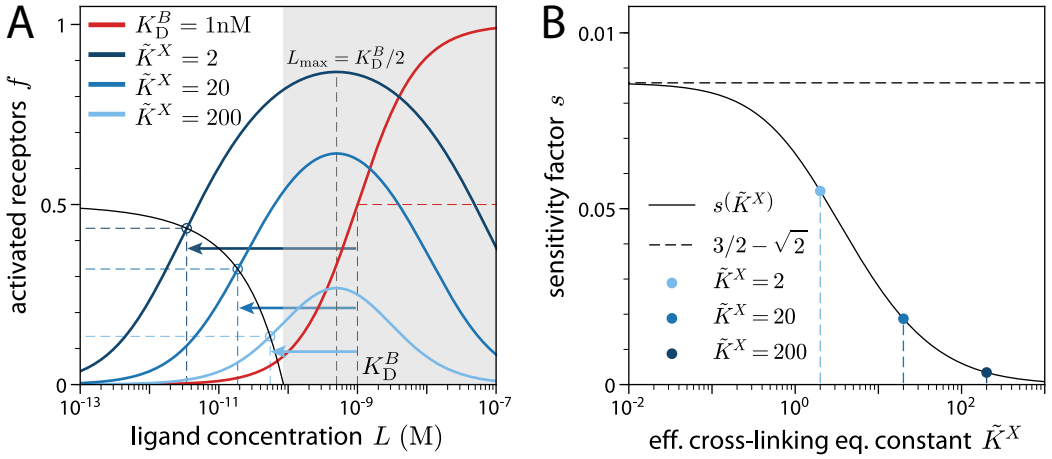

Figure 3.7 | A Enhanced sensitivity of the half activation point for a (homo-) dimeric signaling receptor when compared to a monomeric receptor with equal 3D binding strength. **B** Sensitivity factor s as a function of the nondimensional equilibrium cross-linking strength $\tilde{K}^X$.

is the ratio of two surface concentrations) and $f'_{max}(\tilde{K}^X) > 0$. With increased $\tilde{K}^X$ we also observe a shift of the half activation onset to regions of low ligand concentration, well below the 3D K_D value. Figure 3.7B shows the functional dependence of s on $\tilde{K}^X$. Both limits $\tilde{K}^X \to 0$ and $\tilde{K}^X \to \infty$ are obviously not physiologically relevant, but in-between this explains a significantly shifted onset point for dimeric signaling receptors.

3.7 Dynamic receptor turnover

All considerations so far ignored the fact, that cell surface receptors are exposed to a constant dynamic turnover. This internalization process removes receptors for example by endocytic events and balances the receptor levels on the plasma membrane by the synthesis of new unoccupied receptors.

To account for this well acknowledged feature I also included receptor turnover to the ligand-induced dimerization scheme from the previous sections. Here I considered unregulated turnover, meaning that any membrane bound species will be degraded according to a first-order process with degradation rate λ. This receptor turnover will of course change the total receptor concentrations in the system, such that the previously discussed conservation laws do not hold any longer. To balance the degradation term, free monomers (R_1 and R_2) can be resynthesized into the membrane. This production will be incorporated as a zero-th order process with production rate p. To compare this turnover scheme with the previous equilibrium model, I note that in the turnover scheme the total receptor concentration in steady state will be set by the ratio of the

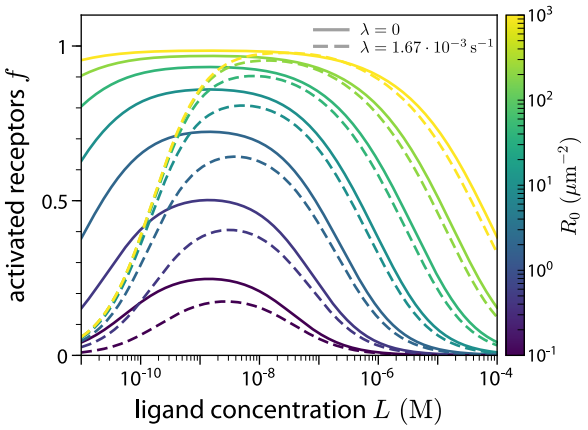

Figure 3.8 | Influence of receptor turnover on the dose response curves. Solid lines show the equilibrium model without, dashed lines with turnover, respectively.

production and degradation rate

$$R_{0,eq.} = \frac{p}{\lambda}. \tag{3.29}$$

In figure 3.8 I used a constant degradation rate of $\lambda = 1.67 \times 10^{-3}\,\mathrm{s}^{-1}$ and chose p to match the R_0 value from the case without turnover according to equation (3.29). This degradation rate corresponds to a mean life time of 10 minutes, which is typical for cytokine receptor complexes.

Figure 3.8 shows a comparison of the dose response between the system with and without turnover for different surface receptor densities R_0 (compare also figure 3.6). While the right half of the dose response is more or less unaffected, in the low concentration regime the turnover rectifies the onset point of the binding curves. This is an interesting observation, since the otherwise observed increase of sensitivity, as also explained in the previous section 3.6, would lead to hyper-sensitive systems for high affinity ligands, as they are not reported experimentally. The result of this more realistic depiction of receptor engagement thus shows the ability to shift the onset points to physiologically feasible regimes and additionally rectifies the onset points. This last aspect seems interesting, since a unified onset point seems somehow a good choice for a signaling system to define a global "off"-state, meaning that no ligand is present. If the onset points for strongly varying conditions and for different ligands are approximately aligned, this would allow the identification of a concentration threshold below which the system can decide that no signal is present.

3.8 Concluding remarks

I have used several simple equilibrium properties of dimeric signaling receptors to illustrate how ligand discrimination is possible based on affinity sensing. I subsequently illustrated how asymmetry, receptor density and more realistic ingredients modulate this mechanism, but all in all convincingly showed that receptor dimerization is a very simple signaling motif which enables robust information processing. For pedagogical reasons I often referred to the homo-dimeric case, which already shows the core elements of the discrimination mechanism. Adding asymmetry to the picture enhances the discrimination performance by making the mechanism robust. Most striking to me is the fact, that these explained features emerge by taking the most simple ligand-receptor model one step further by allowing it two form dimers. Figure 3.9 summarizes many of the findings from this chapter by showing the response profiles for the three discussed receptor models as a function of signal strength L and receptor density R_0 simultaneously.

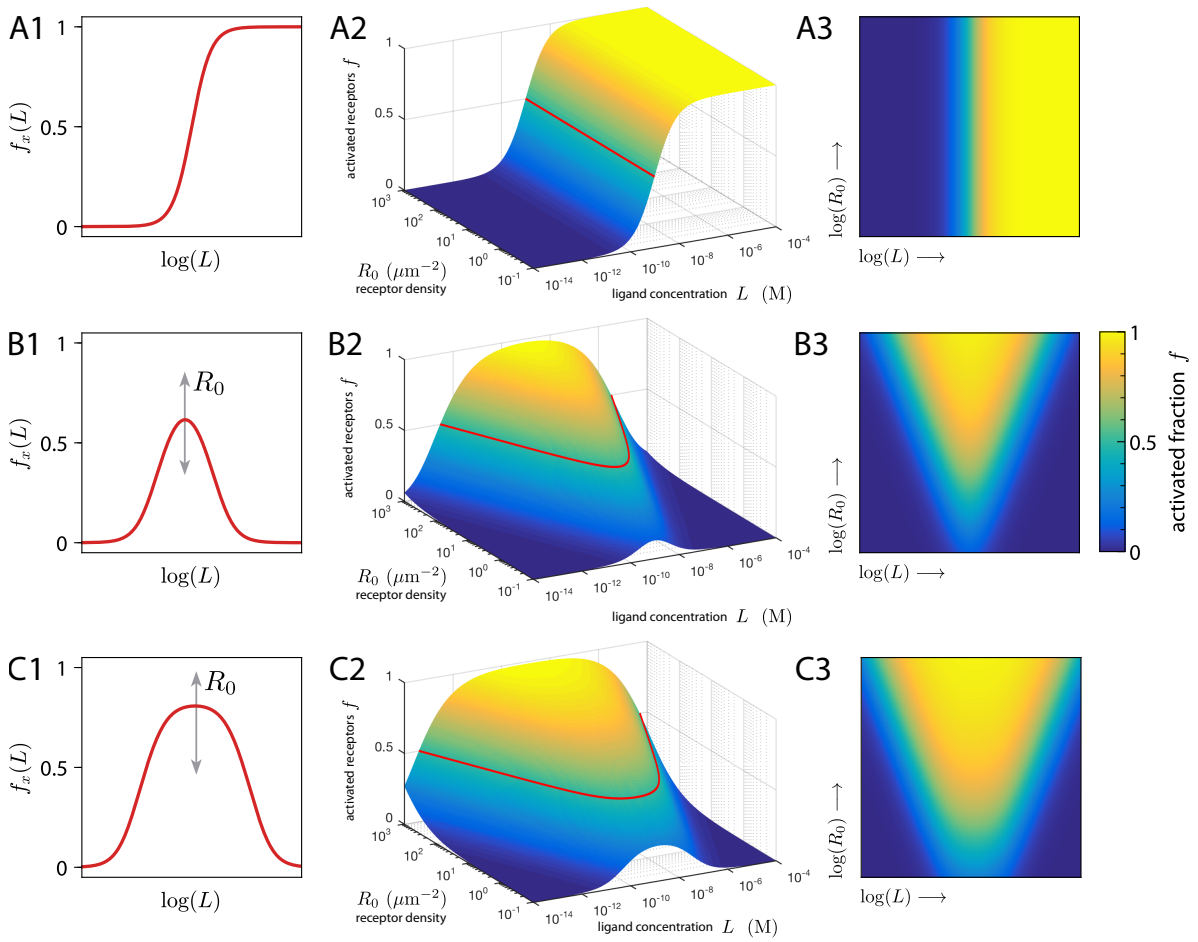

Figure 3.9 | Comparison of the dose response profiles for the three introduced receptor topologies as a function of ligand stimulation and cell receptor surface densities. **A1** shows a sketch of a monomeric response curve with the characteristic hyperbolic saturation kinetics as a function of the ligand concentration L. **A2** shows the monomeric response profile both as a function of ligand concentration and receptor surface density. The independence of R_0 is clearly visible. **A3** shows a top down view on the 3D surface plot of **A2**. The second row **B1-B3** show the same as the first row but now for a homo-dimerizing receptor system while the last row **C1-C3** shows these results for a hetero-dimerizing system, respectively. The most striking difference between a monomer and a dimerizing receptor system (regardless of homo- or hetero-dimerization) is the biphasic nature with respect to ligand stimulation and the lacking modulation with receptor density in the monomeric case. Additionally, a comparison between **B** and **C** shows the broadened response curves for asymmetric dimerization.

4 Information theoretic framework for ligand discrimination

In the previous chapter 3 we explained a ligand discrimination mechanism for signaling receptors based on the non-monotonic binding characteristics of dimeric receptor systems. We will now put these findings in a more formal framework and use an information theoretic analysis to quantify how well a given receptor system can perform the task of ligand discrimination. Information theoretic tools have been successfully applied to address problems in cellular signal transduction and gene regulatory networks in the past [129–134]. Here we will set up a framework to calculate the *mutual information* for a given ligand discrimination task and will then use it to quantify the discrimination performance of the previously suggested mechanism. To show explicitly that asymmetric binding leads to a robust discrimination mechanism, we set up this framework to account for fluctuations in the ligand concentration. Compared to the intrinsic noise of the receptor reactions, due to their finite copy numbers, this is a source of extrinsic variability.

4.1 Input & output variables

The central quantity of this chapter is the mutual information of the ligand discrimination problem. *Mutual information*[1] is a standard information theoretic measure to quantify the dependence between two random variables X and F and is defined as the following symmetric functional

$$I(X,F) = \iint p(x,f)\, \log_2\left(\frac{p(x,f)}{p(x)p(f)}\right) dxdf\,, \tag{4.1}$$

where x and f are realizations of the two random variables X and F, respectively [135–137]. Before we can compute the mutual information for a given task, we must

[1] We use the binary logarithm in the definition of the mutual information. This choice leads to bit as the natural unit of information.

define our input and output variables and specify how we incorporate extrinsic noise in our approach. In the field of signal transduction it suggests itself to think of the first random variable X to represent the input signal, that is measured by the cell (here the signaling receptors). The outcome of this measurement is specified by the second random variable F, which tells us the measured response of this communication channel. For the ligand discrimination task the input signal is simply the identity of the ligand. Therefore we consider X to be a discrete random variable, such that a given x shall stand for the input ligand type which is present. Physically speaking we assume those ligands to be diffusing in the extracellular space surrounding cells such that they can be sensed by the cell surface receptors. In the following we use $\mathcal{X}$ to denote the discrete set of input states, *i.e.* $\mathcal{X} = \{x_1, x_2, \dots\}$. The default scenario we consider here uses two possible input types, *i.e.* two distinct ligands. This means that the random variable X can take two values

$$x \in \mathcal{X} = \{A, B\}\,, \tag{4.2}$$

and we ask the system to tell them apart from each other. As the most simple ligand discrimination task I will refer to this as A–B discrimination. The state $x = A$ simply means that a ligand of type A, and $x = B$ that a ligand of type B is present, respectively. Without any other external knowledge we make the assumption of equal and constant prior probabilities for the input variable X, which here implies

$$p(x) = \frac{1}{2} \quad \text{for} \quad x = A, B. \tag{4.3}$$

Receptor response functions

The output variable of a signal transduction system can be any well defined molecular readout that is accessible to the cell. From this perspective signal cascades are considered to be communication channels which transmit the input signal to cause a downstream response. Typical readouts could be the concentration levels of activated transcription factors or gene expression products (see figure 1.1). Since we are interested in the very early stages of signal initiation (see figure 3.1) we use receptor activation as our molecular readout. Consistent with the previous notation we use f to denote the fraction of activated receptors, as introduced in section 3.1. For this choice the communication channel is given by the receptor module, which translates a given input signal into receptor activation, depending on the type of the receptor system. This means that the output random variable F is set by the response function of a given ligand-receptor system. Given a ligand of type $x \in \mathcal{X}$, which is present at a ligand concentration L

(signal strength), cells can use different receptor-ligand systems to measure the fraction of active receptors f.

To indicate that a response function f belongs to a given input state x, we use corresponding subscripts. Together with the superscripts (M, Ho, He) for the monomeric, homo-dimeric and hetero-dimeric receptor systems this allows us to specify which response function we have in mind. For example, a given ligand $x = A$ with binding parameters specified in a parameter vector $\boldsymbol{\beta}_A$, which cross-links a receptor pair *via* homo-dimerization will have an equilibrium response function $f_A^{\mathrm{Ho}}(L, \boldsymbol{\beta}_A)$. Previously we referred to the functions $f = f(L)$ as dose response curves. Shifting our perspective to the information theoretic approach, they act as *transfer-functions* similar to their definition in signal theory.

4.2 Extrinsic noise in receptor signaling

Next, we wish to put a special focus on the role of extrinsic noise. Our approach how to analyze the influence of extrinsic noise in receptor systems, is to consider extrinsic noise as fluctuations in the ligand concentration L.

We chose this approach, since we want to demonstrate under which conditions which receptor systems are robust ligand sensors, even in very noisy and fluctuating environments. To incorporate these kind of fluctuations we consider the ligand concentration to be distributed according to a specified probability distribution. A very sharply peaked ligand concentration distribution then corresponds to a low noise scenario and a broad distribution represents larger fluctuations in the space of ligand concentrations. We use $\omega(L)$ to denote a given distribution of the ligand concentration L and naturally require them to be properly normalized in the sense, that they satisfy the normalization condition

$$\int_0^\infty \omega(L)\, dL = 1. \tag{4.4}$$

The next logical question is to ask how these distributions look like and if they are the same for different inputs. In order to address this, we condition the ligand concentration distributions on the input variable x and write

$$\omega_x(L) \equiv p(L \,|\, x)\,, \tag{4.5}$$

where we use $\omega_x(L)$ to focus on the distribution itself and the conditional expression on the right hand side for the sake of notational consistency of the probabilistic framework.

4.2.1 Ligand concentration distributions

Real experimental data on true ligand concentrations is hard to find. For this reason we make several assumptions and analyze the ligand discrimination task for two choices of ligand concentration distributions ω. We motivate both below.

Unbiased prior distribution

Ligand concentrations are naturally handled on a logarithmic scale. This is based on the experience that for physiologically realistic processes, both, typical affinities and concentration regimes easily span several orders of magnitude. Having no *a priori* knowledge about the real distribution which cells are exposed to, our first example for ω is motivated by the idea to use the most unbiased prior distribution. By this we mean to chose ω such, that it does not imply any bias and is most uninformative. For a normally scaled quantity y, a uniform distribution would do this job. Ligand concentrations can in this context be thought of as logarithmically scaling quantities $\log(y)$, for which the most unbiased prior is the $\sim 1/y$ distribution. This is known as *Jeffrey's* prior. The books by Jaynes [135] and MacKay [136] provide more background on this topic and on how to choose appropriate prior probability distributions in general. A second motivation for this choice came to our attention through a recent publication which measured the release of cytokine signaling molecules both *in vivo* and *in vitro* to understand the spread and consumption of these signaling molecules in dense cellular tissues [138, 139]. The authors use a diffusion-consumption reaction-diffusion mechanism to explain the spread of the signaling molecules in a cell tissue. By solving for the steady state concentration of this suggested reaction-diffusion model one strikingly also obtains a $\sim 1/L$ distribution. We use these two considerations to motivate our choice and will call this distribution the uninformative prior (up)

$$\omega_{\mathrm{up}}(L) = \begin{cases} \left[\ln\left(\frac{l_{\max}}{l_{\min}}\right) L\right]^{-1} & \text{for} \quad L \in \mathcal{L} = [l_{\min}, l_{\max}] \\ 0 & \text{elsewhere} \end{cases}, \tag{4.6}$$

where we introduced a finite concentration range $\mathcal{L} = [l_{\min}, l_{\max}]$ to normalize the distribution by the normalization constant $\mathcal{N} = \ln(l_{\max}/l_{\min})^{-1}$.

Log-normal distribution

As a second pick we use the log-normal distribution for ligand concentrations. This seems a reasonable choice, since it is naturally confined to a positive support and decays on both sides of a clear localized peak, defined by the scale parameters μ and σ. The density function for our purpose reads

$$\omega_{\mathrm{LN}}(L;\sigma,\mu) = \frac{1}{L\,\sigma\sqrt{2\pi}}\exp\left(\frac{-\big(\ln(L)-\mu\big)^2}{2\sigma^2}\right). \tag{4.7}$$

While $\mu \in \mathbb{R}$ can be any real number, σ is a positive real number $\sigma > 0$. The mode η of the distribution is related to μ by

$$\eta = \exp\big(\mu - \sigma^2\big). \tag{4.8}$$

Hence we determine μ for a given choice of σ and η by using the relation

$$\mu = \ln(\eta) + \sigma^2. \tag{4.9}$$

4.3 Mutual Information of ligand discrimination

Now we have specified the input and output variables and have motivated two choices for the ligand concentration distributions ω. We proceed by explaining how to put all these parts together to calculate the mutual information $I(X,F)$. For the ligand discrimination task the mutual information $I(X,F)$ from (4.1) becomes

$$I(X,F) = \sum_{x\in\mathcal{X}} \int_{\mathcal{F}} p(x,f)\,\log\left(\frac{p(x,f)}{p(x)p(f)}\right)\,df. \tag{4.10}$$

The summation runs over all input states and the f-integration is carried out over all attainable activation levels $\mathcal{F}$, which define the dynamic range of the given ligand-receptor system. Using the standard factorization $p(x,f) = p(f\,|\,x)\,p(x)$ we can rewrite equation (4.10) as

$$I(X,F) = \sum_{x\in\mathcal{X}} p(x) \int_{\mathcal{F}} p(f\,|\,x)\,\log\left(\frac{p(f\,|\,x)}{p(f)}\right)\,df. \tag{4.11}$$

The prior probabilities $p(x)$ are known for all inputs $x \in \mathcal{X}$, since we deliberately set them. To proceed we need to find expressions for the conditional probabilities $p(f\,|\,x)$.

Once we have those, we automatically have full knowledge of the joint distribution *via*

$$p(x, f) = p(f \,|\, x)\, p(x) \tag{4.12}$$

and also can directly calculate the posterior distribution $p(f)$ by

$$p(f) = \sum_{x \in \mathcal{X}} p(f, x) = \sum_{x \in \mathcal{X}} p(f \,|\, x)\, p(x). \tag{4.13}$$

So we have reduced the problem of evaluating the mutual information $I(X, F)$ for the ligand discrimination task according to equation (4.11) to find the conditional distributions $p(f \,|\, x)$. Once we have these, we reiterate that the mutual information can directly be evaluated by computing

$$I(X, F) = \sum_{x \in \mathcal{X}} p(x) \int_{\mathcal{F}} p(f \,|\, x)\, \log \left(\frac{p(f \,|\, x)}{\sum_{x'} p(f \,|\, x')\, p(x')} \right) df. \tag{4.14}$$

4.3.1 Distribution of activated receptors

We fill the missing gap by deriving an recipe on how to calculate the conditional distribution functions $p(f \,|\, x)$, which then in turn permit us to calculate the mutual information. We refer to these conditional distributions as the distributions of activated receptors (conditioned on an input type x). To emphasize that a given input x comes along with a corresponding ligand concentration distribution $\omega_x(L) = p(L \,|\, x)$ we use the following identity

$$p(f \,|\, x) = \int_{\mathcal{L}} \underbrace{p(L \,|\, x)}_{=\omega_x(L)}\, p(f \,|\, L, x)\, dL = \int_{\mathcal{L}} \omega_x(L)\, p(f \,|\, L, x)\, dL\,, \tag{4.15}$$

in order to proceed. To further evaluate the expression in equation (4.15) we need to discuss the term $p(f \,|\, L, x)$, *i.e.* the probability to find a given output value f given an input x and given a precise value for L. The fact that we not only condition this expression on x but at the same time also condition it on a specific value for L makes it clear, that this expression has to be a Delta distribution. It asks for the probability for an exact given value of f, given the type x and an exact value for the ligand concentration L.

$$p\left(\tilde{f} \,|\, L, x\right) = \delta\Big(\tilde{f} - f_x(L)\Big). \tag{4.16}$$

Interpreted under an L-integral this means, that $p\left(\tilde{f} \,|\, L, x\right)$ assures that the L-integrand is only evaluated at those values for L, where the response function $f_x(L)$ equals the said activation level/output value $\tilde{f}$, *i.e.* where

$$f_x(L) = \tilde{f} \tag{4.17}$$

is satisfied. Summarizing, this allows us to find the following formula for $p(f \,|\, x)$ by inserting the expression for $p\left(\tilde{f} \,|\, L, x\right)$ from equation (4.16) into equation (4.15)

$$p\left(\tilde{f} \,|\, x\right) = \int p\left(L \,|\, x\right) \times \delta\left(\tilde{f} \; - f_x(L)\right) \, dL \tag{4.18}$$

$$= \int \underbrace{\omega_x(L)}_{\text{ligand distribution}} \times \; \delta\left(\tilde{f} \quad - \underbrace{f_x(L)}_{\text{receptor response}}\right) dL. \tag{4.19}$$

At this point it might be worthwhile to mention that the receptor response function $f_x(L)$ is only for the simple monomeric ligand-receptor case depending on its affinity $K_{D,x}$ and the concentration level L. For more complex receptor systems f might in general depend on more parameters such as receptor densities R_0 and or further kinetic biochemical parameters, such as multiple K_D's. To illustrate these potential dependencies, in this generic derivation, we write

$$f = f_x(L, \boldsymbol{\beta}_x)\,, \tag{4.20}$$

and condense all other parameters into $\boldsymbol{\beta}_x$. In these expressions above we use $\tilde{f}$ to denote a specific value which the output variable might take and use f to denote the actual response function, which gives rise to this output value. At this point we briefly demonstrate that this approach, to compute the conditional distribution $p(f \,|\, x)$, gives indeed a properly normalized distribution of the variable f. The normalization condition for $p(f \,|\, x)$ reads

$$\int_{\mathcal{F}} p(f \,|\, x)\, df = 1 \qquad \forall\, x \in \mathcal{X} \tag{4.21}$$

which we can verify for our general expression in equation (4.19) by showing that

$$\int_{\mathcal{F}} p(f \mid x)\, df = \iint_{\mathcal{F},\mathcal{L}} p(L \mid x)\, p(f \mid L, x)\, dL\, df \tag{4.22}$$

$$= \int_{\mathcal{F}} \left[\int_{\mathcal{L}} \omega_x(L) \times \delta\left(\tilde{f} - f_x(L, \boldsymbol{\beta}_x)\right) dL \right] df \tag{4.23}$$

$$= \int_{\mathcal{L}} \left[\int_{\mathcal{F}} \omega_x(L) \times \delta\left(\tilde{f} - f_x(L, \boldsymbol{\beta}_x)\right) df \right] dL \tag{4.24}$$

$$= \int_{\mathcal{L}} \omega_x(L)\, dL = 1 \tag{4.25}$$

as required, since we demand ω_x to be a properly normalized distribution. After swapping the integration order in line (4.24) we can carry out the f integration over the δ distribution which simply yields a factor of 1 in the remaining integrand.

Having established all of this, we now proceed in our general recipe on how to actually compute the desired distribution $p\left(\tilde{f} \mid x\right)$. To transform equation (4.19) we make use of the integral form of the generalized scaling property of Dirac's δ-functional

$$\int_{-\infty}^{\infty} f(x)\, \delta\left(g(x)\right) dx = \sum_i \frac{f(x_i)}{|g'(x_i)|}\,, \tag{4.26}$$

where i sums over the zero-crossings of g. If the integration runs only over a finite interval this changes to

$$\int_{a}^{b} f(x)\, \delta\left(g(x)\right) dx = \sum_i \frac{f(x_i)}{|g'(x_i)|}\,, \tag{4.27}$$

where i runs over all roots of g in the domain $[a, b]$. With this property we can rewrite our general expression for the target distribution $p\left(\tilde{f} \mid x\right)$ from equation (4.19) in the form of

$$p\left(\tilde{f} \mid x\right) = \int_{\mathcal{L}} \omega_x(L) \times \delta\left(\tilde{f} - f_x(L, \boldsymbol{\beta}_x)\right) dL \tag{4.28}$$

$$= \sum_i \left(\omega_x(L_i) \times \left| \frac{\partial}{\partial L} \left(\tilde{f} - f_x(L, \boldsymbol{\beta}_x)\right)\Big|_{L=L_i} \right|^{-1} \right) \tag{4.29}$$

$$= \sum_i \left(\omega_x(L_i) \times \left| \frac{\partial}{\partial L} f_x(L, \boldsymbol{\beta}_x)\Big|_{L=L_i} \right|^{-1} \right) \tag{4.30}$$

$$= \sum_i \left(\frac{\omega_x(L_i)}{\left| \frac{\partial}{\partial L} f_x(L, \boldsymbol{\beta}_x)\Big|_{L=L_i} \right|} \right)\,, \tag{4.31}$$

where the summation runs over all i roots of the equation

$$f_x(L, \boldsymbol{\beta}_x) = \tilde{f} \tag{4.32}$$

in the ligand concentration interval $\mathcal{L} = [l_{\min}, l_{\max}]$, for a given activation level $\tilde{f} = \text{const}$.

We repeat this central result for the conditional probability of the output level distribution below

$$p\big(\tilde{f} \,|\, x\big) = \sum_i \left(\frac{\omega_x\left(L_i\right)}{\left| \frac{\partial}{\partial L} f_x(L, \boldsymbol{\beta}_x)\Big|_{L=L_i} \right|} \right), \quad \forall\ L_i \text{ s.t. } f_x(L_i, \boldsymbol{\beta}_x) = \tilde{f} \quad \text{and} \quad L_i \in \mathcal{L}. \tag{4.33}$$

At this point we emphasize that equation (4.33) is still completely general and holds for any valid choice for the ligand concentration distribution $\omega_x(L)$ and for any valid choice for the receptor (dose) response function $f_x(L, \boldsymbol{\beta}_x)$.

This concludes the calculation of $p(f \,|\, x)$. For simple response functions f the evaluation can be done analytically or by using computer algebra systems. For more complex receptor modules we implemented a numerical routine which implements equation (4.33). The solution for $p(f \,|\, x)$ gives access to the full joint distribution $p(f, x)$, which we need to calculate the mutual information $I(X, F)$. To summarize these findings, we give a general recipe in the following section.

4.4 Recipe for general receptor modules

So far all derived results are still generic and do not make any assumption about the underlying receptor module. In this section we briefly outline how one has to proceed for generic response modules f_x. Depending on the complexity of the receptor response function these steps can be performed analytically. We have implemented a numerical counterpart for all of them, such that they can in principle be applied to any reasonable choice for f. This might be relevant if one wishes to extend this ansatz to more complex receptor models in the future. We suggest the following procedure.

1. Given a receptor module (or a more generic input-output system) we start by specifying the **response function**

$$f_x = f_x(L, \boldsymbol{\beta}_x) \qquad \forall \quad x \in \mathcal{X} \tag{4.34}$$

for all inputs x. The response f is a function of the ligand concentration L and in general of several other biophysical parameters such as receptor densities R_i and affinities etc. We group all these dependencies apart from the ligand concentration in a parameter vector $\boldsymbol{\beta}_x$ as before.

2. Specify a **ligand concentration distribution**

$$\omega_x = \omega_x(L) \tag{4.35}$$

for all inputs x. In general one can of course set different distributions for all inputs. For a discussion on appropriate choices for ω see section 4.2.1. The use of finite concentration intervals $\mathcal{L} = [l_{\min}, l_{\max}]$ can be necessary due to normalization requirements, but also due to physiological considerations. On the lower spectrum one should avoid getting below a single particle limit, while of course extremely large concentrations will naturally be unphysiological.

3. According to the choice of the **finite cutoff interval** $\mathcal{L}$ compute the **dynamic range** of realizable activation levels f, by scanning the response function over $\mathcal{L}$. In the most generic form this should allow you to determine the dynamic range $\mathcal{F} = [f_{\min}, f_{\max}] \subset [0, 1]$ of attainable activation levels f according to

$$f_{\min} = \min_{L\in\mathcal{L}} \Big\{ f_x(L, \boldsymbol{\beta}_x) \Big\} \quad \text{and} \quad f_{\max} = \max_{L\in\mathcal{L}} \Big\{ f_x(L, \boldsymbol{\beta}_x) \Big\}. \tag{4.36}$$

Care must be taken, that for multiple inputs, the dynamic range is typically depending on the input state x. This is important for the integration range both in a subsequent analytical or numerical treatment of the ligand discrimination problem. So effectively this step has to be done for all input values $x \in \mathcal{X}$.

4. Compute the **probability distribution of the activation levels** f given an input x, for your given choice of ω_x according to

$$p\big(\tilde{f}\,|\,x\big) = \int_{\mathcal{L}} \omega_x(L) \;\times\; \delta\left(\tilde{f} - f_x(L, \boldsymbol{\beta}_x)\right) dL \tag{4.37}$$

$$= \sum_i \left(\frac{\omega_x\left(L_i\right)}{\left| \frac{\partial}{\partial L} f_x(L, \boldsymbol{\beta}_x)\Big|_{L=L_i} \right|} \right), \quad \forall\ L_i \text{ s.t. } f_x(L, \boldsymbol{\beta}_x) = \tilde{f} \quad \text{and} \quad L_i \in \mathcal{L}. \tag{4.38}$$

which is a properly normalized PDF on the dynamic range interval $\mathcal{F} = [f_{\min}, f_{\max}]$. For simple systems and choices of ω this might be achievable in closed form analytical expressions.

5. Having established an expression for $p(f \mid x)$, we find the joint and the posterior distributions using

$$p(f, x) = p(f \mid x)\, p(x) \tag{4.39}$$
$$p(f) = \sum_{x \in \mathcal{X}} p(x) p(f \mid x)\,, \tag{4.40}$$

where we again assume full knowledge of $p(x)$.

6. Finally calculate the mutual information by using all results from all preceding steps according to

$$I(X, F) = \sum_{x \in \mathcal{X}} p(x) \int_{\mathcal{F}} p(f \mid x)\, \log \left(\frac{p(f \mid x)}{\sum_{x'} p(f \mid x')\, p(x')} \right) df. \tag{4.41}$$

4.5 Application to monomeric inputs

As before in chapter 3, the monomeric receptor is a useful default case. The response function f^{M} shows the already explained hyperbolic saturation kinetics and is the simplest case that we now use as a benchmark. This is suitable because it allows a concrete application of the general recipe from the previous section. In fact it turns out, that one can derive closed form expressions, independent of a choice for ω, for all probability distributions $p(x, f)$, $p(f \mid x)$ and $p(f)$. So we start as before by specifying our response function f as

$$f_x^{\mathrm{M}}(L) = \frac{L}{K_{D,x} + L}\,, \tag{4.42}$$

which we insert in equation (4.38) from the previous general recipe. According to (4.38) we secondly need to calculate the derivative of the receptor response function (4.42) with respect to the ligand concentration L, *i.e.* we compute

$$\frac{\partial}{\partial L} f_x^{\mathrm{M}}(L) = \frac{K_{\mathrm{D},x}}{(K_{\mathrm{D},x} + L)^2}. \tag{4.43}$$

In order to further evaluate the expression as shown in equation (4.33) we first need to determine the roots of the equation

$$f_x(L, R_0) = f_x(L) = \tilde{f} = \frac{L}{K_{\mathrm{D},x} + L} \tag{4.44}$$

for a given constant activation level $\tilde{f} = \text{const}$. This equation has only a single root L_1 at

$$L_1 = \frac{\tilde{f}}{\left(1 - \tilde{f}\right)} K_{\mathrm{D},x}. \tag{4.45}$$

Since the monomeric receptor response (4.42) is strictly monotonically increasing, it is immediately evident, that for a given activation level $\tilde{f}$ there is only a single root L_1. Now we can evaluate our expression for the derivative in equation (4.43) at the root from equation (4.45).

$$\left(\frac{\partial}{\partial L} f_x(L, R_0)\right)\Big|_{L=L_1} = \left(\frac{K_{\mathrm{D},x}}{(K_{\mathrm{D},x} + L)^2}\right)\Big|_{L=L_1} = \frac{K_{\mathrm{D},x}}{\left(K_{\mathrm{D},x} + \frac{\tilde{f}}{1-\tilde{f}} K_{\mathrm{D},x}\right)^2} \tag{4.46}$$

$$= \frac{\left(1 - \tilde{f}\right)^2}{K_{\mathrm{D},x}} \tag{4.47}$$

Now we are all set to compute the desired distribution function of the fraction of activated receptors $p(f \,|\, x)$ for this case. Using equation (4.33), we find

$$p\left(\tilde{f} \,|\, x\right) = \sum_{i=1}^{n_r=1} \left(\frac{\omega_x\left(L_i\right)}{\left|\frac{\partial}{\partial L} f_x(L)\Big|_{L=L_i}\right|}\right) = \frac{\omega_x\left(L_1\right)}{\left|\frac{\partial}{\partial L} f_x(L)\Big|_{L=L_1}\right|} \tag{4.48}$$

$$= \frac{K_{\mathrm{D},x}}{\left(1 - \tilde{f}\right)^2} \, \omega_x\left(\frac{K_{\mathrm{D},x}\, \tilde{f}}{1 - \tilde{f}}\right). \tag{4.49}$$

Note that up to this point we have not specified a specific choice for the ligand concentration distribution function ω, and only made use of the fact that the receptor response function f is that of a monomeric system. Hence the above result is generally valid for any ω in the case of a monomeric receptor system. Below we summarize the central results of this section. Only assuming a hyperbolic input profile $f_x^{\mathrm{M}}(L)$ (4.42) allows us to explicitly find expressions for the conditional distribution $p(f \,|\, x)$, the joint $p(x, f)$

response function	**ligand dist.** $\omega(L)$	$p(f \mid x)$
monomer f^{M}	generic ω	$\frac{K_{\mathrm{D},x}}{(1-f)^2}\,\omega_x\left(\frac{f}{(1-f)}K_{\mathrm{D},x}\right)$
monomer f^{M}	uniform	$\frac{K_{\mathrm{D},x}}{(l_{\max}-l_{\min})(1-f)^2}$
monomer f^{M}	$\sim 1/L$	$\left[\ln\left(\frac{l_{\max}}{l_{\min}}\right) f(1-f)\right]^{-1}$
monomer f^{M}	log-normal	$\frac{\exp\left(-\left(\ln\left(K_{\mathrm{D},x}\frac{f}{1-f}\right)-\mu\right)^2/(2\sigma^2)\right)}{\sigma\sqrt{2\pi}f(1-f)}$

Table 4.1 | Overview over the conditional output distributions $p(f \mid x)$ for a given input state x for different ligand priors $\omega_x(L)$. In all cases we assume monomeric receptor response functions f^{M}.

and $p(f)$ which are true for any valid choice of ω_x.

$$p\left(f \mid x\right) = \frac{K_{\mathrm{D},x}}{(1-f)^2}\;\omega_x\left(\frac{K_{\mathrm{D},x}\,f}{1-f}\right) \qquad \text{dist. of activated receptors given an input } x \tag{4.50}$$

$$p(x,f) = p(x)\,\frac{K_{\mathrm{D},x}}{\left(1-f\right)^2}\;\omega_x\left(\frac{K_{\mathrm{D},x}\,f}{1-f}\right) \qquad \text{joint dist. of the input and output} \tag{4.51}$$

$$p(f) = \sum_{x\in\mathcal{X}} p(x)\,\frac{K_{\mathrm{D},x}}{\left(1-f\right)^2}\;\omega_x\left(\frac{K_{\mathrm{D},x}\,f}{1-f}\right) \qquad \text{posterior dist. of the output} \tag{4.52}$$

If we now specify ligand concentration distributions, we can simply evaluate the above results. Table 4.1 lists the results for the $p(f \mid x)$ distributions for three choices of ω. There we introduced Heaviside step functions to avoid explicit case distinctions. They account for the finite cutoff intervals in ligand concentration space. For a given finite concentration range $\mathcal{L}$ we introduce the following product of two Heaviside step functions in order to implement a finite windowing function

$$\Theta_{\mathcal{L}}(L) = \Theta(L-l_{\min}) \times \Theta(l_{\max}-L). \tag{4.53}$$

4.6 A–B discrimination with monomeric receptors

The previous section applied all steps of our recipe up to the evaluation of the mutual information $I(X, F)$ itself. We now use the results for $p(f \mid x)$ for the monomeric case and discuss the A–B discrimination problem for the uninformative ligand prior distribution ω_{up}. We assume two inputs $x \in \{A, B\}$, for which we assume $K_{\text{D},A} < K_{\text{D},B}$ without loss of generality. Further, we assume that the ligand concentration distribution is the same for both ligands

$$\omega_A(L) = \omega_B(L) =: \omega_{\text{up}}(L). \tag{4.54}$$

From table 4.1 we already know the expression for $p(f \mid x)$ and can use the results to evaluate the mutual information $I(X, F)$ according to equation (4.11). This last integration step is straight forward but cumbersome, which is why we only present the final result.

$$I(X,F) = \underbrace{H(X)}_{\text{input entropy}} \times \begin{cases} 1 & \text{if} \quad \mathcal{F}_A \cap \mathcal{F}_B = \varnothing \\ \ln\left(\dfrac{K_{\text{D},B}}{K_{\text{D},A}}\right) \Big/ \ln\left(\dfrac{l_{\max}}{l_{\min}}\right) & \text{else} \end{cases} \tag{4.55}$$

Here $\mathcal{F}_A$ and $\mathcal{F}_B$ are the dynamic ranges of activation levels of input ligand A and B, respectively. In this form the equation for the mutual information $I(X, F)$ can nicely be understood as the product of a maximal information amplitude and a scaling factor depending on the input affinities and the choices for the input concentration distribution,

$$I(X, F) = I_{\max} \cdot (\text{scaling factor}) \tag{4.56}$$

where the maximal amplitude $I_{\max} = H(X)$ is set by the entropy of the input random variable X. This solution has the following interesting implications for ligand discrimination with monomeric receptors. The information transmission can be tuned as a function of the binding asymmetry

$$\mathcal{A} = \frac{K_{\text{D},B}}{K_{\text{D},A}}. \tag{4.57}$$

This means, the more two monomeric ligands are detuned, *i.e.* show different binding properties, the more information can be transmitted. In the limit of $K_{\text{D},A} = K_{\text{D},B}$ our results of course predicts, that the information is zero, as required. If the choice of $\mathcal{L}$ and the affinities $K_{\text{D},A}$ and $K_{\text{D},B}$ are such, that the dynamic ranges of both inputs

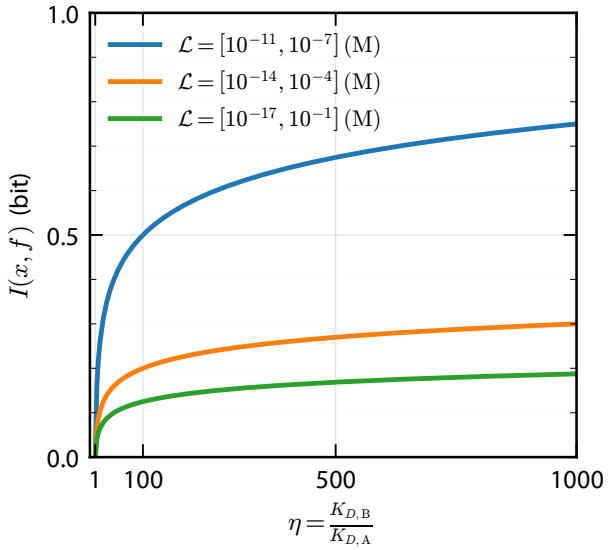

Figure 4.1 | Mutual information $I(X, F)$ as a function of the asymmetry/detuning $\mathcal{A} := K_{\mathrm{D},B}/K_{\mathrm{D},A}$ of the two input affinities. Different colors represent different widths of concentration ranges over which we assumed the $1/L$ ligand concentration distribution. This illustrates, that although the information increases as $\sim \ln(\mathcal{A})$, a broadened concentration range globally pushes the maximal information down.

are disjoint sets, the mutual information is always constant one bit. Although this case is of rather pathological nature, it effectively illustrates how monomeric receptors can discriminate ligands. Conversely, if two ligands happen to have similar affinities, their output distributions will show a significant overlap, such that their information transmission performance suffers tremendously.

4.7 Robust ligand discrimination through asymmetric receptor dimerization

Finally, we apply these results to the dimeric asymmetric hetero-dimerization scheme. For this purpose we consider the following scenario. We consider two receptor systems and ask both of them to perform the A-B discrimination problem. This means we consider a strong and a weak ligand, which trigger a monomeric receptor, and we consider a strong and a weak ligand which use a hetero-dimerizing scheme. For the hetero-dimerizing case we take interferon β and $\alpha 2$ as the strong and the weak ligand, respectively. The parametrization is based on the values from table 3.2 and their response function is f^{He} according to equation (3.22). The two ligands which engage monomeric

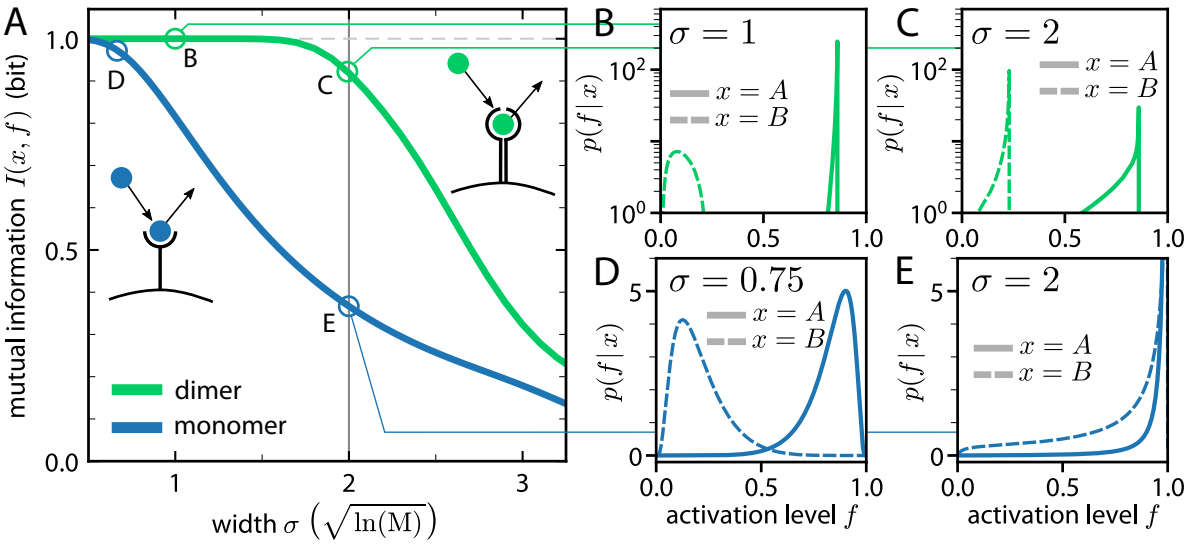

Figure 4.2 | Dimeric cell surface receptors can robustly discriminate weak from strong affinity ligands. **A** Mutual information $I(X,F)$ for two monomeric (blue line) and two dimeric (green line) ligand receptor systems as a function of the width of the log-normal ligand concentration distribution ω_{LN}. By increasing the width of the distribution the dimers maintain a plateau of $I(X,F) = 1$ bit mutual information, allowing A, B discrimination. While the monomer can also achieve perfect discrimination for narrow distributions (small σ) it much faster fails to do so, as one increases the fluctuation magnitude further. In the limit of large σ also the dimers will eventually fail to encode sufficient information for ligand discrimination and the mutual information $I(X,F)$ declines towards zero. **B** and **C** show the conditional output distributions $p(f\,|\,x)$ given an input x for $\sigma = 0.75$ and $\sigma = 2$, respectively. In both cases the solid line denotes the high affinity ligand (input $x = A$), while the dashed line represents the low affinity input ligand ($x = B$). Here we used $K_{\mathrm{D},A} = 3 \cdot 10^{-10}$ M and $K_{\mathrm{D},B} = 8 \cdot 10^{-9}$ M. Analogously **D** and **E** show the $p(f\,|\,x)$ distributions for the dimeric case for $\sigma = 1$ and $\sigma = 2$, respectively. Here again, the solid line denotes the high affinity ligand and the dashed line the low affinity ligand.

receptors have their usual hyperbolic response function f^{M} and are only parameterized by their binding affinities $K_{\mathrm{D},A}$ and $K_{\mathrm{D},B}$, respectively. As before we assume that the ligand concentration distribution is equal for all input ligands and now use the log-normal distribution ω_{LN} as a concentration distribution for all inputs. With these settings we let the monomeric receptor system compete against the hetero-dimeric receptor system. By this we mean the following. We evaluate the mutual information for both receptor systems and compare how much information either of the two receptor systems transmit. For the A–B discrimination an information value of $I = 1$ bit corresponds to perfect ligand discrimination, while zero information means that the receptor system cannot distinguish A from B at all.

For the monomeric system we use the previously derived results for $p(f\,|x)$. For all remaining calculations we restore to our numerical algorithm, which calculates both the remaining $p(f\,|\,x)$ distributions and then feeds them into the formula for the mutual

information $I(X, F)$ in equation (4.11).

The central idea is to increase the width of the ligand concentration distribution systematically and compare the information discrimination performance of both systems as a function of the distribution's width. This corresponds to a systematic increase of concentration fluctuations. Figure 4.2 shows how the mutual information $I(X, F)$ decays as a function of the width of the log-normal distribution. In the limit of very broad distributions we expect both curves to decay to zero information, because in this limit the overlap of the activation profiles makes any ligand indistinguishable. The important question is how fast this decay takes place. Here we clearly observe, that the monomeric system decays much quicker, while the dimeric system can maintain a plateau at 1 bit of information for a much longer range of distribution widths. This plateau can be maintained, because the hetero-dimerizing receptor translates binding affinity into different activation levels, such that the width of the concentration distributions does not alter its output profile by much. Eventually also the hetero-dimerizing system will decay. This happens when the ligand distribution width exceeds the plateau width, such that the activation levels from a strong and a weak ligand start to overlap even for dimeric signaling receptors.

Together, this information theoretic approach shows that the asymmetric binding of signaling dimers allows robust ligand discrimination. This complements our findings from chapter 3.

5 Spatial stochastic receptor dynamics

5.1 Simulation settings and parameter choices

The receptor mechanism of the previous sections will now be put to a test in a spatial and stochastic simulation approach. In this section we show results that were obtained using 2D reactive Brownian Dynamics simulations. Reactions were implemented by the previously discussed *reactive volume method* (see section 2.6). We consider the receptors in a 2D membrane patch of area A as circular particles, with a reactive shell region around them. If two receptors engage in a diffusive encounter, they can react with a forward reaction probability $P_{\text{acc}}^{\mathcal{E}\to b}$ which we defined in equation (2.35).

We set the system size to $\Omega = A = 100\,\mu\text{m}^2$, using a square membrane patch with side length $L_x = 10\,\mu\text{m}$. The choice for the fixed propagation time step is constrained by the spatial resolution s_x that we wish to have. Considering nano-meter sized receptors, we must choose Δt (for $d = 2$) such that the diffusive mean step length $s_x = \sqrt{4D\Delta t}$ is small enough to sufficiently sample the reactive volume around the receptors. Using an estimated receptor radius $r = 5\,\text{nm}$ [128], this imposes the following condition on Δt

$$\Delta t \leq \frac{s_x^2}{4D}\,, \tag{5.1}$$

where D is the diffusion coefficient of the receptor. We used $D_{\text{free}} = 1.1\,\mu\text{m}^2/\text{s}$ for the free microscopic diffusion coefficient of unoccupied receptors. We considered the diffusivities of ligand-bound receptors, which are monomers, as approximately unchanged, since ligand binding often only has a minor effect on the receptor motion. The ligand-induced cross-linking of two receptors to form a dimeric complex on the other hand slows a receptor pair down more significantly [128, 140, 141]. Hence we used $D_{C,\text{free}} = 0.7\,\mu\text{m}^2/\text{s}$ for dimeric receptor complexes, as suggested by You *et al.* [128], who also confirmed that this choice corresponds approximately to the Saffman-Delbrück [142] estimation of the diffusion coefficient. With these considerations in mind we set the propagation time step to $\Delta t = 10^{-5}\,\text{s}$.

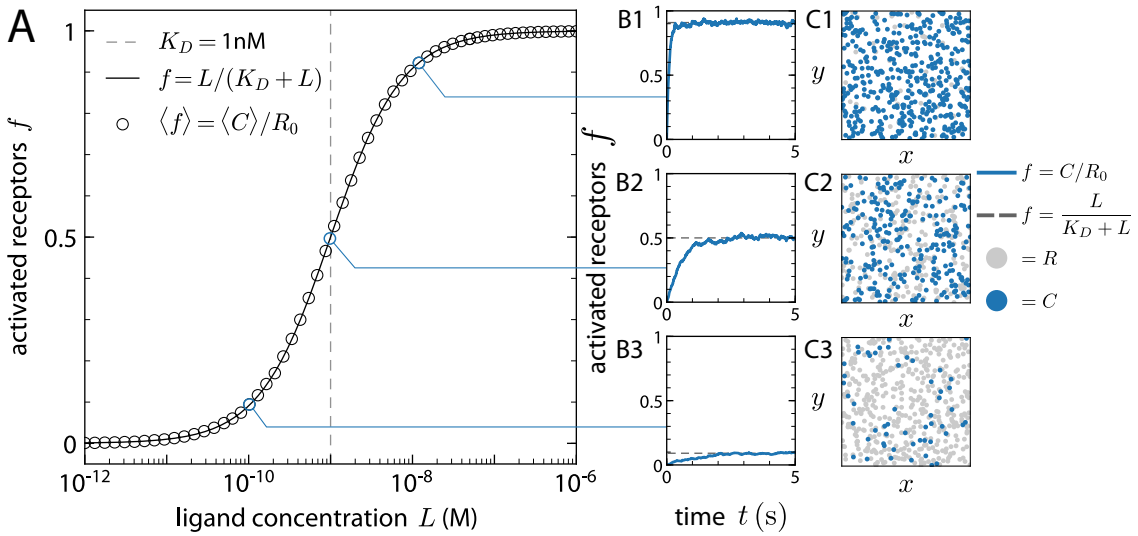

Figure 5.1 | Dose response curve for a monomeric receptor system. **A** shows the dose response curve. f is, as introduced, the fraction of activated receptors. The solid line represents the mean-field equilibrium binding results, while the circles are ensemble averaged results from spatial BD simulations. All results here we obtained using $n_0 = R_0\,\Omega = 500$. Column **B** shows single trajectory time traces of the fraction of activated receptors f, while column **C** shows snapshots of the full system at $t = 10$ seconds. The light gray filled circles denote inactive (unoccupied) receptors, whereas the blue filled circles are activated receptors C. **B1/C1** show results for a ligand concentration of $L = 10$ nM, **B2/C2** for $L = 1$nM and **B3/C3** for $L = 0.1$nM, respectively.

Since all discussed models so far start by ligand binding, we reiterate that in the context of this work we assume that the ligand concentration $L(t)$ will not be significantly depleted by receptor-binding events, and hence assumed it to be constant (*ligand-excess assumption*). This facilitates the reactive implementation of the ligand-binding reactions, since we can make the binding step a pseudo first-order reaction, with a new effective first-order rate constant $k_{\text{on,eff}} = L\,k_{\text{on}}$. This assumption seems to be justified in this context, since the time scales of the diffusive motion of the ligand molecules in the 3D bulk are typically by at least an order of magnitude faster to any reaction time scale of the considerably slower receptor dynamics in the cellular plasma membrane. Therefore it would be wasteful to account explicitly for the ligand movement. In other words, we assume ligand molecules to be well mixed, and only consider the spatial resolution at the receptor level.

In figure 5.1 I show the ensemble averaged results from many independent simulation trajectories for varying signal strength L. Combined they can be compared to the previously discussed dose response curves. The solid black line shows the theoretical solution for the monomeric receptor case and the circles are the data points from the spatial simulations. We find them in excellent agreement with the mean field curve.

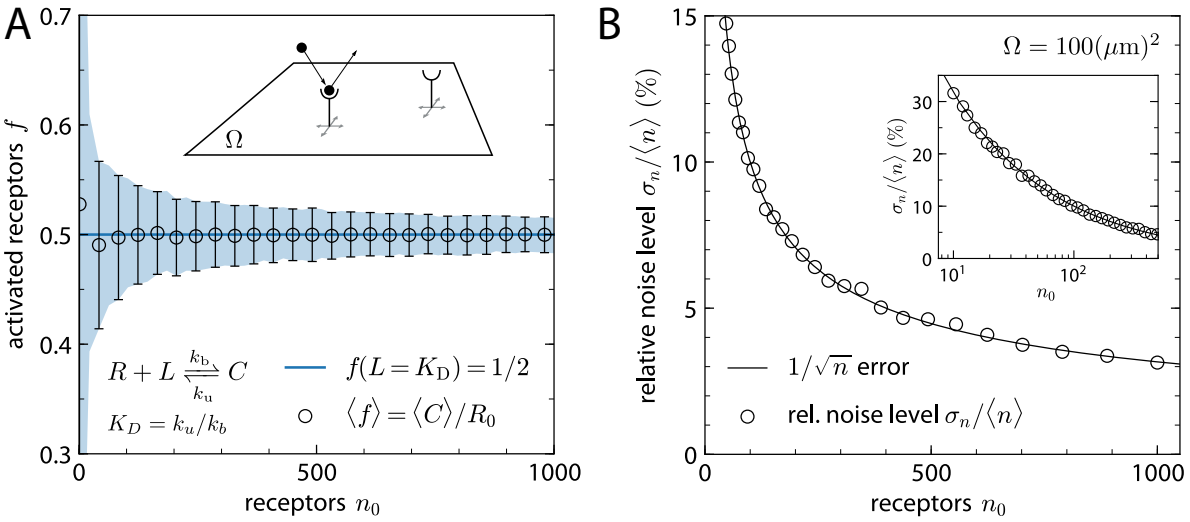

Figure 5.2 | Noise analysis for monomeric receptors in a homogeneous membrane patch of size $\Omega = 100\,\mu\mathrm{m}^2$. **A** shows the fraction of activated receptors f as a function of the receptor copy numbers n_0. With decreasing copy numbers the mean stays centered at $f = 1/2$ for $L = K_\mathrm{D} = 1\mathrm{nM}$, while the fluctuations build up significantly. **B** shows the relative noise level (coefficient of variation CV) $\sigma_n/\langle n \rangle$ versus the receptor copy number in the membrane patch. The noise characteristic follows the counting noise of a Poisson statistic, which scales with $\sim 1/\sqrt{n}$.

The sub-figures to the right also show individual example trajectories for three different ligand concentrations and snapshots of the system after steady state was established for the corresponding configuration. For the monomeric receptor the simulation setup will be parameterized by the choice of R_0, L, k_b and k_u, which I group in a parameter vector $\boldsymbol{\beta}_\mathrm{M} = (L, R_0, k_\mathrm{b}, k_\mathrm{u})^T$ as before.

Noise analysis

One of the main benefits from using a stochastic approach to study a biological reaction-diffusion system is that one gets access to the intrinsic fluctuations of the system. In figure 5.2 I show how the typical noise characteristic varies as a function of the receptor copy numbers in the system. We observe how with reduced copy numbers the noise levels increase while the mean value stays constant around its mean field prediction. For the monomeric receptor engagement, we can in fact exploit that the noise should follow a Poisson statistic, as it is shown in figure 5.2B, where the relative noise amplitude $\sigma_n/\langle n \rangle$ follows the well known counting statistic

$$\frac{\sigma_n}{\langle n \rangle} = \frac{1}{\sqrt{n}}. \tag{5.2}$$

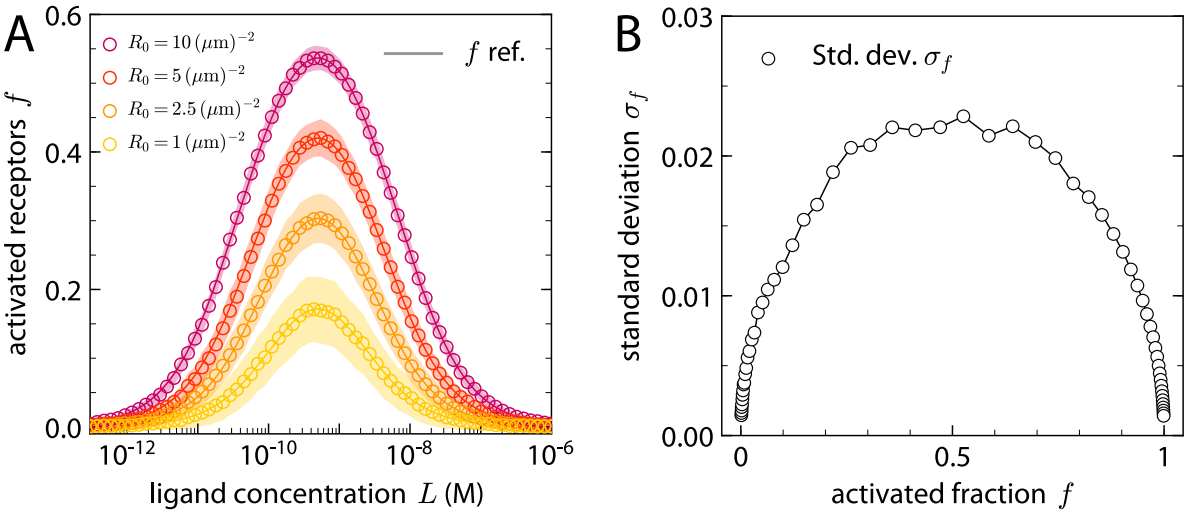

Figure 5.3 | **A** Binding curves for dimeric signaling receptors in a 2D membrane patch by reactive spatial BD simulations. The solid lines show the mean field solution while the empty circles show ensemble averaged simulation results. The shaded regions behind the curves indicate the sample standard deviation from the ensembles for each data point. **B** Noise profile σ_f as a function of the the activation level f.

We take this result to learn that our spatial receptor model faithfully reproduces the expected noise spectrum and can now move on the the dimeric case.

Similar to before we use the same global membrane settings but now look at receptor dimerization in our 2D simulations. We record many trajectories for a different signal strength L and show the results for the dose response curves for several receptor densities R_0 in figure 5.3A. The equilibration time for the dimeric case is limited by the low concentration regime. Small concentrations imply a small reactive flux and set the slowest time scale of the system. When monitoring the transient development of the binding curves towards equilibrium one can observe this effect, since the "right shoulders" of the bell shaped curves appear fast, whereas the "left shoulders" of the bell-shaped profiles slowly rise until they eventually approach their expected mean field value. All in all, we observe that both the monomeric and the dimeric receptor binding modes agree excellently with the equilibrium mean field prediction as specified by equation (3.5) and (3.13).

5.2 Noise models & extensions

This spatial stochastic ansatz enables us to extract valuable information about the noise that is present in the receptor system. In particular, we are interested in how the noise profile changes as a function of a given activation level f. We used the fraction of

activated receptors f extensively as a central molecular readout. The logical next step at this point is to quantify the intrinsic noise of this molecular readout f. A suitable way that we suggest would be to create a noise-model in such a way, that it can be seamlessly integrated into out probabilistic framework from the previous section. To do so, we must extract information about the intrinsic noise from the simulations. In figure 5.3B we extract such a noise profile from our spatial simulation trajectories, which tells us the noise σ_f as a function of f. Due the parabolic resemblance of these noise profiles, we suggest that they could be used to fit and subsequently parameterize a noise model $p_{\text{noise}}(f\,|\tilde{f})$, which for a given level $\tilde{f}$ will give the uncertainty in f. For the above shown profiles one could use a Beta distribution (as the natural extensions of a Binomial distribution to a real valued variable) to fit this profile. This is here motivated by the fact that the variance of the Binomial matches the parabolic profile that we observe here in our study of receptor activation. To connect these ideas to the previous chapter, where we proposed an information theoretic framework for ligand discrimination, this would offer a suitable extension to also account for intrinsic variability of the system. The key idea is the following. Previously we calculated distribution functions for activation levels f, given an input ligand x and called these $p(f\,|\,x)$. In the language of measurement theory this corresponds however to an ideal sensor, since a given activation value $\tilde{f}$ is attained precisely (we silently assumed $p_{\text{noise}}(f\,|\,\tilde{f}) \sim \delta(f-\tilde{f})$). Using the noise profile from a stochastic approach, such as the one shown here, we could convolute this distribution function with the fitted noise model to obtain a noisy version of this distribution function through convolution

$$\hat{p}(f\,|x) = \int_{\mathcal{F}} p(\tilde{f}\,|\;x) p_{\text{noise}}(f\,|\,\tilde{f})\,d\tilde{f}\,, \tag{5.3}$$

where $\mathcal{F}$ is the dynamic range of the fraction of activated receptors f.

A second extension we suggest is to investigate how the receptor dynamics change if one considers spatial inhomogeneities. It is well acknowledged that the cellular plasma membrane is not a homogeneous liquid, but is strongly structured by both lipid inhomogeneities and cytoskeletal components that can create raft-like domains. Such raft-like domains have previously shown to locally increase the receptor density and can thus have a stabilizing effect for receptor aggregation [128]; a clever way how cells can exploit compartmentalization to control reaction processes. Spatial partitioning in general can influence the noise characteristics of common signaling motifs, as it has been shown by Mugler *et al.* [94]. It would be a logical extension to ask how the performance of our ligand discrimination mechanism is modulated by including this higher level of spatial organization of the cellular plasma membrane.

III

Self-organization

6 Min oscillations

One of the most intriguing aspects of the Min system is the impact of geometry on the spatiotemporal patterns. While initial experiments in wild-type cells showed characteristic *pole-to-pole oscillations*, growing *E. coli* cells, which roughly double in length before division, can also give rise to stable oscillations in both daughter cells even before full septum closure [143]. In very long filamentous mutants the pole-to-pole pattern vanishes and several MinDE localization zones emerge in a stripe-like manner (*striped oscillations*), with a characteristic distance of $5\,\mu$m, strongly reminiscent of standing waves [50]. No stable oscillation patterns emerge in spherical cells where MinDE localization appears to be random without stable oscillation axes [144].

Strikingly, the Min system can be reconstituted outside the cellular context using purified components on supported lipid bilayers [56, 145]. Using only fluorescently labeled MinD and MinE and ATP as energy source, traveling surface waves were observed in the form of turning spirals and traveling stripes on flat homogeneous substrates, where MinD proteins form a moving wave-front, that is consumed by MinE at the trailing edge, demonstrating that MinD and MinE alone are indeed sufficient to induce dynamic patterning [56]. Interestingly, these assays work for different lipid species, demonstrating the robustness of the Min oscillations with respect to the detailed values of the binding rates.

Combining this reconstitution approach with membrane patterning, it was shown that the Min system is capable of orienting its oscillation axis along the longest path in the patch and hence in principle capable of sensing the surrounding geometry [146]. More recently the gap between the traveling *in vitro* Min waves and the standing Min waves in live cells was closed, using microfabricated PDMS compartments mimicking the shape of *E. coli* cells [55]. In these biomimetic compartments, which confine the reaction space in 3D, pole-to-pole oscillations were observed, reminiscent of the paradigmatic *in vivo* oscillation mode. Later it was shown that the Min oscillations are indeed sufficient to spatially direct FtsZ-polymerization to midcell, linking two key elements of bacterial cell division in a synthetic bottom-up approach [147].

In order to study the effect of geometry in the physiological context of the cell, one

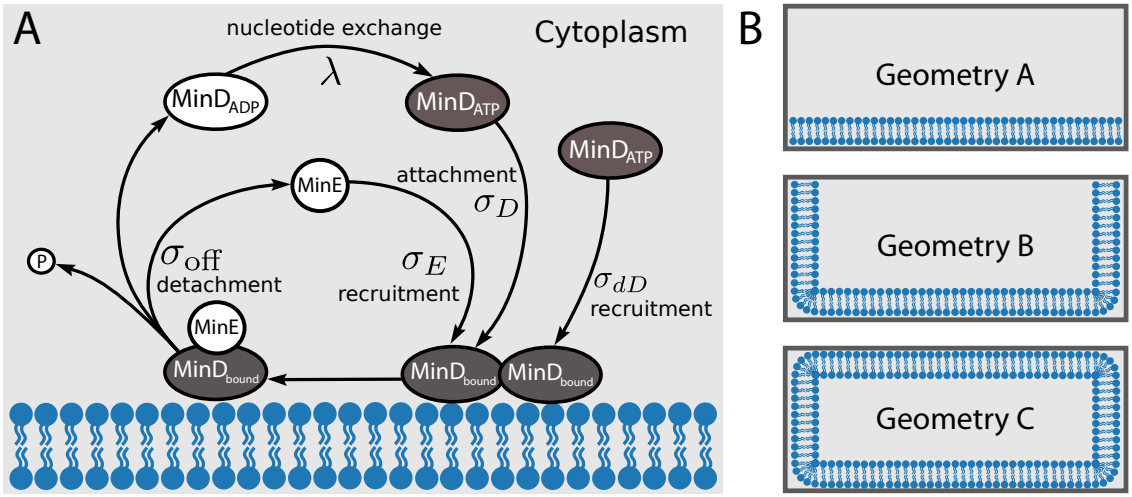

Figure 6.1 | **A** Reaction cycle of the Min system. The full cycle involves membrane attachment, cooperative recruitment, diffusion along the membrane, detachment from the membrane, diffusion and a nucleotide exchange step in the cytosolic bulk. **B** Cross sections of the three simulation geometries used in this work. In geometry A only the bottom is covered with a membrane. Geometry B additionally covers the side walls and in geometry C the full compartment has covered boundaries.

can place growing cells in microfabricated chambers of custom shape [53, 148]. This *cell sculpting* approach allowed the authors to systematically analyze the adaptation of the Min oscillations to compartment geometry and demonstrated experimentally that different oscillation patterns can be stable for the same cell geometry. Using image processing, it was possible to measure the relative frequency of the different modes for a large range of interesting geometries [53]. Figure 6.1B summarizes the different geometries that have been used before in experiments and that are considered here with computer simulations. While geometry A uses a flat membrane patch, similar to flat patterned substrates [146], geometry B corresponds to microfabricated chambers with an open upper side [55, 147]. Geometry C corresponds to the cell sculpting approach [53, 148].

Like for other pattern forming systems, the theory of reaction-diffusion processes offers a suitable framework to address the Min oscillations from a theoretical point of view [42, 43, 149, 150]. Many theoretical models have been proposed to unravel the physical principles behind this intriguing self-organizing protein system and to explain the origin of its rich spatiotemporal dynamics. While all of them rely on a reaction-diffusion mechanism similar to the Turing model, they differ severely in their details. The first class of mathematical models used an effective one-dimensional PDE-approach and relied strongly on phenomenological non-linearities in the reaction terms [151–153]. Although all of them successfully gave rise to pole-to-pole oscillations, they did not allow a clear interpretation of the underlying biomolecular processes and were not in agreement with

all experimental observations, such as MinE-ring formation and the dependence of the oscillation frequency on biological parameters.

The next advance in model building was the focus on the decisive role of MinD aggregation and the relevance of MinD being present in two states (ADP- and ATP-bound) [153, 154]. Very importantly, this highlighted the interplay between unhindered diffusion with a nucleotide exchange reaction in the bulk as a delay element for MinD reattachment [118]. Subsequent models shared a common core framework but still differed strongly in the functional form of the protein binding kinetics and the transport properties of membrane-bound molecules [155, 156]. The main difference between the more recent models was the dimensionality, ranging from one dimension [151–153, 157] to two [146] and three [118, 158–162]. Moreover, the models can be classified as deterministic PDE-models [53, 56, 118, 146, 151–154, 162–165] or using stochastic simulation frameworks [143, 158–161, 165–167], and whether they neglected membrane diffusion [118, 151, 152, 158, 163] or not. While some models contained higher than second order non-linearities in concentrations of the reaction terms [56], it is the prevailing opinion to rely on at most second order non-linearities, allowing for a clear interpretation in terms of bimolecular reactions. Following the same line of thought, a strong effort was made to distill a minimal system that explains the oscillation mechanism without the necessity of spatial templates or prelocalized determinants [163] and neglecting secondary processes like filament formation [160, 161, 163].

The most influential minimal model for the Min system has been suggested by Huang and coworkers [118]. It has been further simplified by discarding cooperative MinD recruitment by MinDE complexes on the membrane [159, 164], allowing a clear view on the core mechanisms: the cycling of MinD between bulk and membrane, cooperativity of MinD-recruitment and diffusion in bulk and along the membrane. Using the minimal model, it has been shown that the canalized transfer of proteins from one polar zone to the other underlies the robustness of the Min oscillations [159, 164]. Because the deterministic variants of the minimal model [118, 164] do not allow us to address the role of stochastic fluctuations, a stochastic and fully three-dimensional version has been introduced to study the effect of stochastic fluctuations in patterned environments [167]. For rectangular patterns of $5\,\mu\text{m} \times 10\,\mu\text{m}$, it was found that the system can be bistable, with transverse pole-to-pole oscillations along the minor and longitudinal striped oscillations along the major axis, respectively. In this early work, it was observed that the stable phase emerged depending on the initial conditions and that sometimes switching occurred, but the statistics were not sufficiently good to observe switching in quantitative detail. Indeed such multistability has been observed experimentally in sculptured cells over a large range of cell shapes [53] and the deterministic minimal

model has been used to explain the relative frequency of the different oscillation patterns for a given shape using a perturbation scheme [162]. However, as a deterministic model, this approach was not able to address the rate with which one pattern stochastically switches into another.

Here we address this important subject by using particle-based Brownian dynamics (BD) computer simulations. Compared to earlier work along these lines [167], we have developed new methods to efficiently simulate and analyze the switching process. We find excellent agreement with experimental data and measure for the first time the switching time of multistable oscillation patterns. We also use our model to confirm that it contains the minimal ingredients for the emergence of Min oscillations. In addition, we use our stochastic model to investigate the three-dimensional concentration profiles in different geometries and in particular the role of edges in membrane-covered compartments. We identify novel oscillation patterns in compartments with membrane-covered walls and find a surprisingly simple (linear) relation between the bound Min protein densities and the volume-to-surface ratio, which might be relevant for geometry sensing by *E. Coli* cells.

6.1 Reaction-diffusion model and parameter choice

For the particle-based simulation, we use the reaction scheme of the minimal model for cooperative attachment [118, 162, 164, 167]. The model uses the following interactions between Min proteins and the inner bacterial membrane (schematically shown in figure 6.1A). Freely diffusing cytoplasmic $\mathrm{MinD_{ATP}}$ can bind to the membrane with a rate constant σ_D

$$\mathrm{MinD_{ATP}} \xrightarrow{\sigma_D} \mathrm{MinD_{bound}}. \tag{6.1a}$$

$\mathrm{MinD_{ATP}}$ preferably binds to regions of high $\mathrm{MinD_{bound}}$ density (cooperative MinD binding)

$$\mathrm{MinD_{ATP}} + \mathrm{MinD_{bound}} \xrightarrow{\sigma_{dD}} 2\ \mathrm{MinD_{bound}}. \tag{6.1b}$$

Membrane-bound MinD also recruits cytoplasmic MinE to the membrane with rate

Parameter	Set **A**	Set **B**	Set **C**	Unit	Description (reaction type)
D_D	2.5	16	16	$\mu m^2/s$	bulk diffusion coefficient of MinD
D_E	2.5	10	10	$\mu m^2/s$	bulk diffusion coefficient of MinE
D_{bound}	0.01	0.013	0.013	$\mu m^2/s$	membrane diffusion coefficient
λ	0.5	1	6	s^{-1}	first order, unimolecular
σ_D	0.025	0.075	0.1	$\mu m/s$	first order, membrane attachment
σ_{dD}	0.0149	0.05[a]	0.1	$\mu m^3/s$	second order, bimolecular
σ_E	0.093	0.25[a]	0.435	$\mu m^3/s$	second order, bimolecular
σ_{off}	0.7	0.33	0.5	s^{-1}	first order, unimolecular
c_D	0.797	0.85	1.0	μM	total MinD concentration
c_E	0.207	0.31	0.5	μM	total MinE concentration
$R_{D/E}$	3.85	2.74	2	—	MinD to MinE ratio

Table 6.1 | Parameters sets used for simulations of the Min system. Set **A** is the main parameter set used here following [118, 167]. Parameter set **B** is taken from [53] and **C** from [162, 164]. [a] The units of the bimolecular reaction rate constants σ_{dD} and σ_E are specified as $\mu m^2 s^{-1}$ in [53].

σ_E, creating a $\text{MinDE}_{\text{bound}}$ complex

$$\text{MinD}_{\text{bound}} + \text{MinE} \xrightarrow{\sigma_E} \text{MinDE}_{\text{bound}}. \tag{6.1c}$$

All membrane-bound proteins diffuse in the plane of the membrane, but with a much smaller diffusion constant than in the bulk $D_{\text{bound}} \ll D_{\text{free}}$. MinE attachment triggers the ATPase activity of MinD. This hydrolysis of the MinD bound ATP to ADP breaks up the membrane-bound MinDE complex and releases MinD_{ADP} and MinE back into the cytoplasmic bulk with rate constant σ_{off}

$$\text{MinDE}_{\text{bound}} \xrightarrow{\sigma_{\text{off}}} \text{MinE} + \text{MinD}_{\text{ADP}}. \tag{6.1d}$$

Finally MinD_{ADP} exchanges ADP by another ATP molecule (nucleotide exchange) with the rate λ

$$\text{MinD}_{\text{ADP}} \xrightarrow{\sigma_\lambda} \text{MinD}_{\text{ATP}}. \tag{6.1e}$$

This completes the reaction cycle. In table 6.1 we list our parameter values as set A. For comparison, we also list parameter values used in other studies (set B in [53] and set C in [162, 164]).

This reaction cycle as defined by the molecular interactions specified in equations

(6.1a) – (6.1e) can readily be translated into a set of nonlinear coupled reaction-diffusion partial differential equations (PDEs). We start by listing the three governing equations for the concentrations of the cytosolic bulk species $c_{\mathrm{D,ATP}}, c_{\mathrm{D,ADP}}$ and c_{E} standing for the cytosolic concentration fields of ATP bound MinD, ADP bound MinD and MinE, respectively.

$$\frac{\partial c_{\mathrm{D,ATP}}}{\partial t} = D_{\mathrm{D}} \nabla^2 c_{\mathrm{D,ATP}} + \lambda\, c_{\mathrm{D,ADP}} \tag{6.2a}$$

$$\frac{\partial c_{\mathrm{D,ADP}}}{\partial t} = D_{\mathrm{D}} \nabla^2 c_{\mathrm{D,ADP}} - \lambda\, c_{\mathrm{D,ADP}} \tag{6.2b}$$

$$\frac{\partial c_{\mathrm{E}}}{\partial t} = D_{\mathrm{E}} \nabla^2 c_{\mathrm{E}}. \tag{6.2c}$$

At this particular point it is worth emphasizing that apart from the unimolecular nucleotide exchange reaction, which converts the ADP bound form of MinD into the ATP bound state (equations (6.2a) – (6.2c)), these are more or less standard passive bulk diffusion PDEs for three molecular species. The two remaining species consider the concentration fields of the membrane bound MinD c_{d} and membrane bound MinDE complexes c_{de}.

$$\frac{\partial c_{\mathrm{d}}}{\partial t} = D_{\mathrm{d}} \nabla_\nu^2 c_{\mathrm{d}} + \Big(\sigma_D + \sigma_{dD} c_{\mathrm{d}}\Big) c_{\mathrm{D,ATP}} - \sigma_E c_{\mathrm{E}} c_{\mathrm{d}} \tag{6.2d}$$

$$\frac{\partial c_{\mathrm{de}}}{\partial t} = D_{\mathrm{de}} \nabla_\nu^2 c_{\mathrm{de}} + \sigma_E c_{\mathrm{E}} c_{\mathrm{d}} - \sigma_{\mathrm{off}} c_{\mathrm{de}}\,, \tag{6.2e}$$

where ∇_ν^2 denotes the Laplacian with respect to the tangential system coordinates. This describes the two dimensional diffusion process for the membrane bound species. To be more precise one should introduce the tangential gradient operator ∇_Γ with respect to a surface $\Gamma = \partial\Omega$, where Ω denotes the full system volume. Using a differentiable field u and $\boldsymbol{\nu}$ being an outer normal to the surface Γ, this tangential projection of the gradient is given by

$$\nabla_\Gamma u = \nabla u - \Big(\nabla u \cdot \boldsymbol{\nu}\Big)\, \boldsymbol{\nu}\,, \tag{6.3}$$

such that the generalization of the Laplacian for curved lower dimensional surface domains Γ is given by the *Laplace-Beltrami* operator $\Delta_\Gamma u = \nabla_\Gamma \nabla_\Gamma u$, here illustrated for a generic differentiable test field u. A more comprehensive treatment of these coupling schemes for reaction-diffusion PDEs in generic system geometries is given in the work by Madzvaduse *et al.* [168].

Up to this point there is no coupling between the bulk species in equations (6.2a) – (6.2c) and the membrane bound species in (6.2d) and (6.2e). This can be achieved by

imposing the following bulk-boundary coupling terms as flux-boundary conditions (also known as *Robin type* boundary conditions) which have to be satisfied by the above set of PDE's.

$$D_{\mathrm{D}} \nabla_{\mu} c_{\mathrm{D,ATP}} \Big|_{\mu=\mu_0} = -\Big(\sigma_D + \sigma_{dD} c_{\mathrm{d}}\Big) c_{\mathrm{D,ATP}} \tag{6.4a}$$

$$D_{\mathrm{D}} \nabla_{\mu} c_{\mathrm{D,ADP}} \Big|_{\mu=\mu_0} = +\sigma_{\mathrm{off}}\, c_{\mathrm{de}} \tag{6.4b}$$

$$D_{\mathrm{E}} \nabla_{\mu} c_{E} \Big|_{\mu=\mu_0} = +\sigma_{\mathrm{off}}\, c_{\mathrm{de}} - \sigma_E\, c_{\mathrm{E}} c_{\mathrm{d}} \tag{6.4c}$$

Here ∇_{μ} stands for the gradient differential operator with respect to the orthogonal coordinate direction μ of the respective coordinate system. The signs of the reaction terms on the right hand side of the coupling equations (6.4a) – (6.4c) give the direction of the flux either onto $(-)$ or off $(+)$ the membrane. D_{d} and D_{de} are the two dimensional diffusion coefficients of the membrane bound $\mathrm{MinD}_{\mathrm{bound}}$ and $\mathrm{MinDE}_{\mathrm{bound}}$ species, respectively. Since we do not consider them to differ by much we will use only a single 2D diffusion coefficient $D_{\mathrm{bound}} = D_{\mathrm{d}} = D_{\mathrm{de}}$ from now on as indicated in table 6.1.

This full deterministic reaction-diffusion model of the Min system in the above shown form (equations (6.2a) - (6.4c)) was in this form established by Halatek *et al.* [164], although it essentially is identical to the reaction model by Huang et al [118] except for a single reaction term in the MinD membrane attachment mode. Huang initially also included a cooperative attachment of MinD by already bound MinDE complexes, resulting in an additional $\pm\sigma_{dD} c_{\mathrm{de}} c_{\mathrm{D,ATP}}$ reaction term in his set of equations (as also used by [159] in their deterministic simulations). Since there was no experimental evidence for this additional degree of cooperativity in the MinD binding mode, this was dropped in the work of Halatek *et al.* [164] and in most of the follow up work thereafter.

The structure of this set of equations clearly reveals that a core element of the Min oscillations is found in the bulk surface coupling as explained above. Although this is a widely acknowledged motif the systematic numerical analysis of reaction-diffusion systems that exhibit this kind of coupling is in my eyes still lacking behind surprisingly. Related work using similar coupling schemes between a passive bulk and reactive membrane as catalytic templates can be found in the work by Gomez-Marin *et al.* [169] for nonlinear Fitzhugh-Nagumo dynamics leading to self-sustained spatiotemporal dynamics, by Rätz *et al.* for Turing instabilities and symmetry breaking in signaling networks [170–172], bulk-surface coupled Cahn-Hilliard systems [173], receptor-ligand dynamics [174] and for generic bulk-surface PDE problems as shown in [168, 175–178].

6.1.1 Simulation algorithm

We use custom-written code to simulate the stochastic dynamics of the Min system with very good statistics. For all simulations we use a fixed discrete time step of $\Delta t = 10^{-4}\,\mathrm{s}$. During every time step each particle is first propagated in space. Thereafter every particle can react according to the previously introduced Min reaction scheme (6.1a) – (6.1e). The movement of both free and membrane-bound particles is realized through Brownian dynamics. Individual molecules are treated as point-like particles without orientation. Therefore we can monitor the propagation separately for each Cartesian coordinate. During a simulation step of Δt the displacements of the diffusing particles with diffusion constant D are drawn from a Gaussian distribution with standard deviation $\sigma_x = \sqrt{2D\Delta t}$ [179] such that

$$x(t + \Delta t) = x(t) + X_\mathrm{G}, \tag{6.5}$$

$$p_{X_\mathrm{G}}(x) = \frac{1}{\sqrt{4\pi D\Delta t}} \exp\left(-\frac{x^2}{4D\Delta t}\right), \tag{6.6}$$

where p_{X_G} is the probability distribution of X_G. The same update step is used for the y and z direction. Free particles in the bulk of the simulated volume undergo three-dimensional diffusion with reflective boundary conditions at the borders of the simulation volume. The membrane-bound particles perform a two-dimensional diffusion on the membrane with a much smaller diffusion constant D_bound (compare table 6.1). Membrane-bound particles are allowed to diffuse between different membrane areas that are in contact with each other.

The different reactions in the Min reaction scheme (6.1a) – (6.1e) can be classified into three different types (more details on the corresponding implementations are given in section 2.7). The first type considered here are first order reactions without explicit spatial dependence. The conversion of $\mathrm{MinD_{ADP}}$ to $\mathrm{MinD_{ATP}}$ and the unbinding of the $\mathrm{MinDE_{bound}}$ complex from the membrane are of this type. Such reactions are treated as a simple Poisson process. For a reaction rate κ, the probability to react during a time step Δt is given by

$$p_\kappa = 1 - \exp\left(-\kappa\Delta t\right). \tag{6.7}$$

The second type is also a first order reaction, but with confinement to a reactive area at a border of the simulated volume. The membrane attachment of $\mathrm{MinD_{ATP}}$ proteins is a reaction of this type. For a given reaction rate σ, we implement these reactions by allowing particles that are closer to the membrane than $d = 0.02\,\mu\mathrm{m}$ to

attempt membrane attachment with a Poisson rate $\kappa = \sigma/d$. This results in a reaction probability of

$$p_\sigma = 1 - \exp\left(-\frac{\sigma}{d}\Delta t\right). \tag{6.8}$$

The last reaction type is a second order reaction between free and membrane-bound particles. The cooperative recruitment of cytosolic $\mathrm{MinD_{ATP}}$ and MinE to membrane-bound MinD are reactions of this third type. In our simulation we adopt the algorithm implemented in the software package Smoldyn, which has been used earlier to simulate the Min system [167]. This algorithm is based on the Smoluchowski framework in which two particles react upon collision [105]. However, the classical treatment by Smoluchowski only considers diffusion-limited reactions and therefore assumes instantaneous reactions upon collision. In order to take finite reaction rates into account, one imposes a radiation boundary condition [104, 119, 180]. From the diffusion constant D, the reaction rate σ and the simulation time step Δt, a reaction radius r_σ is calculated [108]. Whenever a freely diffusing particle comes within the distance of r_σ to a membrane-bound particle, the free particle reacts. For intermediate values of Δt (such as the time step of $10^{-4}\,\mathrm{s}$ that we use for the Min system) the value of $r_\sigma(D, \sigma, \Delta t)$ is obtained numerically [108]. Those numerical values are taken from the Smoldyn software. For example, for parameter set A the reaction radius for the rate σ_{dD} is $r_{\sigma_{dD}} = 0.0091\,\mu\mathrm{m}$, and for σ_E it is $r_{\sigma_E} = 0.0179\,\mu\mathrm{m}$.

In our simulations we use rectangular reaction compartments. We considered three different membrane setups as illustrated in figure 6.1B. To mimic *in vitro* experiments, where substrates or open compartments are functionalized with a membrane layer [55, 146, 147], we place the reactive membrane at the bottom (geometry A) or at the side walls and the bottom of the simulation compartment (geometry B). To simulate rectangular shaped *E. coli* cells, inspired by the cell sculpting approach from [53, 162], fully membrane-covered volumes are used (geometry C). We refer to the long side of the lateral extension as the major or the x-axis, and the smaller side as minor or y-axis, and accordingly consider the compartment height to extend in the z-direction, aligning the rectangular geometry perpendicular with the coordinate frame.

In our simulations we investigate a wide range of compartment dimensions. For a simulation box with a length of $10\,\mu\mathrm{m}$, width of $5\,\mu\mathrm{m}$ and height of $0.5\,\mu\mathrm{m}$, we use 6003 $\mathrm{MinD_{ATP}}$ particles, 6003 $\mathrm{MinD_{ADP}}$ particles and 3124 MinE particles as initial condition [167]. These particle numbers amount to a total MinD concentration of $0.797\mu\mathrm{M}$ and a MinE concentration of $0.207\mu\mathrm{M}$ (see table 6.1 for a comparison). For other simulation compartment sizes we scale the particle numbers linear with the volume,

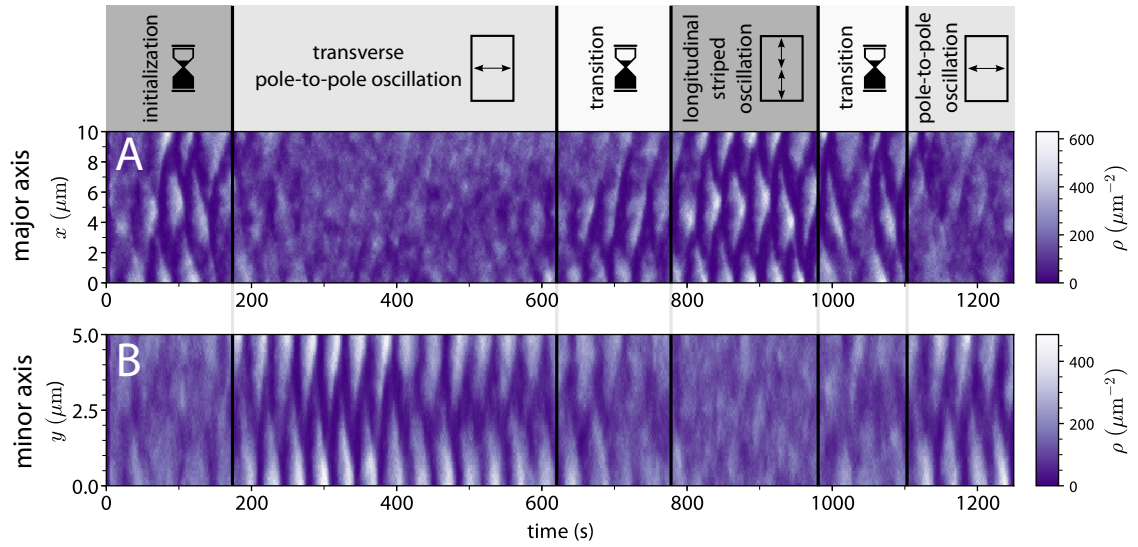

Figure 6.2 | Oscillation mode switching. Shown are density kymographs along both the major and minor axis of the system illustrating stochastic switching between a longitudinal striped oscillation mode (**A**, top row kymograph) and a transverse pole-to-pole oscillation mode (**B**, bottom row kymograph). Starting from an initially uniform particle distribution, first a longitudinal striped oscillation emerges along the major x-axis (top). After 200 s this oscillation stops and a transverse pole-to-pole oscillation along the minor y-axis begins (bottom). The oscillation mode switches again around 700 s and 1100 s. Here we use geometry A and parameter set A. Dimensions are $10\,\mu\text{m} \times 5\,\mu\text{m} \times 0.5\,\mu\text{m}$.

since in experiments *E. coli* bacteria typically have a constant Min protein concentration [53].

6.1.2 Identification of oscillation modes

In our simulations of the Min system different oscillation patterns emerge along the major or minor axis of the simulation compartment. In order to analyze the frequency of different modes and the stability of the oscillations in the large amount of simulation data, an oscillation mode recognition algorithm is needed. Therefore we monitor the MinD protein densities at the poles of the different axes over time. To determine the axis along which the oscillation takes place, we compare the Fourier transformation of the normalized densities over time (ρ_{t_i} where i denotes the discretized time resolution). If an oscillation takes place, there is a dominant peak in the Fourier spectrum and the overall maximal amplitude of the Fourier spectrum is significantly higher than the one from the non-oscillating axis. The same Fourier spectrum is also used to determine the oscillation period T. To differentiate between pole-to-pole oscillations and striped oscillations of a given axis in the system, we extract the phase difference between the density oscillation at the poles of the cell.

When identifying switching events, one has to be more careful because stochastic fluctuations might lead to temporal changes that might be mistaken to be mode switches. For this purpose, we therefore smoothen the data. In detail, we calculate the convolution C_i between the densities over time and a Gaussian time window G_i

$$C_i = \sum_j \rho_{t_j} G_{i-j} \quad \text{where} \quad G_i = \frac{1}{\sqrt{2\pi}\omega} \exp\left(-\frac{(i\tau)^2}{2\omega^2}\right). \tag{6.9}$$

Here τ is the time between successive density measurements and we set $\omega = 100\,\mathrm{s}$ as width of the time window. The current oscillation mode is now determined from the convoluted densities C_i and assigned to the time $i\tau$. In this way, only switches are identified that persist for a sufficiently long time.

6.2 Oscillation pattern analysis

The time averaged density profiles as shown in figure 6.3C and 6.3D are calculated by recording spatial density histograms $\rho = \rho(x_i, t_j)$ of membrane bound protein species for many time points t_j along either of the two coordinate directions ($x_i \in \{x, y\}$ here) and then averaging out the time axis

$$\langle \rho_{x_i} \rangle_t = \frac{1}{(t_{\mathrm{end}} - t_{\mathrm{start}})} \sum_{t_j = t_{\mathrm{start}}}^{t_{\mathrm{end}}} \rho(x_i, t_j)\,. \tag{6.10}$$

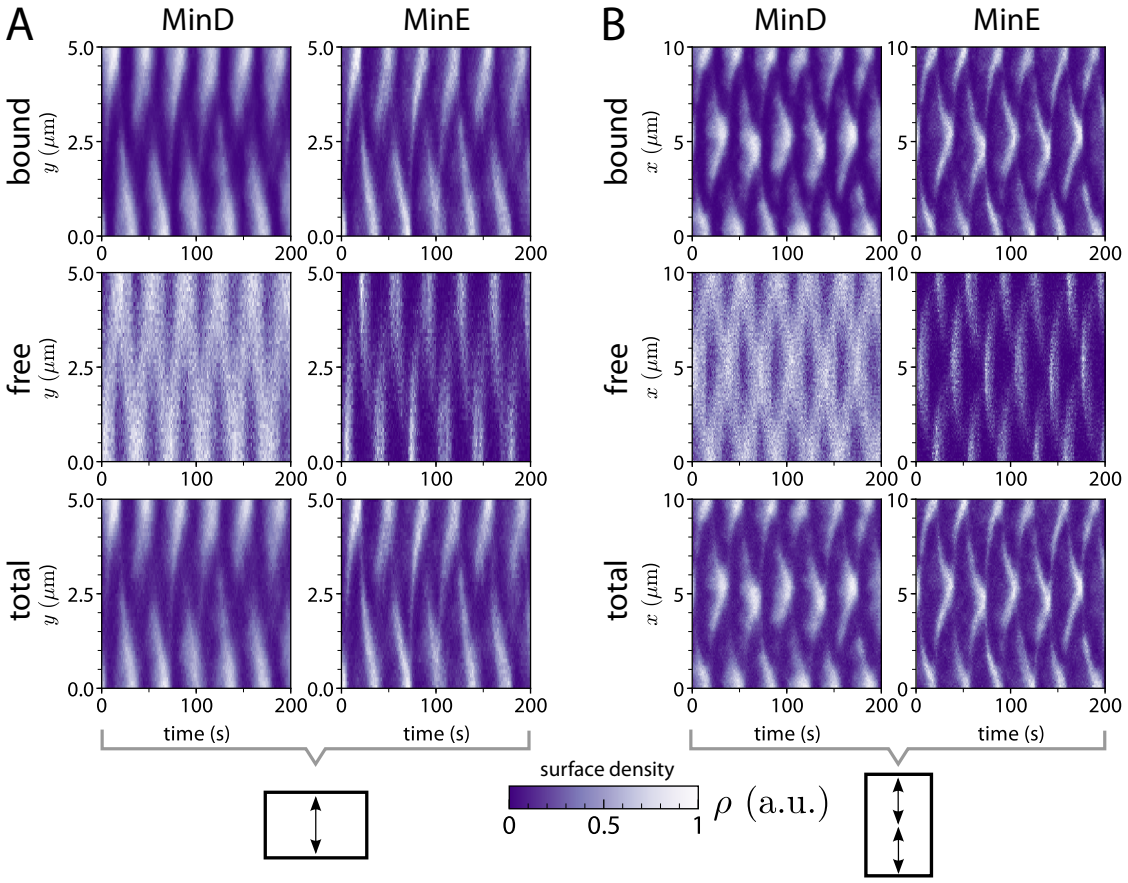

Figure 6.4 | Detailed analysis of simulation results for geometry A. **A** Density kymographs of transverse pole-to-pole oscillations. Left column figures show MinD protein particle densities and right column figures show MinE protein particle densities. The two figures on the top show only particle densities of membrane-bound particles. The two figures in the middle row show particle densities of free particles in the bulk of the simulation volume. The bottom two figures show the total particle densities of both bound and free particles together. **B** Kymographs of longitudinal striped oscillations. The arrangement is the same as in figure 6.4A.

6.2.1 Oscillation patterns in geometry A

First we investigated the oscillations that emerge in geometry A with parameter set A using a rectangular simulation volume with dimensions $10\,\mu\text{m} \times 5\,\mu\text{m} \times 0.5\,\mu\text{m}$ (x, y, z). With this particular choice the width of the system approximately matches the typical length of wild-type *E. coli* cells and the length of the system corresponds to the length of a grown *E. coli* cell which can roughly double in length before septum formation and division. As shown by the kymographs in figure 6.2 and in agreement with the results of Hoffmann *et al.* [167], in our simulations two different oscillation modes occur. Note from the color legend that dark and light colors correspond to low and high concentrations, respectively, as used throughout this work. In the first mode the

Min proteins oscillate along the minor y-axis from one pole to the other (pole-to-pole oscillation). In the second mode the proteins oscillate along the major x-axis between the poles and the middle of the compartment (striped oscillation). The system stochastically switches between the two modes, sometimes *via* a short oscillation along the diagonal of the compartment. The mode switching behavior of the Min system in large volumes is in agreement with the experimental results of Wu *et al.* [53] and cannot be analyzed completely with conventional PDE-models of the Min oscillations because they do not account for the noise in the system leading to the stochastic switch.

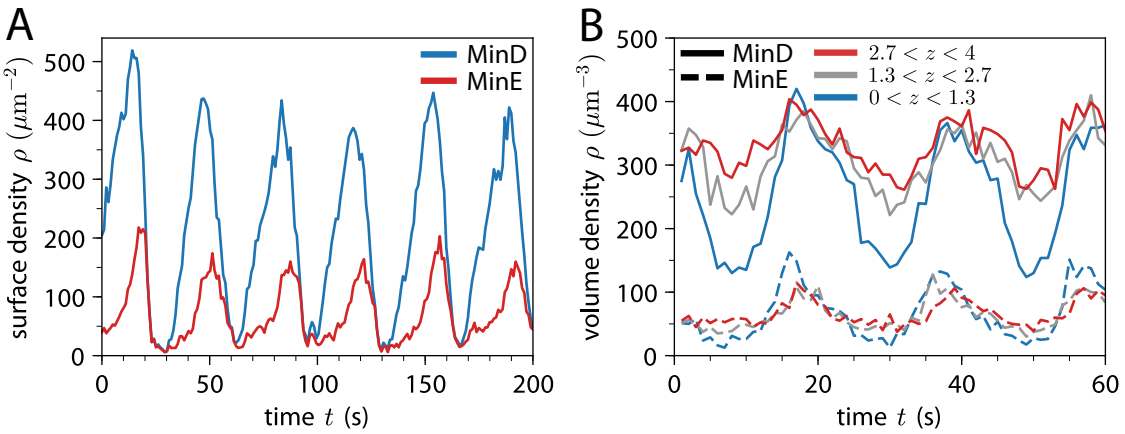

Figure 6.5 | Transient line and height profiles of MinD and MinE proteins. **A** Density change of MinD (blue) and MinE (red) in time during a (transversal) pole-to-pole oscillation at position $y = 4.9\,\mu$m in a compartment of $10\,\mu\text{m} \times 5\,\mu\text{m} \times 0.5\,\mu$m as in figures 6.2, 6.3 and 6.4. **B** Transient density change of non-bound MinD and MinE at different heights above the reactive membrane for a $6\,\mu\text{m} \times 3\,\mu$m bottom area and $4\,\mu$m compartment height.

Detailed analyses of the pole-to-pole and the striped oscillations from figure 6.2 are shown in figure 6.4A and 6.4B, respectively. First, we consider the pole-to-pole oscillations in figure 6.4A. In the kymographs of the bound MinD and MinE proteins (top row figures) we see clusters of bound proteins that detach from the membrane beginning in the middle and from there move towards one of the poles of the compartment in an alternating way. The shapes of the bound MinD protein density clusters in the kymographs have a triangular form, in contrast to the line-like structures of the bound MinE proteins. Those density lines in the bound MinE kymograph show that the MinE proteins form a high density cluster in the middle of the cell which propagates to one of the compartment poles. This behavior is similar to the experimentally observed ringlike structures of MinE proteins in *E. coli* bacteria that travel from the middle to the poles of the cell, leading to the dissociation of MinD proteins from the membrane. The kymographs of the free particles (middle row in figure 6.4A) are averaged over all heights and have the inverse shape of the corresponding kymographs of the bound particles (top row in figure 6.4A). Where the density of bound particles is high, the density of free

particles is low and vice versa. During the simulations the spatial density differences of both MinD and MinE are higher for membrane-bound particles than for free particles in the bulk. Therefore in the two bottom kymographs in figure 6.4A, which are showing total particle densities, the pattern of membrane-bound particles is dominant.

In figure 6.3C and 6.3D the small bottom right insets show the time average density histograms along the minor axis of the same oscillations and are the control measurement, confirming that along this axis no non-uniform spatial profile is emerging, and thus we only observe homogeneous fluctuations around a uniform flat line distribution.

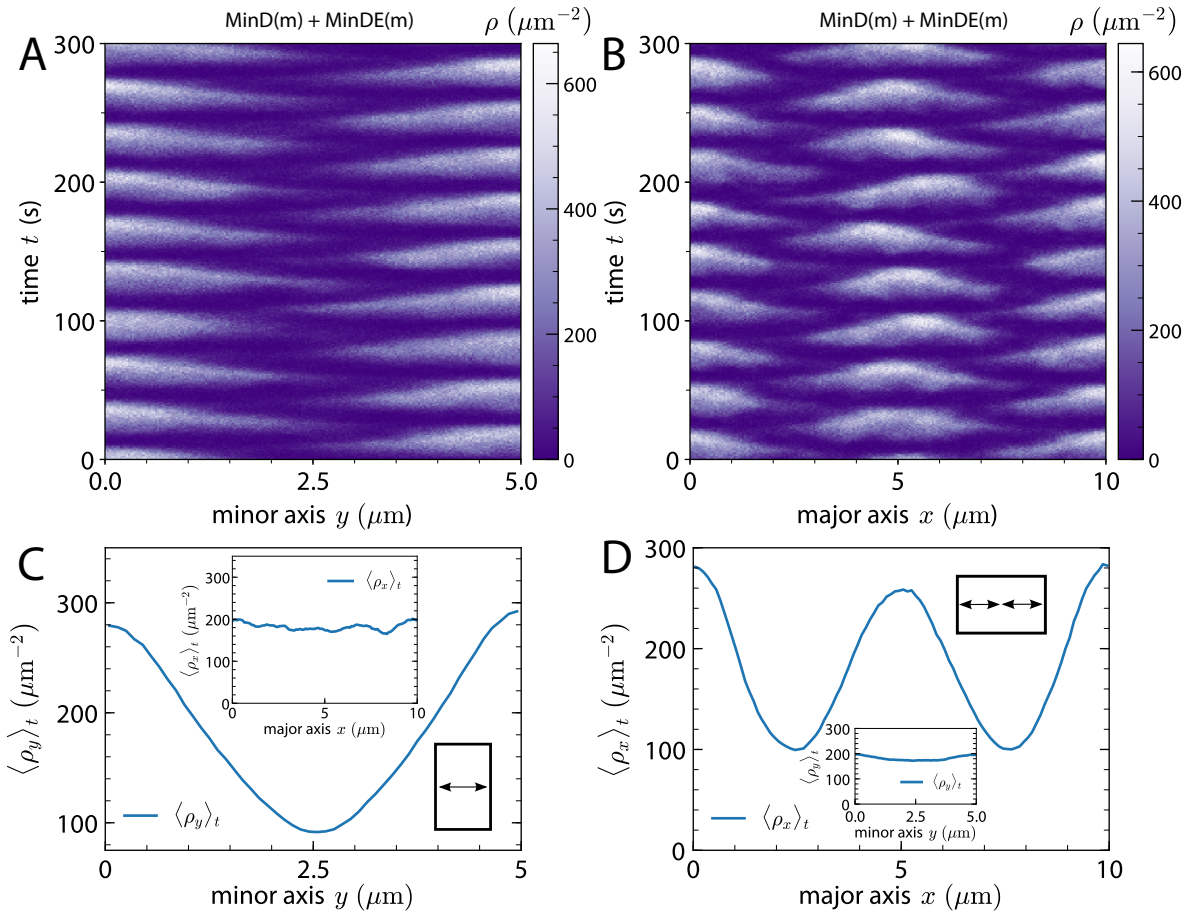

Figure 6.3 | Main oscillation modes in geometry A. **A** depicts a density kymograph of membrane bound MinD and MinDE along the minor axis of the system. **B** shows the same for a striped oscillation mode along the major axis of the system. The colorbars show the surface densities of bound proteins, respectively. **C** Time-averaged density profile along the minor axis of membrane bound MinD and MinDE proteins combined during a pole-to-pole oscillation along the minor axis of the system (Inset: Time-averaged density profile along the major axis of the same oscillation). **D** Time-averaged density profile along the major axis of membrane bound MinD and MinDE proteins during a striped oscillation along the major axis of the system (Inset: Time-averaged density profile along the minor axis of the same oscillation). **C** and **D** show time averaged data using full trajectories from $t_{\mathrm{start}} = 100\,\mathrm{s}$ up to $t_{\mathrm{end}} = 800\,\mathrm{s}$, cutting off the first 100 seconds initialization phase.

The kymographs of the striped oscillation in figure 6.4B have the same structure as the ones of the pole-to-pole oscillations. However, the edges of the bound Min protein clusters in the kymographs, that indicate the traveling Min waves, are curved, in contrast to the straight lines that we see for the pole-to-pole oscillations as shown in figure 6.4A. The time-averaged density profiles of MinD proteins for the pole-to-pole and striped oscillations are shown in figure 6.3C and 6.3D, respectively. As expected the density of the proteins is minimal between the oscillation nodes of the emerging standing wave patterns.

It is highly instructive to compare the time evolution of the MinD and MinE protein densities. In figure 6.5A we plot the time evolution of the particle densities of the transverse pole-to-pole oscillation at a fixed position $y = 4.9\,\mu$m, which is at the edge of the minor axis along which the oscillation takes place. The shape of the transient density profiles is similar to experimentally observed density profiles of traveling Min protein waves on flat membrane surfaces [56, 145]. The period of both oscillation modes was $T = (33.8 \pm 0.1)\,$s, which is in agreement with the results of Huang *et al.* [118].

To analyze the influence of the bulk volume on the oscillations, we have also monitored how the MinD and MinE densities changes at different heights above the membrane. For this we use again geometry A, but now with a bottom surface of only $6\,\mu\text{m} \times 3\,\mu$m, which robustly produces longitudinal pole-to-pole oscillations along the major axis. For a compartment height of $4\,\mu$m the volume was divided in three layers, and for each layer the mean density on one side of the major axis was plotted over time as shown in figure 6.5B. We see that the largest density changes take place in the layer directly above the membrane, however, the oscillations persist up to the top layer even for the highest compartment with $z = 4\,\mu$m. Strikingly, the MinD-density is always much higher than the one of MinE. Furthermore we reduced the compartment height to $0.2\,\mu$m. Interestingly, the pole-to-pole oscillations were still present. This implies that the bulk of the simulation volume has only a mild effect on the oscillations in geometry A, despite the fact that there are appreciable density variations in the bulk.

6.2.2 Essential model elements

We next checked that our model indeed includes the essential elements for the emergence of Min oscillations. Because the MinD-switching between bulk and membrane is clearly indispensable, here we consider the relevance of diffusion on the membrane and of cooperative recruitment. All simulations in this section are carried out using geometry A in a $5\,\mu\text{m} \times 2.5\,\mu\text{m} \times 0.5\,\mu$m compartment geometry. We chose this geometry since

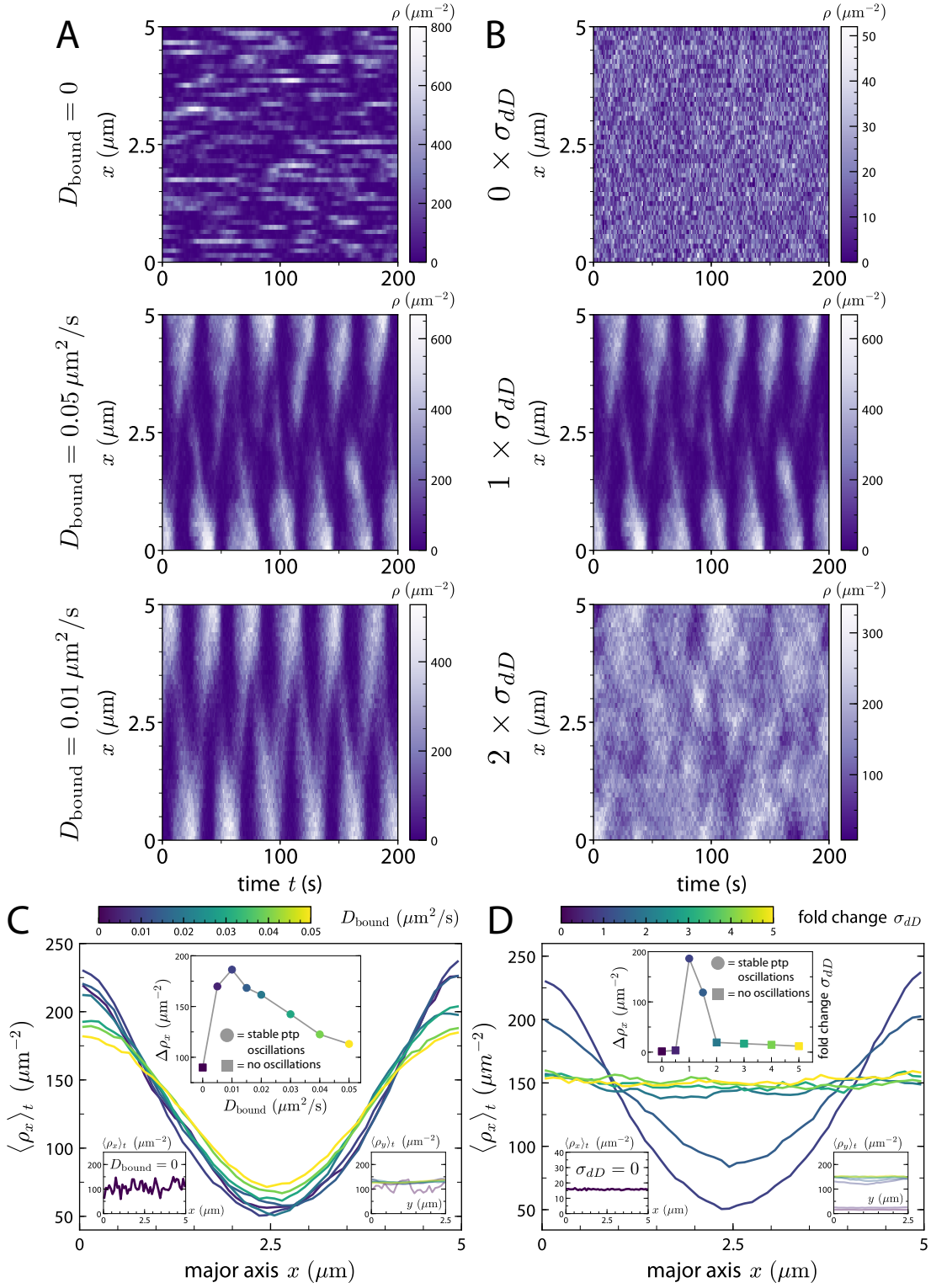

Figure 6.6 | **A** Density kymographs along the major axis for $D_{\mathrm{bound}} = 0\ \mu\mathrm{m}^2/\mathrm{s}$, $D_{\mathrm{bound}} = 0.01\ \mu\mathrm{m}^2/\mathrm{s}$ and $D_{\mathrm{bound}} = 0.05\ \mu\mathrm{m}^2/\mathrm{s}$, respectively. **B** Density kymographs along the major axis for $\sigma_{dD} = 0$, $\sigma_{dD} = 0.0149\,\mu\mathrm{m}^3/\mathrm{s}$ and $\sigma_{dD} = 0.0298\,\mu\mathrm{m}^3/\mathrm{s}$. **C** Time-averaged density profiles for different membrane diffusion-coefficients $D_{\mathbf{bound}}$. **D** Time-averaged density profiles for different cooperative MinD membrane-recruitment rates σ_{dD}.

we expect it to give rise to stable longitudinal pole-to-pole oscillations and hence can closely monitor any deviations from this default oscillation mode. All other parameters were kept fixed and we used parameter set A for this test.

Figure 6.6A shows three kymographs of the system along the major axis. Switching off membrane diffusion entirely (first panel) leads to a loss of stable oscillation patterns. Instead small striped-like MinD-patches emerge erratically on the membrane. The second panel in figure 6.6A shows the default diffusion coefficient of $D_{\text{bound}} = 0.01\ \mu\text{m}^2/\text{s}$ where stable pole-to-pole oscillations emerge along the major axis. By further increasing the membrane-diffusion-coefficient the pole-to-pole oscillations still robustly emerge but increasingly smear out. This behavior is most clearly illustrated by looking at the time-averaged density profiles as shown in figure 6.6C. The inset in figure 6.6C shows that without membrane diffusion, no oscillations emerge at all (square symbol), while a slow diffusivity as used in parameter set A seems optimal.

In a similar fashion we analyzed the influence of the cooperative membrane recruitment of MinD. Figure 6.6B shows three kymographs for no cooperative recruitment ($\sigma_{dD} = 0$), the default value from parameter set A and a two-fold increase, respectively. Without cooperativity in this process no oscillations emerge at all. The second panel shows again the default oscillation mode while already a two-fold increase also leads to unstable behavior without any patterns emerging. This sensitivity with respect to the cooperative recruitment rate σ_{dD} is also summarized in figure 6.6D, which illustrates that only in a very narrow range stable oscillations emerge. Although a complete parameter scan is out of the question at the current stage for reasons of computer time, we conclude that stable Min oscillations emerge only for certain parameter values and that parameter set A performs very well in this respect.

6.2.3 Edge oscillations in geometry B

As we have seen in the preceding section, the simulation compartment height has little influence on the emerging oscillation modes when the membrane only covers the bottom area of the simulation compartment (geometry A). However, when we extend the membrane to cover bottom and side walls of the compartment (geometry B), we find that the oscillation modes change with increasing wall height. First, we consider a compartment that only exhibits longitudinal pole-to-pole oscillations along the major axis (wall height of $0.5\,\mu\text{m}$ and bottom area of $5\,\mu\text{m} \times 2.5\,\mu\text{m}$). In contrast to the flat membrane geometry A, here the MinD protein density decreases in the vicinity of the membrane edges between the side walls and the bottom area, as shown in figure 6.7.

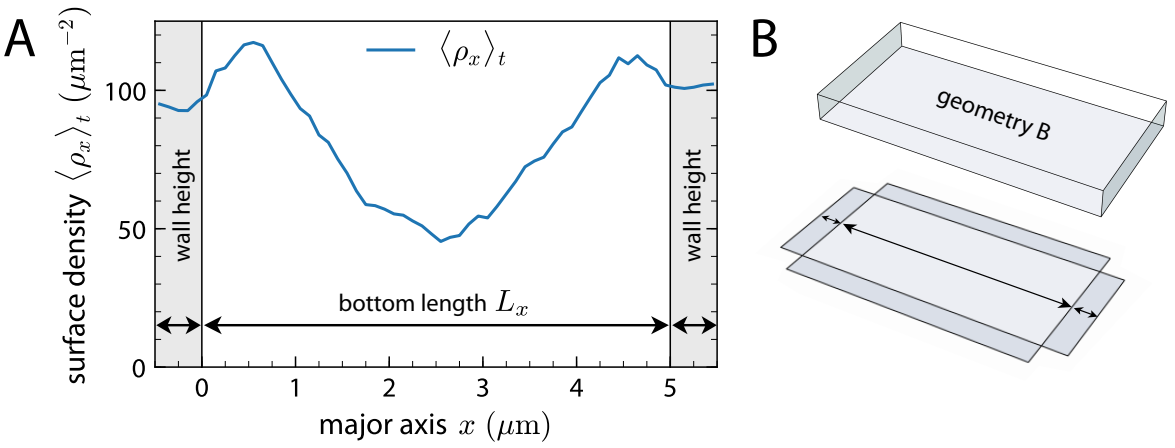

Figure 6.7 | A Average density profile of bound MinD proteins in a simulation where the reactive membrane is extended to the side walls of the compartment (geometry B). The figure shows the density profile on the bottom area of the compartment ($0\,\mu\text{m} \leq x \leq 5\,\mu\text{m}$). Below $x = 0\,\mu$m and above $x = 5\,\mu$m the projected density profile along the side walls of the compartment is shown. **B** Sketch of the simulation geometry B and a top down projection of the side walls for recording the time-averaged surface bound protein densities as shown in **A**.

This is due to the decreased volume per membrane area ratio in the vicinity of the membrane corners, leading to a decreased density of bound MinD proteins in these regions. This effect is clearly visible by comparing the time-averaged density profile in figure 6.7 with the one shown in 6.3C.

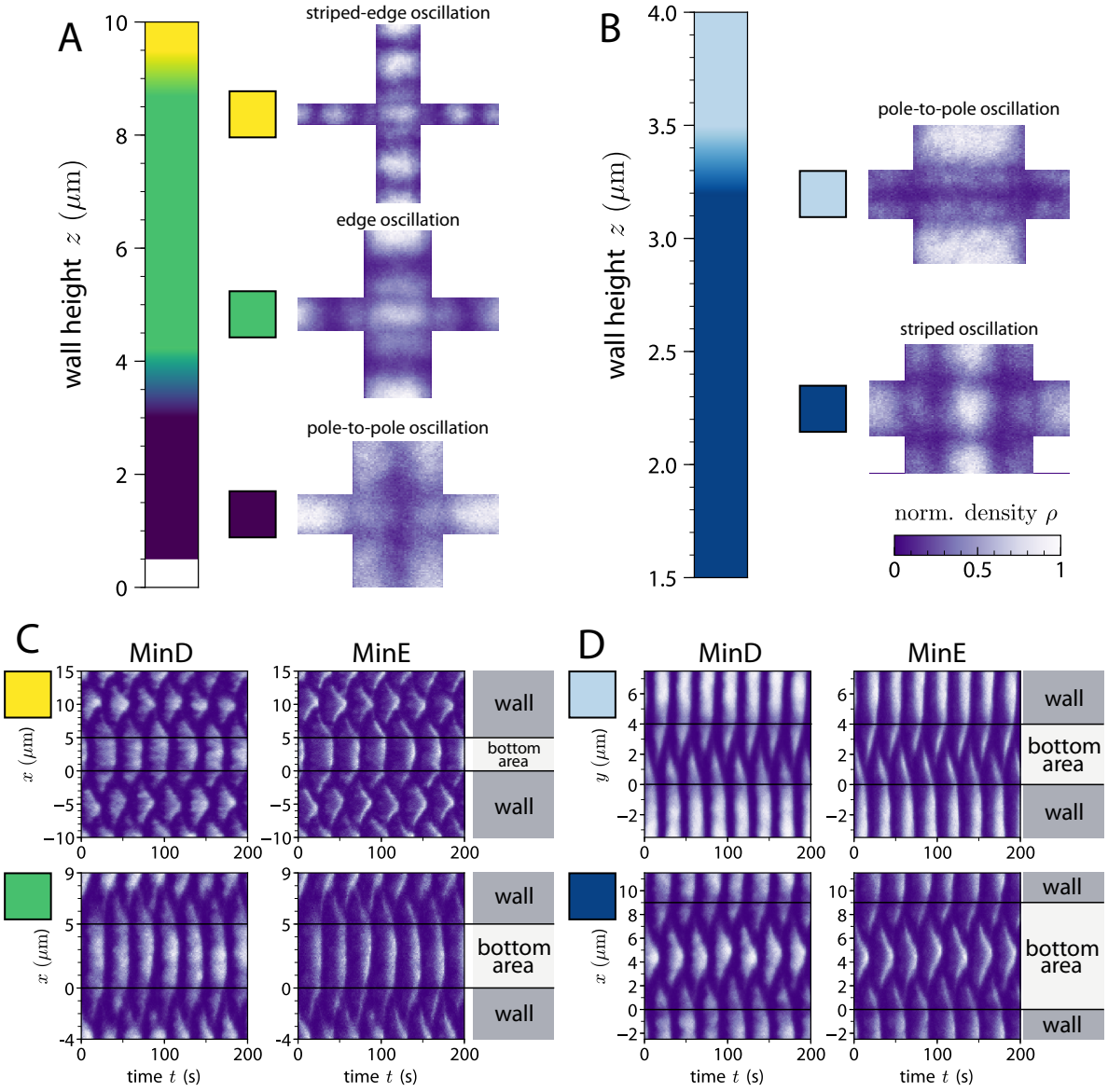

Figure 6.8 | Different edge oscillation modes in geometry B in dependence of the wall height z depicted as time-averaged density plots. **A** The bottom area has dimensions of $x = 5\,\mu$m and $y = 2.5\,\mu$m. Pole-to-pole oscillations are labeled in dark violet (bottom phase), edge oscillations in green and the striped-edge oscillations in yellow. The small region from $z = 0\,\mu$m to approximately $z = 1\,\mu$m is left out in white since in this region no oscillations emerge. **B** The bottom area has dimensions of $x = 9\,\mu$m and $y = 4\,\mu$m. Striped oscillations are labeled in dark blue and pole-to-pole oscillations in light blue. In both A and B the density profiles show time-integrated surface-densities. **C-D** The corresponding kymographs show the densities of the bound MinD and MinE particles along the bottom area and the walls over time. In **C** the yellow phase shows an oscillation in a compartment with height $z = 5\,\mu$m, the green phase uses $z = 9\,\mu$m, the light blue phase in **D** is recorded at $z = 3.5\,\mu$m and the light blue phase at $z = 2.5\,\mu$m, respectively.

The full oscillation pattern is shown in 6.8A for the lowest height value (black label) and resembles a pole-to-pole oscillation for geometry A, but now between the two

opposing walls along the major axis. Now we increase the wall height in increments of $0.5\,\mu$m. The oscillation changes at a wall height of $3.5\,\mu$m to a new oscillation mode (green label). There the proteins start to oscillate between the middle of the bottom area and the upper edges of the walls. This newly identified *edge oscillation* with one polar zone at the bottom and one top polar zone at each of the four side walls persists until the wall height reaches $9.5\,\mu$m. Thereafter the oscillation mode changes to a striped edge oscillation along the walls (yellow label).

In figure 6.8B we show results for a simulation volume that gives rise to striped oscillations along the major axis (bottom area of the length of $9\,\mu$m and width of $4\,\mu$m). At a wall height of $z = 0.5\,\mu$m the simulation gives rise to longitudinal striped oscillations along the major axis or transverse pole-to-pole oscillations along the minor axis. This is the same kind of bistability that we already observed in geometry A using a compartment of $10\,\mu\text{m} \times 5\,\mu\text{m} \times 0.5\,\mu$m. After increasing the wall height to $z = 1.5\,\mu$m the pole-to-pole oscillations along the minor axis disappear and only striped oscillations along the major axis are observed. At the wall height of $z = 3.5\,\mu$m the oscillation mode changes to a large pole-to-pole oscillation along the minor axis and no edge or striped oscillations were observed. Figures 6.8C and 6.8D show the kymographs for the membrane-bound proteins corresponding to figures 6.8A and 6.8B, respectively. These results demonstrate that in geometry B, both the mode selection and the detailed shape of the polar regions can be controlled by the compartment height z.

For an edge oscillation the free MinD protein densities in the bulk of the compartment along one of the bottom area axis (y-axis) and along the walls (z-axis) are shown in figure 6.9A. We see that spatial oscillations in the bulk only take place along the z-axis. On the y-axis kymograph (figure 6.9A top kymograph) the change of the density only takes place along the temporal axis. This corresponds to the change of total numbers of free and bound MinD proteins during the oscillation and no spatial oscillation takes place along the y-axis. On the z-axis kymograph (figure 6.9A bottom kymograph) we observe a spatial pole-to-pole oscillation. In figure 6.9B we show the densities of the free MinD proteins in the bulk of the compartment during the large pole-to-pole oscillation for $z = 4\,\mu$m. We see that the bulk proteins oscillate only along one axis (here the y-axis) and no spatial oscillations occur along the walls (z-axis).

From our study of geometry B, we conclude that in non-flat membrane geometries the oscillations of the Min proteins do not only take place along the membrane, but are rather defined by the canalized transfer of the proteins through the bulk. This shows the importance of three-dimensional simulations for non-flat membrane geometries in order to determine the self-organized oscillation modes.

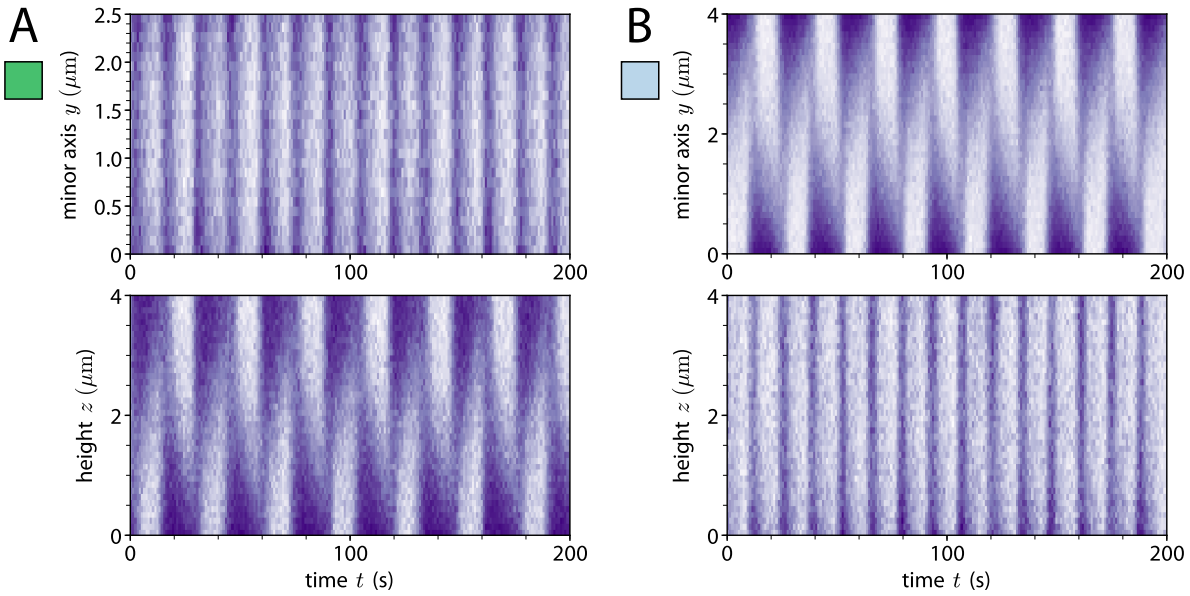

Figure 6.9 | Density kymographs of free MinD particles in geometry B in the bulk of the compartments along different axes over time. **A** Edge oscillation (part of the green phase in figure 6.8A). **B** Pole-to-pole oscillation (part of the light blue phase in figure 6.8B).

6.3 Geometrical determinants of bound particle densities

While analyzing the characteristics of the oscillation patterns, we noticed that it is also very interesting to monitor the copy numbers of all involved species in the system over time. In particular, we wanted to determine the difference between free bulk proteins and membrane bound proteins in our current setup. Figure 6.10 shows one realization of this measurement, where we include the regular kymograph of MinD proteins, but most essentially record the bulk levels of MinD and MinE over time. The steep initial drop in the first few seconds merely reflects that we initialize all particles in the cytosolic bulk. After this we observe a roughly 100 second long rather chaotic initialization phase, which turns into steady fluctuations around a constant mean bulk value μ_n as soon as a stable oscillation mode is found. Strikingly we observed that, while the MinD bulk levels where slightly below 50 %, the levels for MinE were much stronger depleted (see figure 6.10C), dropping below 15 %. Having observed this behavior for a single realization as illustrated here, we then asked ourselves, if this bulk depletion of MinE is a generic property of this oscillation mechanism, using the current concentration and MinD to MinE ratio.

So next we monitored the amount of membrane-bound MinD and MinE proteins

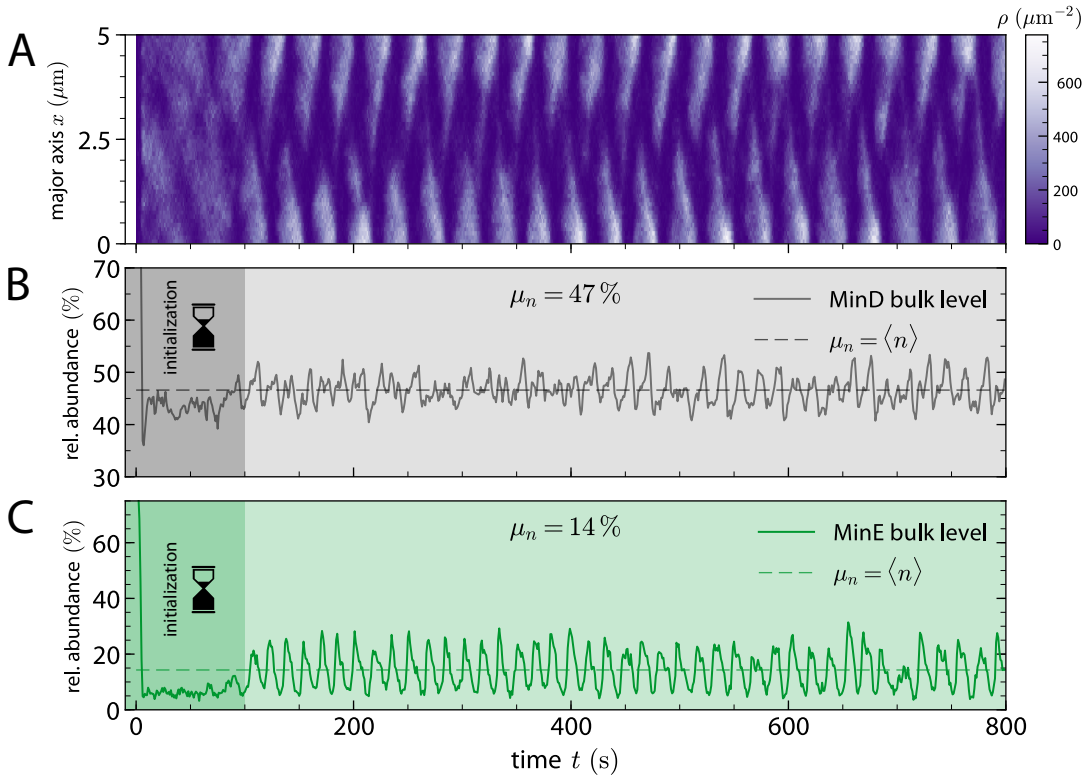

Figure 6.10 | Bulk protein levels during a regular pole-to-pole oscillation. **A** Shows the surface density kymograph of a stable pole-to-pole oscillation along the major axis in a $5\,\mu\text{m} \times 2.5\,\mu\text{m} \times 0.5\,\mu\text{m}$ compartment using geometry A for the first 800 seconds. **B** and **C** show the relative bulk levels of MinD and MinE proteins, respectively. The darker shaded region in the beginning of **B** and **C** marks the initialization phase, which was excluded from averaging to calculate the average bulk level μ_n. All three figures share the same time axis and are aligned accordingly, such that the top kymograph serves as a guide to the eye to illustrate the onset of the regular oscillation pattern.

and compared it to the total amount of proteins in the system, for a large geometric phase space and using all three different membrane topologies (compare figure 6.1B). Interestingly, we observed that these two quantities have a linear dependence $N_{\text{bound}} \propto N_{\text{total}}$ as shown in figure 6.11A. Surprisingly, this relation seems to hold for all geometries and dimensions, as indicated in figure 6.11A by the different symbols (see figure legend). Since we keep the density in our simulations constant, the total amount of proteins scales linearly with the compartment volume ($N_{\text{total}} \propto V$). Overall, we conclude the following relation for the mean bound Min protein density

$$\bar{\rho}_{\text{bound}} = \frac{N_{\text{bound}}}{A} \propto \frac{N_{\text{total}}}{A} \propto \frac{V}{A}\,, \tag{6.11}$$

by normalizing the established scaling with the total reactive membrane area A. Thus the mean bound Min protein density increases linearly with the volume-to-area ratio, as verified by figure 6.11B. Strikingly, we again observe a dramatic difference between

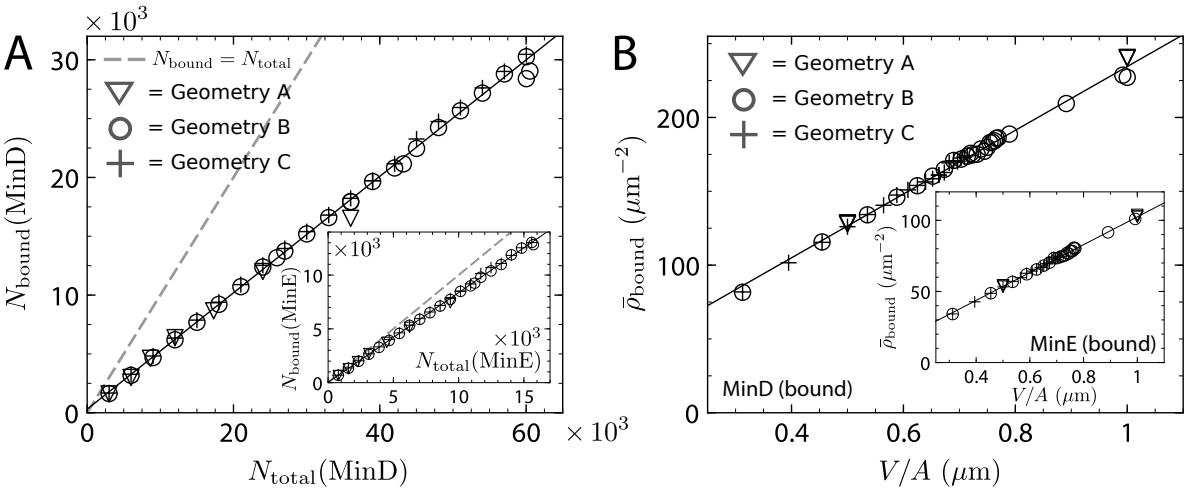

Figure 6.11 | A Relation between the amount of total and membrane-bound MinD particles taken from many independent simulations for various different geometry settings and various different absolute compartment dimensions. The inset shows the same relation for bound MinE particles. Note that MinE is more strongly depleted from the bulk than it is the case for MinD (the dashed gray lines indicate complete depletion at $N_{\mathrm{bound}} = N_{\mathrm{total}}$). **B** Mean density of membrane-bound particles as a function of the volume-to-area ratios V/A for a given compartment geometry. As before, the main figure shows the results for MinD proteins while the inset depicts the mean bound densities $\bar{\rho}_{\mathrm{bound}}$ against the volume-to-area ratio V/A for MinE.

MinD and MinE. Although this scaling is the same for both, MinE is much closer to being completely bound (gray lines), indicating that once a stable oscillation emerges, MinE is almost completely depleted from the bulk.

We next assessed the physiological relevance of these observations. In order to investigate how the volume-to-area ratio V/A changes during cell growth, we approximate the shape of an *E.coli* bacterium by a spherocylinder of length L and width w and evaluate V/A analytically. Since *E. coli* bacteria mainly grow in length and stay constant in width [181], we show the evolution of V/A as function of the cell length L for various fixed cell widths w in figure 6.12A. One clearly sees that V/A remains nearly constant as a function of the cell length L. Recalling that our previous observation stated that the mean membrane-bound Min protein densities $\bar{\rho}_{\mathrm{bound}}$ scale linearly with V/A, this would suggest that living bacteria grow in a fashion that keeps both V/A and thus consequently $\bar{\rho}_{\mathrm{bound}}$ constant, which might be advantageous for the stability and robustness of the Min oscillations and related processes, such as formation of the FtsZ-ring. A similar qualitative behavior is observed if we instead of a spherocylinder would assume an ellipsoidal shape as is shown in figure 6.12B.

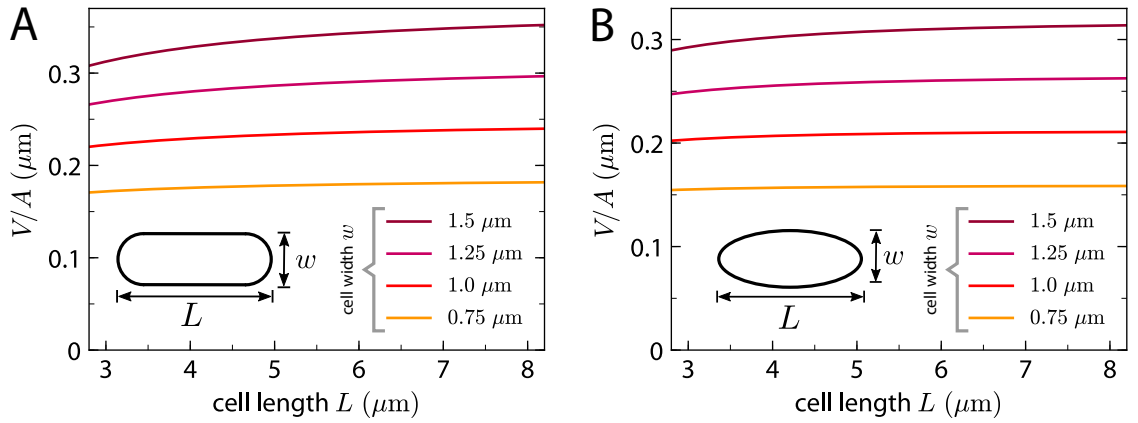

Figure 6.12 | **A** Volume-to-area ratio V/A of a spherocylinder as a function of the cell length L for various cell widths w. **B** A similar relation is observed for an ellipsoidal shape.

6.4 Oscillation mode switching

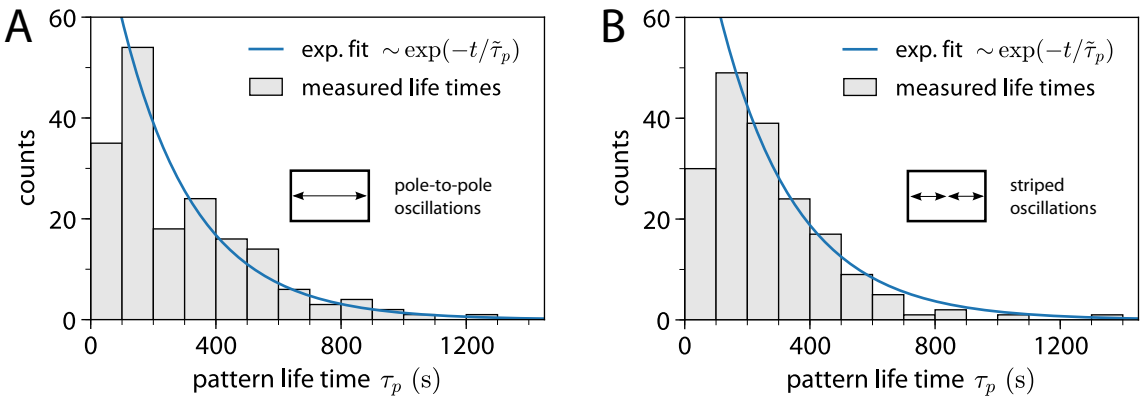

Figure 6.13 | Histograms of oscillation mode life times τ_p for which a given oscillation mode was found to be stable before a mode switch occurred. **A** shows the results for longitudinal pole-to-pole oscillations as illustrated in figure 6.15A. **B** shows the same statistics for the longitudinal striped oscillation mode. In both cases we fitted an exponential decay process to extract the characteristic life time $\tilde{\tau}_p$ for both of the modes.

Above we have seen that multistability is a recurrent phenomenon in the Min system, both in geometries A and B. We next turn to a systematic investigation of the stochastic switching between two different oscillation modes. An oscillation mode transition of this type occurs frequently in a $8\,\mu\text{m} \times 2\,\mu\text{m} \times 0.5\,\mu\text{m}$ compartment using geometry B. In this geometry the Min system gives rise to both pole-to-pole and striped oscillations along the same (major) axis (kymograph in figure 6.15A). We measure the life times (oscillation duration before a mode switch occurs) of the two modes during 50 000 s long simulation trajectories. The resulting histograms of the pattern life times τ_p are

shown in figure 6.13. We can approximate the mode switching as a Poisson process by assuming that the switching probability $p(t)$ obeys $p(t) \propto \exp(-kt)$. Fitting an exponential to the switching times histograms we obtain the switching rates of these processes, where the characteristic pattern life time $\tilde{\tau}_p$ is as usual the inverse switching rate $k_{p_i} = 1/\tilde{\tau}_{p_i}$, here for pattern p_i. Here we neglect the measurements of short life times below $\tau_c = 100\,\mathrm{s}$ since our oscillation mode detection algorithm can miss a mode transition if its life time is shorter. The switching rate for the pole-to-pole oscillation is $k_\mathrm{p} = 0.004\,22\,\mathrm{s}^{-1}$ and for the striped oscillation we find $k_\mathrm{s} = 0.004\,06\,\mathrm{s}^{-1}$, thus the two modes seem to be equally frequent in this case.

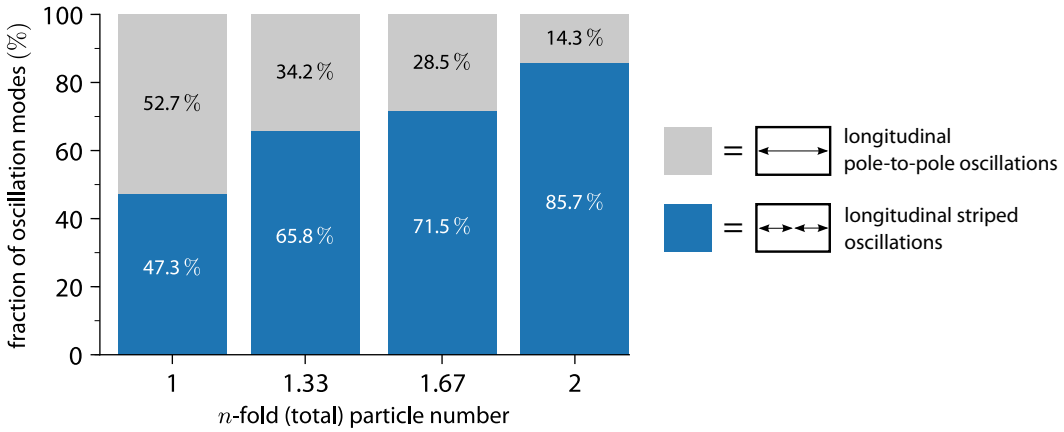

Figure 6.14 | Fraction of pole-to-pole and striped oscillation modes (here both are longitudinal along the major axis of the compartment) in dependence of the amount of particles present in the system volume. These results were obtained using geometry B and parameter set A and correspond to the simulation setting as illustrated in figure 6.15A.

We have also performed the same analysis with identical compartment geometry for the two other parameter sets (set B and C) as presented in table 6.1. Parameter set B gives rise to stable longitudinal pole-to-pole oscillations along the major axis (kymograph in figure 6.15B) in agreement with the results from [53], while parameter set C shows a qualitatively similar switching behavior as parameter set A (data not shown) with frequent mode transitions.

To analyze the effect of the Min protein concentration on the oscillation mode switching, we have performed the same simulation with increased Min protein particle densities using again parameter set A. The resulting fractions of the two oscillation modes during a 50 000 s simulation trajectory are shown in figure 6.14, and their corresponding switching rates k_p and k_s are given in table 6.2. We note that the fraction of striped oscillations increases monotonously with increasing particle density. In agreement with this, the rate k_s decreases with increasing particle density. In contrast, the rate k_p does not show a systematic change and seems to fluctuate strongly. The shift to striped oscillations

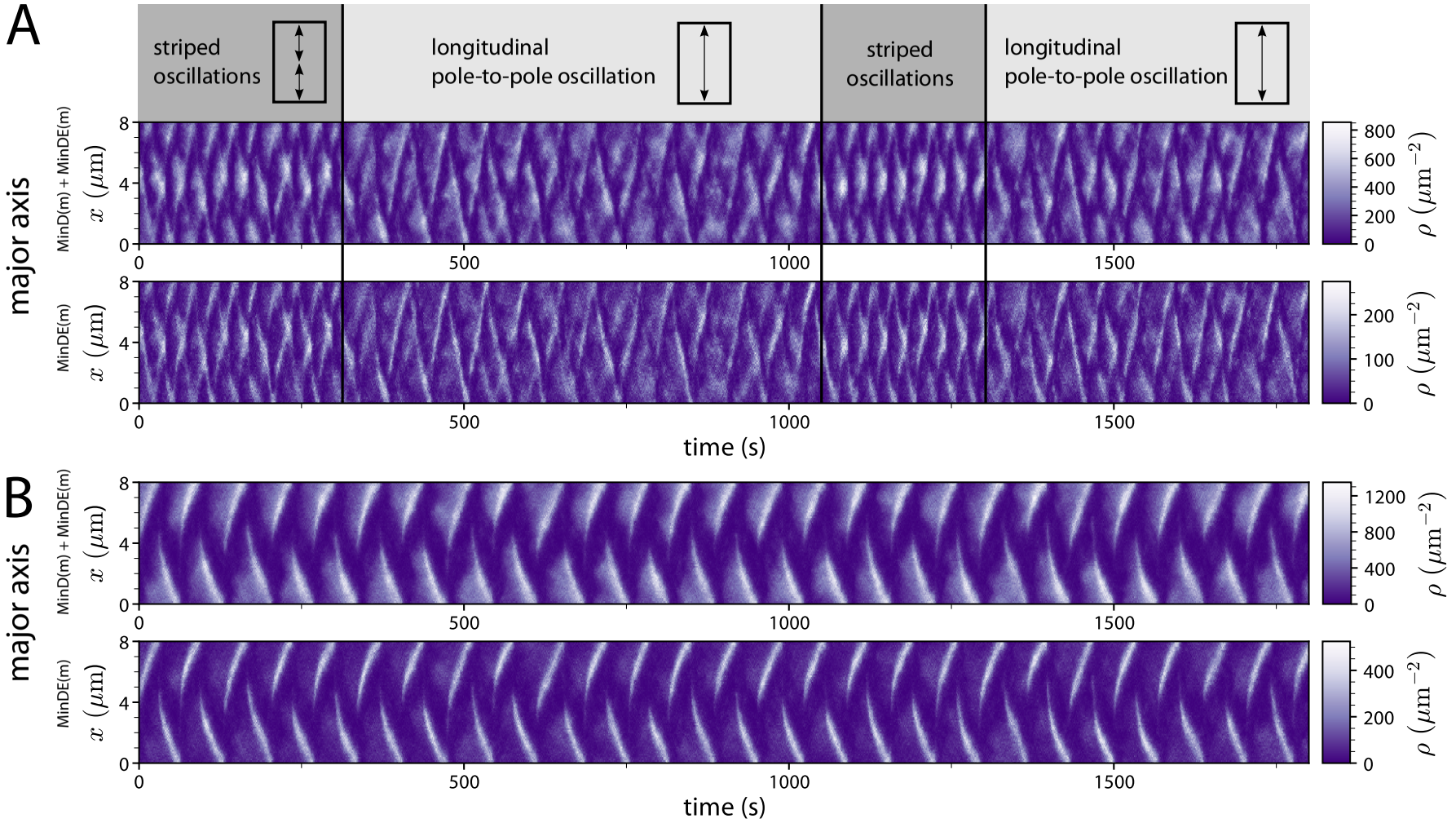

Figure 6.15 | Stochastic oscillation mode switching in geometry B along the major axis of the compartment (longitudinal oscillation mode switching). **A** shows density kymographs of a trajectory using parameter set A, where transitions between longitudinal pole-to-pole oscillations and longitudinal striped oscillations occur in a compartment of dimensions $8\mu\text{m} \times 2\mu\text{m} \times 0.5\mu\text{m}$. The top row in **A** depicts surface densities of all bound molecules (MinD(m) + MinDE(m)), while the lower row shows surface bound MinE (in form of MinDE(m) complexes) only. **B** shows density kymographs using the same compartment geometry as in **A** but with parameter set B instead. Top and bottom row show total and MinE bound protein densities, respectively as before. The time axis was shifted by an offset of $t_{\text{start}} = 1000\,\text{s}$ for both scenarios.

suggests that the Min oscillations can be used not only to sense geometry, but also to sense concentrations.

n-fold particle number	k_p (s^{-1})	k_s (s^{-1})
1	0.0042	0.0041
1.33	0.0065	0.0024
1.67	0.0055	0.0016
2	0.0066	0.0008

Table 6.2 | Switching rates for different protein concentrations (using geometry B and parameter set A as specified in table 6.1).

6.4.1 Phase diagrams for geometry C

Wu *et al.* have experimentally measured the fractions of different oscillation modes of Min proteins in rectangular cell geometries of *E. coli* bacteria of various sizes with constant height [53]. In order to address these observations, we now turn to geometry C, which is a rectangular and fully membrane-covered compartment as sketched in figure 6.1B. Throughout this section we keep the compartment height fixed at $z = 1\,\mu$m, while we vary the length (major axis) between 2 and 10 μm and the width (minor axis) of the compartment between 1 and 5 μm in steps of 1 μm, respectively. To determine the oscillation mode fractions we calculate an ensemble average of the oscillation modes after 500 s simulation time. For each compartment size a sample of 20 independent simulations is used.

In the following analysis we only focus on the three main oscillation modes, which here are longitudinal pole-to-pole and striped oscillations (along the major axis) and transverse pole-to-pole oscillations (along the minor axis). Other oscillation modes as they have been reported in [53] were also observed using our framework, however, due to their low probability, a much higher sample size would be necessary to analyze their occurrence frequency with sufficient statistics. The results for the three oscillation modes are shown in figure 6.16. In general, each of the three oscillation modes dominates in one region of the phase diagram, but the transitions are fuzzy and therefore bistabilities occur. For compartments with length below 7 μm and width below 4 μm, only pole-to-pole oscillations are observed. Most of those oscillations occur along the major axis of the system. The transverse pole-to-pole oscillations along the y-axis emerge most frequently in compartments with quadratic bottom area. Increasing the width further increases the fractions of transverse pole-to-pole oscillations at the expense of

longitudinal pole-to-pole oscillations. Increasing the length for a fixed width shows a sharp transition from longitudinal pole-to-pole to longitudinal striped patterns at around 6 μm. For compartments with length larger than 7 μm, the longitudinal pole-to-pole oscillations vanish almost entirely. In the region of both large long sides (around 7 to 10 μm in length) and large short sides (around 4 to 5 μm in width), the oscillation mode fractions are rather equally shared between longitudinal striped and transverse pole-to-pole oscillations, which is also in line with the bistability that we observed between these two patterns in the 10 μm $\times$ 5 μm $\times$ 0.5 μm compartment of geometry A as shown in section 6.2.1. Figure 6.16C summarizes these findings in a phase diagram that considers only the dominating mode (expect in the regions of clear bistability). Overall we find the determined oscillation mode fractions based on parameter set A and as shown in figure 6.16 to be in excellent agreement with the experimental results as reported by Wu *et al.* [53].

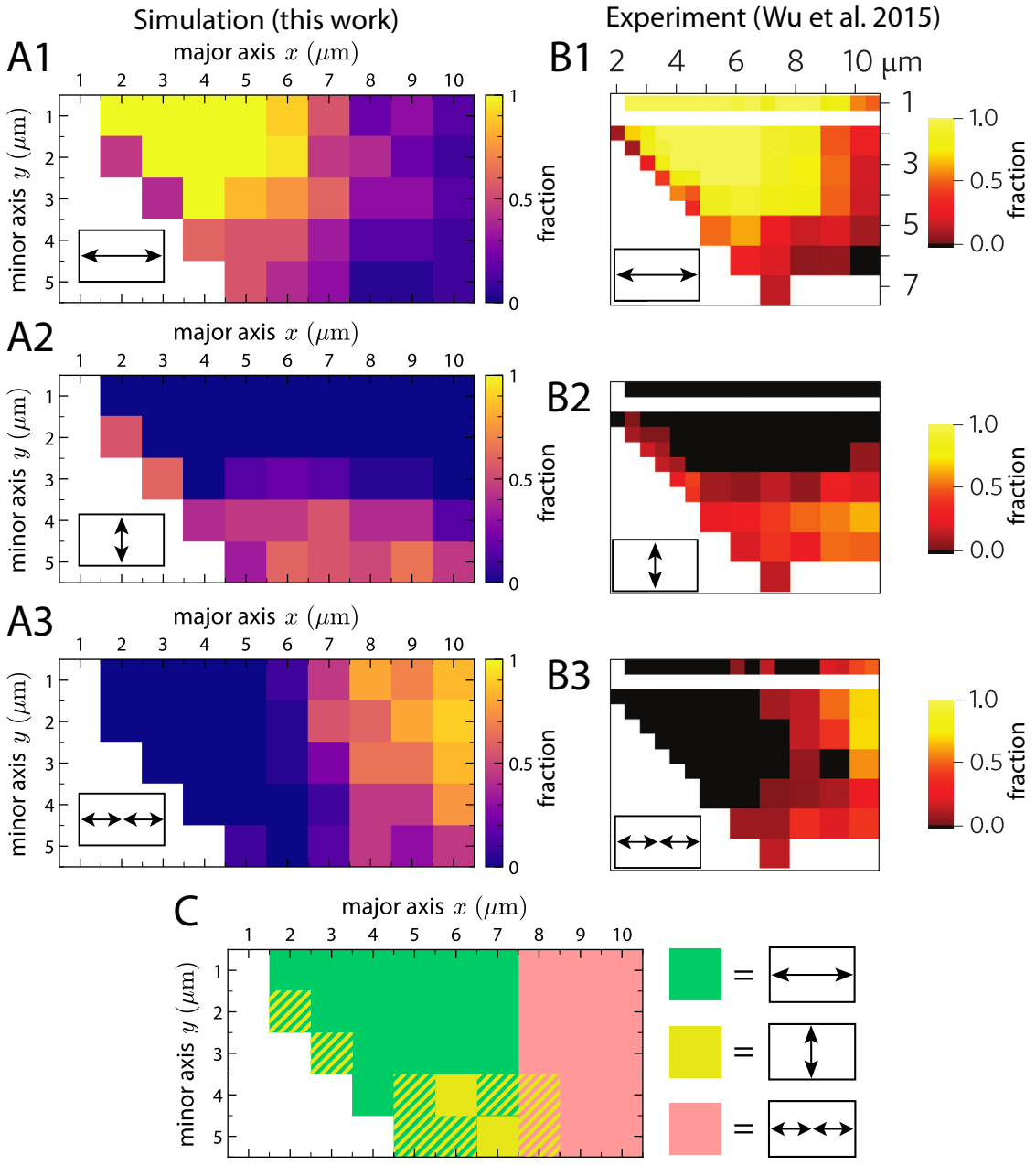

Figure 6.16 | Variation of Min oscillation modes and the relative importance of the three main oscillation modes in geometry C for a wide geometric parameter range. **A1** shows the fractions of longitudinal pole-to-pole oscillations along the major x-axis, **A2** the fractions of transverse pole-to-pole oscillations along the minor y-axis, and **A3** longitudinal striped oscillations along the major x-axis. The second column **B1-B3** shows the same kind of data but now using experimental results from living bacteria, that have been forced into rectangular shapes using a cell sculpting approach. Figures taken from Wu *et al.* [53]. The x and y range in **B2** and **B3** is identical to the one in **B1**. **C** Phase diagram of dominant oscillation modes, according to the shown data in the first column (**A1-A3**). When two modes emerged both with a frequency $> 40\%$, we considered both modes as dominant, as indicated by the striped regions in diagram **C**. White regions in all phase diagrams in this figure indicate unsampled geometries.

6.4.2 Oscillation switching during cell growth

Until now the system geometry that we used in this work was constant over time. Since cells grow it is a naturally occurring question how pattern forming systems, such as the here studied Min system, function when exposed to transiently varying system boundaries. We address this question by analyzing domain growth in our thus far presented framework by continuously letting one axis of our reaction compartments grow over time.

We start with an initial system geometry using dimensions $L_x \times L_y \times L_z = 5 \times 2.5 \times 0.5\,\mu\text{m}^3$ and let the cell length L (here chosen to be $L = L_x$) continuously grow, with a constant growth rate r_g, such that

$$L_x(t) = r_g t + L_{x,0} \quad \text{where} \quad r_g = \dot{L}_x. \tag{6.12}$$

Starting with an initial cell length of $L_{x,0} = L_x(t = 0) = 5\,\mu\text{m}$, we as usual record the surface density of bound MinD proteins and visualize them as a density kymograph as shown in figure 6.17.

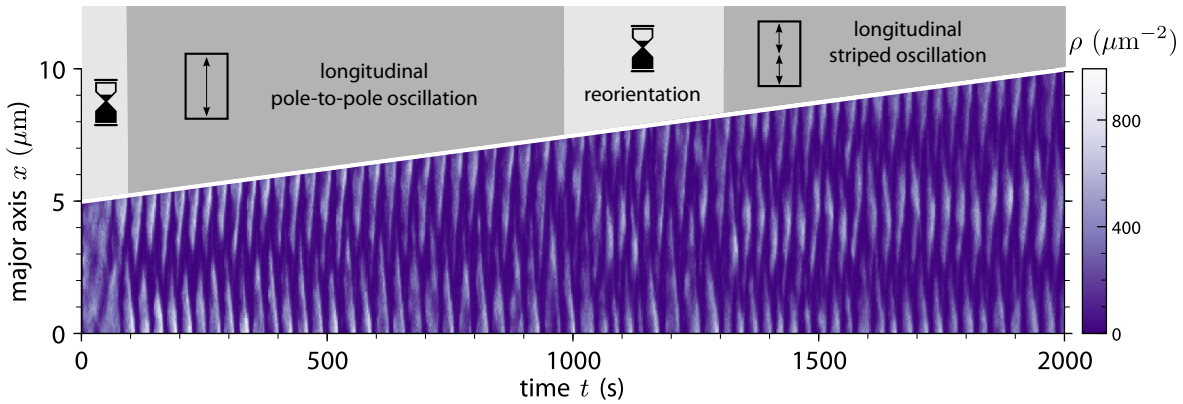

Figure 6.17 | Oscillation mode switching during cell growth. Shown is a surface density kymograph along the major axis of a rectangular compartment using geometry A. All parameters are as before (parameter set A, see table 6.1 for reference) Starting from an initial major axis length $L_x = 5\,\mu\text{m}$, we monitor the surface densities over the course of a simulation trajectory for $t_{\text{obs}} = 2000\,\text{s}$ while the cell length continuously grows with a growth rate r_g. After a brief initialization phase (hour glass symbol) the default pole-to-pole oscillation mode sets in. With increasing cell length ($L = L_x$ here), the initial mode is maintained until $t = 1000\,\text{s}$, where the system reorients its spatial oscillation pattern. At approximately $t = 1350\,\text{s}$ the system settles into a striped longitudinal oscillation mode, which it stays in until the end of the observation time. In the above simulation we used $L_{x,0} = 5\,\mu\text{m}$ and a growth rate of $r_g = 2.5 \times 10^{-3}\,\mu\text{m/s}$.

The first mode that we observe is a longitudinal pole-to-pole oscillation, which is the default mode for a $5\mu\text{m} \times 2.5\,\mu\text{m} \times 0.5\,\mu\text{m}$ reaction geometry. The system remains locked

in this mode over an extension in length from $L_x = 5\,\mu$m up to approximately $L_x = 7\mu$m. This is a nice illustration, that the Min system can maintain an oscillation mode over a transiently varying system geometry and adapt its pattern to the instantaneous domain size. But this adaptive pattern can only be maintained up to a critical length. Exceeding a critical domain length, the system briefly becomes chaotic and rearranges its spatial pattern settling into a new dominating mode given the current domain size. In 6.17 this behavior can be observed between $t = 1000\,$s and $t = 1350\,$s. After this reorientation phase we observe a longitudinal striped oscillation and the system remains locked in this mode for the remainder of the observation time. This is also to be expected, since we approach the target domain length of $L_x = 10\,\mu$m for which we previously reported the occurrence of longitudinal striped modes, as also illustrated in figure 6.3B and figure 6.4B. And of course the transition from a longitudinal pole-to-pole oscillation to a longitudinal striped oscillation when going from $L_x = 5\,\mu$m up to $L_x = 10\,\mu$m is also what our systematic analysis of the geometric parameter space in figure 6.16A1 and 6.16A3 predict. When analyzing the mode selection and the stability of a given oscillation pattern with domain growth as presented in figure 6.17 one must however always keep in mind, that the total protein concentrations are effectively diluted, since we do not consider new protein production due to gene expression in our model. This is also visible in the above kymograph since the peak surface densities go down as the cell length increases. This must be taken into account when analyzing domain growth in more detail, since the oscillations are very much dependent on absolute concentration values of the proteins present in the system.

This is an intriguing example, which nicely illustrates the Min system's capability to sense the domain geometry that it is embedded in.

6.4.3 Measuring the oscillation period

To determine the oscillation period T of a given oscillation mode, we use the spatial histograms of bound protein densities that we by default record for both the major and minor axis of the rectangular system compartments. We denote the spatiotemporal histograms as before as $\rho(x_i, t)$, where x_i can be either the major or the minor axis $x_i \in \{x, y\}$. The most convenient method to determine the period T is to simply look at the Fourier spectrum of this time-varying density signal and detect the maximal peaks in the amplitude spectrum. Once the system has settled into a stable mode, we found that this is a robust method to determine the oscillation period T.

Below we illustrate this routine for a default pole-to-pole oscillation in geometry A

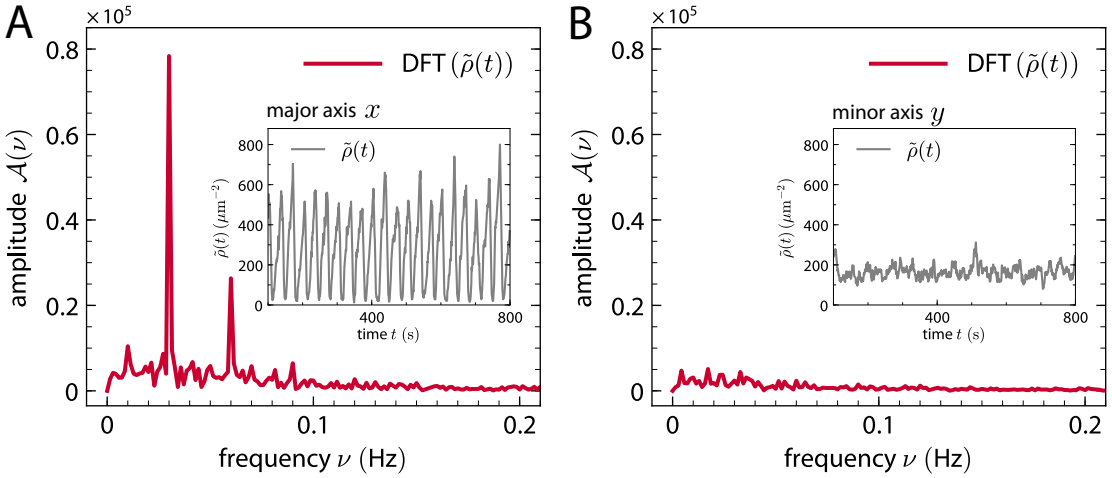

Figure 6.18 | Amplitude spectrum $\mathcal{A}(\nu)$ of the bound protein densities along both the major (**A**) and minor axis (**B**). The clear peak in **A** is a good indicator for the dominant oscillation mode in the system. For better comparison all plots use the same scaling, illustrating that along the minor axis there is no clear structure in the Fourier spectrum. These results use a $t_{\text{obs}} = 800\,\text{s}$ long trajectory in a $5\mu\text{m} \times 2.5\,\mu\text{m} \times 0.5\,\mu\text{m}$ compartment, from which the first 100 s initialization phase were cut off. The inset in both **A** and **B** shows the actual signal $\tilde{\rho}(t)$ on which the DFT is performed, and which is obtained as explained in formula (6.15).

using parameter set A. An exemplary density kymograph for this scenario is shown in figure 6.6A (middle row). For this geometry the system always settles into a stable pole-to-pole oscillation rather quickly. The first step of this analysis is as usual to cut off the initialization phase. To be on the safe side, we typically set the starting time point that we use for further evaluation at $t_{\text{start}} = 100\,\text{s}$. To extract a time-varying oscillatory signal we pick a small band of width l_x in the spatial domain at either of the edges and marginalize the bound density histogram over this small domain $\Delta_{x_i} = [0,\, l_{x_i}]$ (or equivalently $\Delta_{x_i} = [L_{x_i} - l_{x_i},\, L_{x_i}]$) for each recorded time point, resulting in a time series of effective bound protein densities along this band Δ_{x_i}.

This marginalization in the spatial domain can be done by averaging over the band Δ_{x_i} or by taking its maximum (for not too broad band widths both performed equally well and in mutual agreement). The averaging would be performed as

$$\rho_\tau(t) = \Big\langle \rho(x_i, t) \Big\rangle_{x_i \in \Delta_{x_i}}, \tag{6.13}$$

while the alternative to simply take the maximum means to calculate

$$\rho_\tau(t) = \max_{x_i \in \Delta_{x_i}} \Big[\rho(x_i, t)\Big]. \tag{6.14}$$

Then we create our final time series from ρ_τ by shifting ρ_τ by its own mean to obtain

$$\tilde{\rho}(t) = \rho_\tau(t) - \left\langle \rho_\tau(t) \right\rangle_t , \tag{6.15}$$

which we use as the input signal for the actual Fourier analysis. By calculating the discrete Fourier transform (DFT) of this signal we can calculate the amplitude spectrum $\mathcal{A}(\nu)$ by taking the absolute squared value of the Fourier transform

$$\mathcal{F}_\rho(\nu) = \mathrm{FFT}\left[\tilde{\rho}(t)\right] \quad \text{and} \quad \mathcal{A}(\nu) = \left|\mathcal{F}_\rho(\nu)\right|^2 , \tag{6.16}$$

from which we can eventually extract the oscillation period T by identifying the dominant peaks in the spectrum

$$T = \left[\underset{\nu}{\mathrm{argmax}}\, \mathcal{A}(\nu)\right]^{-1} = \frac{1}{\nu_c}. \tag{6.17}$$

Here ν_c stands for the characteristic oscillation frequency of a given oscillation mode. In figure 6.18 these peaks are clearly visible for the dominant oscillation mode (left sub-figure **A**), while they are absent in the spectrum for the minor axis (right sub-figure **B**). For the example shown in figure 6.18 we found the oscillation period to be $T \approx 33.3\,\mathrm{s}$.

The numerical fast Fourier transform (FFT) algorithm we used goes back to Cooley and Tukey [182]. This analysis of the Fourier spectrum was equally useful for the detection of oscillation modes and the transient switching between them. Hence we use an automated version of the above outlined routine for the data evaluation of the switching statistics as they are shown in figure 6.15 and for the mode detection, which allowed us to construct the geometric phase diagram as shown in figure 6.16.

6.5 Single particle tracking (SPT)

One of the great advantages of explicit spatiotemporal simulation tools, is that in principle one has full knowledge of the full system at all times. This can be utilized, in the best case, to extract information on the single particle (molecular) level to infer mechanistic detail about underlying physical processes.

For the Min oscillations we demonstrate this by explicitly showing the results of a single particle tracking applied to a single MinD protein within a $(L_x, L_y, L_z) = (5\,\mu\mathrm{m}, 2.5\,\mu\mathrm{m}, 0.5\,\mu\mathrm{m})$ compartment in figure 6.19. While **A** shows the x and y coordinate position histograms over the full observation time of $t_{\mathrm{obs}} = 700$ s (cutting of the first 100 s initialization phase), **B** & **C** focus on a 15 s long extract of the full trajectory

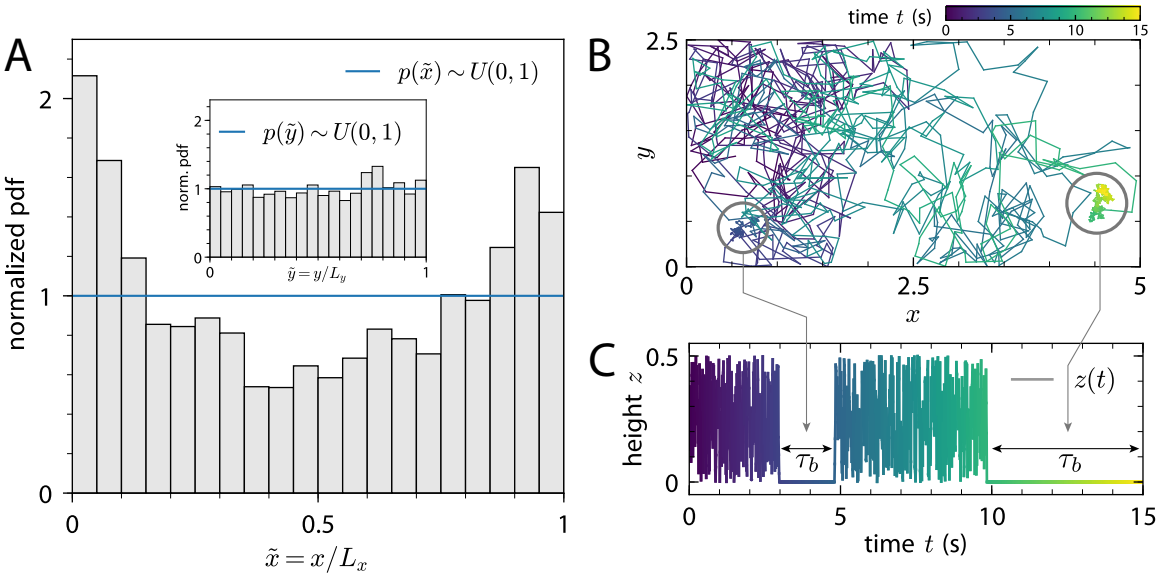

Figure 6.19 | Single particle tracking (SPT) of a single MinD protein. Explicit particle-based simulation techniques allow the tracking of single particles, which is here demonstrated for a single MinD molecule within our simulation framework. **A** shows a position histogram of the x coordinate of a single molecule. The histogram is build from the full time course of a $t_{\text{obs}} = 700$ s trajectory, after cutting of the initial 100 s initialization phase. Even on the single particle (protein) level, the spatial profile shows a clear polar localization at the end caps of the compartment volume for the x coordinate. The y-histogram (along the short axis L_y) shows the expected uniform profile (see **A** inlet). **B** shows a 15 s long x-y projection of the full trajectory of the same MinD molecule within the $5\mu\text{m} \times 2.5\mu\text{m} \times 0.5\mu\text{m}$ compartment. This trajectory begins at $t = 120$s of the real time to stay clear of the chaotic initialization phase until the onset of regular oscillation patterns. **C** illustrates the transient height profile $z(t)$ of the same trajectory. The color code encodes time. This allows a clear inspection of membrane attachments and the corresponding bound times τ_b. The coarseness of the shown trajectory in B can of course by made infinitely small by increasing the sampling frequency $\nu_s = 1/\Delta t_s$ for the trajectory measurements. Here all results are shown for a measurement time step of $\Delta t_s = 0.01$s.

of the same single MinD molecule starting at $t = 120\,\text{s}$ (here shifted to $t = 0$ using a 120 s time offset). Single particle inspections of this kind might not offer the same kind of information as the collective and ensemble averaged data from multiple simulations, but they offer a complementary perspective on the underlying reaction mechanisms. In the past it was questioned, whether single MinD proteins actually oscillate back and forth from one pole to the other. This kind of information, as shown in 6.19, clearly demonstrates, that within the time course of roughly half an oscillation period ($\approx$ 15s) a single MinD molecule can actually move from pole to pole. Of course this does not say, that every molecule undergoes this same behavior, since the molecular diffusive motion at the single particle level is much more erratic and the characteristic pole-to-pole oscillations are obviously a result of collective self-organization. But it still does not fail to illustrate the polar localization and polar attachment to the membrane on the single

molecule level.
From a technical point of view it is worth while mentioning that of course any conventional molecular dynamics type of simulation has in principle full access to all positional information $(x(t), y(t), z(t))$ at all times. For reactive simulation frameworks however, the underlying algorithms and data structures need to be explicitly modified to allow single particle tracking, since any reaction goes along with the deletion of the reactant particles and the creation (new memory allocation) of the product particles. In any straight forward naive implementation the identity of an individual particle which undergoes a reaction event is typically lost. To enable *single particle tracking* one must therefore create unique particle identifiers and keep track of them during reaction events. This means, that for each available reaction channel one must implement a set of rules which specify how particle IDs are converted, conserved, destroyed or created. This is a subtlety which only occurs in reactive particle based simulation frameworks.

6.6 Conclusion

Using a stochastic particle-based simulation framework, we have investigated the stochastic switching between multistable oscillation modes of the Min system in different three-dimensional compartment geometries. Although it is well known that geometrical constraints have a strong impact on the dynamic oscillations of the Min proteins, multistability and mode switching have only recently been investigated in more detail [162, 167]. Our stochastic framework provides a suitable approach to address the question of oscillation mode selection and stability, since it naturally incorporates fluctuations due to finite copy numbers in the system. This allowed us to address the influence of the three-dimensional shape of the compartment and the boundary conditions, with a close match to existing experimental assays (flat supported bilayers [56, 146], functionalized compartments [55, 147], and cell sculpting [53, 162]). For example, we addressed the role of compartment height and demonstrated the emergence of new oscillation modes with increasing height, underlining the importance of an explicit three-dimensional representation of the system. We also showed that diffusion long the membrane and cooperative recruitment are essential elements for the emergence of Min oscillations. In general, particle-based stochastic computer simulations are a great tool for explorative research and in the future could be used to explore more details of the different scenarios that have been suggested for the molecular mechanisms shaping the Min oscillations [157, 165].

Our simulations demonstrated several features that might be related to the physiolog-

ical function of the Min system in *E. coli*. First we observe that there is a dominating length scale of 5μm, which happens to be the natural length of an interphase *E. coli* cell. Second we found a linear relation between the density of membrane-bound Min proteins and the volume-to-surface ratio, which tends to be constant during growth of *E. coli*. Third we observed that the relative frequency of competing oscillation modes depends on concentration, suggesting that the Min oscillations can be used not only to sense geometry, but also concentration. Fourth, we found that stable oscillations strongly deplete MinE from the bulk. For the future, it would be interesting to study possible feedback between protein production and Min oscillations.

For our simulations, we mainly used the established parameter set A from table 6.1 and achieved excellent agreement with experimental results regarding the relative frequency of the three main oscillation modes in different cell geometries [53]. Again the critical length scale around 5 μm plays an important role in transitions between different regimes, which then are the regions of high bistability. However, we also note that different parameter choices lead to different outcomes and that it would be interesting to perform an exhaustive exploration of parameter space to better understand how robustness and multistability depends on kinetic rates, diffusion constants and concentrations. In the future, such a complete scan might become possible by using GPU-code rather than the CPU-code developed here.

Most importantly, however, our stochastic approach allowed us to measure for the first time the switching rates between different competing oscillation patterns of the Min system. This was done for parameter set A from table 6.1. Interestingly, parameter set C gave similar results in this respect, while parameter set B results in very stable oscillations without switching, in agreement with the experimental observations for the cell sculpting experiments [53]. In the future, it would be interesting to investigate more systematically how the effective barriers between two competing oscillation patterns depend on model parameters and compartment geometry. In general, the Min system is an excellent model system to study not only geometry sensing, but also the role of spatiotemporal fluctuations in molecular systems.

IV

Self-assembly

7 Self-assembly of rings and capsids in hydrodynamic flow

In this chapter we study the self-assembly of rings and capsids. Capsids are protein shells, that viruses use as containers for their genomic material. Many of these capsids show a high degree of symmetry and the spherically shaped ones are often icosahedral protein shells. For those, rings emerge as natural assembly intermediates, which is why we study them here as a build-up to full capsid structures. The monomeric building blocks in virus assembly are called *capsomers*, which are proteins or small protein complexes themselves. However, since the assembly topology is universal, we equally have colloidal self-assembly applications in mind. This extends the scope of this work from virus assembly to synthetic soft-matter physics and colloid science. Therefore we refer to the smallest monomeric assembly units as solute particles in a generic way.

We ask the central question, how non-equilibrium conditions can change the assembly process. Here we use shear-flow to disturb the system and study the assembly process as a function of shear strength. Using forced flow conditions makes it necessary to account for hydrodynamic interactions. A continuum description of the *Navier-Stokes* equation will not account for thermal fluctuations and molecular detail, while full microscopic molecular dynamics (MD) simulations fail to reach the desired length and time scales. So-called mesoscopic simulation techniques try to fill the void between these two extremes. Popular choices are *Lattice-Boltzmann* methods (LB) [183–185], *dissipative particle dynamics* (DPD) [186, 187] or *multiparticle collision dynamics* (MPCD) [188, 189]. We use the latter, which provides us with an explicit solvent representation and hydrodynamic interactions. Multiparticle collision dynamics was pioneered by Malevanets and Kapral and since then successfully applied to study the complex dynamics of many soft-matter systems [190–193]. Here we use a hybrid approach by combining MPCD for the solvent and a MD scheme for the larger solute particles.

7.1 MPCD solvent

In stark contrast to the implicit solvent Brownian dynamics methods from chapter 2, MPCD uses an explicit solvent description. The solvent of the system consists of N_s non-interacting point particles of mass m_0 in a simulation volume $\Omega = L_x \times L_y \times L_z$. These solvent particles are propagated forward in time by the application of alternating streaming and collision steps, which form the core of the MPCD method. Although MPCD employs a fixed time step Δt_s in the streaming part of the algorithm, this fixed time step is not an approximation of a continuous time process, as for common BD or MD methods, and therefore it does not have to be small, for the method to be accurate. This is a peculiarity of multiparticle collision dynamics and implies, that the solvent dynamics are well defined at arbitrary time points.

7.1.1 Streaming and collision step

The position of all N_s solvent particles are updated in each iteration assuming ballistic motion

$$\boldsymbol{r}_i(t + \Delta t_s) = \boldsymbol{r}_i(t) + \Delta t_s \, \boldsymbol{v}_i(t) \,, \tag{7.1}$$

where we use $\boldsymbol{r}_i(t)$ and $\boldsymbol{v}_i(t)$ to denote the position and velocity of the i-th solvent particle at time t. The subsequent collision step will lead to a local momentum exchange due to a stochastic collision rule. At the start of the collision step the full system volume is partitioned into equal-sized cubic collision cells of side length a_0, in which then the collision rule is applied locally. Here we implemented the originally proposed *stochastic rotation dynamics* (SRD) version of MPCD [191, 192], which locally rotates relative particle velocities according to

$$\boldsymbol{v}_{i,\xi}(t + \Delta t_s) = \boldsymbol{u}_\xi(t) + \boldsymbol{\mathcal{C}}(\alpha)\Big(\boldsymbol{v}_{i,\xi}(t) - \boldsymbol{u}_\xi(t)\Big). \tag{7.2}$$

We use ξ to index the collision cells, making $\boldsymbol{v}_{i,\xi}$ the velocity of solvent particle i in grid cell ξ and introduce $\boldsymbol{u}_\xi$ as its center-of-mass velocity

$$\boldsymbol{u}_\xi = \frac{1}{N_\xi} \sum_{i \,|\, \boldsymbol{r}_i \in \mathcal{V}_\xi} \boldsymbol{v}_{i,\xi}. \tag{7.3}$$

Further we introduce N_ξ as the number of solvent particles and $\mathcal{V}_\xi$ as the volume of collision cell ξ. $\boldsymbol{\mathcal{C}}$ is a local collision operator. For the SRD version of MPCD $\boldsymbol{\mathcal{C}}$ is a

standard norm-preserving rotation matrix around a random axis with globally fixed rotation angle α. The rotation axis on the other hand is for each collision cell and for each collision step sampled independently. Uniformly distributed points on the unit sphere $\mathbb{S}^2(1)$ are sampled using Marsaglia's classical algorithm [194].

We will from now on express all quantities in terms of intrinsic natural MPCD units. Therefore we define a characteristic time scale τ_0 and express the MPCD time step Δt_s in units of τ_0. The collision cell length a_0 serves as a unit length measure and the unit mass is set by the mass of a single solvent particle m_0. Energy is expressed in multiples of k_BT and we set $k_BT = 1$ during this chapter.

Solvent initialization

At the beginning of each simulation the N_s solvent particles are randomly distributed within the rectangular simulation box and their velocity is set up to follow a *Maxwell Boltzmann* velocity distribution

$$f_v(v = |\boldsymbol{v}|) = 4\pi\sqrt{\left(\frac{m_0}{2k_BT}\right)^3}\,\boldsymbol{v}^2\,\exp\left(-\frac{m_0\boldsymbol{v}^2}{2k_BT}\right). \tag{7.4}$$

This of course means that the velocity components v_i are individually Gaussian distributed and initialized according to

$$v_i \sim \mathcal{N}(\mu_v = 0, \sigma_v^2) \quad \text{with variance} \quad \sigma_v^2 = \frac{k_BT}{m_0}. \tag{7.5}$$

Grid shifting and ghost particles

The MPCD solvent can violate *Galilean invariance* if the mean free path length of the solvent is small compared to the collision cell length a_0. Ihle *et al.* [195] noticed this problem and suggested to randomly shift the collision cell grid before each collision step. This destroys any correlations and successfully restores *Galilean invariance*. Grid-shifting is realized by globally shifting all collision cells by a randomly chosen position vector $\boldsymbol{s} \in \mathbb{R}^3$, where the components of $\boldsymbol{s}$ are independently sampled from a uniform distribution $s_i \sim U(-a_0/2, a_0/2)$. Using a shifted grid for the sorting step, one typically encounters collision cells which are partially cut by the physical system boundaries. Such cut cells will often contain less solvent particles than the bulk average $\langle N_\xi \rangle =: \gamma$. To fix this density inhomogeneity one introduces so called *ghost particles*, to compensate the missing solvent particles [192]. These particles are in our approach however not

created explicitly, but their velocity statistic is correctly accounted for. If collision cell ξ happens to have $N_\xi < \gamma$ solvent particles, we use

$$\boldsymbol{u}_\xi = \frac{1}{\gamma}\left(\sum_{i\,|\,\boldsymbol{r}_i \in \mathcal{V}_\xi} \boldsymbol{v}_i + \boldsymbol{v}_g\right) \tag{7.6}$$

as new center of mass velocity of collision cell ξ, where $\boldsymbol{v}_g$ is the velocity contribution from the cumulated ghost particles. Since the sum of Gaussians is again Gaussian distributed, we sample the components of $\boldsymbol{v}_g$ from a normal distribution with zero mean and variance $\sigma_g^2 = k_B T(\gamma - N_\xi)/m_0$. This mechanism corrects density inhomogeneities and kicks in during the collision step in equation (7.2), whenever $N_\xi < \gamma$ due to steric constraints.

7.1.2 Simulation of Poiseuille flow

The physical properties of a solvent can be characterized by its transport coefficients such as the solvent's viscosity η and diffusion coefficient D. These macroscopic properties of a solvent can be used to verify a solvent implementation. The application of a pressure gradient in a channel between two parallel walls leads to a parabolic Poiseuille flow profile. The simulation of Poiseuille flow has proven to be an instructive and good test case to verify the MPCD solvent model. The dynamic viscosity η can be decomposed into a kinetic (η_{kin}) and a collisional contribution (η_{col}). For both analytical expressions have been derived [188], which relate these quantities to intrinsic MPCD algorithm parameters

$$\eta_{\text{kin}} = \frac{k_B T \Delta t_s \rho_s}{a_0^3}\left(\frac{5\rho_s}{(4 - 2\cos(\alpha) - 2\cos(2\alpha))\,(\rho_s - 1)} - \frac{1}{2}\right) \tag{7.7}$$

$$\eta_{\text{col}} = \frac{(1 - \cos(\alpha))(\rho_s - 1)}{18 a_0 \Delta t_s}\,, \tag{7.8}$$

where ρ_s is introduced as the number density of the solvent. The parabolic flow profile that emerges in Poiseuille flow can now be described both theoretically and numerically measured in the MPCD solvent. We use this setup to check, that the self-emerging flow profile agrees quantitatively with the theoretically predicted profiles as predicted by equations (7.7) and (7.8). In our MPCD approach we use a setup that is schematically depicted in figure 7.1A, setting two solid walls at $x = 0$ and $x = L_x$, while we apply periodic boundary conditions (PBC) in y and z direction. We can now induce a flow profile by applying a uniform forcing term $\boldsymbol{F}_P = \rho_s g \hat{\boldsymbol{e}}_z$ in z direction, with a gravitational forcing strength g. This added forcing contribution was implemented by using the update

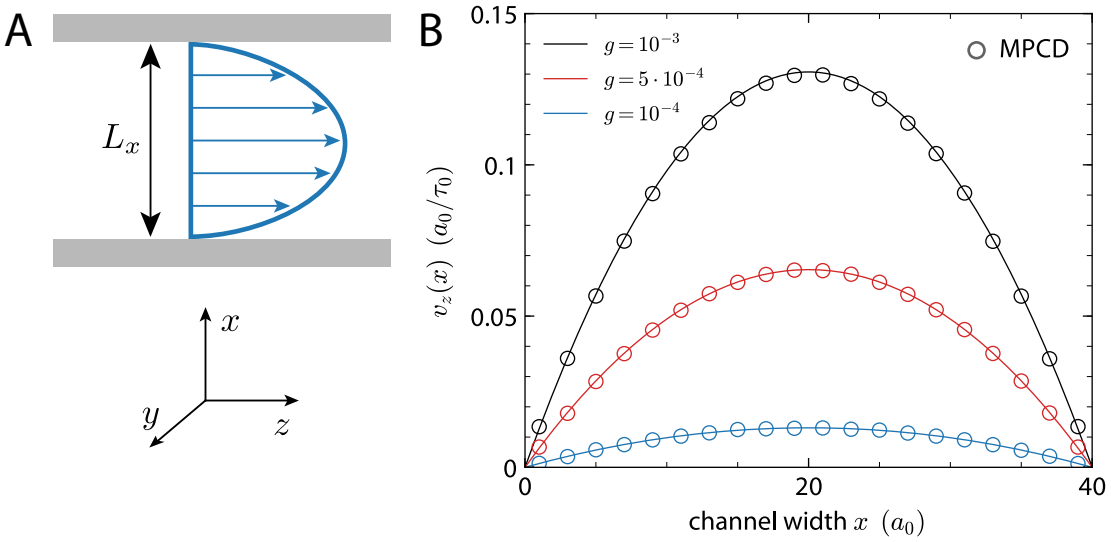

Figure 7.1 | A Poiseuille flow simulation setup. By applying a gravitational forcing strength g in z direction together with no-slip boundary conditions, a parabolic flow profile emerges. **B** Measured and theoretically predicted Poiseuille flow velocity profiles in a rectangular channel of width $L_x = 40\, a_0$. The results shown are obtained for the standard SRD MPCD algorithm, using a rotation angle $\alpha = \pi/2$ and time step $\Delta t_s = 3.476\, \tau_0$. The three different parabolic profiles correspond to three different external forcing strengths g, as indicated in the figure legend. The solid lines are no fit, but the parameter free theoretical predictions according to equation (7.7), (7.8) and (7.11).

scheme

$$\boldsymbol{r}_i(t + \Delta t_s) = \boldsymbol{r}_i(t) + \Delta t_s\, \boldsymbol{v}_i(t) + \frac{1}{2}\Delta t_s^2 g \hat{\boldsymbol{e}}_z \tag{7.9}$$

$$\boldsymbol{v}_i(t + \Delta t_s) = \boldsymbol{v}_i(t) + \Delta t_s g \hat{\boldsymbol{e}}_z \tag{7.10}$$

for the streaming step instead of equation (7.1). We additionally apply no-slip boundary conditions at the channel walls, such that the parabolic flow profile will be self-emerging. For our MPCD approach here we implemented no-slip boundaries by using a so-called *bounce-back rule*, which inverts solvent velocities if they hit a hard wall. The parabolic flow profile is given by

$$v_z(x) = \frac{\rho_s g}{2\eta} x(L_x - x)\,, \tag{7.11}$$

with a maximal velocity amplitude

$$v_0 = v_z(x = L_x/2) = \frac{\rho_s g L_x^2}{\eta} \tag{7.12}$$

at the center of the channel. For a given set of MPCD simulation parameters we can now either use equations (7.7)–(7.8) to get an analytical prediction for the velocity

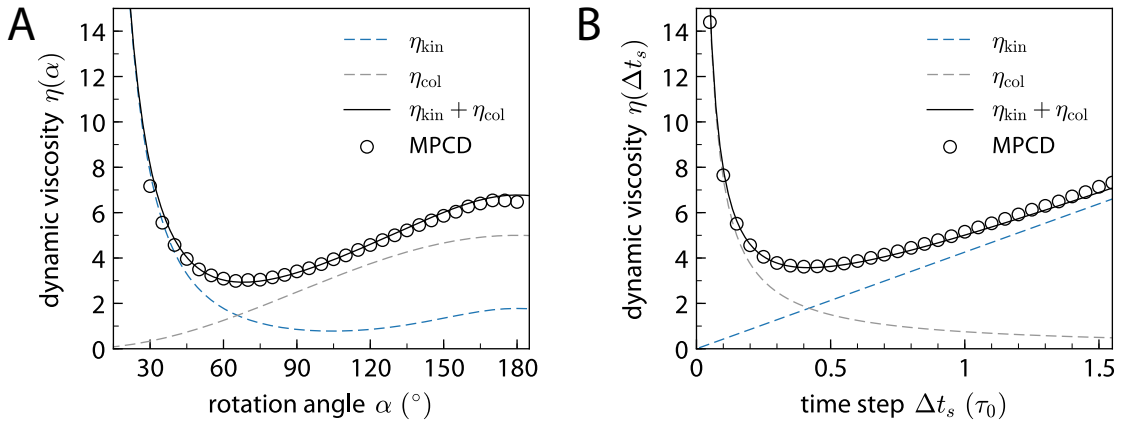

Figure 7.2 | Dynamic viscosity η as a function of the rotation angle α and the MPCD time step Δt_s. **A** shows both measured and theoretically predicted solvent viscosities for $\Delta t_s = 0.2\,\tau_0$ **B** Dynamic viscosity as a function of the time step Δt_s for $\alpha = 120°$. In both cases $\gamma = 10$, $k_B T = 1$ and $g = 0.001$ were used. The dashed lines show the individual contribution from the kinetic and collisional viscosities, respectively. All data were obtained using the SRD MPCD version with grid-shifting and with ghost particles.

profile, or measure it in a simulation and extract the viscosity by fitting equation (7.11). Figure 7.1B shows both the analytical predictions and measured velocity profiles for three different forcing strengths g and we find them to be in very good agreement. Here the solid lines are not obtained from a fit, but they are the analytical prediction for $v_z(x)$ according to equation (7.11). A systematic evaluation of the dynamic viscosity as a function of both the rotation angle α and the MPCD time step Δt_s is shown in figure 7.3. These results show clearly how the intrinsic MPCD parameters can be used to set the solvent's transport properties. Not only is the simulation of Poiseuille flow a good way to test the solvent model, but it also demonstrates the clear strength of this simulation method. The forced flow profiles are not externally imposed but purely self-emerging by the right choice of boundary conditions.

7.1.3 Simulation of shear flow

We used Poiseuille flow to test the transport properties of the pure MPCD solvent. Now we explain how to induce shear flow which we will then apply to our self-assembly setup. To create a linear flow profile we consider again two planar walls at $x = 0$ and at $x = L_x$. We keep the bottom wall fixed and move the upper wall at $x = L_x$ while we apply periodic boundary conditions in all remaining directions. For the fixed lower wall we apply no-slip boundary conditions by using the bounce back rule $\boldsymbol{v}' = -\boldsymbol{v}$, where the prime denotes the solvent velocity after a wall collision. For the upper moving wall we effectively do the same, but in the reference system of the moving wall. The update

rule for solvent particles that hit the moving wall then reads

$$\boldsymbol{v}' = -\Big(\boldsymbol{v} - \boldsymbol{v}_{\text{wall}}\Big) + \boldsymbol{v}_{\text{wall}} \,, \tag{7.13}$$

where $\boldsymbol{v}_{\text{wall}} = v_s \, \hat{\boldsymbol{e}}_z$ and v_s denotes the shear velocity. Additionally we update the ghost particle rule for the moving wall in such a way, that the velocity of a single ghost particle is now sampled from a normal distribution with mean velocity $\mu_g = v_s$. This choice of boundary conditions leads to self-emerging linear flow profiles.

7.2 Solute-solvent coupling

We proceed with the coupling scheme between solute particles and the previously described and tested MPCD solvent. Since we use a patchy particle model for the self-assembling solute particles, we must find a coupling which resolves not only the translational but also the rotational diffusive motion of the embedded solute particles. We use a method that is referred to as *boundary condition solutes*, because it treats solutes as hard boundaries for the solvent particles and couples the two by explicit linear and angular momentum exchange. In particular the angular momentum exchange is essential for our purpose. Patchy particle models are a popular choice to model anisotropic reactivity and require all angular degrees of freedom. We follow a coupling method for solutes which was suggested by Padding *et al.* [196] and Nikoubashman *et al.* [197]. In the streaming step of the algorithm we check for collisions between solvent and solute particles and resolve them by calculating the collision points. Then the particle velocities and positions are updated according to a collision rule and momentum is exchanged. Since the calculation of exact collision points can even for spheres become computationally expensive, we use an approximate method by Padding *et al.* [196]. We demonstrate this collision rule by assuming that a given solvent particle i happens to overlap with a solute after the last streaming step was carried out. The solvent particle's position before this last streaming step was $\boldsymbol{r}_i$ and the overlap position is $\boldsymbol{r}_i'$. We resolve collisions of this kind by approximating the true collision point $\boldsymbol{r}_i^{\text{c}}$ with

$$\tilde{\boldsymbol{r}}_i^{\text{c}} = \boldsymbol{R} + R \frac{(\boldsymbol{r}_i' + \boldsymbol{r}_i)/2 - \boldsymbol{R}}{|(\boldsymbol{r}_i' + \boldsymbol{r}_i)/2 - \boldsymbol{R}|} \,, \tag{7.14}$$

where $\boldsymbol{R}$ and R are the solute position and radius, respectively. This resets the solvent particle's position to the surface of the solute. The new updated velocities are now randomly sampled, which models surface roughness on a microscopic level (a detailed discussion of this issue is found here [196, 198]). This random deflection is considered

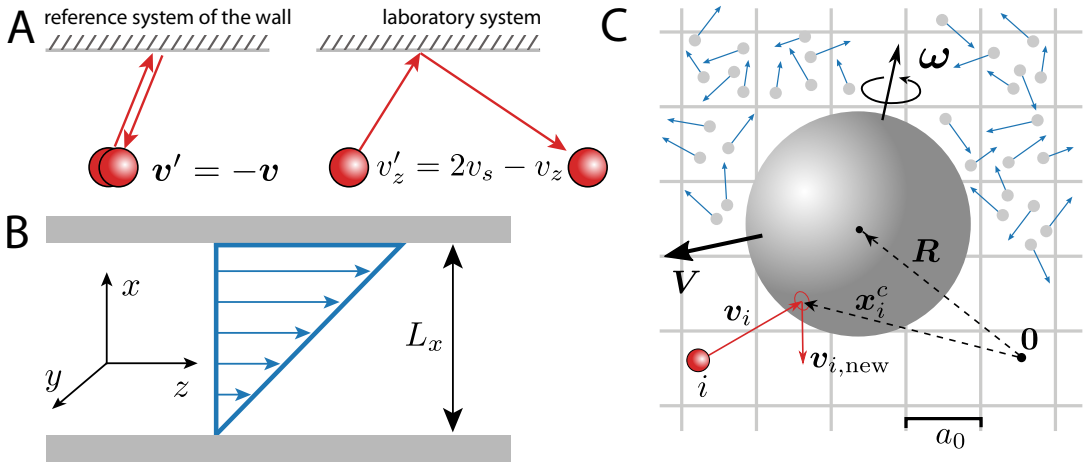

Figure 7.3 | **A** Application of a bounce-back rule creates no-slip boundaries and establishes linear flow profiles for moving walls. **B** Simulation setup for shear flow in a channel between two walls at $x = 0$ and $x = L_x$. **C** Schematic depiction of the solvent-solute coupling. A solute particle with velocity $\boldsymbol{V}$ and angular velocity $\boldsymbol{\omega}$ is embedded in a MPCD solvent. Collision events of solvent particles are resolved through exchange of linear and angular momentum. The small particles in the background represent the MPCD solvent particles, sorted in collision cells (not drawn to scale). The colliding red solvent particle is enlarged to put a focus on collision events.

by decomposing the deflected solvent particle velocities into a tangential ($v_{i,t}$) and a normal ($v_{i,n}$) component, which are sampled from the two probability distributions

$$p(v_{i,t}) = \sqrt{\frac{m_0}{2k_BT}} \exp\left(-\frac{m_0 v_{i,t}^2}{2k_bT}\right) \quad \text{and} \quad p(v_{i,n}) = \frac{m_0 v_{i,n}}{k_BT} \exp\left(-\frac{m_0 v_{i,n}^2}{2k_BT}\right). \tag{7.15}$$

The collision event is concluded by updating both the solvent and solute particle velocities according to

$$\boldsymbol{v}_i' = \boldsymbol{V} + \boldsymbol{\omega} \times \left(\tilde{\boldsymbol{r}}_i^{\text{c}} - \boldsymbol{R}\right) + v_{i,n}\hat{\boldsymbol{e}}_n + v_{i,t}\hat{\boldsymbol{e}}_t \tag{7.16}$$

$$\boldsymbol{V}' = \boldsymbol{V} - \frac{m_0}{M}(\boldsymbol{v}_i' - \boldsymbol{v}_i) \tag{7.17}$$

$$\boldsymbol{\omega}' = \boldsymbol{\omega} - \frac{m_0}{I}\left(\tilde{\boldsymbol{r}}_i^{\text{c}} - \boldsymbol{R}\right) \times \left(\boldsymbol{v}_i' - \boldsymbol{v}_i\right). \tag{7.18}$$

Here primed quantities denote post-collision quantities and M and I are the solute particle's mass and moment of inertia $I = 2MR^2/5$. $\hat{\boldsymbol{e}}_{t,n}$ are tangential and normal unit vectors in the local reference frame of the collision point. We verified this coupling scheme by performing numerous tests to ensure that a single solute particle shows the right diffusive properties. For this purpose we checked that the normal diffusion follows

the Stokes-Einstein relation

$$D = \frac{k_B T}{6\pi\eta R} \tag{7.19}$$

and also calculated normal and angular velocity autocorrelation functions. We tested their quantitative agreement with analytical approximations from Enskog kinetic gas theory and hydrodynamic mode coupling approaches [196].

7.3 Solute interactions & assembly model

Our assembly model is based on a capsid model by Hagan *et al.* [199], which in turn was inspired by the *local rules* approach from Schwartz *et al.* [200]. The key idea of *local rules* is to put specific interaction sites on solute particles, which mediate interactions between them. Then the angular arrangement of these interaction sites encodes the assembly target structure, *i.e.* the local (patch) configuration determines the global structure. As an intermediate step towards full capsid assembly we first focus on self-assembly of rings as assembly intermediates.

7.3.1 WCA repulsion

For the repulsive interaction between two solute particles we chose the Weeks-Chandler-Anderson (WCA) potential [201]. This is a truncated and by the potential depth ε upwards shifted Lennard Jones potential giving rise to a purely repulsive interaction. The potential depends only on the distance R of an interacting particle pair and is given by

$$V_{\mathrm{WCA}}(R) = \begin{cases} 4\varepsilon\left[\left(\frac{\sigma}{R}\right)^{12} - \left(\frac{\sigma}{R}\right)^{6} + \frac{1}{4}\right] & \text{for} \quad R < 2^{1/6}\,\sigma = R_c \\ 0 & \text{for} \quad R \geq 2^{1/6}\,\sigma. \end{cases} \tag{7.20}$$

The potential depth is set by the energy parameter ε and σ marks the characteristic length scale of the potential, which is the length at which the canonical Lennard Jones potential vanishes identically $V_{\mathrm{LJ}}(\sigma) = 0$. For the WCA potential this hence means $V_{\mathrm{WCA}}(\sigma) = \varepsilon$ (see figure 7.4A). The piecewise definition of the WCA potential in equation (7.20) already introduces the critical cutoff distance

$$R_c = 2^{1/6}\,\sigma\,, \tag{7.21}$$

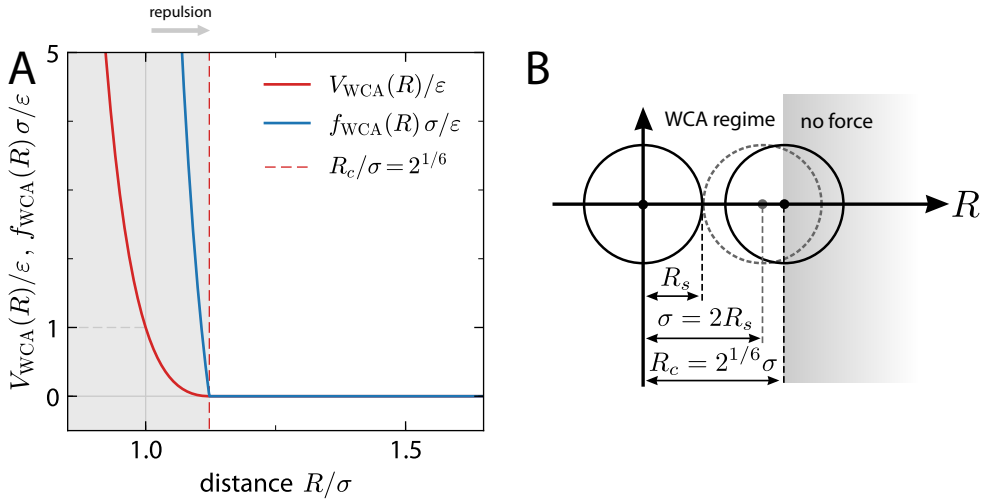

Figure 7.4 | Repulsive particle interactions. **A** shows the WCA potential V_{WCA} (red line) and the resulting force magnitude f_{WCA} in reduced dimensionless form. The WCA is a shifted and truncated Lennard Jones potential, giving rise to a purely repulsive interaction. The light gray shaded region indicates all distances up to the cutoff distance R_c after which two particles stop feeling each other. **B** illustrates the cutoff regime of the above specified WCA potential when using $\sigma = 2R_s$ as characteristic length scale of the potential. We use R to express the distance between two solute particles and R_s to denote the radius of the solute particles.

which defines the critical inter-particle distance up to which two particles see each other *via* this potential here. We use the WCA potential for volume exclusion, hence the radial distance R will be the center-to-center distance $R_{ij} = |\boldsymbol{R}_i - \boldsymbol{R}_j|$ for the repulsive interaction between the i-th and the j solute particle. The repulsive force $\boldsymbol{F}_i$ that is exerted on the i-th particle due to the WCA interaction is calculated by taking the gradient with respect to the i-th particle coordinates

$$\boldsymbol{F}_i = -\nabla_{\boldsymbol{R}_i} V_{\mathrm{WCA}}(R_{ij}) = -\frac{\partial}{\partial \boldsymbol{R}_i} V_{\mathrm{WCA}}(R_{ij}) = f_{\mathrm{WCA}}(R_{ij})\,\frac{\boldsymbol{R}_{ij}}{R_{ij}}. \tag{7.22}$$

We set the characteristic length scale σ equal to the solute particle diameter $\sigma = 2R_s$. The implications of this particular choice are depicted in figure 7.4B. This means that the characteristic WCA length scale σ signifies the inter-particle distance at which two solutes are exactly in contact. With this choice the cutoff distance R_c becomes $R_c = 2^{7/6}\,R_s$.

7.3.2 Attractive pair potentials and patch configurations

For the first self-assembly part we study the self-assembly of pentameric rings. The ring structure can be encoded into solute monomers by decorating them with two patches on their surface as it is shown in figure 7.5. The attractive interactions can then lead to

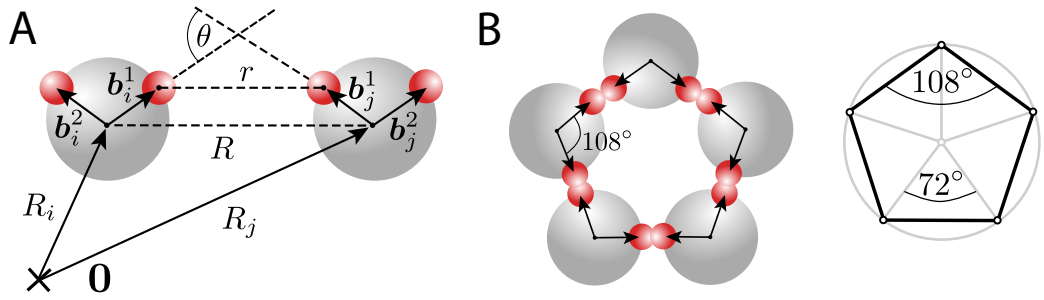

Figure 7.5 | A Patch geometry for pentameric ring self-assembly. Patch distance r and bond angle θ determine the attractive steering towards bond formation. **B** Schematic depiction of the patch configurations for a fully assembled pentameric ring with $\alpha = 108°$.

bond formation. We use bond vectors $\boldsymbol{b}_i^{(k)}$ to denote the k-th interaction patch of the i-th solute particle. Pentameric ring assembly requires the two patches of a single solute particle to be in an equatorial plane with an opening angle $\alpha := \sphericalangle(\boldsymbol{b}^1, \boldsymbol{b}^2)$. For general regular n-sided polygons this angle is given by

$$\alpha_n = \left(\frac{n-2}{n}\right)\pi\,, \tag{7.23}$$

which gives $\alpha_5 = 3\pi/5 = 108°$ for regular pentagons. Here n is of course also the number of monomers that constitute a full ring.

The attractive potential will be determined based on the distance and orientational alignment between two patches from distinct solutes. We use r to denote the patch distance and θ for the primary bond angle. In our assembly model any patch from a given solute can interact with any other patch from any other solute particle in the system. For a given interacting patch pair, we refer to their mutual angle as the primary bond angle θ. From the perspective of this pair, the alignment of the secondary patches will then be accounted for by the secondary dihedral angle φ. For the force and torque calculations due to a given patch configuration, we must now express both angles in terms of the bond vector geometry. For a given solute pair (i, j) they read

$$\theta_{ij} = \arccos\left(-\frac{\boldsymbol{b}_i^1 \cdot \boldsymbol{b}_j^1}{b^2}\right) \quad \text{and} \tag{7.24}$$

$$\phi_{ij} = \arccos\left(-\frac{\left(\boldsymbol{R}_{ij} \times \boldsymbol{b}_j^2\right)\cdot\left(\boldsymbol{b}_i^2 \times \boldsymbol{R}_{ij}\right)}{|\boldsymbol{R}_{ij} \times \boldsymbol{b}_j^2|\;|\boldsymbol{b}_i^2 \times \boldsymbol{R}_{ij}|}\right)\,, \tag{7.25}$$

where $b = |\boldsymbol{b}|$ is the bond vector length and $\boldsymbol{R}_{ij} = \boldsymbol{R}_i - \boldsymbol{R}_j$.

As a function of these coordinates we now specify the attractive potential $V_{\text{attr},i} =$

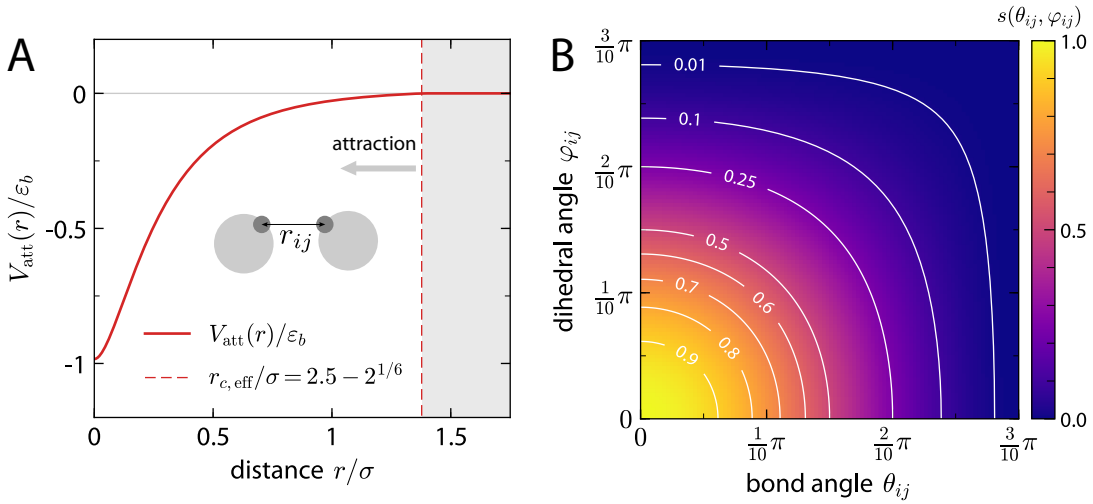

Figure 7.6 | A Radial component $V_{\mathrm{attr}}(r)$ of the attractive potential as a function of the inter-patch distance r. The minimal energy configuration of $-\varepsilon_b$ is attained for $r = 0$. **B** The switching function $s(i, j)$ accounts for the angular alignment of two patches. Both primary and secondary angles are defined to be zero for perfect patch alignment.

$V_{\mathrm{attr},i}(r)\, s(i, j)$ as a product of a purely radial and an angular component, with

$$V_{\mathrm{attr}}(r) = 4\varepsilon_b \left[\left(\frac{\sigma}{r + 2^{1/6}\sigma} \right)^{12} - \left(\frac{\sigma}{r + 2^{1/6}\sigma} \right)^{6} - \left(\frac{\sigma}{r_c} \right)^{12} + \left(\frac{\sigma}{r_c} \right)^{6} \right] \tag{7.26}$$

for $r + 2^{1/6}\sigma < r_c$ and $V_{\mathrm{attr}}(r) = 0$ elsewhere. Here r_c is the attractive potential cutoff length. The angular specificity comes from the switching function $s(i, j)$ [199]

$$s(i, j) = \frac{1}{4} \left(\cos\left(\frac{\theta_{ij}}{\theta_m} \right) + 1 \right) \times \left(\cos\left(\frac{\varphi_{ij}}{\varphi_m} \right) + 1 \right), \tag{7.27}$$

where θ_m and φ_m are cutoff angles beyond which the attractive potential also vanishes identically. This switching function continuously varies from 0 to 1 and thus controls the interaction strength from the radial contribution in dependence of the degree of angular alignment. Figure 7.6 shows both the purely radial contribution (A) and the switching function s (B) independently as a function of the relative patch coordinates. We used the same characteristic length scale σ as for the repulsive WCA potential but defined an independent potential strength ε_b for the attractive part as shown in equation (7.26).

The above described solute-solute pair interactions are then finally summed up to a

Parameter	Value	Description
m_0	1	solvent mass
a_0	1	collision cell unit length
$\Delta t_s/\tau_0$	0.1	MPCD time step
α	130°	MPCD rotation angle
L_x, L_y, L_z	$20\,a_0$	simulation box dimensions
N_s	80000	number of solvent particles
γ	10	avg. # of solvent particles per collision cell
R_s/a_0	2	solute radius
σ/a_0	2	characteristic potential length scale
b/σ	$2^{1/6}$	bond vector length
R_c/σ	$2^{1/6}$	WCA cutoff length
r_c/σ	2.5	attractive potential cutoff length
ε/k_BT	20	WCA potential depth
ε_b/k_BT	60	attractive potential depth
θ_m	$0.2\,\pi$ – $0.3\,\pi$	bond (primary) angle cutoff
φ_m	$0.2\,\pi$ – $0.3\,\pi$	dihedral (secondary) angle cutoff
$\Delta t_{MD}/\Delta t_s$	1/10	MD time step

Table 7.1 | Parameter settings that were used for the solvent and solute model for the self-assembly assay. The upper half is used to specify the MPCD solvent, while the lower part specifies the solute particle model.

total force and torque

$$\boldsymbol{F}_i = -\frac{\partial V}{\partial \boldsymbol{R}_i} \tag{7.28}$$

$$\boldsymbol{\tau}_i = -\sum_k \boldsymbol{b}_i^{(k)} \times \left(\frac{\partial V}{\partial \boldsymbol{b}_i^{(k)}}\right) , \tag{7.29}$$

where the summation for the torque calculation runs over the primary and secondary patch configurations as shown in figure 7.5A. We integrate the equations of motion for the solute particles by a standard molecular dynamics (MD) integrator, which is coupled to the MPCD solvent algorithm in a hybrid way [189]. The MD integration iterates on a second timescale with a higher temporal resolution

$$\Delta t_{MD} = \frac{1}{10}\Delta t_s\,, \tag{7.30}$$

which is used to integrate the solute dynamics in alternation with the solvent MPCD algorithm. Table 7.1 lists the used parameter settings of both the MPCD solvent and the solute model which we use for the following self-assembly part.

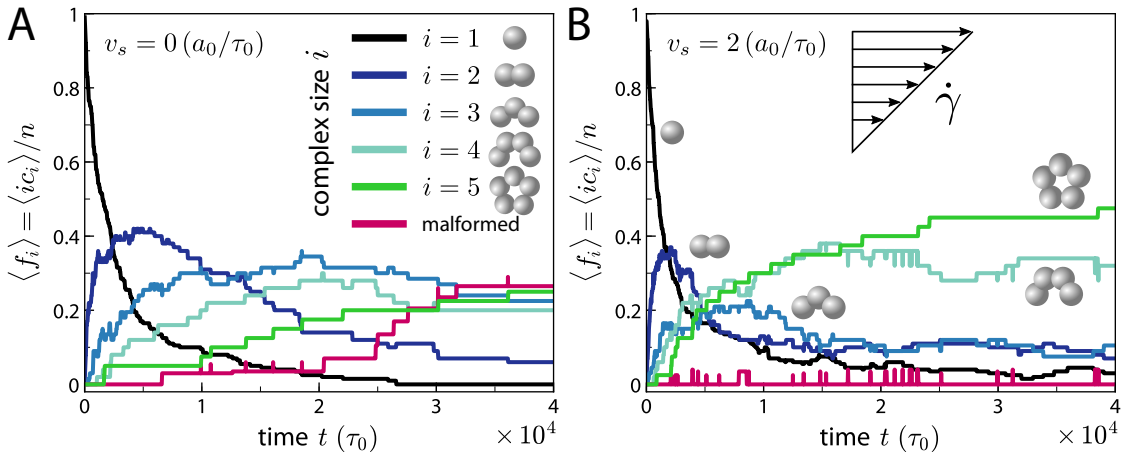

Figure 7.7 | Shear enhanced self-assembly of pentameric rings. Both figures show time traces of different sized complexes. **A** shows the assembly process without and **B** with shear flow. In both cases we used $\theta_m = \varphi_m = 0.2\,\pi$ and $v_s = 0$ (no flow) in **A** and $v_s = 2\,a_0/\tau_0$ in **B**. The trajectories show the ensemble averaged results over independent simulation runs.

7.4 Self-assembly of rings

The general idea of this setup is to learn how non-equilibrium conditions influence the assembly process. Additionally we want to understand how our model parametrization helps or prevents successful assembly. The cutoff values of the interaction potentials control how loosely or how tightly the assembly process is regulated. Using computer simulations for the analysis of self-assembly processes has the additional advantage, that we can always follow all intermediate stages of the complex process at any desired resolution. The first assembly example monitors the transient assembly process of pentameric ring assembly with and without shear flow. Figure 7.7 shows the transient traces of all complex sizes for both scenarios. The results are shown as normalized fractional quantities, where

$$\langle f_i \rangle = \langle ic_i \rangle / n \tag{7.31}$$

shows the fraction of all particles that are in complexes c_i of size i with a total of n monomers in the system.

7.4.1 Flow enhanced assembly properties

The transient traces in figure 7.7 show some hallmarks of self-assembly processes. We observe a monotonous decay of monomers, while we sequentially observe peaks of intermediate sized-complexes appear, which eventually decay as the fraction of particles in

the target structure reaches steady state. Since we use a potential based approach, the assembly structures are not rigid aggregates but have sufficient degrees of freedom to form malformed structures. Although malformations correspond to local energy minima, they can be attained due to steric or non-equilibrium constraints that we can now control in this setup. For pentameric ring assembly we consider all closed rings which are not pentameric or all aggregates of any size which cannot lead to pentameric rings due to kinetic traps as malformed. We note three key observations.

1) Enhanced assembly speed to due flow
From comparing figure 7.7A to 7.7B we see, that the slope of complexes of size four and five has a much steeper onset, which speaks for an accelerated assembly process.

2) More dynamic assembly processes
In a tranquil solvent we rarely observed a closed bond break. This changes in the presence of flow, which leads to more dynamic rearrangement. This is also visible in the time trace of the monomer fraction of figure 7.7B, which is not monotonously decaying, but shows slight variations. The more an assembly process can be made dynamic, the more it is generally speaking unlikely to suffer from kinetic trapping of malformed assembly intermediates. This might be an interesting strategy that can help avoiding kinetic traps for other self-assembly scenarios.

3) Enhanced assembly yield and suppression of malformed structures
If we examine the fraction of pentameric rings and the fraction of malformed complexes for both cases we clearly observe that flow can be used to suppress malformation. Not only this, but also the fraction of pentameric rings has significantly increased in the presence of flow.

7.4.2 Suppression of malformed complexes

Now we look at a second experiment where we increase the cutoff angles to $\theta_m = \varphi_m = 0.3\,\pi$ and vary the shear strength systematically. Now we focus on the dynamic interplay between shear flow, assembly yield and the emergence of malformed complexes. For this reasons we monitor 4-, 5-, and 6-rings and additionally helical structures. All these aggregates apart from the pentameric 5 rings are considered malformations, since they are trapped states that cannot escape local energetic potential minima. Figure 7.8 shows the time traces of these structures for four different shear velocities and 7.8E shows the steady state fractions as a function of shear velocity.

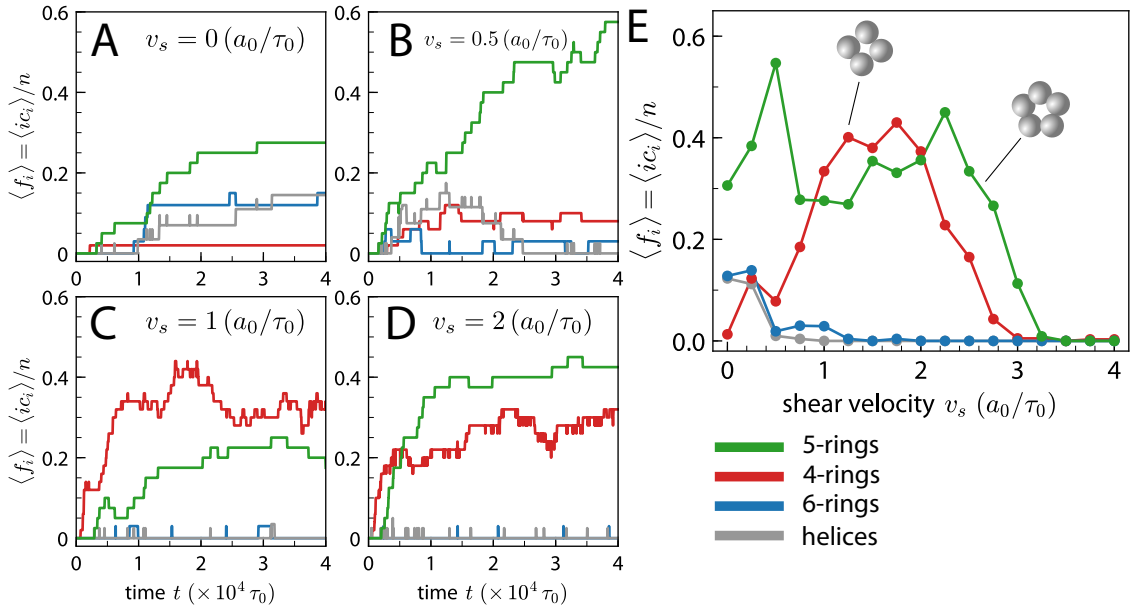

Figure 7.8 | Dynamic interplay between shear strength and malformed complex assembly. **A**–**D** shows time traces for 4-,5-,6-rings and helical structures four different shear velocities v_s. **E** Steady state yields as a function of shear velocity v_s. In all cases we used $\theta_m = \varphi_m = 0.3\,\pi$.

In the absence of flow (7.8A), complexes of all types increase monotonically until they reach steady state. Our intuitive understanding of this observation is that the increased cutoff angles open up the configurational degrees of freedom, which facilitates malformations. For this setup the bond strength seems too high to allow frequent bond breaks. This means that any formed bond will not be able to dynamically rearrange to get out of a malformation. If we now increase the shear strength we first observe that 6-rings and helical structures are very effectively suppressed, which can be explained on the basis, that the configurational phase space can now be more effectively probed. The forced flow becomes sufficiently strong to shift malformed complexes out of local energetic minimal configurations.

Comparing figure 7.8A with 7.8B we also notice an increase in the assembly yield of the desired pentameric target structure, similar to the previous observation in figure 7.7. However, if we further increase shear strength, we can strikingly enhance 4-ring formation (see figure 7.8C). This effect is only observed for a intermediate regime of shear velocities as figure 7.8E indicates. Increasing the shear strength even further, we switch back to the intuitive behavior and push the fraction of malformed 4-rings below the pentameric fraction. The details of this intricate interplay are given in figure 7.8E. Here we observe two key elements. While any flow at all suppresses larger malformed complexes, intermediate flow can enhance 4-ring closure. The increased fluctuations balance the energy penalty of the malformed complexes. This effect happens in a specific

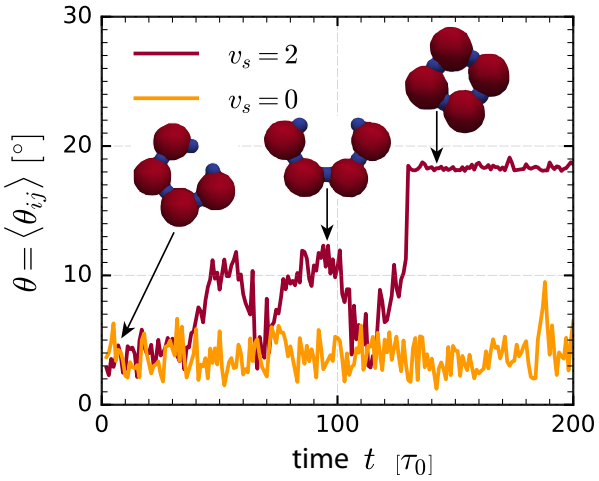

Figure 7.9 | Time course of absolute angular deviation of the mean bond angle $\theta = \langle \theta_{ij} \rangle$ from the ideal pentagonal angle during 4-ring closure.

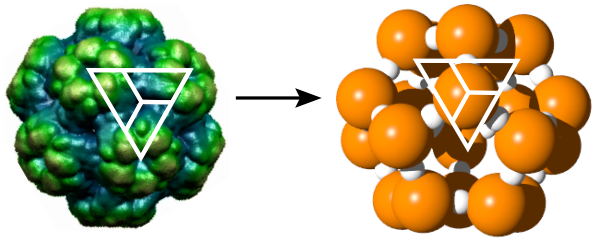

Figure 7.10 | Coarse-grained representation of a virus capsid. **A** shows an X-ray reconstruction of a Brome mosaic virus (taken from the VIPERdb [73]) **B** Capsid model that we use in this self-assembly study. We use spherical capsomers which can assemble into pentameric rings. Twelve pentameric rings make up a complete $T = 1$ capsid with icosahedral symmetry.

shear velocity regime of intermediate shear velocities. Beyond this the target assembly yield increases again until no assembly is possible in the very high shear limit, where eventually all bonds are broken constantly.

Figure 7.9 illustrates how in a certain shear regime we observe shear-assisted four ring formation. It shows how the angular deviation of a 4-ring jumps to a plateau value which it attains in its configuration of a 4-ring, an effect which we only observe to be stable in this flow regime.

7.5 Self-assembly of capsids

7.5.1 Capsid model

Since we are primary interested in the general assembly properties of capsid structures, we here study a simple capsid model as an approximation to an actual $T = 1$ capsid [202]. For more details about coarse-grained capsid we refer to [203]. We use a representation where the monomeric building blocks, the capsomers, correspond to three proteins, such that a full $T = 1$ capsid is made up out of 20 capsomers containing $n = 60$ proteins. We then use our spherical solute particles to represent a single capsomer. In this way a full capsid is made up of twelve pentagons and no hexameric structures. Since our previous ring self-assembly assay stopped at ring formation, we need to introduce a third patch per capsomer/solute particle. Since our capsid model is composed solely of pentagonal rings, every primary bond angle in its final configuration is the $\alpha_5 = 108°$ angle from the regular pentagon. To take the new angular configuration of a third patch into account, we must modify the angular component of the attractive potential. The radial contribution stays unchanged since it only considers the inter-patch distance of a given pair of patches, regardless of secondary and now also tertiary angular constraints. The switching function s however must now be altered to

$$s(i,j) = \frac{1}{8}\left(\cos\left(\frac{\theta_{ij}}{\theta_m}\right)+1\right)\times\left(\cos\left(\frac{\varphi_{ij}^{23}}{\varphi_m}\right)+1\right)\times\left(\cos\left(\frac{\varphi_{ij}^{32}}{\varphi_m}\right)+1\right). \tag{7.32}$$

Here we introduce φ_{ij}^{23} as the angle between the secondary patch of solute i and the tertiary patch of solute j, and φ_{ij}^{32} conversely as the angle between the tertiary patch of solute i and the secondary patch of solute j. Care must be taken to numerate patches consistently.

7.5.2 Results

Now we have all ingredients to observe the assembly dynamics for full capsids with and without shear flow. Figure 7.11 shows time traces of the assembly process for four different shear velocities v_s, where we again used $\theta_m = \varphi_m = 0.2\,\pi$. Interestingly we observe similar assembly characteristic as for the previously studied ring assembly. The comparison of figure 7.11A to 7.11B shows, how the slope of many intermediate sized complexes is significantly steeper and rises faster. We believe that this accelerated assembly is possible due to a faster sampling of the full configurational phase space.

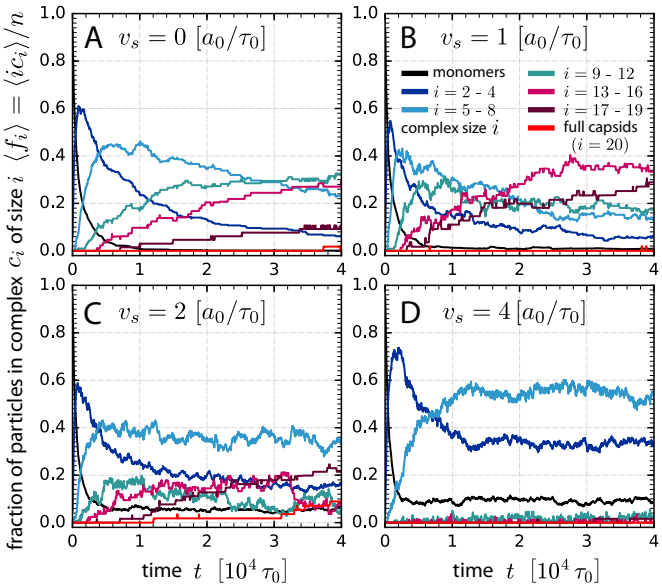

Figure 7.11 | Capsid self-assembly with and without shear flow. **A** shows transient assembly trajectories with no flow present. In **B** – **D** we increased the shear velocity stepwise from $v_s = 1$ to $v_s = 4\,a_0/\tau_0$.

Secondly, we observe a more dynamic assembly process as soon as we apply shear flow. This is clearly visible since the trajectories with shear flow in the system show much more pronounced fluctuations, which must stem from multiple bond breaking events. This increased dynamic rearrangement is a useful mechanism to avoid kinetic traps. And finally we observe that we can find an optimal shear flow regime which helps to enhance the assembly yield of capsids. We show this effect in 7.11C, where this applied flow velocity helps to increase the capsid assembly yield. We believe that this is ensured due to an optimal monomer supply. The role of monomer supply or reversely the fate of monomer starvation for self-assembly problems is well acknowledged, and the role of constant monomer supply for viral capsid assembly has been previously studied by Boettcher *et al.* [204]. Figure 7.12 shows a snapshot of the simulation box where we highlighted a complete capsid in darker colors.

7.6 Concluding remarks

We conclude that in our setup for ring and capsid self-assembly, optimal flow conditions can help to accelerate the assembly process, increase the target yield and suppress malformation. This is however strongly depending on the precise settings and on the strength of the forced flow that is applied. We believe that the use of an hybrid MPCD-MD scheme is a versatile tool to study self-assembly processes such as ring and capsid

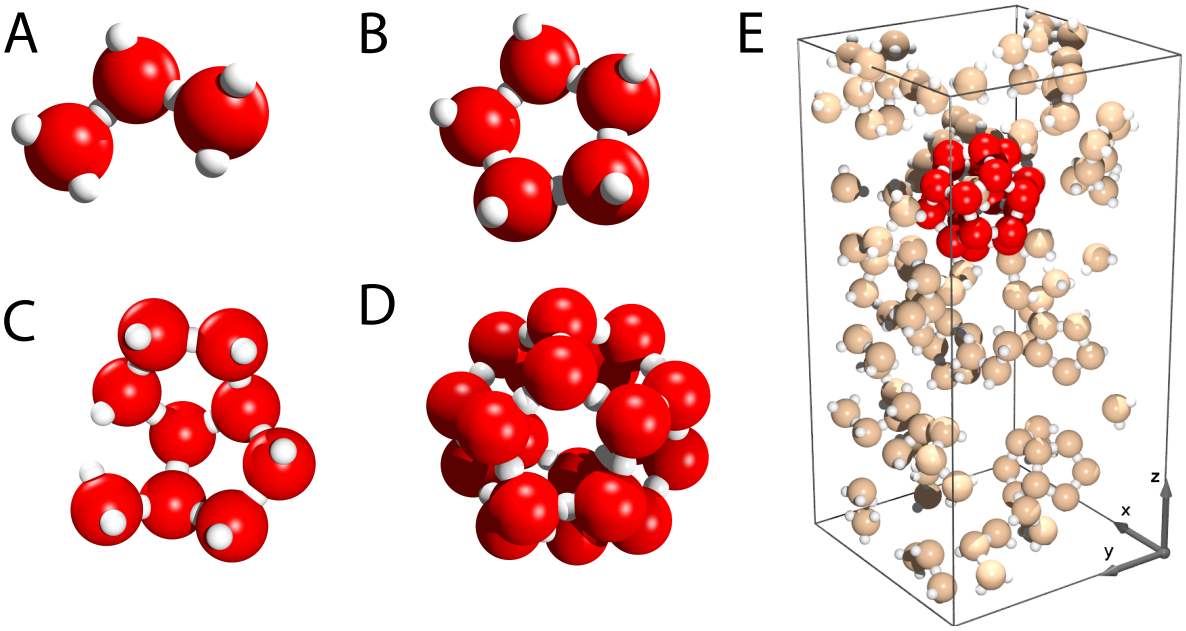

Figure 7.12 | Different stages of capsid assembly. **A**-**D** show different intermediate complexes. **D** shows a simulation snapshot of a box where we observe a completed capsid shell.

formation. The possibility to study the effect of forced flow while having hydrodynamic resolution, is to our mind a very useful tool, which should be continued to shed further light on more complex self-assembly systems. In particular the role of templated or scaffolded assembly might be interesting future extensions.

8 Conclusion

We started this thesis with a focus on particle-based methods for reaction-diffusion dynamics in biological systems. Realizing the fast leap forward on the experimental side, for example by the application of super-resolution techniques in the life sciences, particle-based methods are an ideal complementary tool. They can shed light on new molecular mechanisms and fill gaps, that experiments cannot yet resolve. Additionally, they can be used to test and verify important assumptions about the underlying physical nature of all biological processes. In this role particle-based tools can both confirm existing theories and be used in an explorative way to predict missing links, that help to deepen our mechanistic understanding of relevant biological problems.

In chapter 2 we discussed several approaches that consider biochemical reactions on a single particle level and used different Brownian dynamics methods, which implement biochemical reactions on different levels of molecular detail. An important part of understanding a given problem is the selection of the appropriate tools. In this manner, we contributed to establish different methods with different application strengths and demonstrated several rigorous tests to illustrate how they work. Since molecular reaction events are intrinsically stochastic, these tools are a perfect match to address the role of fluctuations and spatial correlations in biological systems.

The first biological system that we studied in depth was type I interferon signaling. That cells use molecular signals to coordinate the immune response, is a widely acknowledged fact. However, the physical details, of how these complex cellular communication tasks work so seamlessly hand in hand, remain to our perception still highly elusive. The fact that the type I interferon system uses many structurally similar ligands to trigger various different cellular responses is a very puzzling phenomenon. Since all of these ligands share a single receptor pair, we focused on the receptor dynamics of this particular system. In chapter 3 we analyzed the binding modes of different ligand-receptor models and discussed their implications for the problem of ligand discrimination in detail. Curiously, already the equilibrium binding analysis turned out to offer a tuning valve that cells can exploit to perform robust signal recognition. Since receptor dimerization by ligand-induced cross-linking is a common motif in cellular signal transduction, in

particular for receptor tyrosine kinases (RTK), we expect that these results might have equal implications for other receptor systems that share a common binding topology. We complemented these findings by an information theoretic approach in chapter 4. In our perception it suggested itself to go into this direction, since we were driven by the idea to quantify the ligand discrimination task. Our results from this part shed further light on the way how cells in principle process information by using their surface receptors to probe the environment. We clearly demonstrated that asymmetric receptor dimerization enables cells to perform robust affinity sensing. With this part we contributed to answering the fascinating question how cells function robustly in noisy environments. Since we were able to explain this mechanism already with an equilibrium model in combination with our information theoretic analysis, we did not fully uncover the spatial and stochastic contributions of this system. We nevertheless believe them to be of high relevance and plan to continue in this direction. We are convinced that a full spatial and stochastic treatment of the receptor dynamics will provide instructive insights as to how the signal initiation of type I interferons is additionally modulated by the spatial organization of its signaling receptors in the cellular plasma membrane. Our information theoretic framework by itself is set up in such a way, that we believe it to be readily generalizable to related problems in signal transduction.

In chapter 6 we studied the spatiotemporal oscillation patterns of the bacterial Min proteins. The successful demonstration of standing wave patterns in cell-like compartments from recent *in vitro* experiments [55, 147] was an important step forward for synthetic biology. At the same time they put a new focus on the question how geometry tunes pattern formation. The Min system is an ideal candidate for such a question, since its molecular reaction mechanisms are considerably well studied. From a theoretical point of view many pattern forming systems are studied by solving the corresponding partial differential reaction-diffusion equations deterministically. In contrast to this, we used a stochastic simulation approach. This turned out to be very suitable to analyze stochastic switching events and determine how geometrical confinement influences oscillation mode selection. To our satisfaction, these findings agree very nicely with current live cell experiments and helped to improve our understanding of the oscillation mechanism itself. Despite extensive theoretical work on the Min system over the course of the last two decades, it is still fascinating to observe that a full theoretical description of the rich spatiotemporal oscillation dynamics has not yet been established. Although the theory of pattern formation has already found its way into standard text books on nonlinear dynamics, it cannot account for all observed phenomena. This simply means that our current canonical understanding of pattern formation is still incomplete. To understand why this is still challenging for the Min system, we have to simply recall the following facts. The Min proteins form a highly

nonlinear reaction-diffusion system, with a cycling between domains of different spatial dimensionality and global protein conservation laws. All these parts put together give rise to a complicated phase space. By investigating mode switching and multistability we hope to have contributed to better understand the underlying oscillation mechanism at its core. Future work will continue to uncover the role of geometry and the detailed nonlinear reaction schemes for general protein pattern forming systems. If we step away from the Min system for a moment and consider biochemical oscillators in general, our believe is that the coupling of biochemical processes to cell mechanics will prove to be a very exciting and challenging topic for future research in biophysics.

In the last chapter 7 we switched from the self-organization of the Min proteins to the self-assembly of rings and capsids. Inspired by the very efficient self-assembly of viral capsid shells, we wanted to understand how the assembly process can be modulated or tuned by non-equilibrium conditions. We decided to use hydrodynamic flow to disturb the system and used the mesoscopic multiparticle collision dynamics (MPCD) method to account for hydrodynamic interactions. MPCD has seen a drastic increase in popularity over the last years and is a versatile tool to study the dynamics of complex fluids. In practice, we studied the influence of shear flow on the assembly outcome of rings and capsid shells. Our central findings were, that the shear strength can very delicately tune the assembly dynamics, both in a favorable and unfavorable direction. For a given target structure we were able to identify shear flow regimes, which enhanced the assembly yield. At the same time we observed, that the assembly process globally is accelerated due to the presence of flow. In general we concluded that forced flow leads to a faster and more dynamic self-assembly process, based on a faster and better sampling of the configurational phase space of the given assembly structures. Strikingly, we observed that the emergence of malformed structures can be efficiently suppressed in certain shear flow regimes. We believe that our findings offer valuable insights for general self-assembly strategies. Secondly, we think that flow induced assembly enhancement might be an interesting topic for the synthetic design of soft-matter materials. Colloid science is well capable of manufacturing functionalized patchy particles, which can be exposed to external flow to efficiently self-assemble to a desired target structure. Inspired by the viral capsid shells, we could think of synthetic shells as drug containers as a potential application. But also from a purely theoretical point of view we find these observations to be highly interesting, as they show how the complex dynamics of self-assembling systems can be selectively tuned to optimize yields or suppress malformation.

In conclusion, this thesis demonstrates both the strength and the versatility of stochastic particle-based methods to shed further light on the inner workings of biological systems. We find our contributions to the three studied systems to be both interesting

and relevant and hope to have contributed to the goal of deciphering the way of how things really work.

Appendices

A1 Reactive BD calculations

A1.1 Overlap generation distribution $g(r_d, \Delta t)$

The generation distribution for the associative forward move was set up as

$$P_{\text{gen}}^{u\to\mathcal{E}}(\boldsymbol{r}_d, \Delta t) = g(r_d, \Delta t)\,, \tag{A1.1}$$

but we omitted the explicit result for $g(r_d, \Delta t)$ in chapter 2. Direct integration of g for the free diffusion propagator in three dimensions as defined in equation (2.5) is possible and yields

$$g(r_d, \Delta t) = \frac{\sigma}{\sqrt{\pi} 2 r_d}\left[\exp\left(\frac{-(r_d+R)^2}{\sigma^2}\right) - \exp\left(\frac{-(r_d-R)^2}{\sigma^2}\right)\right] + \frac{1}{2}\left[\operatorname{erf}\left(\frac{r_d+R}{\sigma}\right) + \operatorname{erf}\left(\frac{-r_d+R}{\sigma}\right)\right], \tag{A1.2}$$

where $\sigma^2 = 4D\Delta t$ and $\operatorname{erf}(x)$ is the error-function

$$\operatorname{erf}(x) = \frac{2}{\sqrt{\pi}} \int_0^x \exp\left(-\tau^2\right)\, d\tau. \tag{A1.3}$$

A2 Ligand-receptor binding

A2.1 Dimerization dynamics

Homo-dimer solution

In section 3.1 we discussed the equilibrium solution for different receptor-ligand binding modes. To obtain transient dynamics one needs to solve the corresponding set of coupled nonlinear ODEs. For the homo-dimerizing receptor system (3.8a)–(3.8b) as discussed in 3.1.2 this amounts to

$$\frac{dR}{dt} = -2k_b R \cdot L + k_u(RL) - k_a(RL)\, R + 2k_d\, C \tag{A2.1a}$$

$$\frac{d(RL)}{dt} = +2k_b\, R \cdot L - k_u(RL) - k_a\,(RL)\, R + 2k_d\, C \tag{A2.1b}$$

$$\frac{dC}{dt} = +k_a\,(RL)\, R - 2k_d\, C\,. \tag{A2.1c}$$

Having established the full equilibrium solution for C in equation (3.12) of section 3.1.2 we can also immediately find the full system's solution as a function of the equilibrium solution C as

$$R = \Big(1 - \Lambda(\eta_L)\Big)\Big(R_0 - 2C\Big) \quad \text{and} \quad (RL) = \Lambda(\eta_L)\Big(R_0 - 2C\Big). \tag{A2.2a}$$

Hetero-dimer solution

The hetero-dimerization scheme from section 3.1.3 according to equations (3.14a) – (3.14b) leads to the following set of ODEs

$$\frac{\mathrm{d}R_i}{\mathrm{d}t} = -k_{\mathrm{b},i} L \cdot R_i + k_{\mathrm{u},i}(R_iL) - k_{\mathrm{a},i}(R_jL)\, R_i + k_{\mathrm{d},i}\, C \tag{A2.3a}$$

$$\frac{\mathrm{d}(R_iL)}{\mathrm{d}t} = k_{\mathrm{b},i}\, L(R_i) - k_{\mathrm{u},i}\, R_iL - k_{\mathrm{a},j}\,(R_iL)\, R_j + k_{\mathrm{d},j}\, C \tag{A2.3b}$$

$$\frac{\mathrm{d}C}{\mathrm{d}t} = k_{\mathrm{a},1}\, R_1(R_2L) + k_{\mathrm{a},2}\, R_2(R_1L) - (k_{\mathrm{d},1} + k_{\mathrm{d},2})\, C\,, \tag{A2.3c}$$

where the pair of indices (i, j) runs over $\{(1,2),(2,1)\}$ to account for the symmetry of the two assembly pathways. All analytical equilibrium solutions from section 3.1 have

been verified by extensive numerical integration of the above equations to obtain both transient dynamic solutions and steady state results. For all analytical binding curves they were found in perfect agreement.

With the solution for C we also have access to the full equilibrium solution of the hetero-dimerization scheme in the form of

$$R_i = \left(1 - \Lambda_i\right)\left(R_{i,0} - C\right) \quad \text{and} \quad (R_i L) = \Lambda_i \left(R_{i,0} - C\right), \tag{A2.4}$$

for $i = 1, 2$. By proper normalization we can equally express these solutions as fractional quantities.

$$f^{\mathrm{He}}_{R_i} = \frac{R_i}{R_0} = \left(1 - \Lambda_i\right)\left(1 - f^{\mathrm{He}}\right) \tag{A2.5}$$

$$f^{\mathrm{He}}_{R_i L} = \frac{(R_i L)}{R_0} = \Lambda_i \left(1 - f^{\mathrm{He}}\right), \tag{A2.6}$$

again for both receptor chains $i = 1, 2$. Here I used $R_{1,0} = R_{2,0} = R_0$ and $f^{\mathrm{He}} \equiv f^{\mathrm{He}}_C$ as before.

A2.2 Surface-bound ligand

To understand the mechanisms of receptor engagement, it is instructive to look at the fraction of surface bound ligand $f_{L,\mathrm{bound}}$ for a given ligand-receptor binding model. This can help to compare how the two modes of ligand binding from a 3D bulk and via 2D receptor interactions contribute to the formation of activated receptors.

For the monomeric case the fraction of surface-bound ligand simply coincides with the fraction of active receptors, such that we have $f^{\mathrm{M}}_{L,\mathrm{bound}} = f^{\mathrm{M}}_C$. For the homo-dimer system this is however given by

$$f^{\mathrm{Ho}}_{L,\mathrm{bound}} = \frac{RL + C}{R_0}, \tag{A2.7}$$

where the normalization is only R_0 and not $R_0/2$ as it is the case for the homo-dimer fraction C itself. The solution for the dashed lines in figure 3.4B was obtained by using this result from equation (A2.7). Analogously we find the fraction of surface bound ligand to be

$$f^{\mathrm{He}}_{L,\mathrm{bound}} = \frac{R_1 L + R_2 L + C}{R_T} \tag{A2.8}$$

for the hetero-dimeric case, where $R_T = R_{1,0} + R_{2,0}$ denotes the total receptor surface concentration.

Bibliography

[1] W. de Ronde. "Multiplexing Biochemical Signals". PhD thesis. 2012.

[2] D. A. Lauffenburger and J. J. Linderman. *Receptors : models for binding, trafficking, and signaling*. New York: Oxford University Press, 1993.

[3] S. W. Hell and J Wichmann, "Breaking the diffraction resolution limit by stimulated emission: stimulated-emission-depletion fluorescence microscopy.", 1994, *Optics letters*, **19**, 780–2.

[4] T. A. Klar et al., "Fluorescence microscopy with diffraction resolution barrier broken by stimulated emission.", 2000, *Proceedings of the National Academy of Sciences of the United States of America*, **97**, 8206–8210.

[5] M. Bates, T. R. Blosser and X. Zhuang, "Short-range spectroscopic ruler based on a single-molecule optical switch", 2005, *Physical Review Letters*, **94**, 1–4.

[6] E. Betzig et al., "Imaging Intracellular Fluorescent Proteins at Nanometer Resolution", 2006, *Science*, **213**, 1642–1646.

[7] S. T. Hess, T. P. Girirajan and M. D. Mason, "Ultra-High Resolution Imaging by Fluorescence Photoactivation Localization Microscopy", 2006, *Biophysical Journal*, **91**, 4258–4272.

[8] M. J. Rust, M. Bates and X. W. Zhuang, "Sub-diffraction-limit imaging by stochastic optical reconstruction microscopy (STORM)", 2006, *Nat Methods*, **3**, 793–795.

[9] J. Lippincott-Schwartz, "Profile of Eric Betzig, Stefan Hell, and W. E. Moerner, 2014 Nobel Laureates in Chemistry", 2015, *Proceedings of the National Academy of Sciences*, **112**, 201500784.

[10] E. Betzig, "Eric Betzig - Nobel Lecture: Single Molecules, Cells, and Super-Resolution Optics", 2015, **87**, 111–137.

[11] U. S. Alon. *An Introduction to Systems Biology*. Chapman & Hall/CRC mathematical and computational biology series ARRAY(0x4596960). Boca Raton, Fla.: Chapman & Hall/CRC, 2007, XVI, 301 S.

[12] J. J. Tyson, K. C. Chen and B. Novak, "Sniffers, buzzers, toggles and blinkers: Dynamics of regulatory and signaling pathways in the cell", 2003, *Current Opinion in Cell Biology*, **15**, 221–231.

[13] R. G. Endres. *Physical principles in sensing and signaling*. 1. ed. Oxford : Oxford Univ. Press, 2013, XI, 145 S.

[14] R. Phillips, J. Kondev and J. Theriot. *Physical Biology of the Cell*. Repr. London and New York: Garland Science, 2013.

[15] D. Endres and A. Zlotnick, "Model-based Analysis of Assembly Kinetics for Virus Capsids or Other Spherical Polymers", 2002, *Biophysical Journal*, **83**, 1217–1230.

[16] W. S. Bialek. *Biophysics*. Princeton [u.a.]: Princeton Univ. Press, 2012, XII, 640 S.

[17] N Barkai and S Leibler, "Robustness in simple biochemical networks to transfer and process information.", 1997, *Nature*, **387**, 913–917.

[18] U Alon et al., "Robustness in bacterial chemotaxis.", 1999, *Nature*, **397**, 168–171.

[19] J. M. G. Vilar et al., "Mechanisms of noise-resistance in genetic oscillators.", 2002, *Proceedings of the National Academy of Sciences of the United States of America*, **99**, 5988–92.

[20] H. Kitano, "Biological robustness", 2004, *Nature Reviews Genetics*, **5**, 826–837.

[21] H. Kitano, "Towards a theory of biological robustness.", 2007, *Molecular systems biology*, **3**, 137.

[22] J. Piehler et al., "Structural and dynamic determinants of type I interferon receptor assembly and their functional interpretation.", 2012, *Immunological reviews*, **250**, 317–34.

[23] G. Schreiber and J. Piehler, "The molecular basis for functional plasticity in type I interferon signaling", 2015, *Trends in Immunology*, 1–11.

[24] E. Karsenti, "Self-organization in cell biology: a brief history.", 2008, *Nature reviews. Molecular cell biology*, **9**, 255–62.

[25] A. J. Lotka, "Contributions to the theory of periodic reactions", 1910, *J. Phys. Chem.* **14**, 271–274.

[26] A Lotka. *Elements of Physical Biology*. 1925.

[27] W Bray, "A periodic reaction in homogeneous solution and its relation to catalysis", 1921, *J. Am. Chem. Soc.* **43**, 1262–1267.

[28] B Belousov, "A periodic reaction and its mechanism", 1959, *Compilation of Abstracts on Radiation Medicine*, **147**, 145.

[29] A Zhabotinsky, "Periodic processes of malonic acid oxidation in a liquid phase.", 1964, *Biofizika*, **9**, 306–311.

[30] A. M. Zhabotinsky and A. N. Zaikin, "Autowave processes in a distributed chemical system", 1973, *J. Theor. Biol.* **40**, 45–61.

[31] I Prigogine and G Nicolis, "On symmetry-breaking instabilities in dissipative systems", 1967, *J. Chem. Phys.* **46**, 3542–3550.

[32] I Prigogine, G Nicolis and A Babloyantz, "Nonequilibrium problems in biological phenomena", 1974, *Ann. NY Acad. Sci.* **231**, 99–105.

[33] I Prigogine and I Stengers. *Order Out of Chaos*. 1984.

[34] H Haken. *Synergetics: An Introduction*. 1977.

[35] M. E. Janson, "Crosslinkers and motors organize dynamic microtubules to form stable bipolar arrays in fission yeast", 2007, *Cell*, **128**, 357–368.

[36] F. J. Nedelec et al., "Self-organization of microtubules and motors", 1997, *Nature*, **389**, 305–308.

[37] F Nedelec, "Computer simulations reveal motor properties generating stable antiparallel microtubule interactions", 2002, *J. Cell Biol.* **158**, 1005–1015.

[38] F Backouche et al., "Active gels: dynamics of patterning and self-organization", 2006, *Phys. Biol.* **3**, 264–273.

[39] K Kruse et al., "Asters, vortices, and rotating spirals in active gels of polar filaments", 2004, *Phys. Rev. Lett.* **92**, 78101–78104.

[40] B Novak and J. J. Tyson, "Modelling the controls of the eukaryotic cell cycle", 2003, *Biochem. Soc. Trans.* **31**, 1526–1529.

[41] W Sha, "Hysteresis drives cell-cycle transitions in Xenopus laevis egg extracts", 2003, *Proc. Natl Acad. Sci. USA*, **100**, 975–980.

[42] A. M. Turing, "The chemical basis of morphogenesis", 1952, *Philosophical Transactions of the Royal Society of London B: Biological Sciences*, **237**, 37–72.

[43] S. Kondo and T. Miura, "Reaction-Diffusion Model as a Framework for Understanding Biological Pattern Formation", 2010, *Science*, **329**, 1616–1620.

[44] A. M. Nesterenko et al., "Morphogene adsorption as a Turing instability regulator: Theoretical analysis and possible applications in multicellular embryonic systems", 2017, *PLoS ONE*, **12**, 1–22.

[45] S. B. Cooper and P. K. Maini, "The mathematics of nature at the Alan Turing centenary", 2012, *Interface Focus*, **2**, 393–396.

[46] C. Beta and K. Kruse, "Intracellular Oscillations and Waves", 2017, *Annual Review of Condensed Matter Physics*, **8**, annurev–conmatphys–031016–025210.

[47] D. Thalmeier, J. Halatek and E. Frey, "Geometry-induced protein pattern formation", 2016, *Proceedings of the National Academy of Sciences USA*, **113**, 548–553.

[48] P. A. J. de Boer, R. E. Crossley and L. I. Rothfield, "A division inhibitor and a topological specificity factor coded for by the minicell locus determine proper placement of the division septum in E. coli.", 1989, *Cell*, **56**, 641–649.

[49] Z. Hu and J. Lutkenhaus, "Topological regulation of cell division in Escherichia coli involves rapid pole to pole oscillation of the division inhibitor MinC under the control of MinD and MinE", 1999, *Molecular Microbiology*, **34**, 82–90.

[50] D. M. Raskin and P. A. J. de Boer, "Rapid pole-to-pole oscillation of a protein required for directing division to the middle of Escherichia coli.", 1999, *Proceedings of the National Academy of Sciences USA*, **96**, 4971–4976.

[51] D. M. Raskin and P. A. J. de Boer, "MinDE-dependent pole-to-pole oscillation of division inhibitor MinC in Escherichia coli", 1999, *Journal of Bacteriology*, **181**, 6419–6424.

[52] Z. Hu et al., "The MinC component of the division site selection system in Escherichia coli interacts with FtsZ to prevent polymerization", 1999, *Proceedings of the National Academy of Sciences USA*, **96**, 14819–14824.

[53] F. Wu et al., "Symmetry and scale orient Min protein patterns in shaped bacterial sculptures", 2015, *Nature Nanotechnology*, **10**, 719–726.

[54] J. Lutkenhaus, "Tinkering with Acellular Division", 2008, *Science*, **320**, 755–756.

[55] K. Zieske and P. Schwille, "Reconstitution of Pole-to-Pole Oscillations of Min Proteins in Microengineered Polydimethylsiloxane Compartments", 2013, *Angewandte Chemie*, **52**, 459–462.

[56] M. Loose et al., "Spatial Regulators for Bacterial Cell Division Self-Organize into Surface Waves in Vitro", 2008, *Science*, **320**, 789–792.

[57] J. Lutkenhaus and S. G. Addinall, "Bacterial cell division", 1997, *Annual Reviews Biochemistry*, **66**, 93–116.

[58] F. van den Ent, L. Amos and J. Löwe, "Bacterial ancestry of actin and tubulin", 2001, *Current Opinion in Microbiology*, **4**, 634–638.

[59] E. Bi and J. Lutkenhaus, "FtsZ ring structure associated with division in Escherichia coli", 1991, *Nature*, **354**, 161–164.

[60] L. J. Wu and J. Errington, "Nucleoid occlusion and bacterial cell division", 2011, *Nature Reviews Microbiology*, **10**, 8–12.

[61] M. W. Bailey et al., "Evidence for divisome localization mechanisms independent of the Min system and SlmA in Escherichia coli.", 2014, *PLoS genetics*, **10**, e1004504.

[62] P. A. J. de Boer, R. E. Crossley and L. I. Rothfield, "Roles of MinC and MinD in the site-specific septation block mediated by the MinCDE system of Escherichia coli", 1992, *Journal of Bacteriology*, **174**, 63–70.

[63] L. L. Lackner, D. M. Raskin and P. A. J. de Boer, "ATP-dependent interactions between Escherichia coli Min proteins and the phospholipid membrane in vitro", 2003, *Journal of Bacteriology*, **185**, 735–749.

[64] T. H. Szeto et al., "Membrane localization of MinD is mediated by a C-terminal motif that is conserved across eubacteria, archaea, and chloroplasts", 2002, *Proceedings Of The National Academy Of Sciences USA*, **99**, 15693–15698.

[65] T. H. Szeto et al., "The MinD membrane targeting sequence is a transplantable lipid-binding helix", 2003, *Journal of Biological Chemistry*, **278**, 40050–40056.

[66] L. D. Renner and D. B. Weibel, "MinD and MinE interact with anionic phospholipids and regulate division plane formation in Escherichia coli", 2012, *Journal of Biological Chemistry*, **287**, 38835–38844.

[67] J. Lutkenhaus, "Assembly Dynamics of the Bacterial MinCDE System and Spatial Regulation of the Z Ring", 2007, *Annual Review of Biochemistry*, **76**, 539–562.

[68] P. Lenz and L. Søgaard-Andersen, "Temporal and spatial oscillations in bacteria.", 2011, *Nature reviews. Microbiology*, **9**, 565–577.

[69] M. Loose, K. Kruse and P. Schwille, "Protein Self-Organization: Lessons from the Min System", 2011, *Annual Review of Biophysics*, **40**, 315–336.

[70] A. G. Vecchiarelli, K. Mizuuchi and B. E. Funnell, "Surfing biological surfaces: Exploiting the nucleoid for partition and transport in bacteria", 2012, *Molecular Microbiology*, **86**, 513–523.

[71] S. Kretschmer and P. Schwille, "Toward Spatially Regulated Division of Protocells: Insights into the E. coli Min System from in Vitro Studies", 2014, *Life*, **4**, 915–928.

[72] S. Kretschmer and P. Schwille, "Pattern formation on membranes and its role in bacterial cell division", 2016, *Current Opinion in Cell Biology*, **38**, 52–59.

[73] M. Carrillo-Tripp et al., "VIPERdb2: An enhanced and web API enabled relational database for structural virology", 2009, *Nucleic Acids Research*, **37**, 436–442.

[74] J. D. Perlmutter and M. F. Hagan, "Mechanisms of Virus Assembly", 2015, *Annual Review of Physical Chemistry*, **66**, 217–239.

[75] S. C. Glotzer, "Some Assembly Required", 2004, *Science*, **306**, 419–420.

[76] D. T. Gillespie, "A general method for numerically simulation the stochastic time evolution of coupled chemical reactions", 1976, *Journal of Computational Physics*, **22**, 403–434.

[77] D. T. Gillespie, "Exact stochastic simulation of coupled chemical reactions", 1977, *The Journal of Physical Chemistry*, **93555**, 2340–2361.

[78] D. T. Gillespie, "Stochastic simulation of chemical kinetics.", 2007, *Annual review of physical chemistry*, **58**, 35–55.

[79] M. A. Gibson and J. Bruck, "Efficient Exact Stochastic Simulation of Chemical Systems with Many Species and Many Channels", 2000, *The Journal of Physical Chemistry A*, **104**, 1876–1889.

[80] D. T. Gillespie, A. Hellander and L. R. Petzold, "Perspective: Stochastic algorithms for chemical kinetics", 2013, *Journal of Chemical Physics*, **138**, 1–14.

[81] D. Schnoerr, G. Sanguinetti and R. Grima, "Approximation and inference methods for stochastic biochemical kinetics - a tutorial review", 2017, .

[82] Y. Cao, D. T. Gillespie and L. R. Petzold, "Efficient step size selection for the tau-leaping simulation method.", 2006, *The Journal of chemical physics*, **124**, 044109.

[83] J. S. van Zon and P. R. ten Wolde, "Green's-function reaction dynamics: a particle-based approach for simulating biochemical networks in time and space.", 2005, *The Journal of Chemical Physics*, **123**, 234910.

[84] J. S. van Zon and P. ten Wolde, "Simulating Biochemical Networks at the Particle Level and in Time and Space: Green's Function Reaction Dynamics", 2005, *Physical Review Letters*, **94**, 128103.

[85] A. Vijaykumar, P. G. Bolhuis and P. R. Ten Wolde, "Combining molecular dynamics with mesoscopic Green's function reaction dynamics simulations", 2015, *Journal of Chemical Physics*, **143**, .

[86] K. Kaizu et al., "The Berg-Purcell limit revisited", 2014, *Biophysical Journal*, **106**, 976–985.

[87] H. C. Berg and E. M. Purcell, "Physics of chemoreception.", 1977, *Biophysical journal*, **20**, 193–219.

[88] J. Schöneberg and F. Noé, "ReaDDy–a software for particle-based reaction-diffusion dynamics in crowded cellular environments.", 2013, *PloS one*, **8**, e74261.

[89] R. R. Gabdoulline and R. C. Wade, "Simulation of the diffusional association of barnase and barstar", 1997, *Biophys J*, **72**, .

[90] R. R. Gabdoulline and R. C. Wade, "Brownian dynamics simulation of protein-protein diffusional encounter", 1998, *Methods*, **14**, .

[91] J. Schöneberg et al., "Explicit Spatiotemporal Simulation of Receptor-G Protein Coupling in Rod Cell Disk Membranes", 2014, *Biophysical Journal*, **107**, 1042–1053.

[92] K. Takahashi, S. Tanase-Nicola and P. R. ten Wolde, "Spatio-temporal correlations can drastically change the response of a MAPK pathway", 2010, *Proceedings of the National Academy of Sciences*, **107**, 2473–2478.

[93] A. Mugler et al., "Membrane clustering and the role of rebinding in biochemical signaling.", 2012, *Biophysical journal*, **102**, 1069–78.

[94] A. Mugler, F. Tostevin and P. R. ten Wolde, "Spatial partitioning improves the reliability of biochemical signaling.", 2013, *Proceedings of the National Academy of Sciences of the United States of America*, **110**, 5927–32.

[95] S. S. Andrews, "Serial rebinding of ligands to clustered receptors as exemplified by bacterial chemotaxis", 2005, *Physical biology*, **2**, 111–122.

[96] J. S. van Zon et al., "Diffusion of transcription factors can drastically enhance the noise in gene expression.", 2006, *Biophysical Journal*, **91**, 4350–67.

[97] J. Paijmans and P. R. ten Wolde, "Lower bound on the precision of transcriptional regulation and why facilitated diffusion can reduce noise in gene expression", 2014, *Physical Review E*, **90**, 032708.

[98] S. B. van Albada and P. R. ten Wolde, "Enzyme localization can drastically affect signal amplification in signal transduction pathways.", 2007, *PLoS computational biology*, **3**, 1925–34.

[99] J. Schöneberg, A. Ullrich and F. Noé, "Simulation tools for particle-based reaction-diffusion dynamics in continuous space.", 2014, *BMC biophysics*, **7**, 11.

[100] T. R. Sokolowski and P. R. ten Wolde, "Spatial-Stochastic Simulation of Reaction-Diffusion Systems", 2017, 1–31.

[101] S. S. Andrews, T. Dinh and A. P. Arkin, "Stochastic Models of Biological Processes", 2009, *Encyclopedia of Complexity and System Science, Meyers, Robert (Ed.) Volume 9:8730-8749. Springer, NY, 2009*, 8730–8749.

[102] H. S. Carslaw and J. C. Jaeger. *Conduction of heat in solids*. Oxford: Clarendon Press, 1959.

[103] H. C. Berg. *Random Walks in Biology*. Princeton paperbacks. Princeton University Press, 1993.

[104] N. Agmon and A. Szabo, "Theory of reversible diffusion-influenced reactions", 1990, *The Journal of Chemical Physics*, **92**, 5270–5284.

[105] M von Smoluchowski, "Versuch einer mathematischen Theorie der Koagulationskinetik kolloider Lösungen", 1917, *Z. phys. Chem*, **92**, 129–168.

[106] G Schreiber, G Haran and H.-X. Zhou, "Fundamental aspects of protein-protein association kinetics.", 2009, *Chemical reviews*, **109**, 839–60.

[107] S. Milles et al., "Plasticity of an Ultrafast Interaction between Nucleoporins and Nuclear Transport Receptors", 2015, *Cell*, **163**, 734–745.

[108] S. S. Andrews and D. Bray, "Stochastic simulation of chemical reactions with spatial resolution and single molecule detail", 2004, *Physical Biology*, **1**, 137–151.

[109] S. S. Andrews et al., "Detailed simulations of cell biology with Smoldyn 2.1", 2010, *PLoS Computational Biology*, **6**, .

[110] J. Schluttig et al., "Dynamics of protein-protein encounter: a Langevin equation approach with reaction patches.", 2008, *The Journal of chemical physics*, **129**, 155106.

[111] J. Schluttig, C. B. Korn and U. S. Schwarz, "Role of anisotropy for protein-protein encounter", 2010, *Physical Review E*, **81**, 030902.

[112] J. E. Baschek, H. C. R Klein and U. S. Schwarz, "Stochastic dynamics of virus capsid formation: direct versus hierarchical self-assembly.", 2012, *BMC Biophysics*, **5**, 22.

[113] H. C. R. Klein and U. S. Schwarz, "Studying protein assembly with reversible Brownian dynamics of patchy particles", 2014, *Journal of Chemical Physics*, **140**, 184112.

[114] H. C. R. Klein et al., "Computational support for a scaffolding mechanism of centriole assembly", 2016, *Scientific Reports*, **6**, 27075.

[115] M. J. Morelli and P. R. Ten Wolde, "Reaction Brownian dynamics and the effect of spatial fluctuations on the gain of a push-pull network", 2008, *Journal of Chemical Physics*, **129**, .

[116] H. Kim and K. Shin, "Exact Solution of the Reversible Diffusion-Influenced Reaction for an Isolated Pair in Three Dimensions", 1999, *Physical Review Letters*, **82**, 1578–1581.

[117] S. S. Andrews, "Accurate particle-based simulation of adsorption, desorption and partial transmission.", 2009, *Physical biology*, **6**, 046015.

[118] K. C. Huang, Y. Meir and N. S. Wingreen, "Dynamic structures in Escherichia coli: Spontaneous formation of MinE rings and MinD polar zones", 2003, *Proceedings of the National Academy of Sciences USA*, **100**, 12724–12728.

[119] F. C. Collins and G. E. Kimball, "Diffusion-controlled reaction rates", 1949, *Journal of Colloid Science*, **4**, 425–437.

[120] M. Gavutis et al., "Determination of the two-dimensional interaction rate constants of a cytokine receptor complex.", 2006, *Biophysical journal*, **90**, 3345–55.

[121] E. Jaks et al., "Differential receptor subunit affinities of type I interferons govern differential signal activation.", 2007, *Journal of molecular biology*, **366**, 525–39.

[122] S. Lochte et al., "Live cell micropatterning reveals the dynamics of signaling complexes at the plasma membrane", 2014, *The Journal of Cell Biology*, **207**, 407–418.

[123] A. S. Perelson and G. Weisbuch, "Immunology for physicists", 1997, *Reviews of Modern Physics*, **69**, 1219–1268.

[124] A. S. Perelson, "Receptor Clustering on a Cell Surface. II. Theory of Receptor Cross-Linking by Ligands Bearing Two Chemically Distinct Functional Groups", 1980, *Mathematical Biosciences*, 87–110.

[125] N. G. van Kampen. *Stochastic processes in physics and chemistry*. 3. ed. North-Holland personal library. Amsterdam ; Heidelberg [u.a.]: Elsevier, 2007, XVI, 463 S.

[126] A. S. Perelson and C. DeLisi, "Receptor clustering on a cell surface. I. theory of receptor cross-linking by ligands bearing two chemically identical functional groups", 1980, *Mathematical Biosciences*, **48**, 71–110.

[127] A. Whitty et al., "Interaction affinity between cytokine receptor components on the cell surface.", 1998, *Proceedings of the National Academy of Sciences of the United States of America*, **95**, 13165–13170.

[128] C. You et al., "Receptor dimer stabilization by hierarchical plasma membrane microcompartments regulates cytokine signaling", 2016, *Science Advances*, **2**, 1–13.

[129] A. Rhee, R. Cheong and A. Levchenko, "The application of information theory to biochemical signaling systems", 2012, *Physical Biology*, **9**, 045011.

[130] A. Levchenko and I. Nemenman, "Cellular noise and information transmission", 2014, *Current Opinion in Biotechnology*, **28**, 156–164.

[131] G. Rieckh and G. Tkačik, "Noise and Information Transmission in Promoters with Multiple Internal States", 2014, *Biophysical Journal*, **106**, 1194–1204.

[132] A. M. Walczak and G. Tkačik, "Information transmission in genetic regulatory networks: a review", 2011, .

[133] C. G. Bowsher, M. Voliotis and P. S. Swain, "The Fidelity of Dynamic Signaling by Noisy Biomolecular Networks", 2013, *PLoS Computational Biology*, **9**, .

[134] C. G. Bowsher and P. S. Swain, "Environmental sensing, information transfer, and cellular decision-making", 2014, *Current Opinion in Biotechnology*, **28**, 149–155.

[135] E. T. Jaynes. *Probability theory*. 12. print. Cambridge [u.a.]: Cambridge Univ. Press, 2013, XXIX, 727 S.

[136] D. J. C. MacKay. *Information Theory, Inference and Learning Algorithms*. Cambridge University Press, 2003.

[137] A. M. Fraser, "Independent coordinates for strange attractors from mutual information", 1986, *Physical Review A*, **33**, 1134–1140.

[138] A. Oyler-Yaniv et al., "A Tunable Diffusion-Consumption Mechanism of Cytokine Propagation Enables Plasticity in Cell-to-Cell Communication in the Immune System", 2017, *Immunity*, **46**, 609–620.

[139] F. P. Assen and M. Sixt, "The Dynamic Cytokine Niche", 2017, *Immunity*, **46**, 519–520.

[140] M. Gavutis et al., "Lateral ligand-receptor interactions on membranes probed by simultaneous fluorescence-interference detection.", 2005, *Biophysical journal*, **88**, 4289–302.

[141] F. Roder et al., "Rapid Transfer of Transmembrane Proteins for Single Molecule Dimerization Assays in Polymer-Supported Membranes", 2014, .

[142] P. G. Saffman and M Delbruck, "Brownian motion in biological membranes", 1975, *Proc Natl Acad Sci USA*, **72**, 3111–3113.

[143] B. Di Ventura and V. Sourjik, "Self-organized partitioning of dynamically localized proteins in bacterial cell division.", 2011, *Molecular Systems Biology*, **7**, 457.

[144] B. D. Corbin, X.-C. Yu and W. Margolin, "Exploring intracellular space: Function of the Min system in round-shaped Escherichia coli", 2002, *EMBO Journal*, **21**, 1998–2008.

[145] M. Loose et al., "Min protein patterns emerge from rapid rebinding and membrane interaction of MinE", 2011, *Nature Structural & Molecular Biology*, **18**, 577–583.

[146] J. Schweizer et al., "Geometry sensing by self-organized protein patterns", 2012, *Proceedings of the National Academy of Sciences USA*, **109**, 15283–15288.

[147] K. Zieske and P. Schwille, "Reconstitution of self-organizing protein gradients as spatial cues in cell-free systems", 2014, *eLife*, **3**, 1–19.

[148] J. Männik et al., "Robustness and accuracy of cell division in Escherichia coli in diverse cell shapes.", 2012, *Proceedings of the National Academy of Sciences USA*, **109**, 6957–6962.

[149] A. Gierer and H. Meinhardt, "A Theory of Biological Pattern Formation", 1972, *Kybernetik*, **12**, 30–39.

[150] M. C. Cross and P. C. Hohenberg, "Pattern formation outside of equilibrium", 1993, *Reviews of Modern Physics*, **65**, 851–1112.

[151] H. Meinhardt and P. A. J. de Boer, "Pattern formation in Escherichia coli: a model for the pole-to-pole oscillations of Min proteins and the localization of the division site.", 2001, *Proceedings of the National Academy of Sciences USA*, **98**, 14202–14207.

[152] M Howard, A. D. Rutenberg and S de Vet, "Dynamic compartmentalization of bacteria: accurate division in E. coli.", 2001, *Physical Review Letters*, **87**, 278102.

[153] K. Kruse, "A dynamic model for determining the middle of Escherichia coli.", 2002, *Biophysical Journal*, **82**, 618–627.

[154] G. Meacci and K. Kruse, "Min-oscillations in Escherichia coli induced by interactions of membrane-bound proteins.", 2005, *Physical Biology*, **2**, 89–97.

[155] M. Howard and K. Kruse, "Cellular organization by self-organization: Mechanisms and models for Min protein dynamics", 2005, *Journal of Cell Biology*, **168**, 533–536.

[156] K. Kruse, M. Howard and W. Margolin, "An experimentalist's guide to computational modelling of the Min system", 2007, *Molecular Microbiology*, **63**, 1279–1284.

[157] Z. Petrášek and P. Schwille, "Simple membrane-based model of the Min oscillator", 2015, *New Journal of Physics*, **17**, 043023.

[158] R. A. Kerr et al., "Division accuracy in a stochastic model of Min oscillations in Escherichia coli.", 2006, *Proceedings of the National Academy of Sciences USA*, **103**, 347–352.

[159] D. Fange and J. Elf, "Noise-Induced Min Phenotypes in E . coli", 2006, *PLoS Computational Biology*, **2**, 637–648.

[160] F. Tostevin and M. Howard, "A stochastic model of Min oscillations in Escherichia coli and Min protein segregation during cell division", 2005, *Physical Biology*, **3**, 1–12.

[161] N. Pavin, Č. P. Paljetak and V. Krstić, "Min-protein oscillations in Escherichia coli with spontaneous formation of two-stranded filaments in a three-dimensional stochastic reaction-diffusion model", 2006, *Physical Review E*, **73**, 1–5.

[162] F. Wu et al., "Multistability and dynamic transitions of intracellular Min protein patterns", 2016, *Molecular Systems Biology*, **12**, 1–18.

[163] D. A. Drew, M. J. Osborn and L. I. Rothfield, "A polymerization-depolymerization model that accurately generates the self-sustained oscillatory system involved in bacterial division site placement", 2005, *Proceedings of the National Academy of Sciences USA*, **102**, 6114–6118.

[164] J. Halatek and E. Frey, "Highly Canalized MinD Transfer and MinE Sequestration Explain the Origin of Robust MinCDE-Protein Dynamics", 2012, *Cell Reports*, **1**, 741–752.

[165] M. Bonny et al., "Membrane Binding of MinE Allows for a Comprehensive Description of Min-Protein Pattern Formation", 2013, *PLoS Computational Biology*, **9**, e1003347.

[166] M. Howard and A. D. Rutenberg, "Pattern formation inside bacteria: fluctuations due to the low copy number of proteins.", 2003, *Physical Review Letters*, **90**, 128102.

[167] M. Hoffmann and U. S. Schwarz, "Oscillations of Min-proteins in micropatterned environments: a three-dimensional particle-based stochastic simulation approach.", 2014, *Soft Matter*, **10**, 2388–2396.

[168] A. Madzvamuse, A. H. W. Chung and C. Venkataraman, "Stability analysis and simulations of coupled bulk-surface reaction-diffusion systems.", 2015, *Proceedings. Mathematical, physical, and engineering sciences / the Royal Society*, **471**, 20140546.

[169] A. Gomez-Marin, J. Garcia-Ojalvo and J. M. Sancho, "Self-sustained spatiotemporal oscillations induced by membrane-bulk coupling", 2007, *Physical Review Letters*, **98**, 3–6.

[170] A. Rätz and M. Röger, "Turing instabilities in a mathematical model for signaling networks", 2012, *Journal of Mathematical Biology*, **65**, 1215–1244.

[171] A. Rätz and M. Röger, "Symmetry breaking in a bulk–surface reaction–diffusion model for signalling networks", 2014, *Nonlinearity*, **27**, 1805–1827.

[172] A. Rätz, "Turing-type instabilities in bulk–surface reaction–diffusion systems", 2015, *Journal of Computational and Applied Mathematics*, **289**, 142–152.

[173] H. Garcke et al., "A coupled surface-Cahn–Hilliard bulk-diffusion system modeling lipid raft formation in cell membranes", 2016, *Mathematical Models and Methods in Applied Sciences*, **26**, 1149–1189.

[174] C. M. Elliot, R. Thomas and C. Venkataraman, "Coupled bulk-surface free boundary problems arising from mathematical model of receptor-ligand dynamics", 2017, *SIAM J. Math. Anal.* **51**, 2005–2035.

[175] C. M. Elliott and T. Ranner, "Finite element analysis for a coupled bulk-surface partial differential equation", 2013, *IMA Journal of Numerical Analysis*, **33**, 377–402.

[176] A. Madzvamuse and R. Barreira, "Exhibiting cross-diffusion-induced patterns for reaction-diffusion systems on evolving domains and surfaces", 2014, *Physical Review E - Statistical, Nonlinear, and Soft Matter Physics*, **90**, 1–14.

[177] N. Tuncer, A. Madzvamuse and A. J. Meir, "Projected finite elements for reaction-diffusion systems on stationary closed surfaces", 2015, *Applied Numerical Mathematics*, **96**, 45–71.

[178] A. Madzvamuse and A. H. W. Chung, "The bulk-surface finite element method for reaction-diffusion systems on stationary volumes", 2016, *Finite Elements in Analysis and Design*, **108**, 9–21.

[179] H. C. Öttinger. *Stochastic Processes in Polymeric Fluids: Tools and Examples for Developing Simulation Algorithms*. Springer Berlin Heidelberg, 1995.

[180] O. G. Berg, "On diffusion-controlled dissociation", 1978, *Chemical Physics*, **31**, 47–57.

[181] B. Volkmer and M. Heinemann, "Condition-Dependent cell volume and concentration of Escherichia coli to facilitate data conversion for systems biology modeling", 2011, *PLoS ONE*, **6**, 1–6.

[182] J. W. Cooley and J. W. Tukey, "An Algorithm for the Machine Calculation of Complex Fourier Series", 1965, *Mathematics of Computation*, **19**, 297–301.

[183] X. Shan and H. Chen, "Lattice Boltzmann model for simulating flows with multi phases and components", 1993, *Physical Review E*, **47**, 1815–1819.

[184] X. He and L.-S. Luo, "Theory of the lattice Boltzmann method: From the Boltzmann equation to the lattice Boltzmann equation", 1997, *Physical Review E*, **56**, 6811–6817.

[185] G. R. McNamara and G. Zanetti, "Use of the boltzmann equation to simulate lattice-gas automata", 1988, *Physical Review Letters*, **61**, 2332–2335.

[186] P. J. Hoogerbrugge and J. M. V. A. Koelman, "Simulating Microscopic Hydrodynamic Phenomena with Dissipative Particle Dynamics", 1992, *Europhys. Lett*, **19**, 155–160.

[187] P Espanol, "Hydrodynamics from dissipative particle dynamics", 1995, *Phys. Rev. E*, **52**, 1734–1742.

[188] A. Malevanets and R. Kapral, "Mesoscopic model for solvent dynamics", 1999, *Journal of Chemical Physics*, **110**, 8605.

[189] A. Malevanets and R. Kapral, "Solute molecular dynamics in a mesoscale solvent", 2000, *Journal of Chemical Physics*, **112**, 7260.

[190] M. Ripoll, R. G. Winkler and G. Gompper, "Star Polymers in Shear Flow", 2006, *Physical Review Letters*, **96**, 3–6.

[191] R. Kapral, "Multiparticle Collision Dynamics: Simulation of Complex Systems on Mesoscales", 2008, *Advances in Chemical Physics*, **140**, 89–146.

[192] G. Gompper et al. "Multi-Particle Collision Dynamics: A Particle-Based Mesoscale Simulation Approach to the Hydrodynamics of Complex Fluids". In: *Advanced Computer Simulation Approaches for Soft Matter Sciences III*. Ed. by C. Holm and K. Kremer. Berlin, Heidelberg: Springer Berlin Heidelberg, 2009, 1–87. DOI: 10.1007/978-3-540-87706-6_1.

[193] A. Nikoubashman, E. Bianchi and A. Z. Panagiotopoulos, "Self-assembly of Janus particles under shear", 2015, *Soft Matter*, **11**, 3737–3948.

[194] G. Marsaglia, "Choosing a point from the surface of a sphere", 1972, *The Annals of Mathematical Statistics*, **43**, 645–646.

[195] T. Ihle and D. M. Kroll, "Stochastic rotation dynamics: A Galilean-invariant mesoscopic model for fluid flow", 2001, *Physical Review E*, **63**, 0202011–0202014.

[196] J. T. Padding et al., "Stick boundary conditions and rotational velocity autocorrelation functions for colloidal particles in a coarse-grained representation of the solvent", 2005, *Journal of Physics: Condensed Matter*, **17**, 3393–3399.

[197] A. Nikoubashman, C. N. Likos and G. Kahl, "Computer simulations of colloidal particles under flow in microfluidic channels", 2013, *Soft Matter*, **9**, 2603.

[198] Y. Inoue, Y. Chen and H. Ohashi, "Development of a Simulation Model for Solid Objects Suspended in a Fluctuating Fluid", 2002, *Journal of Statistical Physics*, **107**, 85–100.

[199] M. F. Hagan and D. Chandler, "Dynamic Pathways for Viral Capsid Assembly", 2006, *Biophysical Journal*, **91**, 42–54.

[200] R Schwartz et al., "Local Rules Simulation of the Kinetics of Virus Capsid Self-Assembly", 1998, *Biophysical Journal*, **75**, 2626–2636.

[201] H. C. A. John D. Weeks, David Chandler, "Role of Repulsive Forces in Determining the Equilibrium Structure of Simple Liquids", 1971, *Journal of Chemical Physics*, **54**, 5237–5247.

[202] D. L. D. Caspar and A. Klug. "Physical principles in the construction of regular viruses". In: *Cold Spring Harbor Symposia on Quantitative Biology*. **27**. Cold Spring Harbor Laboratory Press. 1962, 1–24.

[203] R. F. Bruinsma and W. S. Klug, "Physics of Viral Shells", 2015, *Annual Review of Condensed Matter Physics*, **6**, 245–268.

[204] M. A. Boettcher, H. C. R. Klein and U. S. Schwarz, "Role of dynamic capsomere supply for viral capsid self-assembly", 2015, *Physical Biology*, **12**, 16014.

List of manuscripts

The following manuscripts have been written up during the course of this thesis. The table below lists the chapters they are based on.

1	Artemij Amiranashvili, Nikolas D. Schnellbächer and Ulrich S. Schwarz. *Stochastic Switching between multistable oscillation patterns of the Min-system*. New Journal of Physics, **18** (2016), 093049	Chapter 2, Chapter 6
2	Nikolas D. Schnellbächer, Nils B. Becker, Thomas Höfer and Ulrich S. Schwarz. *Asymmetric receptor dimerization leads to specific and robust ligand discrimination in the type I interferon system*. In preparation, to be submitted to PNAS	Chapter 3, Chapter 4
3	Fabian B. Fuchs, Nikolas D. Schnellbächer and Ulrich S. Schwarz. *Self-assembly of rings and capsids in hydrodynamic flow*. In preparation, to be submitted to J. Chem. Phys.	Chapter 7
4	Siegfried Hänselmann, Nikolas D. Schnellbächer, Ulrich S. Schwarz, Dirk-Peter Herten. *Dimerization dynamics of the interferon alpha receptor at single molecule resolution*. In preparation	Chapter 2, Chapter 5

Danksagung

An erster Stelle möchte ich mich bei Ulrich Schwarz für die Betreuung meiner Arbeit bedanken. Ohne seine Unterstützung wäre diese nicht möglich gewesen. Ich konnte in vielen gemeinsamen Diskussionen viel über Physik im Allgemeinen und Biophysik im Speziellen lernen und bin für die Möglichkeit Mitglied seiner Arbeitsgruppe sein zu können sehr dankbar. Die Teilnahmen an zahlreichen Konferenzen empfand ich als große Bereicherung und wertvolle Erfahrung, um mich wissenschaftlich weiter zu entwickeln.

Ich möchte mich ebenso bei Prof. Heinz Horner für sein Interesse an meiner Arbeit bedanken, für die er zweiter Gutachter ist.

Ein ganz besonderer Dank geht an die Arbeitsgruppe Schwarz, einschließlich aller ehemaligen Mitglieder, mit denen ich eine wirklich tolle Zeit verbringen durfte. Das sind Thorsten Erdmann, Jérôme Soiné, Julian Weichsel, Philipp Albert, Max Hoffmann, Christoph Brandt, Anna Battista, Felix Frey, Dimitri Probst, Julia Jäger, Nils Klughammer und Justin Grewe. Insbesondere die gemeinsamen DPG Konferenzen werden mir in bester Erinnerung bleiben. Für viele gemeinsame Bürotage gilt außerdem besonderer Dank Marco Linke, dem ich ebenso für viele Python Tipps danke, sowie Anil Kumar Dasanna, der mit mir das BioQuant auch gerne am Wochenende besucht. Ich bedanke mich außerdem besonders bei Heinrich Klein für viele anregende Diskussionen zur Selbstassemblierung und zu teilchenbasierten Simulationsmethoden sowie vielen Themen darüber hinaus. Ein riesiger Dank gilt Nils Becker für zahlreiche Diskussionen. Ich bin für deine Art Probleme zu lösen sehr dankbar und konnte sehr viel aus unseren gemeinsamen Gesprächen lernen. Ich habe zudem mit Artemij Amiranashvili, Fabian Fuchs, Tom Kaufmann, Anna Huhn und Nils Klughammer die Gelegenheit bekommen, mit sehr motivierten Studenten zusammen arbeiten zu können und dabei nicht nur fachlich große Freude gehabt. Ich möchte natürlich auch allen Korrekturlesern meiner Arbeit ganz herzlich für Ihre Unterstützung danken. Weiterhin danke ich der BioQuant IT, insbesondere Melinda Feucht für Ihre stetige Bereitschaft und Hilfe bei der Wartung unserer IT Systeme. Ganz besonders möchte ich auch Sonja Bartsch und Melanie Steiert im Philosophenweg 19 danken. Ich war zwar örtlich getrennt, freute mich jedoch über jeden Besuch und die stets nette und freundliche Stimmung bei euch auf dem Berg. Ich bedanke mich zudem bei dem ImmunoQuant Projekt für meine Finanzierung und bei der HGS MathComp sowie der Studienstiftung des deutschen Volkes für ideelle Unterstützung und spannende Seminare und Workshops. Ich danke allen meinen Freunden, die mich auf meinem Weg unterstützt haben und an mich glauben.

Ganz besonders danke ich Hannah für deine Zeit und deine Geduld während der Entstehung dieser Arbeit und für alles was du bist. Ich bedanke mich bei meinem Bruder Fabian, der immer für mich da ist. Zum Schluss bedanke ich mich ganz außerordentlich bei meinen Eltern für ihre bedingungslose Unterstützung und alles was sie mir ermöglicht haben. Dafür bedanke ich mich zutiefst.